Monte Carlo tools and analysis methods for understanding the ANTARES experiment and predicting its sensitivity to Dark Matter.

David J.L. Bailey
Wolfson College, Oxford

Thesis submitted in fulfilment of the requirements for the degree of Doctor of Philosophy at the University of Oxford

Trinity Term, 2002

Abstract

The ANTARES neutrino telescope, which is currently under construction, consists of an array of around 1000 photomultiplier tubes, each of which is sensitive to the arrival of a single photon, instrumenting a cylindrical volume 350 m tall and 180 m in diameter. This array will be deployed, anchored to the sea bed at a depth of 2.4 km, at a site in the Mediterranean approximately 40 km off the south coast of France. By detecting the small amount of Cherenkov light produced by muons (and other charged particles) created in the interactions of high energy neutrinos, it is possible to reconstruct the directions of the neutrinos and attempt to associate them with astrophysical sources.

Using this technique, ANTARES aims to study a range of some of the most energetic astrophysical sources in the Universe (including active galactic nuclei, gamma-ray bursts and galactic micro-quasars) and probe the mechanisms for particle acceleration within these sources. ANTARES is also aiming to identify the nature of the Dark Matter in the Universe by searching for neutrinos produced by the annihilation of Weakly Interacting Massive Particles (WIMPs) which have accumulated at the centre of massive bodies such as the Earth and the Sun and close to the Galactic Centre.

A range of different simulation and analysis techniques are needed to understand the capabilities of the ANTARES detector and its sensitivity to different sources of neutrinos. In this thesis, methods of simulating both the particles produced in high energy neutrino interactions and the response of the detector to these particles are developed and extended. Using these simulations it is shown that, to understand the performance of ANTARES, a detailed understanding of the theoretical and experimental inputs to these simulations is needed, and that, currently, this understanding is severely limited by our knowledge of the optical properties of the water at the ANTARES site.

Using these simulation methods, the expected performance of the ANTARES detector is calculated and an angular resolution of $\sim 0.23^\circ$ and average effective area for muons of around 20000 m^2 corresponding to a differential neutrino flux proportional to E_ν^{-2} is predicted. The overall performance is comparable with other leading experiments in the field and shows that ANTARES can make an important contribution to searches for astrophysical sources of neutrinos. The sensitivity of ANTARES to fluxes of neutrinos produced by WIMP annihilation in the centre of the Sun and of the Galaxy is also calculated for the first time and, depending on the model predictions of the neutrino energies produced in these annihilations, is found to improve on existing experimental limits by up to a factor of five. Furthermore, with this sensitivity, ANTARES will be able to detect or exclude some of the theoretically favoured parameter space for WIMPs with masses between 100 and 300 GeV and will probe regions of this parameter space which are inaccessible to current and planned direct searches for the scattering of WIMPs from nucleons.

To my parents, who have given me the chance to learn throughout my life, and to Helen, who made me realise that some things are even more important.

Acknowledgements

Many different people have helped me in one way or another during the course of this thesis and without whom I would not have reached the point I'm at today. In Oxford, I would like to thank my supervisors: Serap Tilav and Susan Cooper, both of whom have pointed me in the right direction when I've been getting lost and provided much encouragement when the going got tough. I'd also like to thank Susan for being brave enough to read through this thesis and letting me know when I was being unnecessarily obscure. I'd also like to thank Wolfgang Schuster for many interesting discussions and Martin Moorhead who inspired me to become involved in ANTARES in the first place.

I have received help and support from too many members of the ANTARES Collaboration to mention them all individually here but I would particularly like to thank Jürgen Brunner for tirelessly answering my questions on the ANTARES software and Lee Thompson for his support both in my work for ANTARES and during my DPhil in general. I'd also like to thank my other colleagues in the Neutralino Working Group for many discussions, suggestions and new ideas for making my work with them some of my most enjoyable times on ANTARES. Additionally, I'd like to thank Teresa Montaruli for her support and encouragement and for making sure I always had to know what I was talking about.

I would like to thank my wife, Helen, who has kept me focussed on what is really important and made sure that I've kept going, even when I wanted to stop. I would like to thank my family, in particular my parents, who have always supported me in whatever I wanted to do. Finally, I would like to thank one more group of people without whom the last three years would have been far less entertaining. To all my friends both still in Oxford and those who have moved on, I would like to say thank you for being a complete distraction from work and giving my life some perspective. In particular, to Sarah Lipscomb for being the only person more eager to go to the pub than me and to Phil and Sarah Hannay for giving Buffy a home for us all.

Contents

Introduction **1**

1 High energy neutrinos from cosmic sources **3**
1.1 Neutrinos in the Standard Model . . . 3
1.1.1 Neutrinos - past, present and future . . . 4
1.1.2 Neutrino production mechanisms . . . 8
1.2 Cosmic accelerators and cosmic rays . . . 9
1.2.1 Particle acceleration in the Universe . . . 10
1.2.2 Cosmic rays at the Earth and the cosmic ray spectrum . . . 10
1.2.3 Atmospheric muons and atmospheric neutrinos . . . 11
1.3 Neutrinos from astrophysical sources . . . 14
1.3.1 Why look for neutrinos? . . . 14
1.3.2 Neutrino production in cosmic accelerators . . . 15
1.3.3 Candidate astrophysical sources for ANTARES . . . 18
1.3.4 Limits on the astrophysical neutrino flux . . . 19
1.4 Dark matter and the MSSM . . . 20
1.4.1 Dark matter in the Universe . . . 21
1.4.2 Candidates for Dark Matter . . . 23
1.4.3 Dark Matter and Supersymmetry . . . 24
1.4.4 Neutrino production from neutralino annihilation . . . 27
1.5 Summary . . . 31

2 The age of neutrino telescopes **33**
2.1 Principles of detection . . . 33
2.1.1 Neutrino interactions and muon propagation . . . 34
2.1.2 Water / ice Cherenkov detectors . . . 35
2.1.3 Muon reconstruction . . . 36
2.2 Water / ice Cherenkov telescopes and other techniques . . . 37
2.2.1 MACRO, Baksan and Super-Kamiokande . . . 37
2.2.2 Dumand, Baikal and Nestor . . . 38
2.2.3 Amanda and ICECUBE . . . 39
2.2.4 Alternative techniques for high energy neutrino detection . . . 40
2.2.5 Summary of experimental techniques . . . 41
2.3 The ANTARES experiment . . . 41
2.3.1 The ANTARES detector . . . 41
2.3.2 Detector calibration and electronics . . . 44

2.3.3 The ANTARES site . . . 49
2.4 Summary . . . 51

3 Neutrino event generation methods **53**
3.1 Simulation overview and generation requirements . . . 53
3.1.1 Generation geometry . . . 54
3.1.2 Simulation requirements . . . 55
3.2 Neutrino interaction models . . . 56
3.2.1 Simulation tools . . . 56
3.2.2 Neutrino interactions . . . 57
3.2.3 Parton Distribution Functions . . . 62
3.2.4 Overall systematic effects in simulating neutrino interactions . . . 64
3.3 High energy muon propagation . . . 64
3.3.1 Muon energy losses at high energies . . . 64
3.3.2 Maximum muon ranges in rock and water . . . 68
3.3.3 Effective muon ranges . . . 70
3.4 Event generation method . . . 70
3.4.1 Simulation scheme . . . 71
3.4.2 Neutrino fluxes and event weights . . . 74
3.4.3 Verification of the optimisation cuts . . . 78
3.4.4 Results and general discussion . . . 83
3.5 Summary . . . 88

4 Detector Monte Carlo simulation and medium parameters **91**
4.1 Detector Monte Carlo simulation . . . 92
4.1.1 General simulation scheme . . . 93
4.1.2 Photon table generation . . . 94
4.1.3 Muon tracking and shower simulation . . . 98
4.1.4 Muon simulation results . . . 100
4.1.5 Hadronic shower simulation and results . . . 102
4.2 Scattering models and photon absorption . . . 104
4.2.1 Theoretical and empirical models . . . 104
4.2.2 Choice of scattering models . . . 108
4.2.3 Photon absorption at the ANTARES site . . . 110
4.2.4 Effect on the expected arrival times . . . 110
4.3 Arrival time spread from a wavelength dependent refractive index . . . 112
4.3.1 Refractive indices in water . . . 113
4.3.2 Photon propagation simulation . . . 115
4.3.3 Results and discussion . . . 115
4.3.4 Application to the detector MC . . . 117
4.4 Summary . . . 119

5 The ANTARES detector performance **121**
5.1 Reconstruction and analysis methods . . . 121
5.1.1 “Triggering” . . . 122

5.1.2 Reconstruction and selection . . . 123
5.1.3 Angular resolution and efficiency . . . 123
5.2 Systematic errors from event generation models . . . 124
5.2.1 Hadronic shower simulation . . . 125
5.2.2 Parton distribution functions and neutrino cross-sections . . . 126
5.2.3 Muon propagation code . . . 128
5.2.4 Neutrino flux models . . . 130
5.2.5 Summary of systematic effects from the event generation . . . 131
5.3 The effect of the water properties . . . 132
5.3.1 Event rates . . . 132
5.3.2 Angular resolution . . . 134
5.3.3 Summary and conclusions . . . 135
5.4 ANTARES Detector performance . . . 136
5.4.1 Choice of simulation parameters . . . 137
5.4.2 Presentation of effective areas and effective volumes . . . 138
5.4.3 Effective areas for neutrinos . . . 143
5.4.4 Effective areas for muons . . . 148
5.4.5 Muon and neutrino angular resolution . . . 152
5.5 Summary . . . 154

6 ANTARES sensitivity to Dark Matter 157
6.1 Effective volumes for neutrinos from the Sun and Galactic Centre . . . 159
6.1.1 Effective volumes for different selection cones . . . 159
6.1.2 Zenith angle position of the Sun and Galactic Centre . . . 160
6.1.3 Effective volumes for each source . . . 161
6.2 Neutrino effective areas . . . 161
6.2.1 Conversion of effective volumes to effective areas . . . 162
6.2.2 Effective areas as a function of neutralino mass . . . 162
6.3 Atmospheric neutrino backgrounds . . . 164
6.4 Predicted flux limits as a function of M_χ . . . 165
6.4.1 Method of setting limits . . . 166
6.4.2 Neutrino flux limits at the ANTARES detector . . . 167
6.4.3 Muon flux limits at the ANTARES detector . . . 171
6.4.4 Comparison to mSUGRA model predictions . . . 174
6.4.5 Areas for future improvement . . . 176
6.5 Summary . . . 177

7 Summary, conclusions and future prospects 179
7.1 Simulation methods . . . 179
7.2 ANTARES detector performance . . . 180
7.3 Prospects for the future . . . 181

A Effective muon ranges 183
A.1 Effective muon range simulation . . . 183
A.2 Results in a single medium . . . 185

A.3 Results and fits for a general combination of two media . . . 186
A.4 Discussion . . . 187
A.5 Summary . . . 189

B Tabulated data and detailed results **191**
B.1 Event generation tables . . . 191
B.1.1 Neutrino interactions . . . 191
B.1.2 Muon propagation . . . 192
B.2 Detector Monte Carlo tables . . . 197
B.3 Setting limits on Poisson distributed data . . . 198
B.4 Point source neutrino flux limits . . . 199

C Production parameters **201**

D Simulation packages **203**
D.1 Dark Matter . . . 203
D.1.1 DarkSUSY . . . 203
D.1.2 Suspect . . . 204
D.2 Event generators . . . 205
D.2.1 LEPTO . . . 205
D.2.2 PDFlib . . . 205
D.2.3 PYTHIA/JETSET . . . 206
D.2.4 RSQ . . . 206
D.3 Muon propagation . . . 206
D.3.1 MUM . . . 206
D.3.2 MUSIC . . . 207
D.3.3 PropMu . . . 207
D.4 Detector Simulation . . . 207
D.4.1 GEANT 3 . . . 208
D.4.2 Geasim . . . 208
D.5 Summary . . . 208

Bibliography **209**

List of Figures

1.1 Particle content of the Standard Model 5
1.2 Neutrino production mechanisms 9
1.3 Particle acceleration in an Active Galactic Nucleus 11
1.4 The cosmic ray spectrum 12
1.5 Muon and neutrino fluxes at a depth of 2.3 km 13
1.6 Photon absorption on the microwave background 15
1.7 The high energy cosmic ray spectrum 17
1.8 Measured galactic rotation curves 21
1.9 Predicted neutrino fluxes in mSUGRA Dark Matter models 29
1.10 Neutrino energies at the Earth from neutralino annihilation 30

2.1 Principles of detection for a neutrino telescope 34
2.2 Overview of the ANTARES Detector 42
2.3 Line layout for the ANTARES detector 43
2.4 Optical module attenuation and PMT Quantum Efficiency 45
2.5 Angular efficiency of the ANTARES Optical Module 46
2.6 The location of the ANTARES Site 49
2.7 Optical background at the ANTARES Site 51

3.1 Detector geometry definition for the event generation 54
3.2 Neutrino-nucleon charged current cross-sections for Deep Inelastic Scattering 59
3.3 Contribution of resonant and Quasi-Elastic scattering to the total cross-section 61
3.4 Relative neutrino cross-sections for different PDFs 63
3.5 Muon energy loss processes in matter 65
3.6 Average muon interaction lengths and energy losses in rock 66
3.7 Muon survival probabilities and maximum ranges 69
3.8 Overview of the event generation scheme 73
3.9 Comparison of muon neutrino flux predictions 77
3.10 Earth density profile and neutrino absorption 79
3.11 Muon events at the can as a function of the muon range cut 80
3.12 Muon events at the can as a function of the neutrino direction cut 81
3.13 Events at the can for atmospheric and E^{-2} neutrinos 84
3.14 Neutrino vertex locations and muon propagation distances 85
3.15 Neutrino angular distributions 86
3.16 Median muon scattered directions at the can 87

4.1 Detector Monte Carlo simulation overview 95

4.2 Geometry for calculating the photon tables 98
4.3 Number of photons detected as a function of distance 101
4.4 Origin of Cherenkov light generated in KM3 and Geasim 103
4.5 Particle, Rayleigh and overall angular distributions 105
4.6 Henyey-Greenstein angular distributions 106
4.7 Scattering models in the $\lambda_{scat} - \langle\cos\theta\rangle$ plane 109
4.8 Arrival time delay for different scattering models 111
4.9 Water and PMT properties as a function of wavelength 114
4.10 Arrival time delays using the phase and group velocities 116
4.11 Arrival time delays with and without scattering 117
4.12 Arrival time delays for muons in the ANTARES detector MC 118

5.1 Ratio of event rates with and without the hadronic shower 125
5.2 Selected events, interaction and event rates with different PDFs 127
5.3 Event rates and angular resolution with PropMu and MUM 129
5.4 Atmospheric neutrino rates with different flux models 131
5.5 Relative event rates for different water models 133
5.6 Neutrino angular resolutions for different water models 135
5.7 Effective areas for neutrinos 144
5.8 Neutrino flux limits for known point source searches 147
5.9 Effective areas for muons 149
5.10 Muon fluxes for an E^{-2} neutrino flux 151
5.11 Angular resolution for neutrinos and muons 153

6.1 Effective volumes for isotropic upgoing neutrinos 160
6.2 Location of the Sun and Galactic Centre as seen from ANTARES 161
6.3 Effective areas for neutrinos as a function of neutralino mass 163
6.4 Atmospheric neutrino rates as a function of zenith angle 165
6.5 Neutrino flux limits for the Sun and Galactic Centre 168
6.6 Optimum cone sizes for the detection of Dark Matter 170
6.7 Neutrino to muon flux conversion coefficients from DarkSUSY 172
6.8 Muon flux limits for Dark Matter detection by ANTARES after 1 and 3 years 173
6.9 Muon flux predictions from an mSUGRA scan 175
6.10 Predicted muon fluxes and spin-independent scattering cross-sections 176

A.1 Simulation geometry for the effective muon range calculation 184
A.2 Simulated effective muon ranges in rock and water 186
A.3 Fitted effective muon ranges in rock and water 188
A.4 Fit parameters for the muon effective range 189

B.1 Fitted effective muon ranges in rock and water 196
B.2 Neutrino flux sensitivities at different cut-offs 199

List of Tables

3.1 Default and adjusted kinematic limits in LEPTO 58
3.2 Differences between the LEPTO and Gandhi et al. cross-sections 60
3.3 Summary of cut gains in the event generation 83

4.1 Numbers of detected photons for 4 muon energies 101
4.2 Hadronic shower contribution to Cherenkov light production 103
4.3 Scattering models used in the detector performance study 108
4.4 Fit parameters for the Quan and Fry refractive index curve 113

5.1 Averaged muon effective areas 152

6.1 Atmospheric neutrino background rates tracking the Sun and Galactic Centre 166
6.2 90% confidence limits on the signal event rate 167

A.1 Effective muon ranges in rock and water 190

B.1 Neutrino charged-current cross-sections 191
B.2 Mean inelasticities for neutrino charged current interactions 192
B.3 Muon ranges in rock for PropMu as a function of survival probability 193
B.4 Muon ranges in water for PropMu as a function of survival probability . . . 193
B.5 Muon ranges in rock for MUM as a function of survival probability 194
B.6 Muon ranges in water for MUM as a function of survival probability 194
B.7 Effective muon range fit parameters for PropMu 195
B.8 Effective muon range fit parameters for MUM 195
B.9 Petzold's data for the angular distribution of particle scattering 197
B.10 PMT effective areas in ANTARES simulations 198

C.1 Input parameters for the event generation 202
C.2 Input parameters for the detector Monte Carlo 202

Glossary

AGN Active Galactic Nuclei. Galaxies believed to have a central supermassive black hole (i.e. the nucleus) and which show long "jets" of relativistic radio emitting material. The jets provide evidence for particle acceleration.

ANTARES Astronomy with a Neutrino Telescope and Abyss environmental RESearch. An underwater array of photomultipliers currently under construction in the Mediterranean to study astrophysical sources of neutrinos by detecting the Cherenkov light emission from the charged products of neutrino interactions close to the detector.

ARS The front end electronics for the ANTARES PMT. As well as providing control functionality, it digitises the PMT hits either as simple amplitudes and times or as a full waveform. Two ARS work together for each PMT to minimise dead time.

Can A cylinder surrounding the instrumented volume of the detector and exceeding it in size by several hundred metres. It defines the volume within which Cherenkov light is generated in the detector Monte Carlo.

CMB Cosmic Microwave Background. Believed to be a relic of the cooling of the Universe after the Big Bang. Fluctuations in the Cosmic Microwave Background show density fluctations at the surface of last scattering (when the cooling of the Universe allowed neutral hydrogen to form and the photon mean free path increased dramatically). Angular correlations between these fluctuations can provide information on the cosmology of the Universe.

Dark Matter Generically, Dark Matter is any matter in the Universe which is not observed by the emission of electromagnetic radiation. This can include failed stars and planets and free or gravitationally bound particles such as neutrinos or hypothesised massive particles which are relics of the early Universe.

DIS Deep Inelastic Scattering. A scattering process with a large four-momentum transfer where some of the transfered energy is absorbed into the internal degrees of freedom of the target system. Here, it describes the interaction of a high energy muon neutrino with a nucleon via the exchange of a W boson, producing a muon and a range of hadrons in the final state.

GRB Gamma Ray Bursts are some of the most energetic objects in the Universe. They are observed at cosmological distances and typical models involve the collapse or merger of massive objects, releasing huge amounts of energy.

LSP The Lightest Supersymmetric Particle. If R-Parity is conserved, the LSP is unable to decay and therefore, depending on its mass and couplings, is a particle candidate for Cold Dark Matter.

MSSM The "Minimal" Supersymmetric Standard Model. A minimal extension of the Standard Model to include supersymmetric particles and their interactions. It is minimal in the sense that it contains just the particles of the Standard Model and their supersymmetric partners.

OM Optical Module. The basic unit of the ANTARES detector. A pressure resistant glass sphere housing the PMT and its electronics set into a transparent gel which is optically matched with the glass.

PDF Parton Distribution Function. The distribution of particle momenta in nucleons (typically expressed for the proton). It contributes to the calculation of differential and total cross-sections for neutrino interactions.

PMT Photomultiplier tube. A device for detecting single photons using the photoelectric effect and amplifying the signal produced by use of a large potential difference to accelerate the photoelectron onto a series of metal dynodes.

QE Quasi-Elastic scattering. Scattering where the invariant mass, though not the nature, of the target system remains unchanged following the interaction. Here, it refers to the interaction of a neutrino with a nucleon producing a lepton and an recoiling nucleon of the opposite type (e.g. a proton changes to a neutron).

RES Resonant scattering. The interaction of a neutrino with a nucleon producing either an excited state of that nucleon or the Δ resonance and a charged lepton.

Supersymmetry A symmetry of elementary particles relating bosons to fermions and vice versa. In the context of the Standard Model, supersymmetry predicts partners, with opposite statistics but otherwise identical properties, for each of the Standard Model particles. If supersymmetry is realised in nature, it cannot be exact as these partners would already have been observed.

TTS Transit Time Spread. The intrinsic spread in arrival times for a PMT for photoelectrons produced on different areas of the photocathode responding slightly differently to the accelerating voltage. The time resolution for detecting single photons.

WIMP Weakly Interacting Massive Particle. A generic candidate for Dark Matter in the Universe (of which the neutralino is an example). It is favoured by some simulations of structure formation.

Introduction

The ANTARES Experiment [1] is a neutrino telescope which is currently being constructed for deployment in the deep Mediterranean 40 km off the south coast of France. It is aiming to detect high energy neutrinos with energies between 5 GeV and 100 PeV in order to study particle acceleration in astrophysical sources, search for the annihilation of Dark Matter at the centre of the Earth, Sun and the Galaxy and to measure the oscillation parameters of atmospheric neutrinos. In addition, ANTARES will make a contribution to the understanding of the properties of the deep ocean. This thesis will concentrate on two aspects of the above range: high energy neutrino astrophysics and Dark Matter.

The ANTARES detector consists of an array of photomultiplier tubes (PMTs) which will instrument a cylindrical volume roughly 350 m in height and 180 m in diameter. These PMTs will detect the Cherenkov light produced by muons, electrons and charged hadrons created in high energy neutrino interactions within the detector volume and the surrounding medium. The long ranges of high energy muons allows them to be detected even when the original neutrino interaction is some distance away from the instrumented volume of the detector. An accurate measurement of the times and positions of the detected Cherenkov photons allows for the reconstruction of the muon direction, and hence the correlated neutrino direction, and for the possible identification of sources of high energy neutrinos.

In Chapter 1, the properties of neutrinos and their use both in neutrino astrophysics and in searching for the existence of Dark Matter are discussed. A number of pieces of evidence as to why we might expect to observe neutrinos from these sources will also be given. This will be followed, in Chapter 2, by a description of the general technique of large volume water Cherenkov detectors which use PMTs embedded in a transparent natural medium to detect Cherenkov light. Following a brief overview of other experiments in the field, there will be a detailed description of ANTARES, concentrating on the aspects relevant to the simulations and analyses described in this thesis.

In Chapter 3 and Chapter 4, a set of simulations developed and adapted to simulate neutrino interactions and muon propagation in a large volume around the ANTARES detector and the response of the PMTs to Cherenkov light produced by muons, electrons and hadrons passing through the instrumented volume are described. The simulation discussed in Chapter 3 is a method developed to simulate the complete range of neutrino energies visible to ANTARES in an efficient and unbiased way. In doing this, several potential sources of systematic errors are identified and evaluated (either directly in Chapter 3 or in terms of the reconstructed events in Chapter 5). The simulation described in Chapter 4 is one of the standard ANTARES detector Monte Carlo simulations. This simulation has been extended, as described in this thesis, to include the additional Cherenkov light produced by the shower of hadrons at the neutrino interaction vertex and a full wavelength dependent description of the refractive indices in water. A range of different models of the optical properties of the water are also defined for further investigation.

Using the results of the simulations developed in the previous two chapters, we then go on to predict the performance of the ANTARES detector. In Chapter 5, we will investigate the effect of different assumptions in the event generation and detector simulation. We will then calculate the detector performance using a method which is universally applicable and independent of any source model and present the results in a manner which can be used for further calculations or comparisons with other experiments, giving an example calculation for a typical astrophysical source.

Finally, in Chapter 6, we will apply the analysis methods developed in the previous chapter to the problem of the indirect detection of Dark Matter. We will concentrate on the annihilation of Dark Matter at the centre of the Sun and of the Galaxy and derive the limits ANTARES would be able to set after one and three years of observation. We will show both the method used to calculate these limits and how such limits compare to those published by other groups.

The ANTARES experiment is currently in the construction phase and the new developments (in both simulation methods and analysis techniques) described here will hopefully aid the understanding of the first data which the experiment takes. In addition, the analysis described in Chapter 6 will allow ANTARES to search for Dark Matter in the Universe. In more general terms, the work described in this thesis represents a contribution to the aim of building a km^3 scale neutrino telescope in the Mediterranean and beginning the era of neutrino astronomy.

Chapter 1

High energy neutrinos from cosmic sources

In this chapter we describe the place of neutrinos in the Standard Model of particle physics, why they are of interest in general and specifically in terms of their production in astrophysical sources and in the annihilation of Dark Matter. As part of this discussion, we show that power law energy spectra are a typical feature of neutrino fluxes from astrophysical sources and that, using the high energy cosmic ray spectrum, a upper bound can be placed on the neutrino flux from certain classes of sources. We also show that, based on various assumptions about the nature of Dark Matter, integral fluxes of neutrinos up to 10^{12} km^{-2}yr^{-1} could be expected and would be within the sensitivity of upcoming experiments. We also show distributions of neutrino energies from Dark Matter annihilation derived purely from Standard Model physics which we will use in Chapter 6 to relate neutrino energies to neutralino mass in the prediction of the sensitivity of ANTARES for the indirect detection of Dark Matter.

Neutrinos are the most elusive of the particles of the Standard Model. Their interaction cross-sections are so small that huge detectors are required to observe even a few events. Their masses are sufficiently small that they cannot currently be measured, even indirectly, and they are electrically neutral. Although they might appear relatively uninteresting, it is exactly these properties which makes them such a fascinating subject for study.

In this chapter, the basic properties of neutrinos in the context of the Standard Model of particle physics will be discussed and two possible mechanisms of neutrino production outside the laboratory (accelerated protons in astrophysical sources and through the annihilation of Dark Matter particles) will be described. It will then be seen that the detection of neutrinos from these sources would provide important insights into a wide range of subject areas in modern particle physics, astrophysics and cosmology. Some of the techniques required to build, model and understand an experiment which is capable of detecting these neutrinos is then the subject of the rest of this thesis.

1.1 Neutrinos in the Standard Model

The history of neutrinos dates back over seventy years to the early days of particle physics and quantum theory. Today, they present an outstanding problem in particle physics, that of neutrino oscillations, where different types of neutrinos transform as they pass through matter or even empty space. In the future, they promise new insights into fundamental theories of particle physics, astrophysics and cosmology. This rich history and future will be discussed in Section 1.1.1. Despite the current uncertainty in the exact properties of the neutrinos, it is possible to make general statements about the how they might be produced in cosmic sources. These properties will be discussed in Section 1.1.2.

1.1.1 Neutrinos - past, present and future

In this section, the history and significance of neutrinos in particle physics will be discussed and the current measurements of their properties will be mentioned. Finally, there will be a few brief words on the roles neutrinos have to play in the future of physics.

Neutrinos in the past

The existence of the (electron) neutrino was postulated by Wolfgang Pauli [2] in late 1930 to explain the apparent lack of momentum conservation implied by the continuous spectrum observed in radioactive beta decays. It was another 25 years before neutrinos, produced by a nuclear reactor, were discovered by Cowan and Reines [3] in their water, cadmium and scintillator based detector.

Since that time, neutrinos have been artificially produced and used in particle physics experiments in reactors [4] and accelerators [5] around the world. They have also been detected as products of the interaction of high energy protons in the upper atmosphere [6], from the nuclear reactions powering the Sun [7] and, in 1987, from a supernova in a nearby galaxy [8, 9]. This last case was the first and remains the only detection of neutrinos originating from outside the solar system. However, there is a strong expectation that many other extra-solar sources of neutrinos exist and that we may be close to discovering them. The application of one possible experimental technique for this is the subject of Chapter 2. The reasons for believing this detection may be near will be discussed in the remainder of this chapter.

Neutrinos in the present

Following the experimental discovery of the neutrino by Cowan and Reines, neutrinos were first shown to always have negative helicity [10] (i.e. the spin and momentum are aligned in opposite directions) by measuring the helicity of gamma-rays produced during the radioactive decay of Europium-152 (knowing the nuclear spin states of the parent and daughter nuclei in the decay, the helicities of the photon and the neutrino must match). It was then identified that there were at least two different types of neutrino, one associated with the electron and one with the muon from the observation [11] of the production of muons in the interactions of neutrinos produced by charged pion decay (which was already known to decay into final states predominately involving muons). These experiments, along with many others, have

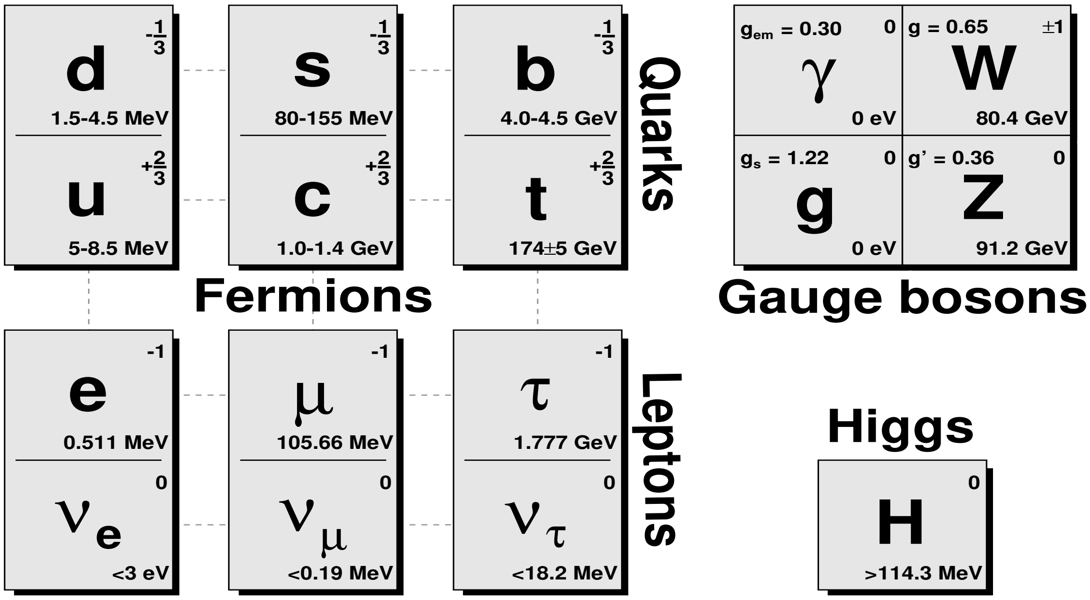

Figure 1.1: Particle content and structure of the Standard Model. Particle masses, charges and the gauge couplings (taken from [12]) are shown. The particles are grouped into the fundamental fermions (quarks and leptons) and bosons and the fermions are further grouped into the three generations of the Standard Model. The electroweak gauge couplings are connected via $g_{em} = g \sin\theta_W = g' \cos\theta_W$ where $\sin^2\theta_W \simeq 0.23$ and are related to the more usual coupling constants by $\alpha = g^2/4\pi$. The strong coupling constant (which runs with energy) is specified at M_Z.

experimentally established neutrinos as neutral partners of the charged leptons and helped to shape our understanding of weak interactions in the Standard Model.

Neutrinos are now understood to be three of the seventeen fundamental particles that make up the Standard Model of particle physics. The particle content, properties and couplings of the Standard Model are shown in Figure 1.1. The fundamental fermions (quarks and leptons) are grouped into three generations of increasing mass. Particle interactions in the Standard Model are mediated by gauge boson exchange: photons for electromagnetic interactions, W and Z bosons for weak interactions and gluons for the strong force.

In the Standard Model, neutrinos are massless, electrically neutral and do not couple to gluons. They only couple to other Standard Model particles via weak interactions mediated by W and Z bosons. In all Standard Model interactions, the difference between the number of leptons and the number of anti-leptons is preserved (lepton number conservation) and, hence, neutrinos are always associated with (i.e. produced with or from) charged leptons of the same generation or produced as particle-antiparticle pairs.

In addition to the basic properties described above, it is postulated that neutrinos can change flavour, or “oscillate”, even when propagating through free space. If neutrinos have mass and the flavour eigenstates (as produced by specific interactions) are not the same as the mass eigenstates, the neutrino flavours can mix. For simplicity, this is normally expressed in terms of the mixing of two flavours as, for example, for oscillations between muon and tau type neutrinos produced as a beam of ν_μ:

$$
\begin{aligned}
P(\nu_\mu \to \nu_\tau) &= \sin^2(2\theta)\sin^2(1.27\Delta m^2 \frac{L}{E}) \\
P(\nu_\mu \to \nu_\mu) &= 1 - \sin^2(2\theta)\sin^2(1.27\Delta m^2 \frac{L}{E})
\end{aligned}
\tag{1.1}
$$

where Δm^2 is the mass difference between the two neutrino flavours (in eV^2), θ is a mixing angle, L is the neutrino path length (in m) and E is the neutrino energy (in MeV). By making measurements (as discussed below) of the disappearance or appearance for different neutrino flavours over different energy ranges and baselines, measurements of the mixing angles and mass splittings can be made and hence provide an insight into physics beyond the Standard Model.

In this thesis, we shall be concentrating on muon type neutrinos (and anti-neutrinos) and their weak interactions via exchanges of W-bosons as these have the most advantageous experimental signatures for the types of experiments discussed in Chapter 2. In the remainder of this section, we shall discuss the experimental evidence for the basic properties of the neutrinos described above. Except where explicitly noted, the values quoted here are the world averages obtained by the Particle Data Group [12]:

Mass No direct measurement of any neutrino mass has been made. Direct limits have been set for each generation from studies of the endpoints of tritium β-decay experiments of less than 3 eV for the case of electron neutrinos, and less than 0.19 MeV and 18.2 MeV from pion and tau lepton decays from accelerator experiments for muon and tau type neutrinos respectively. However, indirect measurements of the neutrino mass splittings (actually Δm^2) from neutrino oscillation experiments as discussed below provide much tighter constraints on the neutrino masses with differences typically less than 1 eV.

Charge Limits have been set on the charges for all three neutrino flavours of around 10^{-14} in units of the electron charge based on observational limits on the energy loss rates of the sun and of red giant stars in globular clusters resulting from the electromagnetic production (and subsequent escape) of neutrinos.

Oscillations Significant discrepancies have been observed between expected fluxes of neutrinos from "natural" sources and measurements. Observations of the ratio of electron to muon type neutrinos produced by proton interactions in the upper atmosphere and measurements of their zenith angle and energy distributions in Super-Kamiokande [13, 14] have consistently shown a deficit of muon type neutrinos compared to expectations. An accurate measurement of both the flux of electron type and the total flux of neutrinos produced by nuclear fusion reactions in the sun by SNO [15, 16] has shown that whilst the total neutrino flux is consistent with solar models, the electron type neutrino flux is deficient by roughly a factor of three.

The hypothesis of neutrino oscillations cannot only describe the general features of these experiments but can also be fitted to the detailed measurements of neutrino fluxes, energy and angular distributions to provide a measurement of the oscillation parameters $\sin^2(2\theta)$ and Δm^2 for each of the mixings. This experimental confirmation of neutrino oscillations implies that at least two of the flavours of neutrinos must be massive (to produce the measured Δm^2) and therefore is one of the first solid indications of physics beyond the Standard Model.

Interactions Neutrinos only couple weakly to other Standard Model particles via the exchanges of W and Z bosons. As seen in Figure 1.1, the electroweak coupling is of similar strength to the electromagnetic coupling - it is the large mass of the W and Z bosons and hence the limited range of their exchange which makes the interactions of neutrinos weak. The subject of neutrino interactions is covered in more detail in Section 3.2 in the context of high energy neutrino-nucleon scattering.

Stability Neutrinos are believed to be stable (within the Standard Model) and, as far as measurements are possible, experimental results support this with lifetimes greater than 50 years for electron neutrinos and 80 μs for muon neutrinos (taking the extremes of the mass and mean life / mass values from [12])[1]. In addition, attempts to fit the neutrino oscillation data including neutrino decays [17] are disfavoured [18] compared to the oscillation hypothesis by the SuperKamiokande data at a confidence level greater than 95%. Finally, limits on the contribution of radiative neutrino decay (i.e. to a lighter neutrino and a photon) to the infrared background from the observation of TeV gamma-ray spectra [19] suggest partial lifetimes longer than 10^{12} years for neutrinos with masses between 0.5 and 2 eV.

Number of families The number of families of light (i.e. lighter than half the Z mass) neutrinos is very well constrained by fits to the Z resonance peak from LEP [12] to 3.00 ± 0.06.

The possibility to make a measurement of neutrino oscillations with ANTARES was first investigated in [20] and further work is still ongoing. For the purposes of this thesis we will neglect this except in assuming that neutrinos coming from astrophysical sources are completely mixed (i.e. have a 1:1:1 flavour ratio) regardless of the ratio of neutrino types produced. We shall discuss the detailed properties of neutrino interactions and how they are modeled for ANTARES in Chapter 3.

Neutrinos in the future

Even though current understanding of neutrinos is lacking in some areas (specifically, in both the origin and size of neutrino masses, mixing angles and whether neutrinos and antineutrinos are distinct), both future experiments and theoretical models are being created to extend our understanding of neutrinos beyond the Standard Model.

Precision measurements of neutrino mass differences, mixings and CP violation are planned at a dedicated neutrino factory [21, 22] which is the subject of much current research

[1]The latter value is more a reflection of the large limit on the mass and the difficulties in performing such an experiment than a particularly strong constraint on the lifetime.

and development. In addition, new experiments to measure solar and atmospheric neutrinos [23, 24] and to look for neutrinos from outside the solar system [25] are planned.

Speculative theories of physics beyond the Standard Model imply unusual properties for neutrinos such as a rapid increase in the neutrino interaction cross-section for centre of mass energies above 1 TeV in low energy quantum gravity models [26] or modified oscillation probabilities in models with large extra dimensions [27]. The details of these models are not critical to this thesis (where the neutrino physics is largely that derived and extrapolated from the Standard Model) but, whatever surprises the future presents us with, it is certain that neutrino physics will have an important influence on our understanding of it.

1.1.2 Neutrino production mechanisms

Neutrino interactions, in the absence of any "new physics", are reasonably well understood and several general statements can be made about how neutrinos are produced in a range of scenarios. This will be relevant in showing that neutrinos are a possible consequence of both astrophysical accelerators (see Section 1.3) and annihilating Dark Matter (see Section 1.4). There are three general possibilities for the production of neutrinos in cosmic sources:

- The interactions and decays of hadrons will, in general, produce charged pions at some point along the decay chain whose primary decay mode ($> 99.98\%$) is to muons and muon neutrinos. The muons then decay (essentially 100% of the time) to electrons and muon and electron neutrinos.

$$\begin{aligned}(\text{hadrons}) \rightarrow \quad \pi^+ \rightarrow \mu^+ + \nu_\mu \rightarrow \quad & e^+ + \nu_\mu + \overline{\nu}_\mu + \nu_e \\ (\text{hadrons}) \rightarrow \quad \pi^- \rightarrow \mu^- + \overline{\nu}_\mu \rightarrow \quad & e^- + \nu_\mu + \overline{\nu}_\mu + \overline{\nu}_e \end{aligned} \tag{1.2}$$

- Particle annihilation to quark, W or lepton pairs which subsequently decay to give neutrinos. For example, for a general particle χ, annihilating in this case to a pair of W bosons:

$$\chi + \overline{\chi} \rightarrow W^+ + W^- \rightarrow \mu^+ + \mu^- + \nu_\mu + \overline{\nu}_\mu \tag{1.3}$$

  The products depend on the annihilation channel but, where quarks, W or Z bosons or muons or tau leptons are involved, the final state will include neutrinos. In this example, the muons would subsequently decay to give more neutrinos.

- During the collapse of massive stars, the temperature and density of the core region increases such that neutrinos can be produced in copious numbers either through charged current absorption and emission processes:

$$\begin{aligned} p + e^- \quad & \leftrightarrow \quad n + \nu_e \\ n + e^+ \quad & \leftrightarrow \quad p + \overline{\nu}_e \end{aligned} \tag{1.4}$$

  or, for all neutrino types, by pair production in electron-positron annihilation:

$$e^+ + e^- \leftrightarrow \nu + \overline{\nu} \tag{1.5}$$

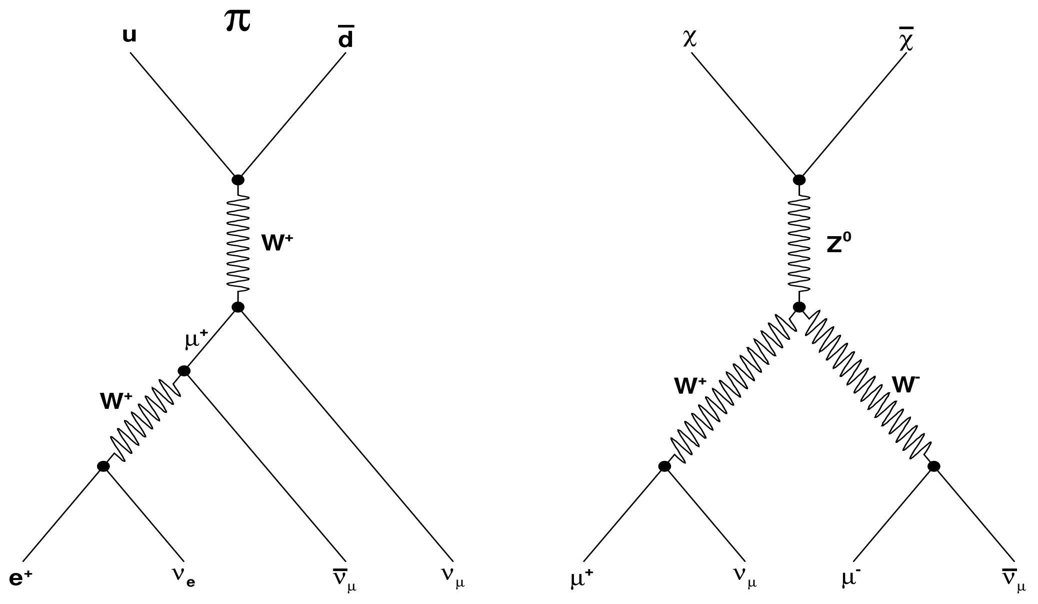

Figure 1.2: Production mechanisms for neutrinos in hadronic decays (left) and particle annihilation (right). Note that the scheme shown in the right hand diagram is purely illustrative as, for a specific particle χ, different annihilations channels may be favoured.

These neutrinos, with typical energies of tens of MeV, diffuse out of the core over a timescale of a few seconds and carry away a large fraction of the gravitational binding energy of the core. What remains is a degenerate neutron star from which the collapsing shell rebounds yielding the supernova explosion.

The first two processes are represented by the diagrams in Figure 1.2. The first will be significant in the production of neutrinos in astrophysical sources, the second in Dark Matter searches. Neutrinos produced in Supernova explosions (as detected by [8, 9]) are of too low energy to be detected by ANTARES and we will therefore not discuss this possibility further.

1.2 Cosmic accelerators and cosmic rays

As in high energy physics laboratories, high energy particles in the universe can be produced by acceleration[2]. The existence of these high energy particles can be deduced from observations on the Earth, both of the electromagnetic radiation produced by various distant objects and from the flux of high energy particles incident on the atmosphere. Although currently not observed directly, it is then only a small logical step to conclude that high energy neutrinos are produced as a result of this acceleration. In the following sections, the observational evidence for particle acceleration and the possibilities for neutrino production will be discussed.

[2]Or, alternatively, from the decay of superheavy particles which are relics of the early universe. This possibility is potentially interesting for the highest energy cosmic rays but is not discussed further here.

1.2.1 Particle acceleration in the Universe

There are several pieces of observational evidence for particle acceleration in various astrophysical objects. Two of the strongest pieces of evidence which have implications for high energy neutrino production are Active Galactic Nuclei (AGNs, see Figure 1.3) and Gamma Ray Bursts (GRBs):

Active Galactic Nuclei Galaxies with long "jets" of radio-emitting material exiting a very compact nucleus. The observed nuclei are sufficiently small that they are believed to be supermassive black holes. The radio emission from the jets is mainly electron synchrotron radiation as high energy electrons are accelerated in the galactic and extragalactic magnetic fields. In addition to the indirect evidence for particle acceleration from the electron synchrotron radiation, sequential images of the radio jets have shown distinct moving "blobs" of material exiting the nucleus with relativistic velocities.

Gamma Ray Bursts Amongst the most energetic objects in the universe producing short "bursts" of gamma rays followed by "afterglows" lasting several months. Their origin is unclear and there are many different models (see the review in [28]) though the short timescale of the bursts (typically of order seconds) imply an intense localised explosion at the heart of the GRB which will produce an electron and photon "fireball". The observation of very luminous bursts with a large fraction of their luminosities above 1 MeV implies [29] that bulk Lorentz factors in the bursts must be significantly larger than unity to allow photons to escape without producing e^+e^- pairs. Furthermore, many models favour beamed jets which again naturally imply acceleration and bulk relativistic motion in the GRB fireball.

The above two categories of objects (as two of many possible examples) show that there is particle acceleration to very high energies in various astrophysical objects. For AGNs, the observation of electron synchrotron radiation only implies that electrons are accelerated. However, were protons (or in general, any hadron) also to be accelerated, then neutrino production would be an inevitable consequence via interactions with the local medium to produce pions and then neutrinos via decay schemes such as that shown in the left hand plot of Figure 1.2. The open question is whether protons are also accelerated and at what level. We shall return briefly to discuss various candidate astrophysical neutrino sources in Section 1.3.

1.2.2 Cosmic rays at the Earth and the cosmic ray spectrum

Arguably the first experiments in particle physics (see [31] for reprints of early papers in cosmic ray and particle physics) involved studying the ionising radiation passing through the Earth's atmosphere, first observed by Victor Hess using an electrometer suspended underneath a balloon at 5000 m above sea level. Following this, the discovery of the positron and the muon in similar experiments marked the start of the field of "cosmic ray physics".

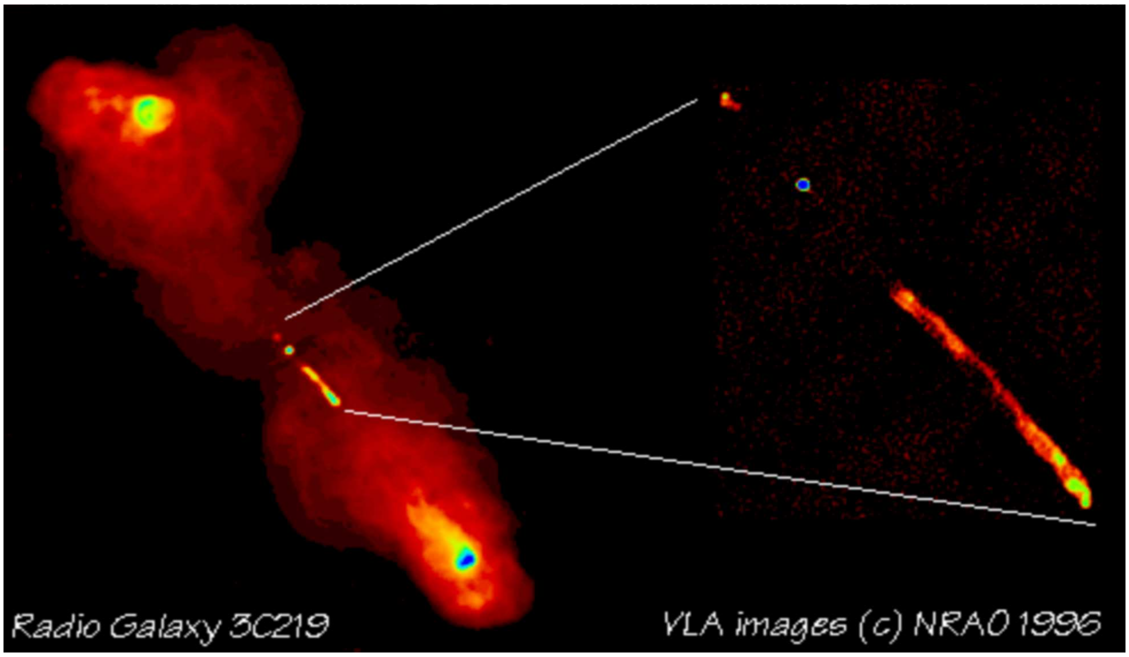

Figure 1.3: Particle acceleration in an Active Galactic Nucleus: VLA Radio image of 3C219 showing two jets with small scale blobs of material close to the core spreading into radio "lobes" as the material is decelerated (taken from [30]).

The cosmic ray spectrum has now been measured over a large range of energies as shown in Figure 1.4. Above 10^{10} eV, the spectrum can be characterised by power-laws over large ranges of energies. The region between 10^{10} and 10^{15} eV can be fitted with a spectral index of around -2.7 and mainly consists of protons believed to originate at the sites of galactic supernovae. For energies between 10^{15} and 10^{17} the galactic magnetic field cannot contain the accelerated particles and the spectrum steepens around the point termed the "knee". The spectral index above the knee is approximately -3 and the flux becomes dominated by heavier nuclei such as carbon and iron [32].

Above 3×10^{18} eV, at the point termed the "ankle", the spectrum flattens again and the composition again becomes dominated by protons. This suggests that the flux at these energies originates from extra-galactic sources (as protons at this energy could not be contained within the galaxy by the galactic magnetic field). In general terms, the hadronic nature of the cosmic ray flux gives clear evidence that there are astrophysical sources in which hadrons are accelerated. The proton dominated cosmic ray flux above the ankle suggests that there are at least some extra-galactic sources which accelerate protons and are hence possible sources of high energy neutrinos.

1.2.3 Atmospheric muons and atmospheric neutrinos

Regardless of their origin, these high energy particles will interact with nuclei in the upper atmosphere and produce pions which subsequently decay to muons. The energy of the muons produced in these decays is such that a significant fraction of them can reach the surface

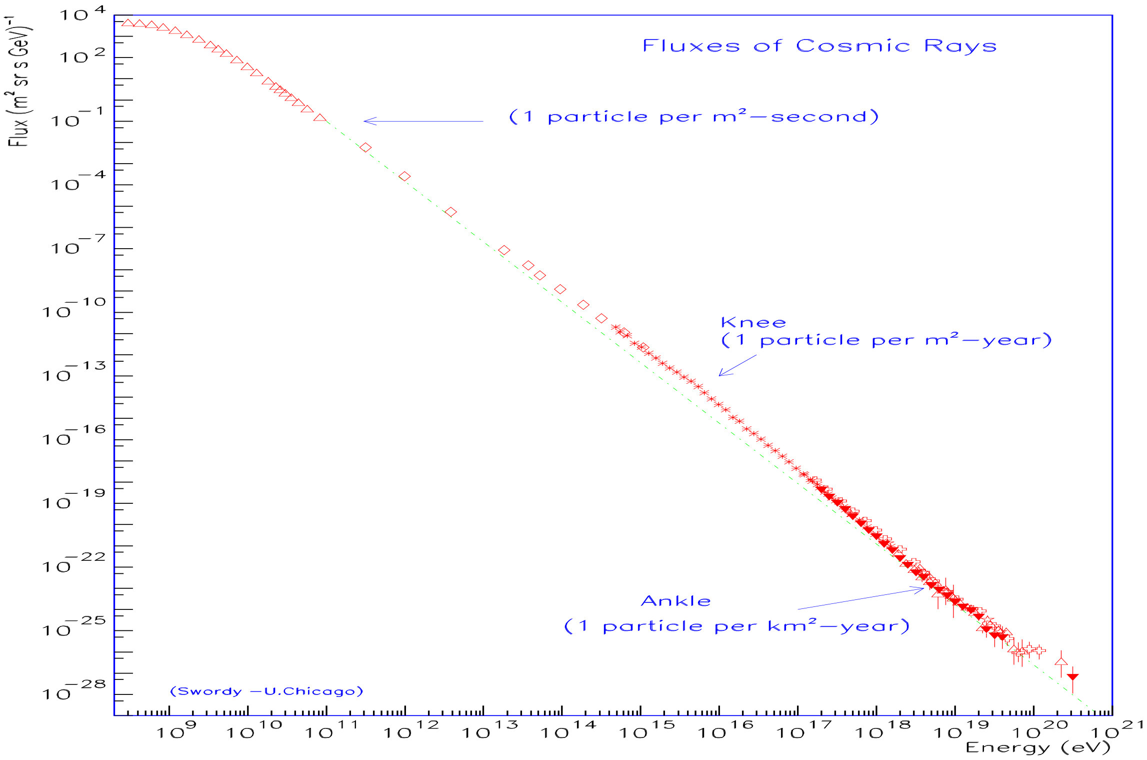

Figure 1.4: The measured cosmic ray spectrum between 10^8 and 10^{21} eV. The spectral index below the knee is -2.7 and steepens to -3 between the knee and the ankle. Above the ankle, it flattens again with a spectral index of -2.7. The data is from the LEAP, Akeno, Fly's Eye, Yaktustk, Proton and Haverah Park experiments [33].

of the Earth and even penetrate to depths of several kilometres before decaying or being stopped. These are termed atmospheric muons.

At any given depth beneath the surface of the Earth, there will therefore be a flux of downward going muons. The muon flux above 1 TeV at a depth of 2.3 km beneath the surface of the sea (corresponding to the site for the ANTARES experiment) is shown in Figure 1.5. These muons will produce measurable signals in a detector which must be understood and rejected to be able to observe the upward going muons produced by neutrinos from any potential astrophysical source. How this is achieved in ANTARES will be mentioned in Section 5.1.

In addition to forming the background to any neutrino signal, the atmospheric muons themselves can carry useful information. Firstly, they can act as a high-statistics calibration of a detector (for example using the reduction in muon flux in the direction of the moon to measure the angular resolution as described in [34] for ANTARES). Secondly, information about high energy proton interactions is contained in the muon flux observed at an experiment (for example, the measurement of the distribution of gluon momenta within the proton as described in [35]).

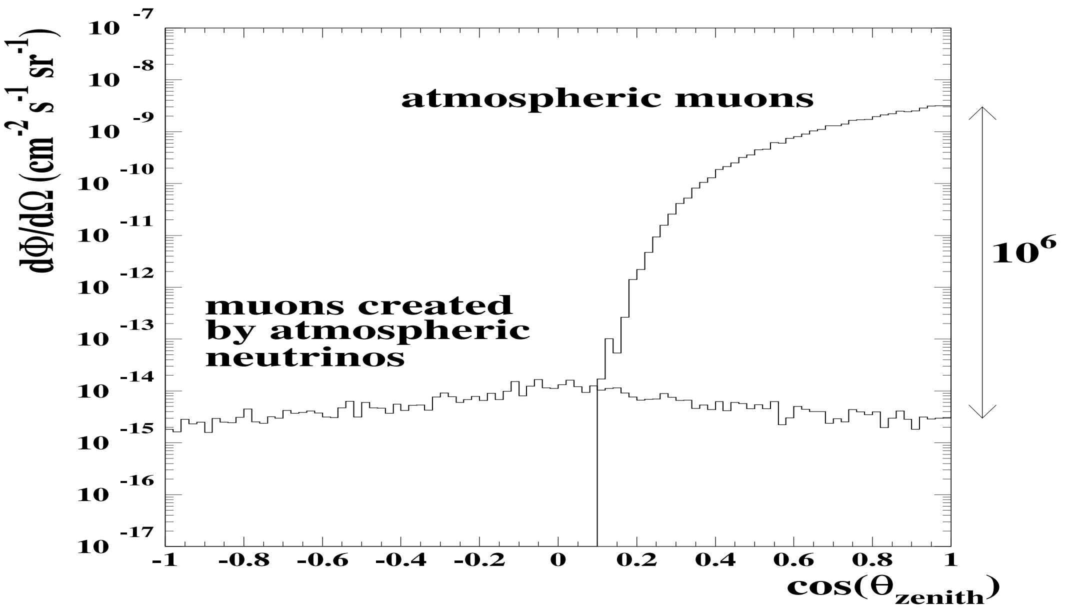

Figure 1.5: Muon and neutrino fluxes above 1 TeV at a depth of 2.3 km in the deep ocean (taken from [1]). For muons coming vertically downwards, the atmospheric muon flux exceeds that from atmospheric neutrinos by a factor of 10^6.

Some (energy dependent) fraction of the atmospheric muons described above will decay in flight in the atmosphere and inevitably produce both muon and electron neutrinos (by a similar scheme to that in Figure 1.2). There is therefore a flux of high energy neutrinos produced by cosmic ray interactions and, as the neutrinos can penetrate the Earth, the flux is from all directions. These are the atmospheric neutrinos.

A small fraction of the muon type neutrinos will interact in the Earth to produce muons, the flux of which is also shown in Figure 1.5. It is upward going muons produced by these interactions which are the characteristic signal of a neutrino interaction near underground and underwater detectors. Numerically, the downward going atmospheric muon flux outnumbers that produced by neutrinos by a factor of order 10^6 as shown in Figure 1.5. The experimental challenge is to be able to identify the upward going muons produced by neutrino interactions from the downward going atmospheric muon flux and is a prerequisite to being able to study neutrinos from any source

Many detailed calculations of the atmospheric neutrino flux have been performed (see [36] for a recent review) and measurements of the fluxes of these neutrinos form the basis of some neutrino oscillation measurements (for example [14]). For the purposes of searches for neutrinos from astrophysical sources and from Dark Matter annihilation (see Section 1.4), these atmospheric neutrinos are one of the backgrounds to the physics signals and hence must be understood. The description of the different atmospheric neutrino fluxes will be discussed in the context of event generation in Chapter 3 and the effect on the observed event rate in ANTARES will be shown in Section 5.2.4.

1.3 Neutrinos from astrophysical sources

It has been suggested that electrons, at least, are accelerated in extra-galactic astrophysical sources and that high energy protons (and nuclei) are observed arriving at the Earth. It is therefore possible that protons are also accelerated to high energy in these sources. If this is the case and these accelerated protons interact within such a source, neutrinos will also be produced via the production of pions as described in Section 1.1.2.

1.3.1 Why look for neutrinos?

Given that neutrinos are so difficult to detect because of their weak interactions, why is it advantageous to study distant, energetic astrophysical sources with neutrinos? There are other, easier ways to study these sources. However, these alternative techniques have inherent limitations:

Photons The most obvious messengers for astrophysical sources - they are produced in large quantities and can be detected over a wide energy range. However, they can be absorbed in the hot, dense sources of interest here and, at energies above a few TeV, interact with the the infrared and cosmic microwave background, producing electron-positron pairs (an effect first noted in [37]). This effect is illustrated in Figure 1.6 showing that, for gamma rays with energies above a few TeV, it is not possible to see much beyond the local group of galaxies.

Protons The arrival directions of cosmic rays can be measured with the intention of associating them with a particular source. However, measurements of the high energy cosmic ray flux have found it to be isotropic. This is as a result of the deviation of the path of the proton by magnetic fields between the source and the Earth. These magnetic fields are sufficiently complex that they essentially randomise the directions of all high energy protons arriving at the Earth except, possibly, at the very highest energies. In addition, at very high energies (above 10^{20} eV), the high energy protons see the cosmic microwave background as gamma ray photons with sufficient energy to produce pions (via the excitation of the-Δ resonance) and are strongly absorbed[3] (the GZK effect [38, 39]). This is also shown in Figure 1.6.

Neutrinos are distinct from other particles in that they are electrically neutral and weakly interacting. They therefore can travel enormous distances without being absorbed or deflected. They can also escape from the dense cores of the potential sources and therefore provide the only direct information on the processes driving the particle acceleration.

Taking this last point one stage further, it is also possible that there are high energy objects in the universe which have not been observed (or at least not observed as energetic sources) as any high energy photons produced will either be absorbed within the source

[3] The observation of cosmic rays with energies greater than this cutoff at 10^{20} eV is an outstanding problem in cosmic ray physics as there appear to be no sources within the cutoff distance capable of producing them.

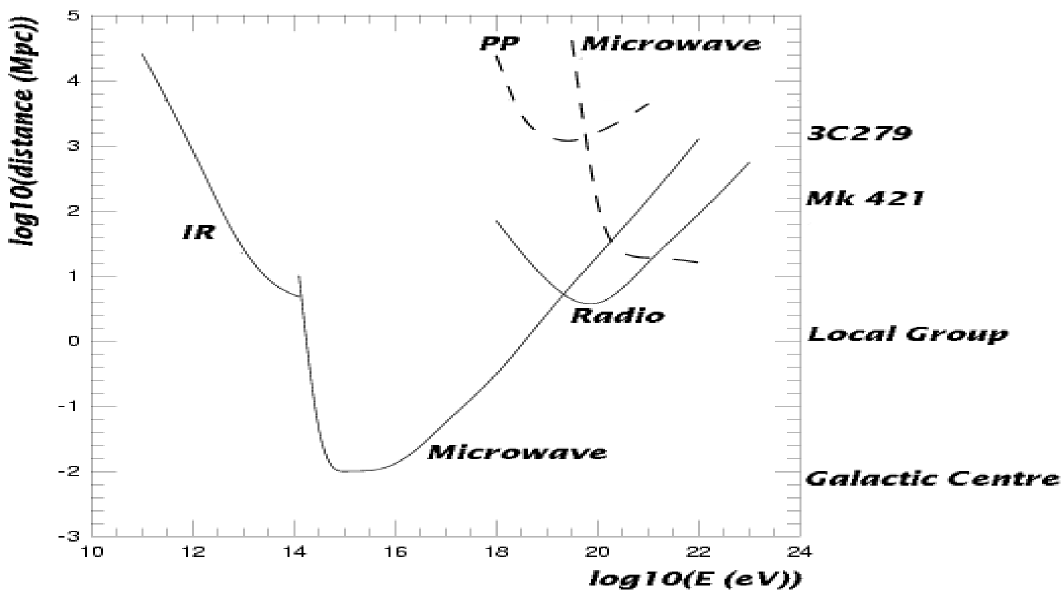

Figure 1.6: The absorption length of photons (solid) on the infra-red, microwave and radio backgrounds and protons (dashed) on the microwave background and via direct pair production. The distances to the galactic centre, nearby galaxies in the local group, the active galaxy Markarian 421 and the gamma-ray emitting quasar 3C279 are also marked (taken from [40]).

or before reaching the Earth. Hence, by searching for high energy neutrinos, there is the potential to discover a previously undetected class of high energy objects[4]. This last point is in itself a powerful motivation for building an experiment to detect high energy neutrinos from astrophysical sources.

If the arrival of these neutrinos at the Earth can be detected and the direction of the neutrino can be measured with reasonable accuracy then it becomes possible to study the production of neutrinos in such sources. As the neutrinos themselves may be the only high energy particles which can escape from these sources, they provide a unique insight into the high energy physics of these objects.

1.3.2 Neutrino production in cosmic accelerators

A common feature of many astrophysical sources (such as those described in Section 1.2.1) is that particles are accelerated as they cross "shocks" (i.e. interfaces between moving regions of material leaving the source with different speeds). There are many different detailed mechanisms for shock acceleration but they all rely on the fact that the net force exerted on individual particles changes on crossing the shock front and hence they experience an

[4]There have been this kind of unexpected discovery with almost every new "window" for astronomy. For example, Karl Jansky's discovery of a strong radio source at the centre of the galaxy whilst investigating the origins of terrestrial radio interference.

acceleration. In this section, we briefly discuss one possible mechanism and show why, in very general terms, it leads to power law energy distributions.

A range of possibilities for particle acceleration is discussed in [41]. Most relevant to the production of high energy neutrinos is what is termed "first order Fermi acceleration" where shocks propagate through the medium with a much greater velocity than the speed of sound in that medium and there is some mechanism which randomises the particle directions (scattering in the complex magnetic fields in the accelerated plasma for example). Consider an already energetic particle on the downstream side of the shock. On crossing the shock front and entering the (more energetic) shocked medium, the particle gains energy and has its direction randomised as it scatters in the shocked medium. Some fraction of these particles will re-cross the shock front and have their direction randomised again. Now, because the shock is strong (i.e. fast), it can catch up with the particles again and repeat the process, potentially many times.

Consider some average increase in particle energy per crossing β and some probability P that the particle remains within the accelerating region by scattering after the shock crossing. For N_0 particles starting with energy E_0 and after k collisions there will be $N = N_0 \times P^k$ particles each with an energy of $E = E_0 \times \beta^k$. We can then eliminate k and calculate the number of particles which reach or exceed an energy of E_n during acceleration:

$$N(E \geq E_n) = N_0 \times \left(\frac{E_n}{E_0}\right)^{\frac{\log P}{\log \beta}} \tag{1.6}$$

Therefore, the number of particles in some energy interval $E \rightarrow E + dE$ is obtained by differentiating the above expression:

$$N(E_n) \propto E_n^{\frac{\log P}{\log \beta} - 1} \tag{1.7}$$

Clearly the above description is much simplified and the parameters P and β will clearly depend on both the source and the scattering mechanism on either side of the shock. However, even from this general treatment we can see that power law spectra (or more generally combinations of power law spectra) are an essential feature of particle acceleration in astrophysical sources and are widely observed (e.g. in the cosmic ray spectrum).

From the above, the choice of the index for the power law spectrum is unknown. In general we will aim to present results for ANTARES in a model independent way which can be applied to a range of potential source models. However, it will also be useful to apply our calculations to some "generic model" of astrophysical neutrinos.

Following the discussions in [42, 43] (which relate the spectra and normalisation of extragalactic neutrino fluxes to the high energy cosmic ray spectrum), the distribution of very high energy cosmic rays (above 10^{19} eV) can be fitted by a cosmological distribution of sources with a differential proton energy spectrum in the source proportional to E_p^{-2} (and modified by an exponential GZK cut-off at 5×10^{19} eV) as shown in Figure 1.7. If some of these protons interact with photons in their sources, they will produce pions which will

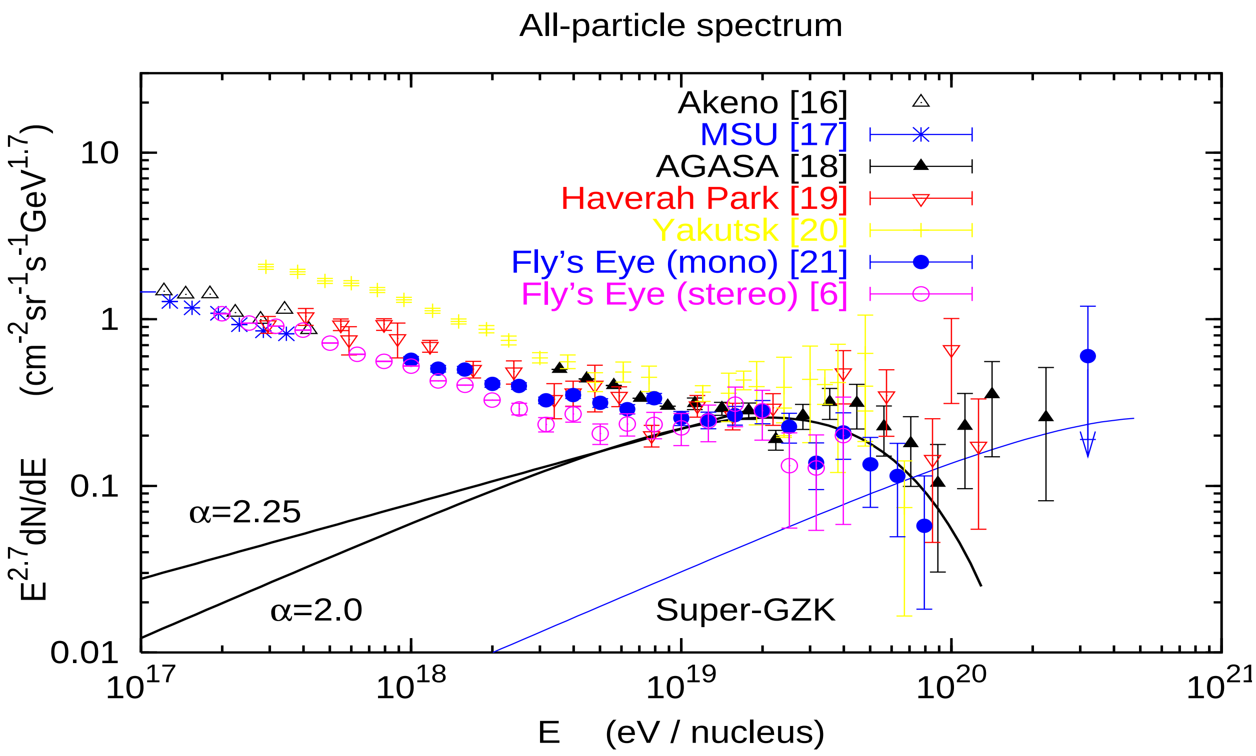

Figure 1.7: The high energy cosmic ray spectrum. The data points show the various experimental measurements. The two curves entering at the bottom left of the plot show fits for a power law spectrum with index α to the data above 10^{19} eV (taken from [43]).

then decay to give neutrinos. Given that the fraction of the proton energy transferred to a neutrino produced in such an interaction is roughly independent of the proton energy [42], the neutrino spectrum should follow the proton energy spectrum at the source and be proportional to E_ν^{-2}.

At this point, we should note that, for the neutrino energies observable in ANTARES, we are relying on an unbroken extrapolation of this high energy spectrum down to much lower energies (neutrino energies of order 100 TeV) where the extra-galactic component would only be a small fraction of the total[5]. Therefore, assuming an E_ν^{-2} spectrum down to these energies, whilst consistent with the overall picture of shock acceleration and the very high energy cosmic ray spectrum, is not necessarily supported by the available data. However, this spectrum is typically used as a generic astrophysical neutrino source spectrum in discussions of general detector performances and in comparing different experiments in the field. In this thesis we shall therefore use it in making general statements about the event generation method described in Chapter 3 and in an example calculation of the performance of ANTARES in Section 5.4. Clearly, this is only a reference point for the wide range of possible astrophysical sources but it does allow for quick comparisons or general statements to be made about different aspects of different experiments.

[5]As seen in Section 1.2.2, the cosmic ray spectrum is dominated by heavy nuclei from galactic sources at the proton energies required (around 10^{16} eV) to produce 100 TeV neutrinos.

1.3.3 Candidate astrophysical sources for ANTARES

In the preceding sections we saw both evidence for cosmic accelerators and high energy hadrons in the Universe and suggested that a connection between the two would imply the production of neutrinos, the observation of which would give a unique insight into the nature of such sources. There are a wide variety of models for specific sources or categories of sources. The emphasis of this thesis with regards to astrophysical sources of high energy neutrinos is in the development of simulation and analysis methods which will aid the understanding of such sources in the ANTARES experiment. We therefore give some general examples of potential neutrino source models to motivate such a study without going into great depth on any particular source (a more comprehensive review of potential sources is given in [44]).

AGNs There are many models of hadronic acceleration and neutrino production in AGNs (for example the proton blazar models of [45, 46]). However, these models are not without controversy: Firstly, protons are harder to accelerate in shocks (as they are more massive and therefore less easily confined to the acceleration region). Similarly, once accelerated, protons lose energy through synchrotron radiation only slowly which is hard to reconcile with the observed variability in TeV gamma-rays [47] on timescales of 15 minutes. Furthermore, the "double-humped" spectral energy distribution of blazars observed at MeV and TeV energies is difficult to reproduce in models dominated by proton acceleration. Finally, observations of AGNs can, in general, be explained by electron synchrotron radiation without the need for proton acceleration. Taken together, these points mean that models of neutrino production from AGNs are considered highly speculative.

Diffuse fluxes Following the approach first described in [48], there are many models where the neutrino fluxes from individual AGNs are integrated to give a diffuse flux of neutrinos which may exceed the atmospheric neutrino flux above 100 TeV. Of course, the detailed predictions depend on the viability of AGN (or other constant neutrino point source) models.

GRBs A currently favoured model of neutrino production in GRBs is that in [49] where protons in the relativistic fireball produced by the GRB photoproduce pions which decay to neutrinos. An alternative is the model described in [50] where relativistic "cannonballs" of matter pass through a supernova shell to produce neutrinos.

Micro-quasars Galactic micro-quasars are believed to be binary systems consisting of a compact object (i.e. a neutron star or black hole) with a massive companion transferring matter to the compact object and exhibiting jets visible in X-rays. If these jets consist of a electron-proton plasma, then it is suggested [51] that TeV neutrinos should be associated with transient events in these objects and [52] then gives predictions of neutrino fluxes at the Earth from these sources.

A detection of high energy neutrinos from these (or other unknown) sources would provide an important insight into both the astrophysical natures of these sources and on the fundamental physics driving the acceleration. The models above suggest that such a detection may be possible with either the current or the next generation of high energy neutrino detectors.

1.3.4 Limits on the astrophysical neutrino flux

In the sections above we gave a highly simplified description of particle acceleration and neutrino production in astrophysical sources and then gave examples of some candidate sources. To motivate the choice of an E_ν^{-2} neutrino spectrum for a generic source we used the shape of the observed high energy cosmic ray spectrum. We can use the normalisation of this spectrum to place an upper limit on the diffuse neutrino flux from extra-galactic sources. Following the approach of Waxman and Bahcall in [42], the maximum neutrino intensity I_{max} $(\nu_\mu + \overline{\nu}_\mu)$ for an E^{-2} spectrum based on fits to the high energy cosmic ray spectrum as shown in Figure 1.7 is given as:

$$I_{max} = 1.5 \times 10^{-8} \xi_Z \ \mathrm{GeV cm^{-2} s^{-1} sr^{-1}} \tag{1.8}$$

where ξ_Z is of order unity and depends on the model for the change of proton emission for different sources at different redshifts. For the purposes of this thesis, we shall take the largest value in [42] of $\xi_Z \approx 3$ (and therefore set the weakest possible bound). This therefore gives an upper bound on the differential neutrino flux, Φ, from extra-galactic sources for both muon neutrino and anti-neutrinos of:

$$\Phi_{\nu_\mu} \leq 2.25 \times 10^{-8} E_\nu^{-2} \ \mathrm{GeV^{-1} cm^{-2} s^{-1} sr^{-1}} \tag{1.9}$$

Finally, we assume that neutrinos in the source are produced in the ratio $\nu_e : \nu_\mu : \nu_\tau = 1 : 2 : 0$ (which is what would be expected from the pion decay processes as shown in Figure 1.2) and that neutrino oscillations over the extremely long distances between the source and the Earth mix these neutrinos into the ratio $1 : 1 : 1$. The upper bound on the ν_μ flux (and similarly the $\overline{\nu}_\mu$ flux) then becomes:

$$\Phi_{\nu_\mu} \approx 10^{-4} \times E_\nu^{-2} \ \mathrm{GeV^{-1} m^{-2} s^{-1} sr^{-1}} \tag{1.10}$$

It is this version of the bound we shall refer to in Section 5.2 when looking at atmospheric neutrino fluxes and in Section 5.4 when considering diffuse neutrino fluxes. This bound is interesting as the flux is close to the experimental sensitivity of the current and next generation of neutrino detectors. However, the robustness of this bound and its applicability to different high energy astrophysical sources is not without controversy:

- It only applies to "optically thin" sources for the photoproduction of pions (i.e. those where the proton mean free path for interaction with photons in the source is larger than the size of the source region). There are therefore classes of sources which can generate neutrinos without adding to the high energy cosmic ray proton spectrum and are therefore not affected by this limit.

- It was noted in [53] that the bound in [42] assumes an extrapolation of the extra-galactic cosmic ray flux (and hence the neutrino flux) from the fitted region above 10^{19} eV to the interesting region for neutrino telescopes around 10^{15} eV. This extrapolation is highly model dependent.

- Also in [53], it was noted that the role of magnetic fields and the uncertainty in the photohadronic interactions of the protons can also affect any bound by a large factor as these effects would restrict the numbers of protons which are able to escape from a source.

The effect of all these points is to weaken any possible bound (which provides fewer constraints from a theoretical point of view but a more accessible range of parameter space for the experiments). However, as discussed in [54], models which evade the bound on these grounds rely on several ad hoc assumptions concerning the optical depth or the size of the magnetic fields and the bound is therefore robust for the vast majority of scenarios[6]. It is also noted in [54] that, depending on the fraction of protons in the observed cosmic ray spectrum between 10^{14} eV and 10^{17} eV, the upper bound could be raised (with a dependence of E_ν^{-1} rather than E_ν^{-2}) for neutrinos energies below 10 PeV which again widens the range of parameter space available to neutrino telescopes which operate in this energy range.

Though there are clearly limitations in determining a bound on the high energy neutrino flux from astrophysical sources, this bound is interesting as it is close to the levels which high energy neutrino experiments are able to probe and therefore gives a target sensitivity for the detection of neutrinos from astrophysical sources. The (original version of the) bound in [42] is often used as a benchmark flux for presenting and comparing results, which is how it is used in this thesis.

1.4 Dark matter and the MSSM

The previous section discussed neutrinos produced by accelerated hadrons either in distant astrophysical objects or by their interactions in the Earth's atmosphere. An alternative mechanism for high energy neutrino production is through the decay or annihilation of heavy particles in the vicinity of the Earth. There is strong motivation for the existence of such particles as relics of the early universe from some extensions of the Standard Model and hence, there is the possibility to make fundamental progress in our understanding of the underlying physics of the universe by searching for neutrinos produced by these particles.

[6] In [54], they do not rule out sources where only neutrinos can escape the source which, by construction, have not been observed as high energy sources. Models of such sources are, by necessity, highly speculative.

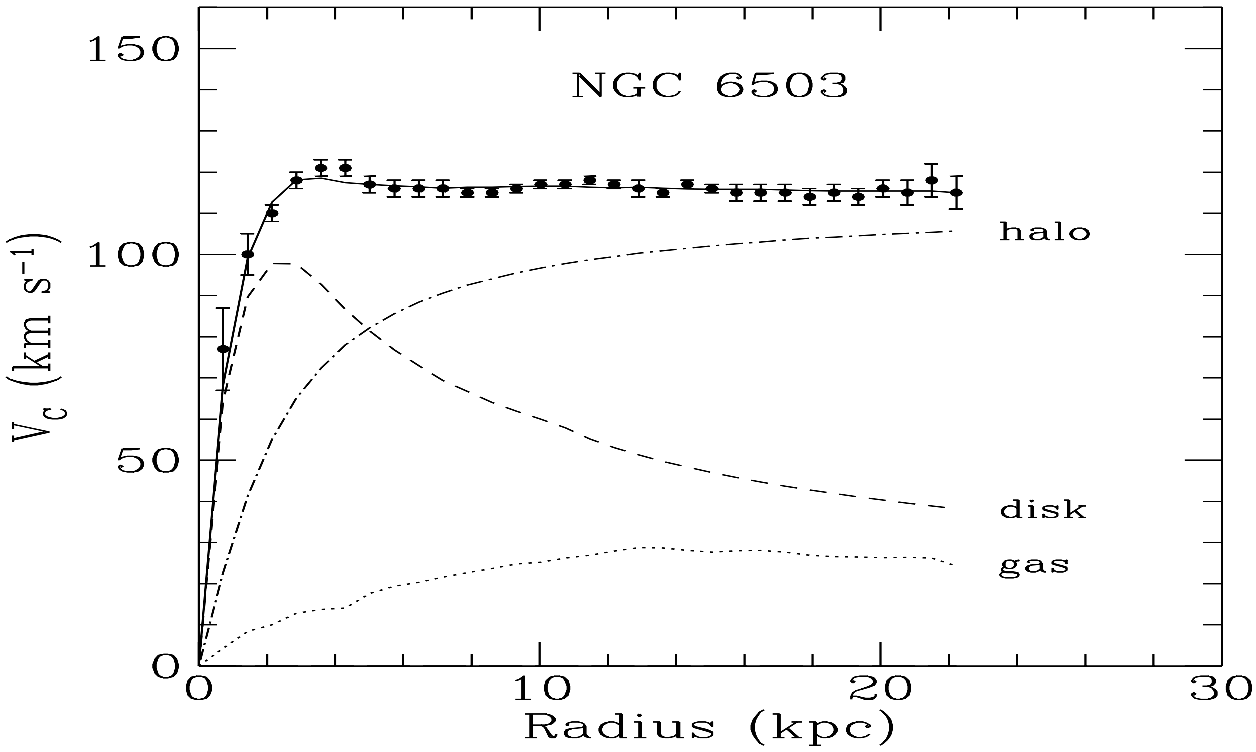

Figure 1.8: The measured galactic rotation curve for NGC 6503 showing the contribution to the mass contained within a radius r in terms of its contribution to the rotational velocity from the luminous matter (disk), the interstellar medium (gas) and the required dark halo contribution (taken from [55]).

1.4.1 Dark matter in the Universe

A variety of measurements suggest that the amount of matter we can directly observe by detecting emitted photons is insufficient to explain a number of other observations (following the review in [55]):

Galactic rotation curves The rates of rotation of spiral galaxies, measured using the microwave emission of neutral hydrogen have a constant value out to radii greatly exceeding the luminous matter in the galaxy as shown in Figure 1.8. Consider the central force (in the plane of the galaxy) on a unit "test mass" at a radius r. This force is proportional to mass contained within that radius. Therefore, we can write the rotation velocity at radius r in terms of the contained mass:

$$\frac{v^2}{r} = \frac{G_N}{r^2}\int_0^r M(r)dr \tag{1.11}$$

where v is the rotation velocity at radius r and $M(r)$ is the mass contained in the interval r to $r + dr$. A constant rotation velocity to large radii therefore implies that $M(r)$ is constant beyond the visible extent of the galaxy and that there is therefore a large "halo" of unobserved matter surrounding the galaxy extending to many times the radius of the luminous matter.

Clusters of galaxies Measurements of the mass of the Coma cluster of galaxies counting the mass in stars (i.e. visible matter), the mass in gas (from X-ray measurements) and the total mass (using the gravitational lensing of distant galaxies) show that the total mass exceeds the contribution from both stars and gas by a significant amount (up to an order of magnitude depending on the methods used). Again, this is a strong indication that there is a large amount of non-luminous matter present.

Big Bang Nucleosynthesis (BBN) The abundances of the light elements (for example helium, deuterium and lithium) can be measured from the strength of their absorption lines in light from distant galaxies. Using predictions of the primordial abundances of light elements in Big Bang Nucleosynthesis [56], recent measurements of the primordial ratio of deuterium to hydrogen [57] from the absorption spectra of quasars imply a baryon density of:

$$\Omega_B h^2 = 0.025 \pm 0.001 \tag{1.12}$$

where h is the Hubble constant in units of km s^{-1} Mpc^{-1} divided by 100 and the density is given in units of the critical density, $\Omega_{crit} \equiv 1$, the total density required to just close the Universe. There is a strong belief (both theoretical and from the cosmic microwave background measurements discussed below) that the total density of the Universe is close to one (in these units). These measurements therefore imply that a significant amount of the density of the Universe is contained in something other than baryonic matter.

The first two points above are evidence that the amount of matter we observe directly is insufficient to explain direct observations (of galactic dynamics and gravitation lensing). The third point implies that less than 10% (with the exact value depending on the Hubble constant) of the critical density of the Universe is contained in baryonic matter.

Recent measurements of the angular power spectrum of the Cosmic Microwave Background (CMB) described in [58, 59] constrain the total density of the Universe to be close to unity. Restricting the analysis to models where the age of the Universe is greater than 10 Gyr and $0.45 \leq h \leq 0.9$, the analysis in [58] finds (with compatible results obtained by an independent analysis of the same data in [59]):

$$\begin{aligned}
\Omega_{tot} &= 1.03\,^{+0.06}_{-0.06} \\
\Omega_B\, h^2 &= 0.021\,^{+0.004}_{-0.003} \\
\Omega_{CDM}\, h^2 &= 0.12\,^{+0.05}_{-0.05} \\
\Omega_\Lambda &= 0.52\,^{+0.20}_{-0.20}
\end{aligned} \tag{1.13}$$

where Ω_{tot} is the total energy density of the Universe, Ω_B is the baryon density and Ω_{CDM} is the density in "Cold Dark Matter" (non-relativistic relic particles as discussed below). Ω_Λ is the energy density due to the "cosmological constant" which is usually associated with the vacuum energy of the Universe.

The total density is compatible with unity and the baryon density is comparable with that obtained from Big Bang Nucleosynthesis calculations and measurements of the abundances of light elements discussed above. Taken together, these two results imply that a large fraction of the energy density of the Universe is contained in something other than baryonic matter. Exactly how much of this "missing density" is contained in Dark Matter is an open question but the measurements above suggest that there is around five times the amount of cold dark matter than baryonic matter.

It is possible to further constrain the above measurements using additional information in the fitting of the CMB spectrum. In [58], the above fits are further constrained by measurements of large scale structure (whose formation depends on the density fluctuations in the early Universe), measurements of type Ia supernovae and placing a stronger constraint on the allowed values of the Hubble constant. These additional constraints reduce the errors on the above estimates (whilst remaining within the ranges quoted above) and provide tighter constraints on the allowed cosmology without altering the qualitative conclusions.

Taking all the points discussed in this section together, there is a great deal of observational evidence that a large fraction of the matter in the Universe is non-baryonic and that such matter is present in the galactic halo (and in the halos of other galaxies). The agreement between the baryon density based on BBN calculations and the measured abundances of the light elements and the analysis of the angular power spectrum of the CMB show that there is a consistent picture of the early Universe and that Dark Matter is a key component of it. Given this evidence for the existence of Dark Matter, we can now go on to look at suitable non-baryonic candidates.

1.4.2 Candidates for Dark Matter

As we saw in the section above, there is a strong body of evidence supporting the existence of a non-baryonic component of the matter in the Universe. However, this is only half the story. We also need a suitable candidate for this component. The requirements on this candidate are that it is "dark" (obviously), that there is a mechanism to produce and preserve a cosmologically significant density from the early Universe and it has properties such that it has not been observed with the current level of experiments. Following the discussion in [55], we can group these candidates into three broad categories:

Hot Dark Matter (HDM) Particles which were moving at relativistic velocities during the era of galaxy formation. One such candidate is the Standard Model neutrino with a mass less than 100 eV. This possibility isn't ruled out by the current limits on neutrino mass and the low interaction cross-section for these relic neutrinos precludes their detection. However, according to modern N-body simulations, such a particle alone cannot account for the formation of large scale structure observed in the Universe today (due to the need to preserve the densitiy fluctuations in the early Universe to allow galaxies to form).

Cold Dark Matter (CDM) Non-relativistic particles produced in the Big Bang. Such particles are favoured by simulations of large scale structure formation. There are several possibilities of which the more promising are axions[7] and WIMPs - Weakly Interacting Massive Particles. This latter candidate is the subject of the analysis in this thesis and, as we shall see below, has a strong motivation in extensions of the Standard Model.

Other possibilities The simplest alternative to either pure HDM or pure CDM is "mixed" Dark Matter which is just some combination of HDM and CDM. Additionally, there are proposals such as primordial black holes, topological defects and modifications of Newtonian gravity on large scales which have not been experimentally ruled out.

As we saw above, one of the favoured generic Dark Matter candidates is a WIMP. It is weakly interacting which ensures it has not been experimentally detected and massive so it can make up the required missing matter. In the next section we shall see that there is a natural WIMP candidate in some extensions of the Standard Model of particle physics.

1.4.3 Dark Matter and Supersymmetry

The Standard Model of particle physics has been remarkably successful (given accurately measured inputs such as particle masses and fundamental coupling strengths) in predicting the results of a wide range of particle physics experiments. In fact, no current experimental measurement has been found to (significantly) contradict the Standard Model. However, this situation cannot persist as there are a number of problems in extrapolating the Standard Model to higher energies.

The fall and rise of the Standard Model

Successful though the Standard Model has been as a theory, there are strong suggestions that it is not the final answer. There are no predictions of the fundamental particle masses and couplings and no explanation of why there are three generations of particles or why masses increase over the three generations. The values of the coupling constants for strong, electromagnetic and weak interactions change with the energy scale of the interaction (due to loop corrections to the tree level interactions) - in the Standard Model they do not converge on a single value at high energies (as is required of a fully unified theory). In addition to the problems with the problems with the Standard Model itself, there is also no real mechanism to include gravity which must become significant at the Planck scale (the energy scale at which gravitational interactions become comparable in strength to electroweak and strong interactions - roughly $M_P \sim (G_N)^{-\frac{1}{2}} \sim 10^{19}$ GeV). This also immediately suggests that, because of the difference in energy scale of the electroweak interactions of the SM and this

[7] Which are motivated by a possible solution to the absence of CP violation in the strong interaction. A large part of the available parameter space for axions has, however, almost been ruled out by searches for axion conversion to photons in magnetic fields.

scale (i.e. the large size of $\frac{M_P}{M_W}$), it is likely that there is some "new physics" somewhere within this range to bridge this gap.

More specifically, the bare mass of the (SM) Higgs boson is subject to radiative corrections from fermion loops which are quadratically divergent and depend on some high energy scale for "new physics" (either the Planck scale or some lower energy unification scale of the strong and electroweak forces, $M_{GUT} \sim 10^{16}$ GeV) to limit these contributions. These corrections will be many orders of magnitude larger than a Higgs mass of below ~ 1 TeV as required by electroweak fits to the SM and would require a remarkable amount of "fine tuning" of the parameters of the SM to ensure these corrections could cancel to give the required Higgs mass. This immediately suggests some new physics beyond the SM at energies of around 1 TeV to avoid this fine tuning of parameters.

One solution to this is to introduce an additional symmetry between fermions and bosons which gives every SM particle a "Supersymmetric" partner with the opposite statistics (i.e. a bosonic partner for each fermion and vice versa) but the same mass and couplings. The presence of these extra particles automatically cancels virtually all of the quadratic divergences in the mass of the Higgs (as they give an identical contribution as the SM particles but with an opposite sign). Such a mechanism also modifies the running of the coupling constants and leads to their unification at high energies. If supersymmetry exists, it cannot be exact (it is said to be broken by some unknown mechanism) as we would have already observed the supersymmetric partners of the SM particles. The supersymmetric particles must, however, be reasonably close in mass to the SM ones otherwise we are required to fine tune our parameters again.

This is a very much simplified account of the failings of the Standard Model and the introduction of Supersymmetry to address some of these problems. This area is discussed in more detail in [60]. Whilst it solves the problem of the Higgs mass and gauge coupling unification, it does so at a cost. The Standard Model has 19 free parameters. General supersymmetric models have over 100 (consisting of the extra particle masses, couplings and CP violation parameters). This makes definite predictions using Supersymmetry very difficult to obtain and generally predictions are given over some scan of the parameter space. The results of one such scan relating to Dark Matter detection will be discussed below.

The Lightest Supersymmetric Particle

We saw above that Supersymmetry can solve the problem of finely tuned radiative corrections to the Higgs mass. However, the most general formulation of supersymmetry would allow protons to decay to a positron and a pion, a process which is very strongly constrained by direct searches (the mean life of which is greater than 1.6×10^{25} from [12]). To avoid this, one can construct a multiplicative quantum number called R-parity:

$$\mathrm{R} = (-1)^{3(\mathrm{B}-\mathrm{L})+2\mathrm{S}} \tag{1.14}$$

where B and L are the baryon and lepton numbers of a particle and S is its spin. This quantity is +1 for Standard Model particles and -1 for their supersymmetric partners (the difference arising from the difference in the spins). If this is conserved, or at least the rate of R-parity violating interactions is very low which is implied by the proton decay searches, then the following must be true:

- The proton is stable (and lepton and baryon number are conserved).
- Supersymmetric particles must be produced in pairs.
- The Lightest Supersymmetric Particle (LSP) is stable.
- Supersymmetric particles must decay into states with an odd number of LSPs.

These last two items mean that if large numbers of supersymmetric particles were produced in the early Universe, they will have decayed to a large number of LSPs which would then be stable and remain until the present day. They therefore make a strong candidate for the WIMP suggested by the evidence for Dark Matter above and we can use the properties of supersymmetric models to make predictions about the nature of Dark Matter in the Universe today. In the discussion that follows, we require that the LSP is the lightest neutralino χ (a mixture of the supersymmetric partners of the photon and Z and Higgs bosons) as this possibility, which is the case for a wide range of models, has suitable annihilation channels for the production of neutrinos.

Supersymmetric models and assumptions

There are many different models of Supersymmetry and not all of them have an LSP which is stable or can exist in cosmologically significant numbers. In the next section we shall describe the production of neutrinos from WIMP annihilation in the context of one model. As we stated above, there can be over 100 free parameters in such models. To make quantitative predictions about supersymmetric Dark Matter, we need some way of constraining these models.

The approach used here to present calculations of neutrino fluxes from Dark Matter annihilation is called "minimal Supergravity" or mSUGRA (see the discussion in this context in [55, 60]). It is assumed that supersymmetry is broken by gravitational interactions with some additional "new physics" beyond the description above which otherwise would only become visible at the Planck scale. One result of this mechanism is that it requires common masses for the scalar particles, m_0, the gauginos, $m_{\frac{1}{2}}$ (and has a common trilinear coupling, A_0 and two other parameters, $\tan\beta$, the tangent of the ratio of the Higgs' vacuum expectation values and a sign, μ). These are all specified at the GUT scale. These can then be related to the particle masses and couplings at low energies using what are termed the "Renormalisation Group Equations" (where the common masses and couplings at the GUT scale are evolved to the individual parameters at electroweak scale depending on the radiative corrections to the bare parameters at different energies).

1.4.4 Neutrino production from neutralino annihilation

In the sections above, we gave experimental support for the existence of Dark Matter and described Weakly Interacting Massive Particles (WIMPs) as a potential candidate. We then pointed out how the Lightest Supersymmetric Particle (LSP) in some extensions of the Standard Model is a natural WIMP candidate. In this section we describe the process where WIMPs in the galaxy can become gravitationally bound at the centres of massive objects and how this can lead to observable fluxes of neutrinos. We then give some example predictions for different parameters in the mSUGRA model.

Neutralino capture and annihilation

In general, we expect a population of WIMPs in the galactic halo (as suggested by the rotation curve measurements described above). The following general mechanism will lead to the production of neutrinos which are potentially observable at the Earth:

- The WIMPs in the galactic halo will pass through massive bodies in the galaxy. Most interesting for terrestrial observers are the Earth and Sun (due to their proximity) and the Galactic Centre (due to the very high mass concentrated at the centre).
- These WIMPs can lose energy by scattering off nuclei in the Earth and Sun (as described in [61] and references therein) or near the Galactic Centre [62].
- Over time, WIMPs concentrate near the centres of these bodies and annihilate producing Standard Model particles. The exact rate depends on the time the WIMPs have had to accumulate and the annihilation cross-section.
- The products of these annihilations will, in general, decay and produce neutrinos. The neutrinos will be able to escape from the centre of these bodies and would potentially be visible as a neutrino flux at the surface of the Earth.

The predictions described in the next section are based on the work described in [61, 63] and correspond to the observable neutrino flux from the Sun. Although these are subject to significant uncertainties in the assumed distribution of WIMPs in the solar system[8] and the calculation of the relic density and annihilation cross-sections in the parameters of Supersymmetry, the general method is well founded. Any predictions made must be considered as possibilities to motive experimental searches rather than definite statements about Dark Matter or supersymmetry.

The original motivation for searching for Dark Matter at the Galactic Centre was given in [62] where the possibility of a strong enhancement, or "spike", in the Dark Matter density close to the central black hole and a corresponding increase in the annihilation rate to a

[8] In [64] a new population of WIMPs from scattering in the planets in the solar system was described. In addition, other authors [65] have modeled "clumpy" halos though this would affect Direct Detection experiments (which depend on the local WIMP density now) more than the indirect detection method described here (which depends on the WIMP densities averaged over a long time period).

level where neutrino flux is accessible to the current generation of experiments. However, the expected synchrotron emission from the annihilation electrons and positrons in such a process gives values which exceed current experimental observations by many orders of magnitude [66] leading to the exclusion of the models in [62]. This constraint can be avoided if the neutralinos have masses approaching of order 1 TeV (which does, however, imply lower annihilation rates as fewer WIMPs are needed to make up the Dark Matter) and furthermore, the above synchrotron emission can then be used to explain the radio observations of the galactic centre [67].

However, it has also been noted that dynamical effects of the growth of the central black hole will disrupt the formation of the spike and exclude the possibility of a neutrino signal [68]. Specifically, for a spike which is sufficiently pronounced to give a detectable neutrino signal to form, it is concluded that the majority of black hole growth must occur within 50 pc of the centre of the Dark Matter halo and that the growth must have occurred on timescales longer than 10^7 years. If the black hole is formed outside this distance and falls into the centre of the Dark Matter halo, or is formed from a violent merger of two or more black holes, then the growth of the Dark Matter spike would be disrupted and there would hence be no neutrino signal. Although conditions suitable for the formation of the Dark Matter spike are not inconceivable, they are by no means favoured. As a result of this, we must note that a null result from the galactic centre does not necessarily allow us to place limits on either Supersymmetry or the nature of Dark Matter.

Whilst the possibility of neutrinos from neutralino annihilation at the centre of the Sun can be reconciled with current experimental knowledge, it is much harder to support the idea of neutrinos from neutralino annihilation from the Galactic Centre. However, for the purposes of this thesis (specifically the analysis in Chapter 6), we proceed from an experimental point of view and estimate our sensitivity for both possibilities.

Predicted neutrino fluxes

We can see from the sections above that there is strong evidence for the existence of a non-baryonic form of Dark Matter and a suitable candidate for it in Supersymmetric extensions of the Standard Model. We have also seen that there is a mechanism by which these particles can produce a flux of neutrinos from the centre of the Sun and Galaxy.

In Figure 1.9, we show predicted neutrino fluxes from the Sun corresponding to neutralino annihilation across the $m_{\frac{1}{2}} - m_0$ parameter space of mSUGRA taken from work performed within the ANTARES Collaboration (from [69, 70] with similar results found elsewhere in e.g. [71]). For the results in Figure 1.9, the other mSUGRA inputs (for reference: $A_0 = 0$, $\mu > 0$ and $\tan\beta = 45$) are given at the GUT scale and correspond to similar regions of parameter space as studied for accelerator experiments (see, for example the ATLAS reference points in [72]). These parameters are evolved to the electroweak scale using the Suspect [73] package to give the particle masses and couplings. In this it is required that electroweak symmetry breaking (EWSB) occurs and that the lightest neutralino is the LSP. These are then taken as inputs for DarkSUSY [63] (described in more detail, along with the other simulation codes used in this thesis, in Appendix D) which gives predictions of

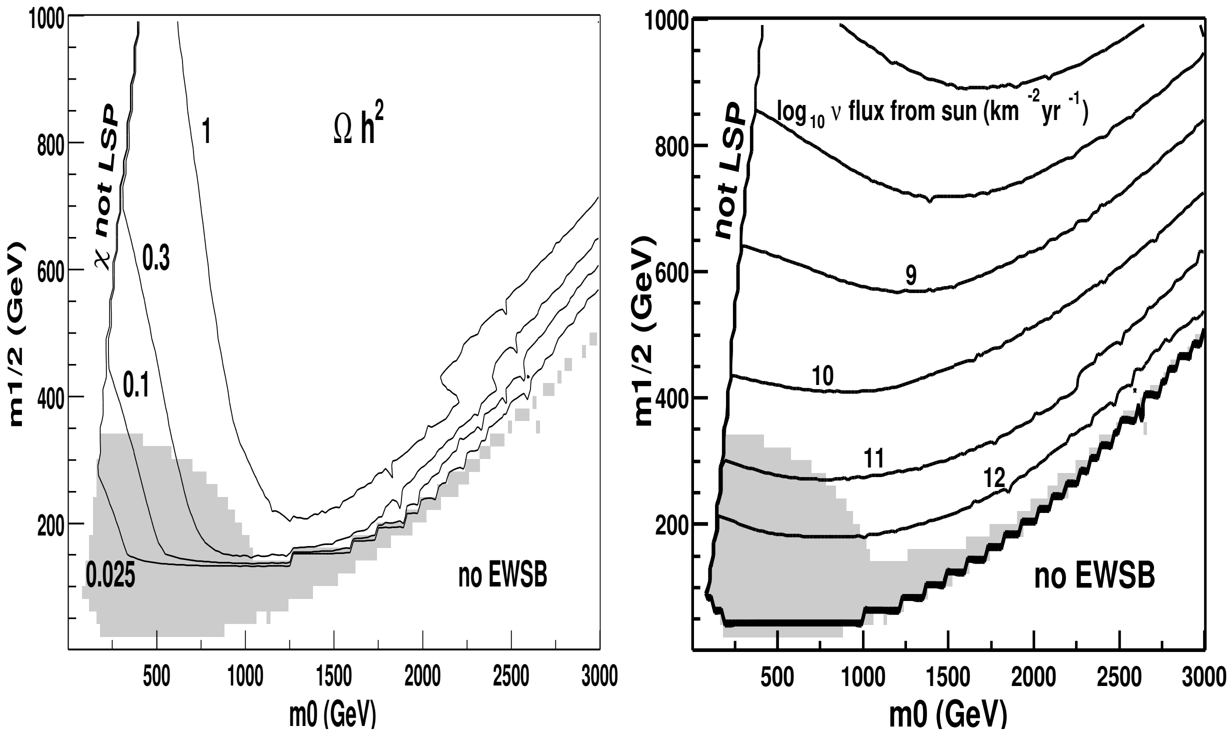

Figure 1.9: Dark Matter models in the $m_{\frac{1}{2}} - m_0$ parameter space. The left hand figure shows the allowed regions of parameter space constrained by requiring EWSB occurs, the χ is the LSP and a cosmologically significant density of WIMPs is predicted. The shaded region is excluded by accelerator constraints. The right hand figure shows the predicted integral neutrino flux for the same region. Neutrino fluxes over 10^{12} km^{-2}yr^{-1} are predicted for some regions of parameter space (taken from [69]).

the integral neutrino flux at each point as shown, applying accelerator and cosmological constraints to exclude unphysical models.

At each point in the parameter space shown in Figure 1.9 not only can we predict the integral neutrino flux, but we can also calculate the expected muon fluxes on a surface in the Earth and the direct couplings between the WIMPs and nucleons. Using these, we can compare the sensitivity of indirect detection experiments searching for muons produced by neutrinos from Dark Matter annihilation to these model predictions and compare indirect detection experiments to direct detection experiments, which search for WIMP-nucleon scattering. We shall perform these comparisons for the expected sensitivity of ANTARES in Chapter 6.

Neutrino energy distributions from neutralino annihilation

Above we saw some examples of predicted integral neutrino fluxes for different Dark Matter models. As stated previously, the neutralino annihilation is assumed to be to Standard Model particles which then decay to give neutrinos. The mSUGRA parameters taken as inputs to the models give the neutralino mass and its branching ratios into different channels (pairs of

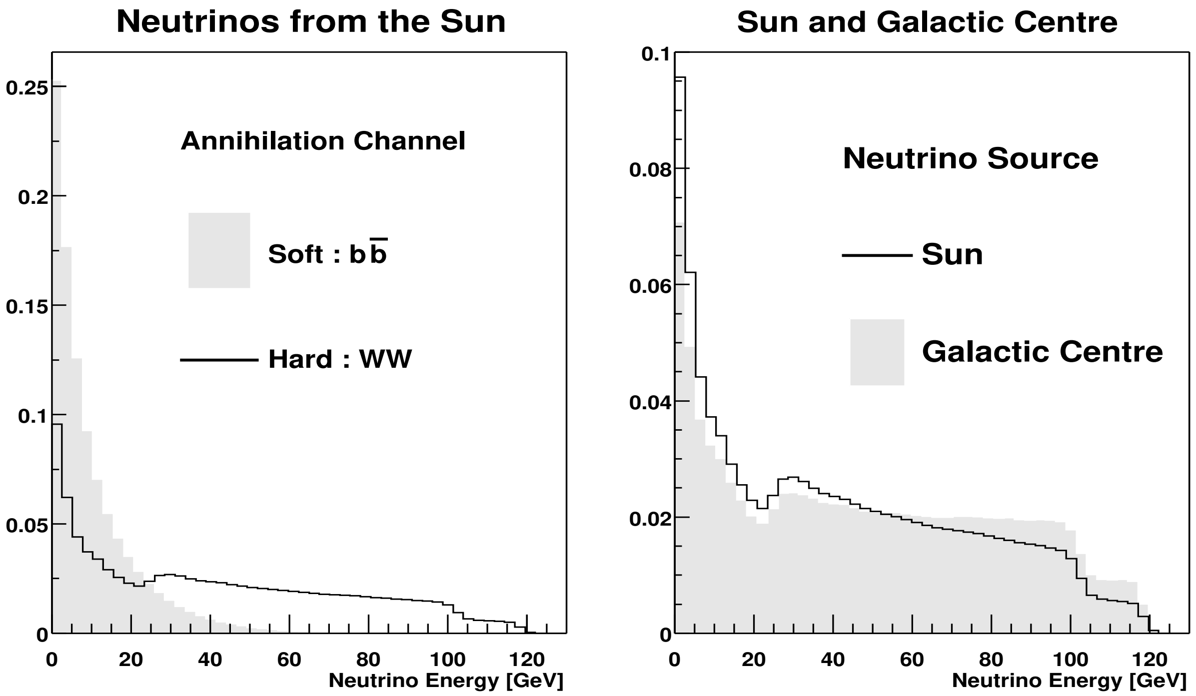

Figure 1.10: Hard and soft neutrino energy distributions from neutralino annihilation from the Sun and comparing the Sun and Galactic Centre for the hard channel. The neutralino mass is 130 GeV in these cases.

gauge bosons, quarks or leptons). The branching ratios will be different for each point in the supersymmetric parameter space and each model will therefore give a different distribution of neutrino energies.

In the analysis described in Chapter 6, we will aim to estimate the sensitivity of the ANTARES experiment to the indirect detection of neutralinos of different masses. Therefore, we need some connection between the neutralino mass and the distributions of neutrino energies it produces. To reflect the complete range of models (with their different branching ratios), we therefore take the two extremes of neutrino energy distributions for each neutralino mass: "soft", giving the lowest energy neutrinos and typically corresponding to annihilation to heavy quarks[9] and "hard", giving the highest energy neutrinos corresponding to annihilation to W pairs (or τ pairs below $M\chi = M_W$).

In Figure 1.10 we show the hard and soft neutrino distributions for neutralino annihilation in the Sun and the Earth corresponding to a neutralino mass of 130 GeV as calculated by DarkSUSY which in turn uses parameterisations of particles decays and the subsequent hadronisation from PYTHIA [74]. Note that all the information contained within these plots is based on Standard Model physics - by selecting the extreme neutralino annihilation

[9] The annihilation cross-section to fermions is proportional to $(\frac{m_f}{m_\chi})^2$ [55] and therefore annihilation to light quarks is strongly suppressed and can, in general, be neglected. For the same reason, direct annihilation into neutrinos is forbidden.

channels, we can assert that for any specific supersymmetric model, we will observe a neutrino energy distribution somewhere between those shown here.

In the left hand plots of Figure 1.10 we can see the difference between the hard (W^+W^-) and soft ($b\bar{b}$) distributions for a neutralino mass of 130 GeV with both distributions normalised to unity. There is a clear difference in both the shape of the distributions and therefore the fraction of decays which would produce events above some energy threshold. This effect will be seen in the results in Chapter 6.

For neutrinos annihilating at the centre of the Earth, the column density of matter between the annihilation site and a detector at the surface of the Earth is insufficient to significantly affect the neutrino energy spectrum. Within DarkSUSY, there are no direct predictions for the neutrino energies from the Galactic Centre. However, the column density of matter is also relatively small and most of the neutrinos produced by neutralino annihilation arise from short lived particles which will decay before the immediate medium has a significant effect so we can use the predictions for the neutrino energies from the Earth[10].

For the Sun, the column density of matter from the centre to its surface can be significant and cause the higher energy neutrinos (which have the higher interaction cross-sections) to be preferentially absorbed giving an overall lower energy (or softer) spectrum. This is implemented in DarkSUSY based on parameterised Pythia simulations and is shown in the right hand plots of Figure 1.10. This difference will be seen in the results in Chapter 6 where we will use the differential distributions shown above to relate neutralino mass to neutrino energies in the detector.

1.5 Summary

In this chapter we have described the properties of neutrinos and why they are of interest in modern experimental and theoretical particle physics and in astrophysics.

- We have described the place of neutrinos in the Standard Model of particle physics and given two general examples of how they might be produced by accelerated hadrons or particle annihilation (Section 1.1).
- We described two general pieces of evidence for particle acceleration in astrophysical sources in the Universe and for accelerated hadrons arriving at the Earth. These hadrons also produce both muons and neutrinos in the atmosphere which is their direct relevance in this thesis (Section 1.2).
- We described why neutrinos are a unique source of information about the high energy Universe and gave an example of a potential acceleration mechanism in shocks in

[10] It is possible that for some models for the Galactic Centre there will be an additional contribution from e.g. muons which can propagate some distance and decay before being stopped. This will have the effect of both increasing the integral neutrino flux in the model predictions and producing a much softer spectrum which will result in higher flux limits. However, as both the neutrino flux predictions and the limits we set are affected in the same manner, this will not affect any conclusions drawn with respect to specific models provided the same assumption is made consistently.

astrophysical objects. This mechanism suggests both potential astrophysical sources of neutrinos and how they can be related to the observed cosmic ray flux (Section 1.3).

- We described the evidence for the existence of Dark Matter in the Universe and suggested that a particle candidate in some extensions of the Standard Model is a possibility (Section 1.4).
- We described how these particles can accumulate at the centres of massive bodies and annihilate to produce neutrinos. We can also use models of Dark Matter annihilation to make predictions of the expected neutrino flux to motivate indirect searches for Dark Matter in the current generation of neutrino detectors (Section 1.4.4).

We have tried to concentrate on general reasons for expecting neutrinos from astrophysical sources and from Dark Matter annihilation. For the former, this is motivated by the observation of astrophysical accelerators and high energy protons (and nuclei) arriving at the Earth. Using a generic model of shock acceleration in astrophysical sources we can see that power law spectra are an essential feature of such sources and a range of potential models exist. A limit can also be placed on the expected neutrino flux from some classes of source (Eq. (1.10)) and this is used as a benchmark flux in the rest of this thesis.

Whilst the evidence for Dark Matter itself is reasonably strong and the LSP (here required to be the neutralino) in supersymmetric extensions of the Standard Model provides a well motivated candidate, individual model predictions are subject to a large degree of uncertainty (not least in the details of supersymmetry, assuming that it exists at all). The general mechanism for neutrino production by neutralino annihilation is reasonable but the range of possible models is huge.

For these reasons, we choose not to develop simulations or analyses based on any particular model for either astrophysical neutrino sources or Dark Matter annihilation. Instead, the approach adopted in this thesis is to develop simulation and analysis methods capable of making general predictions about the performance of the ANTARES experiment (which will be described in Chapter 2) and its sensitivity to a wide range of possible astrophysical and Dark Matter models.

Finally, in terms of the prediction of the sensitivity to Dark Matter (see Chapter 6) we do need some input from theoretical models to connect the neutralino mass to the neutrino energy distribution it produces on annihilation. In this we take two extremes for the branching ratios into Standard Model particles to cover the range of possible models. This ensures that our estimates cover all the possible parameter space and depend only on Standard Model physics.

Chapter 2

The age of neutrino telescopes

In this chapter we shall describe the general principles by which high energy neutrino telescopes operate. We shall then give a brief overview of other experiments in the field which employ this technique or have been used to address similar areas of physics (as described in Chapter 1). Finally, we shall give a description of the ANTARES experiment in terms of its general construction and with respect to the calibration and environmental factors which could affect its performance. We will show that these factors are either taken into account in the simulations developed in Chapter 3 and Chapter 4 or can be safely neglected.

As seen in the previous section, neutrinos have a number of unique properties which makes them a powerful tool for studying high energy astrophysics and Dark Matter (amongst other topics). Foremost amongst these is their low interaction cross-section with any kind of matter which allows them to escape otherwise obscured sources, reaching the Earth undeflected and relatively unattenuated. However, this also makes them incredibly difficult to detect. In this chapter, a general technique to detect high energy neutrinos is described and a brief overview of the history of such experiments is given. The link between these experiments and astrophysics and the aim of accurately determining the directions of the detected neutrinos often leads to these experiments being called "neutrino telescopes". The ANTARES experiment [1], on which this thesis is based, is one example of such an experiment. The final section of this chapter is dedicated to the details of ANTARES which are relevant to the topics discussed in the remaining chapters of this thesis.

2.1 Principles of detection

Neutrinos arrive from all directions at a given site for a detector. A small fraction of these neutrinos interact with the material surrounding the instrumented volume of the detector producing high energy charged particles. The detectors themselves are typically arrays of Photomultiplier Tubes (PMTs) in a transparent medium. Those particles which approach the instrumented volume of the detector are detected by their Cherenkov light emissions. An overview of this process is shown in Figure 2.1.

The neutrinos arriving at the detector can pass through the Earth but cosmic ray muons (and other particles) cannot. Whereas the downward going flux of muons produced by cosmic ray interactions (as shown in Figure 1.5, page 13) greatly exceeds that from neutrino

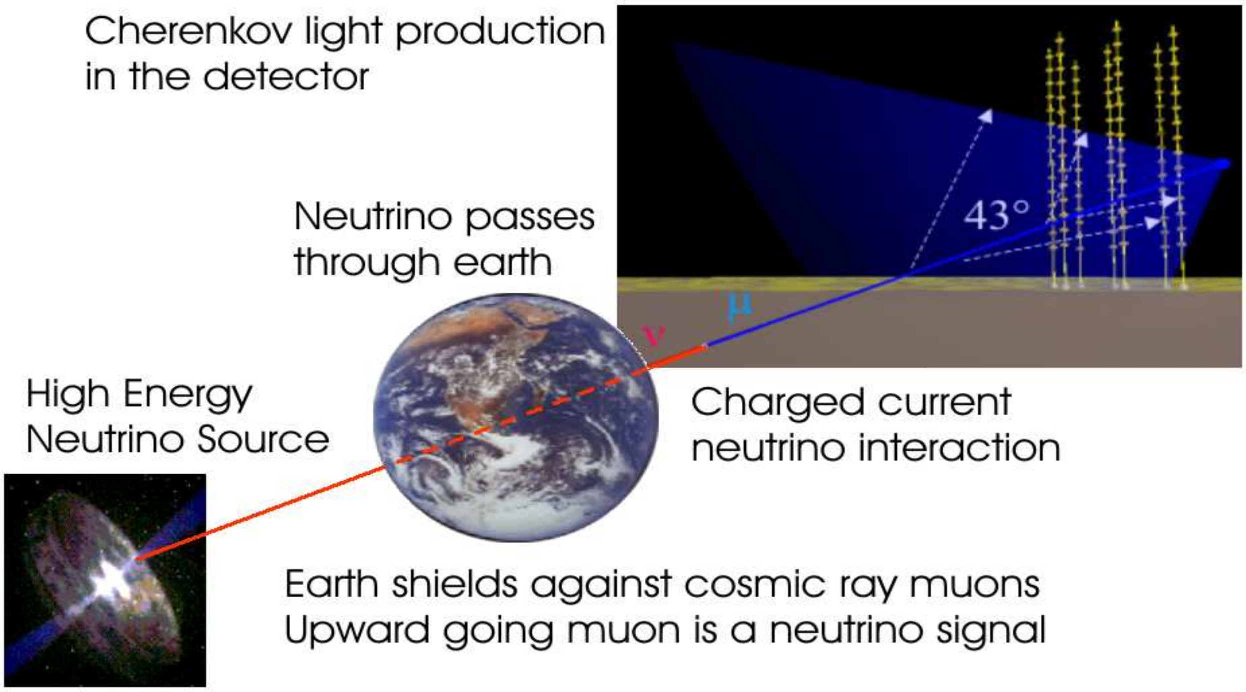

Figure 2.1: Principles of detection for a neutrino telescope showing the creation of upward going muons which pass through the detector emitting Cherenkov light. Searching for upward going muons uses the Earth as a shield against cosmic ray muons and therefore such an observation provides an unambiguous signal of a neutrino interaction near the detector.

interactions, the observation of an upward going muon will be an unambiguous signal of a neutrino interaction near the detector. A measurement of the direction of the muon passing through the detector will then allow the neutrino direction to be inferred (they are almost co-linear for high energy neutrino interactions as will be discussed in Chapter 3) and associated with a particular source.

2.1.1 Neutrino interactions and muon propagation

In terms of neutrino astronomy and Dark Matter searches, the most interesting interactions are muon neutrino (or anti-neutrino) charged current interactions with nucleons which produce high energy muons with extremely long ranges in matter (compared to electrons which produce compact showers of particles and tau leptons which decay quickly). This allows muons produced some distance away from the instrumented volume of the detector to be observed. The basic interaction is:

$$\nu_\mu + N \longrightarrow \mu^- + X \tag{2.1}$$

where N is either a proton or a neutron and X is, in general, one or more hadrons forming a shower at the neutrino interaction vertex.

The details of this interaction and how it is simulated in the ANTARES experiment will be discussed in Chapter 3 including a detailed evaluation of the simulation packages used and their limitations in Section 3.2. The interaction becomes more favourable for the observation of neutrino interactions at high energies due to the steeply rising neutrino cross-section (which is roughly proportional to energy up to 10 TeV).

Similarly, the range of the produced muon increases with energy (roughly proportional to the log of the starting muon energy) which again favours the observation of high energy neutrinos. Clearly, the details of muon energy losses in matter will be critical in understanding the expected rate of events from a particular source. This is investigated in Section 3.3 using two different simulation codes.

Both of these potential gains with increasing energy are offset to some extend by the steeply falling power law neutrino fluxes typical of astrophysical sources as seen in Section 1.3. The competition between these effects will determine the muon flux observed at the detector for a given source and hence how likely ANTARES is to be able to observe it.

An additional reaction of interest is that of electron type neutrinos producing large electromagnetic showers within the detector. This has been studied in detail for ANTARES as described in [75] with a dedicated simulation and analysis method but will not be discussed further here as it is, in general, less efficient than detecting long range muons from muon neutrino interactions as the shower has to be contained within the instrumented volume.

2.1.2 Water / ice Cherenkov detectors

High energy particles moving through a medium with a velocity greater than the speed of light in that medium give off visible light with a wavelength spectrum proportional to $\frac{1}{\lambda^2}$. This process is known as the Cherenkov effect and corresponds to the coherent emission of electromagnetic waves along the relativistic particle track.

For a particle moving through a medium with refractive index n where the particle velocity $\beta \left(= \frac{v}{c}\right) > \frac{1}{n}$, the number of photons, N, generated within a wavelength interval $d\lambda$ per unit distance dx is given by the Frank-Tamm formula (derived from the $\frac{dE}{dx}$ relation given in [76]):

$$\frac{d^2N}{dxd\lambda} = \frac{2\pi\alpha}{\lambda^2} \times \left(1 - \frac{1}{\beta^2 n^2}\right) \tag{2.2}$$

If we take a wavelength range of 300 nm to 600 nm (which will be seen to roughly correspond to the sensitive range of ANTARES in Section 2.3) and a typical refractive index for water of 1.35, assuming that $\beta = 1$ and n is approximately independent of wavelength in the range given above, we can integrate Eq. (2.2) to give the number of Cherenkov photons per unit distance as:

$$\frac{dN}{dx} = 2\pi\alpha \times \left(1 - \frac{1}{n^2}\right) \times 1.67 \times 10^6 \ \ \mathrm{m}^{-1} \tag{2.3}$$

Another key property of Cherenkov light is that it is only emitted within a small range of angles with respect to the direction of the particle track. This angle, usually termed the Cherenkov angle, θ_{Ch}, is given by:

$$\cos\theta_{Ch} = \frac{1}{\beta n} \tag{2.4}$$

Again, in the approximation that $\beta = 1$ and taking $n = 1.35$, this gives an angle of $42.2°$ in water and allows us to express the number of Cherenkov photons per metre using Eq. (2.3) and Eq. (2.4) as:

$$\frac{dN}{dx} = 76500 \times \sin^2\theta_{Ch} \;\; \mathrm{m}^{-1} \tag{2.5}$$

Eq. (2.5) is used in the detector Monte Carlo (described in Chapter 4) to calculate the amount of Cherenkov light emitted from all charged particle tracks. Eq. (2.4) is used in both the detector Monte Carlo (Chapter 4) and muon reconstruction (Chapter 5) to calculate expected arrival times for hit PMTs with respect to the Monte Carlo and candidate reconstructed muon tracks.

With relatively few photons produced per metre segment of particle track[1], both an exceptionally transparent medium and exceptionally sensitive detectors are required. For the medium, deep water and Antarctic ice have been used in previous and current experiments. Large area PMTs sensitive to single photons provide the best possible detectors. Such experiments are discussed in Section 2.2 along with alternative techniques for detecting high energy neutrino interactions which cannot scale up to the huge volumes required to detect the types of sources discussed in Chapter 1.

2.1.3 Muon reconstruction

Experiments of the type described above aim to measure the directions of muons passing through their instrumented volumes by detecting the arrival times of Cherenkov photons on detectors with known positions. This information is then fitted to a set of muon track parameters. One method for this used in the ANTARES experiment is described in Section 5.1 but, in general, the principle is to perform a maximum likelihood fit on the difference between the measured PMT hit times and those expected for Cherenkov light production given a knowledge of the Cherenkov angle (Eq. (2.4)) and the speed of light in water (as discussed in Section 4.3).

We shall see in Section 3.4.4 and Section 5.4.5 that, at high energies, the neutrino and the muon it produces are almost co-linear and that a measurements of the direction of the muon passing through the detector give an accurate estimation of the direction of the neutrino that produced it. Given this, it is then possible to try and associate high energy neutrinos

[1] 1 m of muon track corresponds to roughly 3 ns and a light output of 10^5 photons. In the time, a 60 W light bulb emits around 10^{11} visible photons (assuming 20% of the energy is turned into visible light).

with a particular astrophysical source (such as those described in Section 1.3.3) or site for Dark Matter annihilation (Section 1.4.4).

In principle, it is also possible to reconstruct the muon energy though this is technically much more challenging due to the relatively small number of photons detected and the optical background noise (see Section 2.3.3). At low energies, for events completely contained in the detector, this is achieved by estimating the muon track length which is itself proportional to the muon energy. At high energies, the number of detected photons gives a measure of the muon energy loss which is in turn proportional to the muon energy. However, neither of these methods are applicable to all neutrino energies nor are they robust with the current generation of simulation and reconstruction codes. This possibility is therefore not discussed further in this thesis.

2.2 Water / ice Cherenkov telescopes and other techniques

In the previous section we described the general principles of large water (or ice) Cherenkov detectors to detect and reconstruct upward going muons produced by the interaction of high energy neutrinos. In addition to the technique described above, other methods have been employed to search for high energy neutrinos. In this section, we will give a brief history of such experiments and describe those which are either forerunners or contemporaries of ANTARES or have published results in areas relevant to ANTARES (specifically in the indirect detection of Dark Matter in Chapter 6).

2.2.1 MACRO, Baksan and Super-Kamiokande

Before describing the history of large water Cherenkov detectors as outlined in the previous section, we shall briefly mention three experiments which have performed indirect searches for Dark Matter (as described in Section 1.4.4). We will compare our results of Chapter 6 to those obtained by these experiments. These experiments are:

Baksan The oldest and longest running of the three experiments described here, Baksan (specifically the Baksan Underground Scintillator Telescope [77]) used several large volumes of scintillator to measure the trajectories of throughgoing charged particles and therefore measure and set limits on fluxes of muons observed from neutrino interactions.

MACRO The MACRO (Monopole Astrophysics and Cosmic Ray Observatory) experiment [78] was originally designed to search for magnetic monopoles. It used a combination of scintillators and streamer tubes which provided a good sensitivity to the passage of charged particles and therefore to upward going muons from neutrino interactions. The experiment was based in the Gran Sasso laboratory under 3.7 km (water equivalent) of rock to shield against cosmic ray muons.

Super-Kamiokande Based in the Kamioka mine in Japan, Super-Kamiokande [13] consisted of 50000 tonnes of ultra-pure water surrounded by 13000 photomultiplier tubes at the time the results presented in Chapter 6 were derived. The accident at the Super-Kamiokande experiment in Nov. 2001 caused a large fraction of these PMTs to be destroyed. Work is currently underway to rebuild the detector with a reduced density of PMTs.

These experiments have several features in common. They are all sensitive to the passage of charged particles and are all sited under significant amounts of material to reduce the flux of downward going cosmic ray muons. However, they are all constructed in artificial caverns underground which means that it is very difficult (i.e. expensive) to scale these concepts up to larger detectors (though, in this respect, detectors with a Megaton of detector medium are currently being discussed). In addition, the sensitive medium (scintillator or ultra-pure water) has to be manufactured which again limits the size to which these detectors can scale. An alternative technique is to use a natural medium which, provided it is sufficiently transparent to allow the observation of Cherenkov light from muon tracks some distance away, can provide a large sensitive volume in a natural environment. As we shall see in the following section, the most obvious choice is the deep ocean.

2.2.2 Dumand, Baikal and Nestor

The idea to use deep ocean water as a medium for detecting muons produced by high energy neutrinos was first discussed over 40 years ago (for example, in [79]). Since this time, several experiments have attempted to exploit this idea with varying degrees of success. In all cases, the general principles are those described in Section 2.1. However, the experimental challenges in each case are different.

DUMAND The Dumand experiment [80] based in Hawaii was the first attempt to construct an underwater neutrino telescope. Although the project was cancelled in 1996, a great deal of the experience gained in terms of site exploration, detector construction and deployment and simulation has passed on to the next generation of experiments. Dumand was a pioneering experiment which was arguably ahead of its time in terms of the required technology and infrastructure.

Baikal The Baikal neutrino telescope (deployed in Lake Baikal in Siberia) consists of 200 PMTs on a three dimensional frame consisting of 8 separate lines [81]. Its performance is limited by the maximum depth at which it can be deployed (around 1300 m) which affects the cosmic ray muon background and the optical properties of the water with absorption lengths typically a factor of 3 shorter than those found in the deep ocean. In winter, the surface of Lake Baikal freezes which gives it the advantage over the deep ocean sites that the detector can be deployed from a solid surface.

Nestor The Nestor experiment [82] is an ongoing experiment to construct a neutrino telescope in the Mediterranean constructed around rigid "pylons" at a depth of 3800 m.

In contrast to the previous two experiments, it benefits from a deep site with excellent optical properties. The experiment is still in the Research and Development phase.

In general terms, the deep ocean provides a clear natural medium with relatively small amounts of photon scattering. The latter is important in the reconstruction of muon directions as scattering will reduce the numbers of Cherenkov photons seen and cause their arrival times to be spread out around the expected time (which is used in the maximum likelihood fit for the muon track parameters). This will be discussed in more detail in Section 5.3 in the context of the ANTARES experiment.

In addition to the optical properties of the water, the infrastructure required to support the installation and operation of an array of PMTs in the deep ocean is significant. For this reason, an alternative was sought in the transparent ice of the Antarctic.

2.2.3 Amanda and ICECUBE

Perhaps surprisingly, ice at a depth of several kilometers below the surface at the South Pole has much longer absorption lengths than the water found in the deep ocean. This makes it a promising candidate for siting a neutrino telescope as the individual PMTs can be placed further apart to detect the same amount of Cherenkov light and hence give a bigger overall detector. Another advantage is that optical background noise (from radioactive decays and light emitted by living creatures) is virtually absent in deep ice. As we shall see in discussing the ANTARES site below, such optical noise adds a significant contribution to the total amount of light detected. Finally, as for the Baikal experiment, the detector can be deployed from a solid platform and, with the American scientific and military facilities already present at the South Pole, a great deal of the required infrastructure is already in place.

The above would suggest that deep ice is a superior candidate for constructing large volume neutrino telescopes. However, the scattering of photons in ice is significantly more likely than in deep ocean water and has a significant effect on the accuracy with which muon directions can be reconstructed. In addition to the effect on the overall performance, various factors affecting the homogeneity of the ice (such as layers of dust or small air bubbles) make modeling and understanding such an experiment significantly more difficult compared to water. The competition between these different parameters ensures that attempts are being made to exploit both media with competitive results.

The AMANDA experiment (Antarctic Muon And Neutrino Detector Array [83, 84] is an array of PMTs embedded in the Antarctic ice at a depth of up to 2 km. In its current state, referred to as "Amanda II", it consists of 19 separate lines supporting a total of 677 PMTs. The previous incarnation of AMANDA, referred to as "Amanda B10" consists of 302 optical modules on 10 lines. In [83], results have been presented for Amanda B10 for measurements of atmospheric neutrinos and searches for Dark Matter and astrophysical sources of neutrinos.

Despite the current lack of results from Amanda II, a broadly similar collaboration is planning to extend the concept of a deep ice neutrino telescope at the South Pole to instrument an area of approximately one cubic kilometre. This is the ICECUBE [25] experiment. The projected physics performance shown in [25] is impressive with significant improvements anticipated over the current generation of experiments. The accuracy with which muon directions can be reconstructed will still be somewhat limited by the optical properties of the ice. Furthermore, due to its location at the South Pole, both Amanda and ICECUBE are unable to observe the sky in the direction of the Galactic Centre where a number of comparatively local high energy neutrino sources are anticipated (for example, the possibility of Dark Matter annihilation at the Galactic Centre as described in Section 1.4.4).

2.2.4 Alternative techniques for high energy neutrino detection

In addition to the experiments described above, several other techniques have been proposed to search for high energy neutrinos from cosmic sources. Three such techniques: radio Cherenkov detection, surface detectors and horizontal air showers are discussed below.

Radio Cherenkov detection - RICE

When high energy electron type neutrinos interact in matter they can produce electrons which then form electromagnetic showers of electrons and positrons. In addition to the Cherenkov light produced by individual charged particles in the shower, the shower as a whole can coherently emit Cherenkov radiation at wavelengths large compared to the shower size [85]. This places the radiation in the radio region of the spectrum and, for electron neutrino induced showers above 1 PeV, is potentially detectable by relatively inexpensive radio antennae.

The RICE experiment [86] consists of an array of sixteen radio receivers embedded in the Antarctic ice at the South Pole. The receivers are arranged in a 200 m cube at depths of between 100 and 300 m below the surface of the ice[2]. Even with this relatively small array and only one month of data, competitive limits on the fluxes of high energy electron neutrinos have been set [86] in the PeV to EeV energy range although these do not yet impact on theoretical predictions.

Surface detectors

Another proposed technique for the detection of high energy neutrinos is arrays of downward looking PMTs on the surface of a (natural or artificial) lake (e.g. [87]). Given a high enough density of PMTs, the Cherenkov light from upward going muons can be distinguished from the atmospheric muon flux (which, on the surface, is more than 10^{10} times larger than the upward going muon flux [44]). However, the technical difficulties in constructing a suitable light-tight container and in scaling up to areas of a km^2 mean this technique has never been successfully exploited.

[2]The RICE receivers actually use the same holes drilled for the AMANDA experiment to minimise the deployment costs.

Horizontal Air Showers

A third proposed technique is to search for horizontal air showers from high energy neutrino interactions in the atmosphere or in the upper layers of the Earth's crust. At or close to the horizontal, the electromagnetic component of showers initiated by high energy (hadronic) cosmic rays is strongly attenuated by the atmosphere and hence the observation of a shower at these zenith angles is indicative of a deeply penetrating primary, for example a neutrino. The detection of such showers may be possible with the upcoming Auger observatory [88, 89].

2.2.5 Summary of experimental techniques

We have seen above that a variety of techniques have been or are going to be applied to experimental searches for high energy neutrinos from extra-terrestrial sources. The technique of embedding photomultipliers in an optically transparent natural medium appears to be promising in scaling up to the kinds of sizes required to test some of the models for neutrinos from astrophysical sources (such as those described in Section 1.3.3). The two proposed natural media, deep ocean and Antarctic ice, have both advantages and disadvantages with respect to the other. Given this, and the complementarity in sky coverage which would be obtained by having neutrino telescopes both hemispheres[3], having a neutrino telescope in the deep ocean in the northern hemisphere would greatly compliment existing searches for astrophysical neutrinos. In the next section, we describe one such project, ANTARES, on which this thesis is based.

2.3 The ANTARES experiment

In this section we describe the design of the ANTARES neutrino telescope which is currently under construction at a site 40 km off the south coast of France at a depth of 2.4 km below the surface of the sea. We also describe some of the in situ measurements of optical properties and background at this site which will affect the simulations and results presented in the remainder of this thesis. The parameters of the ANTARES detector are specified in [90] and where not otherwise noted, the information contained within this section is drawn from that source.

2.3.1 The ANTARES detector

A schematic overview of the ANTARES detector is shown in Figure 2.2. The detector consists of 10 independent lines. Each line supports a total of 90 photomultiplier tubes (PMTs). Each PMT is contained within a glass sphere which can withstand the pressure of the ocean down to a depth of greater than 6 km which is more than sufficient for the

[3] For example, the galactic centre is in the southern sky and hence is only visible to a neutrino telescope in the northern hemisphere.

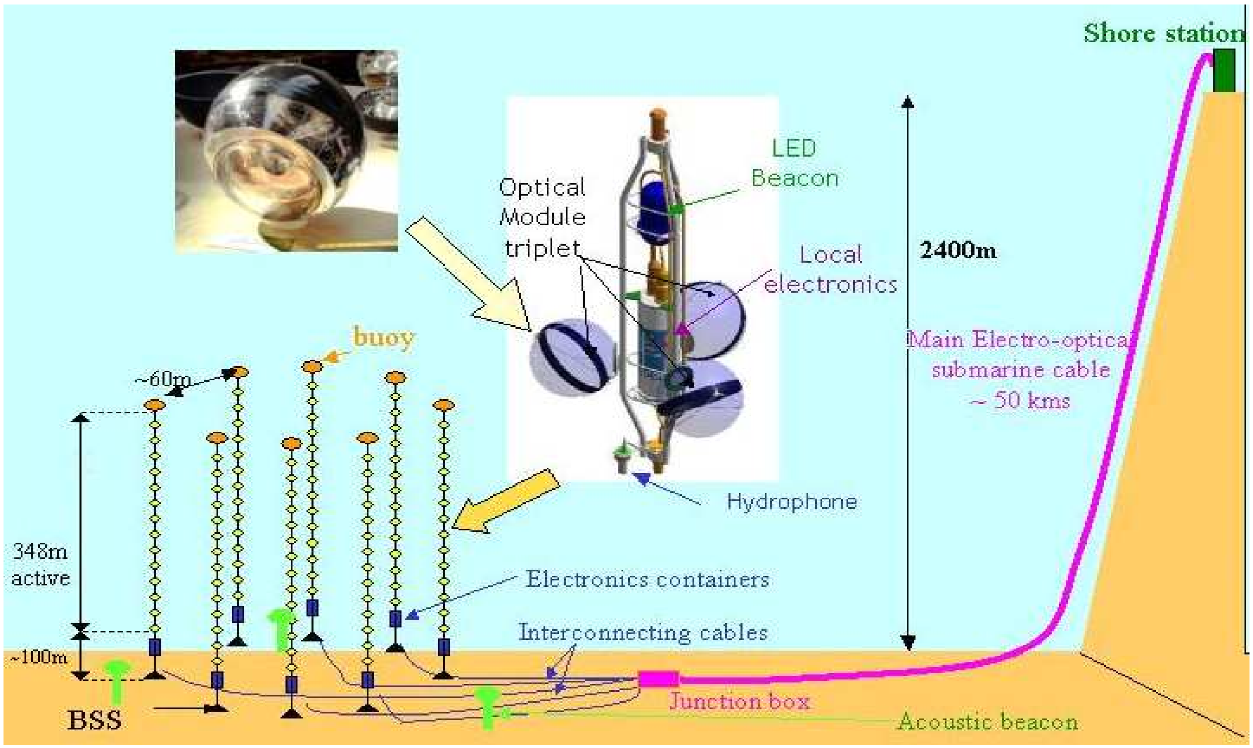

Figure 2.2: A schematic overview of the ANTARES detector showing the dimensions and separations of the detector elements and the structure of the triplets of optical modules at each storey of the detector.

ANTARES site at a depth of 2.4 km. The combination of the PMT in the glass sphere and the immediately related electronics is referred to as an Optical Module (OM).

The Optical Modules are arranged in triplets (as shown in the inset in Figure 2.2) which are mechanically supported on the lines looking downwards at an angle of 45 degrees to the line and equally spaced at intervals of 120 degrees in azimuthal angle. Each triplet of OMs is associated with a local electronics container which provides an interface to the detector control system and data acquisition. Each triplet of OMs and the associated electronics defines a "storey" of the detector. In addition to the optical modules, some storeys also support hydrophones, tiltmeters, compasses and LED beacons which are used in measuring the position and calibrating the time resolution of the detector (see "Calibration" below).

Each storey of the detector is separated by 12 m. Five of these storeys form a sector which is the smallest unit in the detector which forms a complete system in terms of acquiring and reading out data. Six of these sectors are then grouped together to form a line which therefore contains 90 OMs on 30 storeys. The active length of each line 348 m. There is around 100 m of line at the bottom which is uninstrumented to raise the instrumented volume away from the sea bed (to provide a greater region for observing Cherenkov light from upgoing particles). Each line is anchored to the sea bed where the electronics for controlling the individual parts of the line and supplying the power are located. The lines are held in an approximately vertical position by a buoy attached to the upper end.

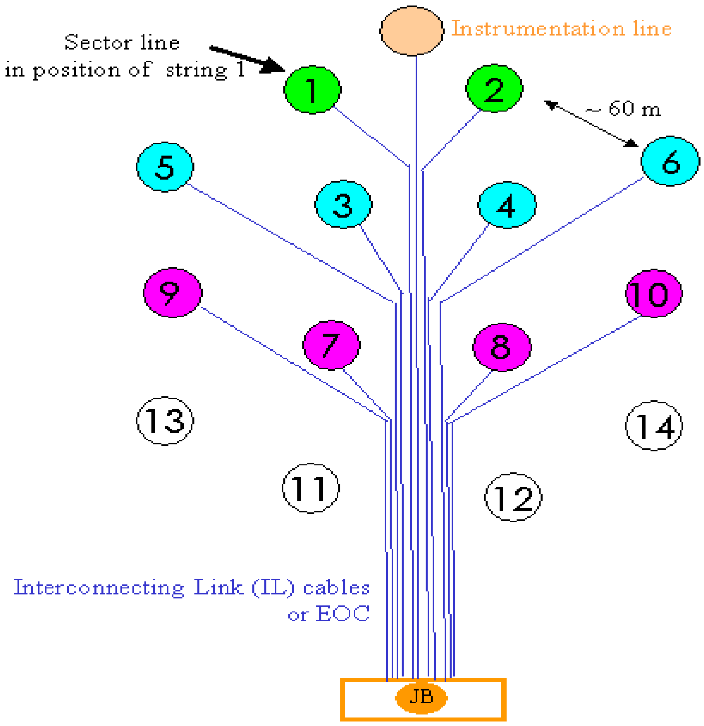

Figure 2.3: Layout of the lines for the ANTARES detector. Lines 1-10 will be deployed in the first phase of the detector in numerical order with 2 the first year and then 4 for each of the two following years. Lines 11-14 will be built and deployed if funds allow.

The lines are arranged on the sea bed as shown in Figure 2.3. Neighbouring lines are separated by 60 m. Initially, one of the sectors described above (and one extra storey) will be deployed in position 1 to test all aspects of the detector. The lines will then be deployed in sequence with two the first year and four for each of the following two years. It is intended to begin deployment during this year (2002). In addition to the detector lines as described above, an additional "instrumentation line" will be deployed to perform detailed oceanographic measurements which, whilst of indirect interest to ANTARES, will not be discussed further here. The first phase of the detector will consist of 10 lines (numbered 1 to 10 in Figure 2.3) and that is the version used in this thesis. The possibility to add an extra four lines is included in the design if the financial demands can be met.

Finally, the whole detector is connected to a single "Junction Box" which distributes power and control signals to the detector and through which the data taken by the detector is routed. This is connected to the detector control room on shore where the data is received and processed.

The design of the ANTARES detector was originally determined from Monte Carlo studies of different string, storey and OM separations [91] based on the goal of detecting neutrinos from astrophysical sources. This gave an optimal configuration of 80 m between strings and 16 m between storeys. The design described above has been adjusted to have 60 m between adjacent strings (which is the minimum distance technically possible in terms of deployment and roughly corresponds to the absorption length of light in sea water) and 12 m between stories (meaning a 10 GeV vertical muon can produce hits on five adjacent stories). Both of these changes reduce the energy threshold of the detector and improve the sensitivity to low energy neutrinos which facilitates making a measurement of the atmospheric neutrino oscillation parameters and searching for Dark Matter.

In the following section we will discuss the various aspects of the ANTARES detector which are directly relevant to the simulations and results described in this thesis. This will cover various aspects of calibration and electronics which could affect the performance of the detector as presented in Chapter 5 and Chapter 6.

2.3.2 Detector calibration and electronics

In the previous section, we gave a general discussion of the ANTARES detector. A complete description is given in [90]. In this section, we will concentrate on just those aspects of the detector which are directly relevant to the simulations and results given in this thesis. This is mainly concerned with two aspects: the optical module performance and the electronics systems as these will both directly affect the data acquired by the detector.

Optical Modules

The ANTARES Optical Module [92] is a pressure resistant glass sphere with a diameter of 17 inches. It contains a PMT with a photocathode diameter of 10 inches which is fixed to the front of the glass sphere by embedding it in a gel whose refractive index is chosen to match that of the glass. The PMT is surrounded by a μ-metal cage which acts as a shield against the Earth's magnetic field.

The measured optical properties of these components are shown in Figure 2.4 for the range of wavelengths of interest for Cherenkov light production in ANTARES. The efficiency of the PMT is expressed as the product of the quantum efficiency (the probability that a single photon yields a photoelectron within the PMT) and the collection efficiency (the probability that an electron inside the PMT is accelerated onto the first dynode). This quantity is shown in plot (a) in Figure 2.4 and is close to its maximum value between 320 nm and 520 nm. We shall see in Section 4.2.3 that this is close the the range of wavelengths where the absorption length in the water around the ANTARES detector is longest. We therefore expect that the majority of detected Cherenkov photons will be in this wavelength range. The absorption lengths in the glass and the gel are also shown. In the region of interest defined above, they are significantly longer than the path lengths of photons in these media and therefore will not have a dramatic effect on the efficiency.

The measurements shown in Figure 2.4 give the efficiency of the OM at normal incidence. In addition to this, the angular efficiency of the OM has been measured [92] using Cherenkov light produced by downward going atmospheric muons passing through a closed tank of pure water. These results are shown in Figure 2.5 and include a comparison with simulations of the Optical Module. The peak at $\sim 42°$ corresponds to Cherenkov light from vertical muons arriving at normal incidence to the OM.

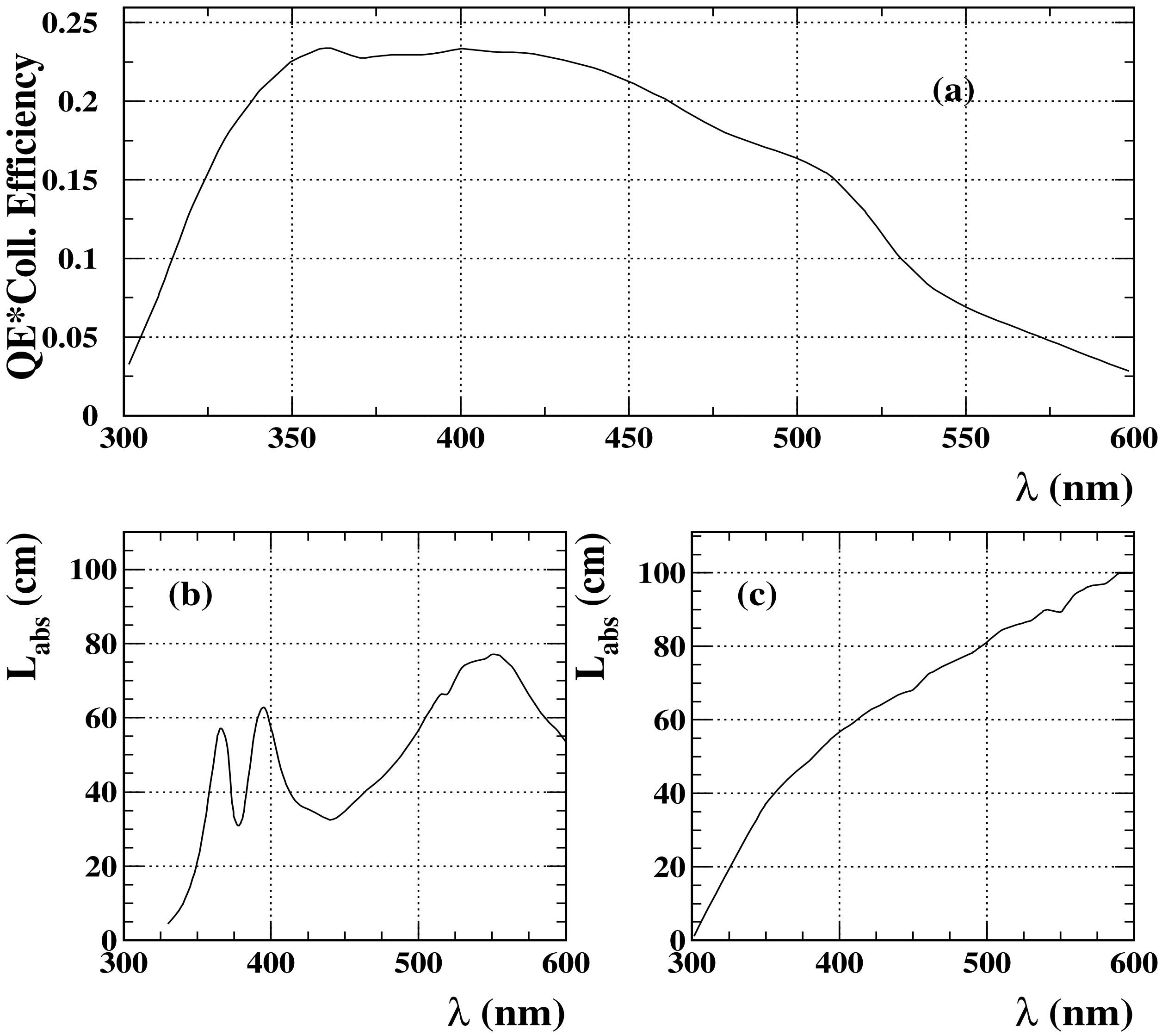

Figure 2.4: The combined quantum and collection efficiency of the ANTARES PMTs (a) and the absorption lengths of glass sphere (b) and optical gel (c) in the ANTARES Optical Module (taken from [92])

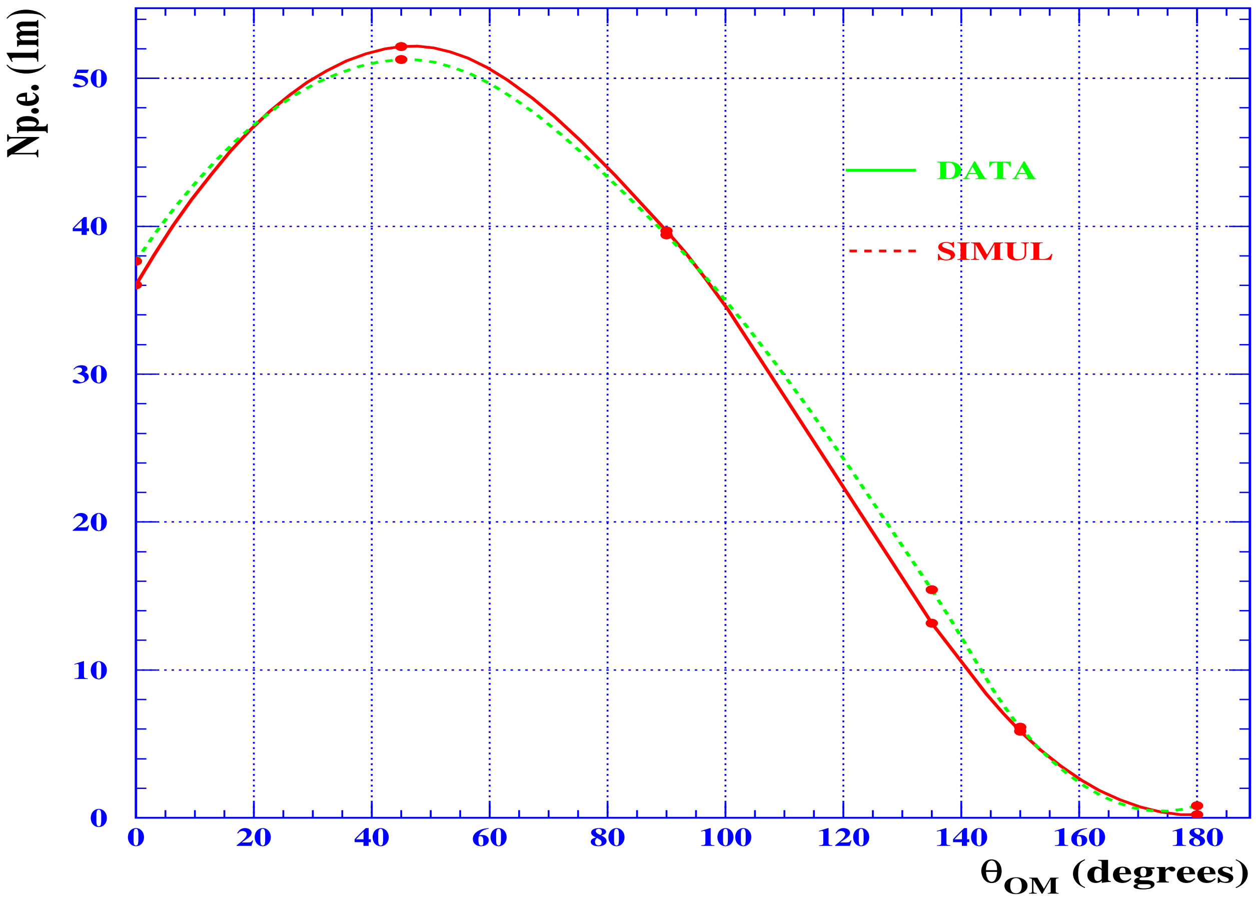

Figure 2.5: The angular efficiency of the ANTARES Optical Module measured using Cherenkov light from downward going atmospheric muons. Simulation results are shown for comparison.

The wavelength and angular dependences of the Optical Module efficiency are important inputs to the ANTARES detector Monte Carlo (as described in Chapter 4). They are combined to give an "effective area" for the OMs (defined in Eq. (4.1), page 97) for use in the detector simulations.

Electronics

The ANTARES electronics are based around an ASIC (Application Specific Integrated Circuit) called the ARS (Analogue Ring Sampler [93]). The ARS is a complex chip which performs many functions related to control and data acquisition in the ANTARES detector. Its importance in this thesis is the digitisation and readout of PMT hits. In this section, we shall briefly describe the full operation of the ARS. In Section 4.1.3, we shall describe the scheme actually used in the simulations presented in this thesis.

The ARS can read out PMT hits in two ways based on an analysis of the pulse shape produced by the PMT. There is a low level threshold on the pulse amplitude which defines the minimum pulse height. If a signal is above this level, its maximum amplitude and time over threshold are compared to predefined values. This leads to two possibilities:

SPE Mode Provided the maximum amplitude and time over threshold remain below values chosen to be suitable for "Single Photoelectrons" (SPEs) in the PMT, the hit time (i.e. the time of the low level threshold crossing) and integrated amplitude (over a time of 25 ns from the first threshold crossing) are recorded in one of 16 memory cells. There is a dead time of 250 ns associated with each SPE event.

Waveform For events with an unusually high amplitude or a long time over threshold (e.g. a pulse consisting of many photoelectrons or two photons arriving within a short time window), the pulse waveform is digitised in 128 samples at a rate of up to 1 GHz. The deadtime after receiving a waveform event is approximately 2 μs.

In any OM, there are two ARS chips which pass control between them to avoid excessive dead time whilst one is digitising. The data is read out on receipt of a trigger which can be due to a cluster of hits on one storey, a set of hits on one string or a set of hits over the whole detector and, in general, causes an entire string or the whole detector to be read out. This trigger is flexible as values governing each of the parameters above can be set with the detector deployed via control commands from the shore. The exact parameters, whose values aren't currently defined, will depend on the conditions at the ANTARES site and the detailed physics requirements of the experiment at that time.

The waveform mode can also be disabled to reduce the amount of data being sent to shore. The principle difference between SPE and waveform modes in terms of the muon reconstruction is in the separation of closely spaced multiple hits. For SPE events, all hits within a 25 ns integration window are merged. For waveform events, separation depends on the width of the PMT pulses and the sampling rate. Typically, two hits separated by 10 ns can be distinguished. It has been shown [94] that the difference between these two in terms of the high energy muon reconstruction is negligible and in Section 4.1.3 we shall describe an electronics simulation scheme corresponding to the SPE mode only.

Calibration

In terms of the detector performance, there are two main calibrations which must be performed accurately. It is required [90] that the timing resolution of each element of the ANTARES detector should be around 1 ns. Values much larger than this would significantly degrade the accuracy with which ANTARES could reconstruct the directions of muon tracks. This overall calibration relies on an accurate knowledge of both the position of each of the OMs and their timing spread and offset relative to some externally defined clock.

Positional calibration is achieved by means of a system of acoustic beacons placed on and around the detector and acoustic detectors (hydrophones) placed on each storey of each line. In addition, a tiltmeter and compass are placed on each storey to measure the orientation of each OM along the line. This system gives a relative measurement of the position and orientation of each element of the detector to better than 10 cm (which corresponds to less than 0.5 ns propagation time of light in water). The absolute calibration comes from GPS measurements of the line positions on deployment. It has been shown [95] that this is sufficient to have a negligible effect on the reconstruction given the calibration data available. Therefore, in the simulations in this thesis, we assume that we know the detector alignment in reconstructing muon tracks[4].

The timing resolution of the detector is dominated by the PMT Transit Time Spread (TTS - the spread in measured times due to different impact points on the photocathode) which is of order 1.3 ns. In combination with the effect of the wavelength dependence of the refractive index on the propagation times of Cherenkov light which introduces a spread of order ± 1 ns at 40 m from the muon track (see Section 4.3), this gives an irreducible spread in the measured PMT hit times. The requirement of the timing calibration is that it is sufficiently better than these two effects.

Timing calibration for ANTARES is performed by a combination of three systems [96]:

- The internal clock which propagates through the detector is used to measure the relative time offsets of each storey's internal clock with respect to the on-shore master clock. The jitter in the returning clock signal is designed to be less than 0.25 ns.

- The PMT Transit Time (TT - the time taken between the photon being absorbed and the signal appearing on the last dynode) is measured in situ using an LED embedded within each Optical Module which is fired at a known time. The transit time is given by the difference between the LED trigger and the PMT hit time as measured by the ARS. The uncertainty in the LED pulse time and hence the accuracy of the calibration is less than 0.5 ns.

- An "Optical Beacon" fixed to some of the storeys of the detector is capable of illuminating nearby storey on the adjacent lines. A "Laser Beacon" fixed to the bottom of each line can illuminate the bottom half of the detector. This provides both an individual time calibration of all the OMs and a redundant measurement for the lower half of the detector. The relative time offset of each OM can be obtained with an accuracy of less than 0.3 ns.

The combination of these systems will give a calibration of the time offsets for each OM in the detector with respect to some well known reference clock of better than 0.5 ns. Given the PMT TTS and dispersion effects mentioned above, this is sufficient not to degrade the performance of the detector. In the simulations that follow, we only take account of the TTS of each PMT and the dispersion and we assume we know the individual time offsets of each OM using the calibration systems described above.

[4]There are software tools available to simulate the distortion of the detector due to the deep ocean currents and then reconstruct the position of the detector based on simulated calibration data. The results in [95] used these tools to draw the conclusions above. Given that the effect is negligible, we neglect both the distortion of the detector and its subsequent reconstruction.

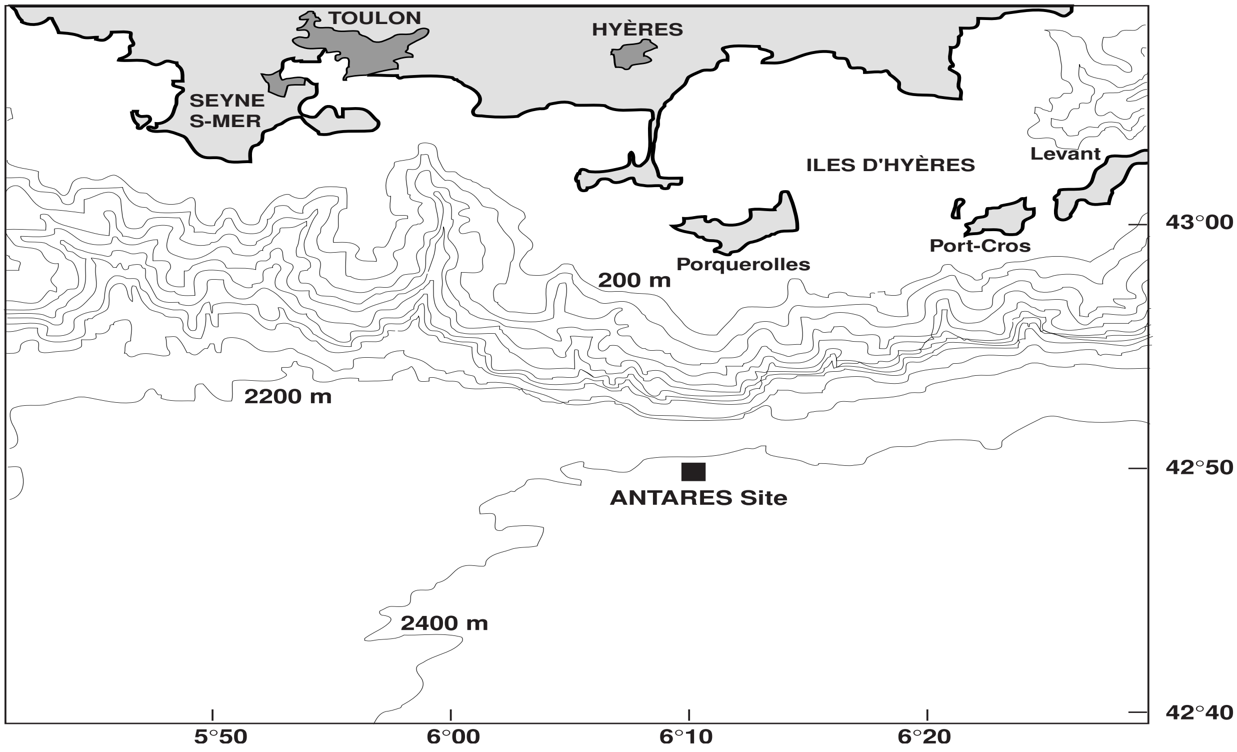

Figure 2.6: The location of the ANTARES Site at a distance of roughly 40 km from the south coast of France. The depth is 2.4 km on a relatively flat region of the sea bed.

2.3.3 The ANTARES site

In the sections above we have concentrated on the ANTARES detector itself. However, as the detector uses the natural medium of the deep ocean to form its active volume, the optical properties of the water and the natural backgrounds at the ANTARES site will also have an important effect on the performance. As shown in Figure 2.6, the ANTARES site is located approximately 40 km off the south coast of France and is at a depth of 2.4 km.

Optical properties

The optical properties of the deep ocean at the ANTARES site will be discussed in some detail in Section 4.2 in the context of the detector simulation and in Section 5.3 in terms of their effect on the detector performance. Measurements [97, 98] suggest that the absorption length in blue light (around 470 nm) in the region of the maximum sensitivity of the ANTARES PMTs to Cherenkov light is between 50 m and 60 m which, by construction, is approximately the spacing between the detector lines. The effect of scattering is small (compared to that in ice as discussed in Section 2.2.3 for example) but not negligible. There is currently some uncertainty surrounding the exact scattering properties of the water (which will be discussed in Section 5.3) but the general indication is that the overall scattering length is longer than 30 m for blue light.

Optical Background

Background light in the deep ocean is dominated by two contributions. The first is from radioactive decays of potassium-40 which yields either an electron or a high energy photon:

$$\beta - \text{decay} \qquad {}^{40}K \to {}^{40}Ca + e^- + \overline{\nu}_e \qquad \text{Br} = 89.3\% \tag{2.6}$$

$$\text{e} - \text{capture} \qquad {}^{40}K \to {}^{40}Ar^* + \nu_e \to {}^{40}Ar + \gamma \qquad \text{Br} = 10.5\% \tag{2.7}$$

The electron in the β-decay process has a maximum energy of 1.3 MeV and the energy of the γ is 1.5 MeV. The γ-ray scatters to produce Compton electrons. In both cases, the electrons have sufficient energy to give Cherenkov photons in water. This produces a continuous and random optical background giving a predicted rate of around 25 kHz on a single 10 inch PMT (from [99] based on the measured salinity and attenuation lengths at the ANTARES site).

The second contribution to the optical background at the ANTARES site is that from bioluminescent organisms. A measurement [100] of the optical background on a 8 inch PMT at the ANTARES site over a time of ten minutes is shown in Figure 2.7. Two components to the optical background are clear. The first is a continuous component of around 40 kHz (corresponding to $\sim$ 60 kHz on the 10 inch PMTs to be used in the ANTARES detector). On top of this are large "spikes" of bioluminescent activity assumed to be close to the PMT which can give transient rates of over 1 MHz.

The difference between the predicted background rate of 25 kHz from potassium-40 decays and that observed is attributed to bioluminescent organisms producing low levels of light or being some distance from the PMTs. In the simulations described in Chapter 4 we include a random background of PMT hits with a rate of 60 kHz (corresponding to the baseline of the measurement in Figure 2.7) which we assume to be uncorrelated between different PMTs. In the current generation of simulations, we neglect the contribution of the bioluminescence spikes which will either increase the background rate on individual PMTs over a short time period or, in the case of very high rates, introduce some dead time on affected PMTs. This will have some effect on the performance but this should be small as only a small number numbers of PMTs will be affected at any one time as the bioluminescence bursts were seen to be uncorrelated over large distances.

Biofouling and sedimentation

The final consideration is that of the accumulation of organic material on the surface of the Optical Modules and of sedimentation on the upward facing regions. For the area of the OM corresponding to the PMT photocathode, the decrease in observed light intensity has been observed to be less than 2% over one year [101]. This should therefore have a negligible effect on the efficiency of the ANTARES OMs at detecting Cherenkov light over the lifetime of the experiment.

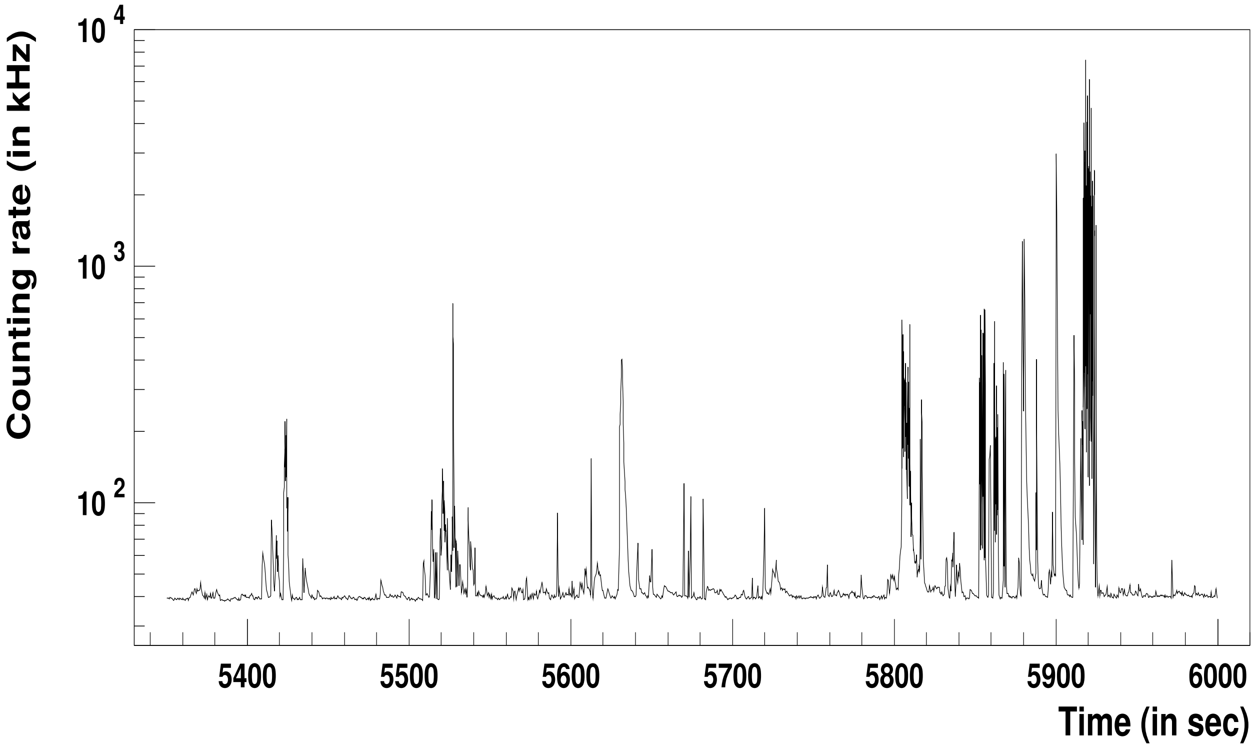

Figure 2.7: Measurement of the optical background at the ANTARES Site on an 8 inch PMT (taken from [100]) showing a continuous component with a rate of 40 kHz and random "spikes" due to bioluminescence.

2.4 Summary

In this chapter we have described the general principles by which an underwater neutrino telescope detects muons produced by high energy neutrinos and outlined some of the advantages of such a technique. We have also described other experiments which address the same areas of physics and then gave a detailed description of the ANTARES detector.

- We described how a transparent natural medium can be used to support an array of Photomultiplier Tubes (PMTs) which can be used to detect the Cherenkov light produced by high energy muons. Given accurate timing information, this light is then used to reconstruct the muon direction which, in turn, provides information about high energy sources of neutrinos (Section 2.1).
- We gave a brief history of both experiments which have published experimental limits for the indirect detection of Dark Matter (which we will compare our expected sensitivity to in Chapter 6) and those which seek to exploit large volumes of water or ice as a medium for detecting high energy neutrinos (Section 2.2).
- We described the ANTARES experiment both in terms of its general construction and design and with respect to the specific areas which are relevant to the simulations and results described in the remainder of this thesis (Section 2.3).

The general technique of using a natural, transparent medium is advantageous because of the large volume which can be instrumented at comparatively little cost (which is not true for experiments such as those described in Section 2.2.1 which rely on the excavation of the detector volume). In addition, the long range of high energy muons allows for neutrino interactions some distance outside the instrumented volume to be observed. The use of such a technique does require the medium to be exceptionally clear to be able to detect enough Cherenkov light to reconstruct muon tracks.

In terms of the ANTARES experiment, we saw that the response of the ANTARES Optical Module as a function of wavelength (i.e. in terms of the optical properties of the glass sphere and the gel and in terms of the combined quantum and collection efficiencies of the PMT) and the angular response to Cherenkov light has been measured and these results are used in the simulations described in Chapter 4. We also described the details of the electronics which will digitise the PMT hits and how this might affect the performance. Again, this is taken into account in the simulations in Chapter 4. We also discussed the various calibrations required to allow the accurate reconstruction of muon tracks passing through the detector and showed that, based on the expected performances of all the available systems, the timing resolution is dominated by the PMT Transit Time Spread and the wavelength dependence of the refractive index. It has also been shown in Monte Carlo studies that our knowledge of the detector alignment and timing calibration does not affect the performance and where therefore can safely neglect these timing calibration effects in our future simulations.

Finally, we considered the effect of the optical properties of the ANTARES site. In general, both absorption and scattering are favourable for the construction of a neutrino telescope of the type discussed in this chapter. We shall investigate the effect of different scattering models on the detector performance on Section 5.3. The optical background on each PMT consists of a continuous component with a rate of around 60 kHz on a 10 inch PMT (of the type used by ANTARES) and short spikes corresponding to the activity of bioluminescent organisms. As this second contribution is relatively short-lived and localised, we shall only consider the continuous component in the simulations described here.

In the following two chapters we shall develop simulation methods capable of modeling high energy neutrino interactions around the detector and simulating the detector response to the passage of the particles produced by these interactions taking into account the different media around the detector and the properties of photon propagation in the water. In Chapter 5 we shall investigate some of the systematic effects on the final detector response associated with the assumptions in these simulations and give a general method of describing the detector performance. Finally, in Chapter 6, we shall apply all of these methods to predict the sensitivity of ANTARES for the indirect detection of Dark Matter.

Chapter 3

Neutrino event generation methods

In this chapter, the tools required to simulate neutrino interactions in the media around the ANTARES detector and to propagate muons large distances through these media are described and evaluated. The simulated neutrino cross-sections and interaction kinematics are compared with published results and found to agree to within 5%. Several additional sources of systematic errors are identified and evaluated. The propagation of high energy muons is discussed and the maximum ranges of muons in different media are calculated and tabulated at different energies for further use in these simulations. Finally, a fast method for simulating neutrino interactions for ANTARES is developed using the tools discussed previously and suitable event weights are derived for redistributing the generated events according to different neutrino fluxes. The optimisations made in this method are checked to ensure the results are unbiased.

To study the performance of the ANTARES detector in detail and predict its response to a range of different neutrino sources, two distinct stages of simulation are required. Firstly, it is necessary to accurately model the interaction of neutrinos in the media in and around the instrumented volume of the detector and propagate the resulting particles until they are at a detectable distance from the PMTs. This stage is the subject of this chapter. Secondly, the response of the detector to the Cherenkov light produced by these particles within the instrumented volume must be determined. This second part is described in Chapter 4.

In this chapter, we describe a simulation program which generates neutrino events for ANTARES. In this context, we develop a method for simulating large numbers of neutrino interactions and evaluate some of the uncertainties in this calculation arising from the choice of neutrino interaction model and muon propagation code. As part of this evaluation, we also provide a parameterisation of muon ranges in rock and water which are used in the optimisation of this code and in calculating the detector effective areas in Chapter 5.

3.1 Simulation overview and generation requirements

There are a few general considerations which apply to any method of simulating neutrino interactions for an experiment such as ANTARES. These include the location of the detector with respect to the surrounding media, the interactions which need to be considered and the treatment of the interaction products.

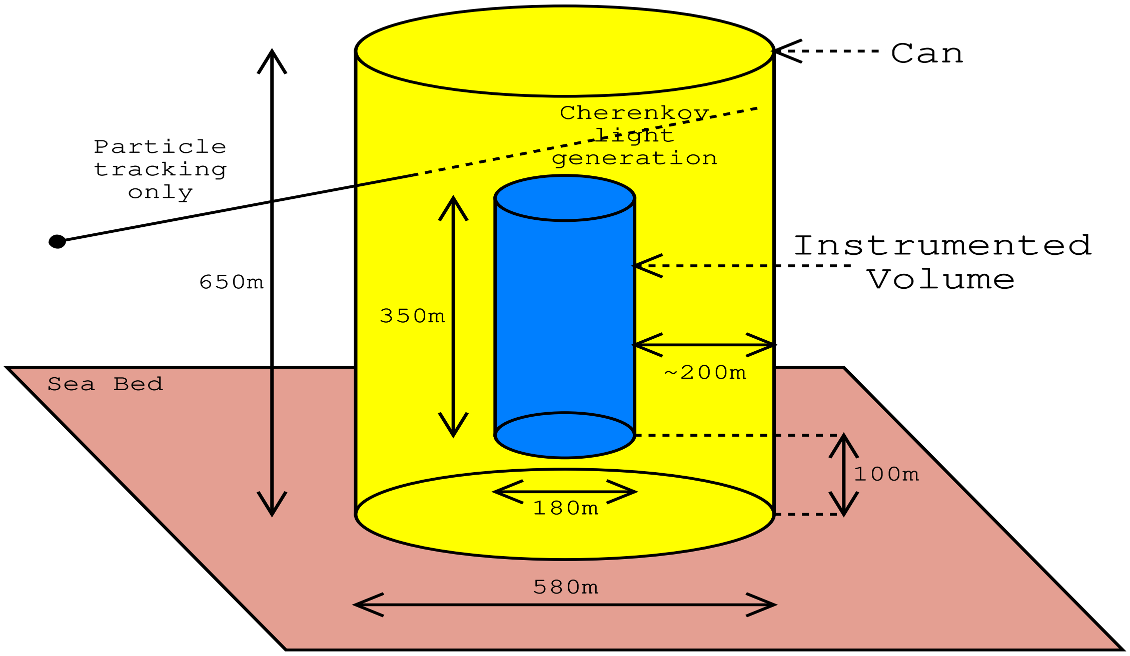

Figure 3.1: Definition of the detector geometry for the event generation stage of the simulation. The can size shown exceeds the instrumented volume by ∼200 m except from below where it is bounded by the sea bed from within which no Cherenkov light can emerge.

3.1.1 Generation geometry

For the purposes of generating neutrino interactions, we treat the instrumented volume of the detector as a cylinder which contains all the PMTs. Surrounding this volume is a larger cylinder, which we call the "can". The can defines the volume within which Cherenkov light is generated in the detector Monte Carlo (see Chapter 4) to determine the detector response. Outside this volume, only particle energy losses in propagation are considered. Inside it, a full simulation including the generation of Cherenkov light must be performed. The geometry of this simulation scheme is shown in Figure 3.1

At this point it should be noted that the can is purely an artifact of the simulation method. In this chapter, neutrinos which interact inside the can are referred to as "volume events". Neutrinos which interact outside the can and only produce a muon crossing its surface are referred to as "surface events". This distinction is useful as it means that only particles which can reach the can need be generated and tracked and the detector response only needs to be calculated for particles whilst they are within the can. However, surface and volume events must be treated equivalently in the event generation and a method which ensures this is described in Section 3.4. In addition, no presentation of the detector performance of sensitivity should depend on the distinction between surface and volume events or the size of the can. One method to achieve this is discussed in Section 5.4.

For any given simulation, it should also be the case that the can is sufficiently large to contain the volume within which the vast majority of the Cherenkov light detected by the experiment is generated. For the case shown in Figure 3.1, a distance of 200 m around the instrumented volume is chosen which is roughly 3 times the longest absorption length at the ANTARES site [1]. This choice will be justified in Section 4.1.4 for through-going muons and Section 4.1.5 for neutrinos interacting within the can.

3.1.2 Simulation requirements

The aim of any generation method is to provide distributions of particles created by neutrino interactions, both on the surface of and inside the can for further processing by the detector Monte Carlo. The aim here is to produce a tool which is suitable for the full range of neutrino studies in ANTARES from neutrino oscillations to high energy astrophysics with the majority of detected neutrinos in a range of energies from tens of GeV (limited by the energy threshold of muon detection of around 10 GeV) to a few PeV (where the absorption of neutrinos in the Earth strongly attenuates the upward neutrino flux).

The typical uncertainties in this energy range which enter into most results involving these simulations should each be understood or at a level on the rate of events of less than $\sim 5\%$ to be safely neglected. The rationale for this figure is that it is below the level of uncertainty from our knowledge of the water properties (see Section 5.3) and that with around 2000 atmospheric neutrino events per year, any systematic effect will not be seen with any real significance above the statistical fluctuations in the data.

To meet these aims, the following general requirements must be satisfied:

- The relevant neutrino interactions from energies of a few GeV up to tens of PeV must be correctly simulated to conservatively include the interesting energy range. At high energies this is dominated by Deep Inelastic Scattering (DIS). At low energies, Quasi-Elastic (QE) scattering and both nucleon and Δ resonances (RES) with central values below 2 GeV are important and contribute to the total cross-section at a level of around 10% [102].
- Neutrinos interacting both inside the can (volume events) and outside the can (surface events) should be simulated in the same package in the correct proportions.
- For events inside the can, the production of the hadronic shower at the interaction vertex must be simulated as charged secondary particles can contribute to the total amount of Cherenkov light observed.
- For events outside the can, high energy muons must be tracked until they are stopped or reach the surface of the can.
- The effect of the different media (rock and water) around the detector must be taken into account in both the neutrino interactions and muon propagation.
- For high energy neutrinos, the probability of absorption in the Earth must be calculated given the neutrino interaction cross-section and an Earth density profile.

The following sections describe how each of these requirements are met and how the choice of models affects the final distributions produced.

3.2 Neutrino interaction models

The primary interactions of interest for ANTARES are charged current muon neutrino (or anti-neutrino) interactions with nucleons:

$$\nu_\mu + N \overset{Charged\ Current}{\longrightarrow} \mu^- + X \overset{hadronisation}{\longrightarrow} \mu^- + (hadrons) \tag{3.1}$$

At the neutrino interaction vertex, the rate of interactions is determined by the total neutrino-nucleon cross-section. The cross-sections will in turn depend on the distribution of momenta between the partons within the nucleons - the Parton Distribution Functions (PDFs). The kinematics of the outgoing muons are determined by the differential neutrino cross-sections in the Bjorken x and y variables (or equivalently, x and Q^2). The structure of the hadronic shower after the interaction will be determined by interactions between the quarks and gluons in the subsequent hadronisation of the struck nucleus.

In this section, neutrino cross-sections and interaction kinematics will be evaluated using a range of PDFs, target nuclei and kinematic limits to evaluate the uncertainty in final results arising from these choices. It will be shown that, once the range of the kinematic variables are defined, the dominant uncertainty is in the neutrino cross-section from the choice of PDF. These results will be compared to those of Gandhi et al. [103] where careful numerical evaluations of neutrino cross-sections and mean inelasticities, $\langle y \rangle$, are made for different Parton Distribution Functions with careful attention paid to the regions relevant for high energy neutrino astronomy.

3.2.1 Simulation tools

Most of the tools to perform these simulations are available within the CERNlib [104] package. For the Deep Inelastic Scattering part of the neutrino interaction, the LEPTO [105] code provides the following facilities:

- Integration of the differential cross-sections over a specified kinematic range to give the total cross-section.
- Sampling of the kinematic properties of the outgoing muon from the differential cross-section.
- Hadronisation of the quark-gluon system in the target nucleus using the Lund string model via calls to the PYTHIA 5.7 / JETSET 7.4 package [74] to give the initial particles in the hadronic shower.

This is done using a particular PDF, either taken from those built into LEPTO or via calls to the Parton Distribution Function library PDFlib 8.04 [106] for access to up-to-date calculations of PDFs using recent accelerator data.

Only the DIS contribution to the total cross-section is included in LEPTO. In DIS, the neutrino interacts with an individual parton within the nucleus to produce a muon. The inter-parton interactions only become important in the hadronisation of the coloured interaction products after the charged current exchange.

To simulate the low energy Quasi-Elastic scattering:

$$\nu_\mu + N \xrightarrow{CC} \mu^- + N' \tag{3.2}$$

and nucleon and Δ resonances (all with central values below 2 GeV):

$$\nu_\mu + N \xrightarrow{CC} \mu^- + N^*/\Delta \xrightarrow{decay} \mu^- + (hadrons) \tag{3.3}$$

we use the RSQ package [107] which includes a description of the (hadronic) multiplicity and distribution of particles in the final state parameterised from experimental observations.

3.2.2 Neutrino interactions

Using the tools described in the previous section, we can determine the contribution of the various processes to the total neutrino cross-section and look at the effect of the interaction medium on the cross-section.

Deep Inelastic Scattering Charged Current interactions

The principal contribution to the overall event rate is from Deep Inelastic neutrino-nucleon Scattering. As the interaction cross-section differs for protons and neutrons, the total cross-section depends on the target nucleus. The generic choice is an "isoscalar" nucleus with equal numbers of protons and neutrons and this is the basis for the discussion in this section and the calculations in [103]. The validity of this approximation for interactions in water will be discussed later and shown to introduce an error of less than 5%.

For an isoscalar nucleus consisting of nucleons of mass M, the electroweak leading order differential cross-section per nucleon in the kinematic variables x and y is (from [103]):

$$\frac{d^2\sigma}{dxdy} = \frac{2G_F^2 M E_\nu}{\pi} \left(\frac{M_W^2}{Q^2 + M_W^2}\right)^2 \left[xq(x,Q^2) + x\overline{q}(x,Q^2)(1-y)^2\right] \tag{3.4}$$

where $q(x,Q^2)$ and $\overline{q}(x,Q^2)$ are the quark and anti-quark distribution functions as functions of the kinematic variables x and Q^2. The above formula is specifically for neutrinos. For anti-neutrinos, we can simply exchange q and $\overline{q}$. Charge conservation means that a neutrino initiating a W^+ charged current exchange to produce a negative muon will interact with (d,s,b) quarks and ($\overline{u}$,$\overline{c}$,$\overline{t}$) anti-quarks. Conversely, an anti-neutrino exchanging a W^- will interact with (u,c,t) quarks and ($\overline{d}$,$\overline{s}$,$\overline{b}$) anti-quarks. Hence, neutrino and anti-neutrino interactions will have different cross-sections and distributions of kinematic variables. The effect

Variable	Description	Default	Adjusted
Bjorken-x	Fraction of the nucleon momentum carried by the struck parton	$10^{-4} < x < 1.$	$10^{-4} < x < 1.$
Bjorken-y	Inelasticity of the interaction. i.e. $E_{\text{lepton}} = (1-y)E_{\text{neutrino}}$	$0 < y < 1$	$0 < y < 1$
Q^2 [GeV^2]	Four momentum transfer	$4 < Q^2 < 10^8$	$0.1 < Q^2 < 10^{10}$
W^2 [GeV^2]	Invariant mass of the hadronic system	$5 < W^2 < 10^8$	$2 < W^2 < 10^{10}$
ν [GeV]	Energy component of the four-momentum transfer	$1 < \nu < 10^8$	$1 < \nu < 10^{10}$
E_l [GeV]	Energy of the scattered lepton	$1 < E_l < 10^8$	$1 < E_l < 10^{10}$

Table 3.1: The default and adjusted kinematic limits used for the LEPTO calculation of the total cross-section and in drawing the kinematic variables for neutrino interactions.

of these different quark distribution functions on the total cross-section will be discussed briefly in Section 3.2.3.

The LEPTO code integrates the differential cross-section of Eq. (3.4) over a specified range of the kinematic variables, giving a total cross-section for interactions within this kinematic range. Before comparing the LEPTO results with those in [103], we first comment on the choice of kinematic limits in LEPTO itself. In calculating the cross-section and drawing kinematic variables for individual events, LEPTO restricts itself to ranges in several parameters (tuned for efficient simulations in accelerator experiments) which must be adjusted to include the full range of neutrino interactions relevant to ANTARES. The default limits are shown in Table 3.1, as are the adjusted ones we use below.

Using the CTEQ3D Parton Distribution Functions [108] from PDFlib, we can use LEPTO to perform this integration and compare the total cross-sections and the mean inelasticities $\langle y \rangle$ to those of Gandhi et al. as shown in Figure 3.2 for an isoscalar nucleus as a function of neutrino energy. The individual data points from Gandhi et al. are given in Appendix B in Table B.1 and Table B.2 along with the values extracted from the simulations corresponding to the results shown in Figure 3.2.

The dashed curves in Figure 3.2 show the integrated cross-section and mean inelasticities with the default limits. In our case, we are potentially interested in neutrino interactions with energies as low as a few GeV. The default values of Q^2 and W^2 restrict the phase-space available at low energies and hence reduce the cross-section. Hence, we need to reduce the lower limits on these variables. This is not without problems as the DIS description of neutrino scattering breaks down at low energies[1]. However, the default values are too high to reproduce the detailed cross-section calculations of Gandhi et al. so we reduce the minimum values of Q^2 and W^2 down to 0.1 GeV and 2 GeV respectively.

The LEPTO code is accurate up to lepton energies of 10 TeV [105]. Above this we rely on an extrapolation of the model to calculate the cross-section and kinematics. We extend

[1] The assumption that the interaction of an individual parton can be treated independently of all the others described as a tree level charged current exchange no longer holds for example.

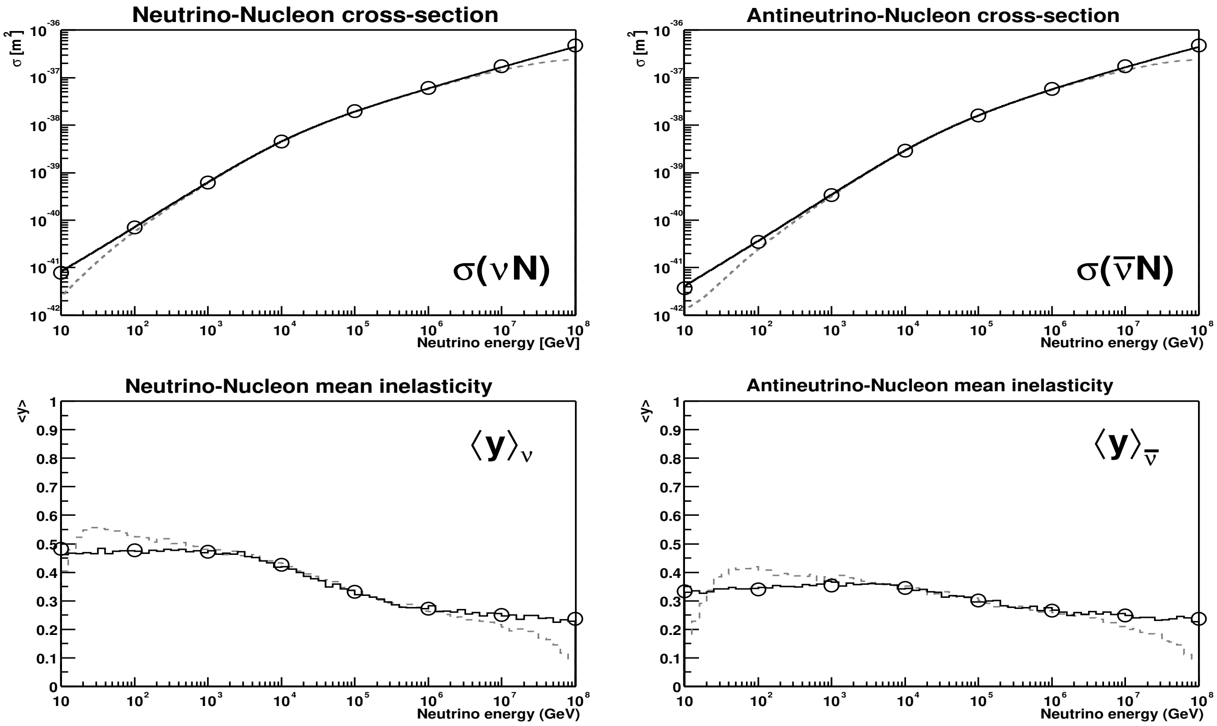

Figure 3.2: Neutrino (left) and anti-neutrino (right) charged current cross-sections (top) and mean inelasticities $\langle y \rangle$ (bottom) for DIS interactions. Calculations are shown using LEPTO with the default cuts (dashed) and the adjusted cuts (solid - see text). The data from Gandhi et al. [103] are plotted as 'O' showing the agreement with the adjusted cuts.

the upper limits on Q^2, W^2, ν and E_{lepton} to 10^{10} GeV to allow this extrapolation to be made for neutrino energies up to 10^8 GeV without running close to these limits.

It is important to check that these modifications to the default LEPTO limits can correctly reproduce the results calculated from the more considered calculation of Gandhi et al. to have confidence in both the low energy description of DIS and the high energy extrapolation with these adjusted cuts. The percentage differences between the values calculated by Gandhi et al. in [103] and those extracted from LEPTO are given in Table 3.2 (calculated as $\frac{\sigma_{\mathrm{LEPTO}} - \sigma_{\mathrm{Gandhi}}}{\sigma_{\mathrm{Gandhi}}}$).

At $E_\nu = 10$ GeV, the differences in the cross-section are at the level of 10%. However, this is nearly an order of magnitude better than the situation with the default cuts. The mean inelasticity (which determines the muon energy) is better reproduced at the level of 4% for neutrinos and 1% for anti-neutrinos. By 100 GeV, the differences are smaller and are at the level of 5%.

We can see from Table 3.2 that up to 10 PeV, the cross-section is reproduced correctly to the level of 5% and the mean-inelasticity to better than 1.5%. Even up to 100 PeV, the discrepancies are at the levels of 7% and 5% respectively. We shall return to the calculation of the high energy cross-sections in the section on PDFs but for now we state that the numerical procedures in LEPTO reproduce calculated high energy cross-sections to better

E_ν (GeV)	$\Delta\sigma(\nu N)$	$\Delta\sigma(\overline{\nu}N)$	$\Delta\langle y\rangle(\nu N)$	$\Delta\langle y\rangle(\overline{\nu}N)$
10^1	8.00	12.77	-4.32	-0.98
10^2	3.34	5.92	-0.59	2.24
10^3	2.12	3.41	-0.92	3.42
10^4	0.44	1.48	-1.38	-0.57
10^5	-1.04	-0.37	-3.37	-1.93
10^6	-2.19	-2.04	3.50	0.62
10^7	-4.75	-4.47	-1.27	-0.16
10^8	-7.25	-7.22	-3.85	-4.45

Table 3.2: Percentage differences between neutrino nucleon cross-sections and mean inelasticities calculated by LEPTO and from Gandhi et al.

than 5% up to 10 PeV. We shall see later that this is smaller than the uncertainty in the cross-section from our knowledge of PDFs at low-x.

We have shown that using LEPTO as a tool for generating high energy neutrino interactions, it can be made to reproduce both the cross-sections and the event kinematics (specifically, the values of Bjorken-y which determines the scattered lepton energy - the most important parameter for ANTARES) compared to published calculations in [103] to within approximately better than 5% for the most interesting energies between 100 and 10^7 GeV (and only marginally worse outside this range). This will be taken to be sufficient for the purposes of this thesis and the code will be used to conduct further studies with regard to ANTARES.

Contribution of Quasi-Elastic and Resonant events

Quasi-Elastic and resonant events have a cross-section which tends to a constant value for neutrino energies above about 5 GeV (see e.g. Figure 7.12 in [107] for the total charged current cross-sections for Quasi-Elastic and resonant events). Once above this value (and hence in the region of interest for ANTARES), the total Quasi-Elastic and resonant cross-sections are about 1.5×10^{-42} m^2 (1.6×10^{-42} m^2) for neutrinos (anti-neutrinos). This is compared to a DIS cross-section which rises approximately linearly[2] with neutrino (anti-neutrino) energy from 3×10^{-42} m^2 (1.5×10^{-42} m^2) at 5 GeV. Hence, we expect the importance of the Quasi-Elastic and resonant events to diminish quickly with energy.

The contribution of each of these channels, extracted from the combined LEPTO/RSQ code, to the total anti-neutrino cross-section as a function of neutrino energy is shown in Figure 3.3 (the results for neutrinos are similar but with an even smaller contribution from QE and resonance channels). The DIS contribution is always the largest and dominates above a few tens of GeV. Therefore, whilst the contribution of the QE and resonance channels cannot be completely neglected, their contribution to the overall event rate will be small and the uncertainties from these channels can be neglected.

[2] This linear increase holds up to energies of about 10 TeV where the effect of the W propagator in the differential cross-section acts to suppress the total cross-section.

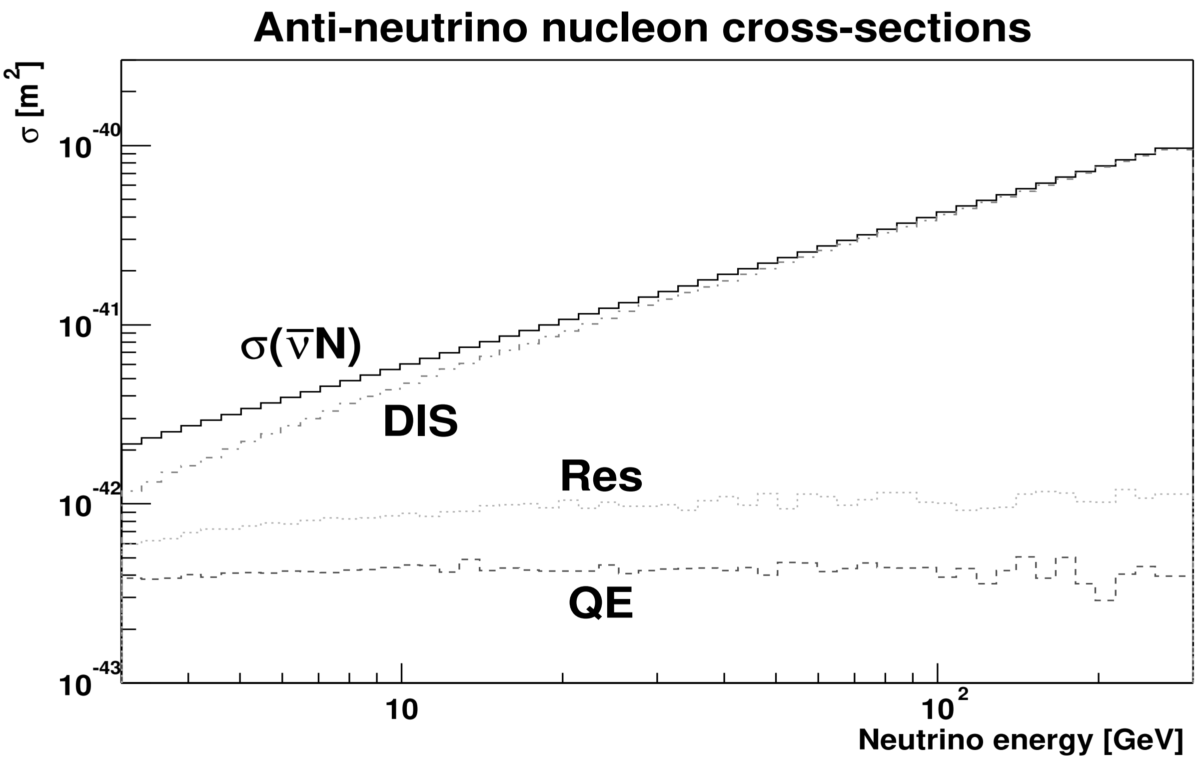

Figure 3.3: Total cross-section for anti-neutrino interactions showing the dominant contribution of Deep Inelastic Scattering (DIS) and the smaller contributions of Resonant (RES), Quasi-Elastic (QE) interactions. For neutrinos, the DIS contribution is even larger.

Effect of the choice of medium on cross-sections and kinematics

The discussion up to this point has been based on isoscalar nuclei. The two media of interest in ANTARES are "standard rock" (A=22, Z=11 and $\rho = 2.65\,\mathrm{g\,cm^{-3}}$ - taken from [109]) and water (A=18, Z=10 and $\rho = 1\,\mathrm{g\,cm^{-3}}$). Whilst standard rock is an isoscalar nucleus corresponding to the results above, the water is not and this will have an effect on the total cross-section for each type of nucleus. The relative importance of the two media will depend on the direction and energy of the neutrinos.

The generation scheme employed in both LEPTO and RSQ requires an initial choice of target medium which cannot be changed during the generation as it requires a time consuming recalculation of the cross-sections in each case. As our choice of medium is fixed, it is important to understand the difference this assumption could have on the final results. There are two principal differences between the two media: target density and nuclear composition. The target density is taken care of in the generation stage by working in "water equivalent units" where the density is set to one and all distances rescaled accordingly (see Section 3.3 for a discussion of water equivalent units and Section 3.4 for how it is taken account of in the final event generation). This leaves the target composition which, once the density has been scaled out, is expressed as an average cross-section per nucleon.

The cross-section per nucleon is calculated by summing over the individual nucleons and dividing by the total number of nucleons (and hence neglecting nuclear effects). Therefore, for a nucleus of atomic number Z and mass number A, we have a total cross-section per nucleon of:

$$\sigma_N^{total} = \frac{Z}{A}\sigma_p + \frac{(A-Z)}{A}\sigma_n \tag{3.5}$$

where σ_p and σ_n are the neutrino-proton and neutrino-neutron cross-sections respectively. We can then write the cross-section per nucleon for water as:

$$\sigma_{H_2O} = \frac{10}{18}\sigma_p + \frac{8}{18}\sigma_n = \frac{1}{2}(\sigma_p + \sigma_n) + \frac{1}{18}(\sigma_p - \sigma_n) = \sigma_{\text{iso}} + \frac{1}{18}(\sigma_p - \sigma_n) \tag{3.6}$$

The largest possible error introduced by assuming the wrong medium would be when either σ_p or σ_n is 0 and the cross-section is totally determined by the other. This would introduce an error in the cross-section of order 6%. Naively, at low energies when the valence quark distribution dominates, we would expect $\frac{\sigma_p}{\sigma_n} \sim \frac{1}{2}$ for neutrinos (and the reverse for anti-neutrinos) in which case the difference between the isoscalar and water cross-section is of the order of 3%. At high energies, the low-x distribution of the sea quarks dominates and we would expect the effect to be even smaller.

The cross-sections and $\langle y \rangle$ extracted from LEPTO for water are visibly identical to those for rock in Figure 3.2 with differences of less than 4% for both at all energies, in line with the expectations above. Whilst this error is already small, its effect can additionally be minimised by choosing the medium appropriate to a particular simulation: water for low energies when most vertices are in the can and rock for high energy upgoing events where most events start within the rock. For the remainder of this thesis, we neglect this effect and perform all simulations with an isoscalar target.

3.2.3 Parton Distribution Functions

Finally, we come to the question of the appropriate choice of Parton Distribution Function for the following simulations. As mentioned above, the choice of PDF enters into both the cross-section and kinematics calculations via the quark distribution functions $q(x, Q^2)$. These PDFs are extracted from electron-proton collision data at HERA and fixed target experiments (see [110] for a review).

Following the choices in [103], we calculate the total neutrino nucleon and anti-neutrino nucleon cross-sections for four PDFs taken from PDFlib:

CTEQ3D [108] The reference choice in [103] and in this thesis.

CTEQ5D [111] An updated version of CTEQ3D. The extrapolation of the PDFs to low-x differs from CTEQ3D.

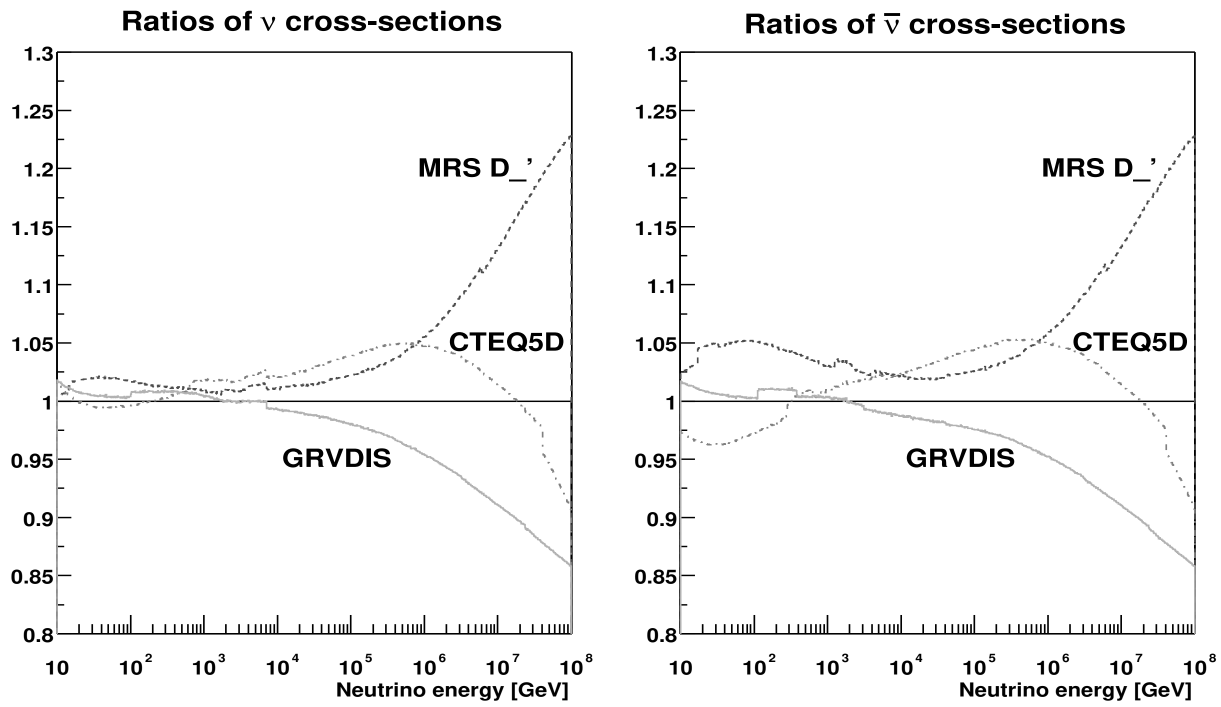

Figure 3.4: Ratios of neutrino (left) and anti-neutrino (right) cross-sections for various PDFs compared to those for CTEQ3D for neutrino energies between 10 and 10^8 GeV.

GRVDIS [112] Referenced by SuperKamiokande in [14] for (relatively) low energy neutrinos in their atmospheric neutrino analysis.

MRS D_′ **[113]** A different scheme is used to extrapolate to low-x which slightly overestimates existing data. As stated in [103], this can be used to provide an estimate of an upper limit on the cross-section.

For high energy neutrino interactions, most neutrino interactions correspond to the low-x and high-Q^2 region of the kinematic phase space which is unfortunately the region of greatest uncertainty in the calculations and fitting of PDFs. Therefore, it is important that we test this uncertainty with a range of PDFs. The ratios of cross-sections to CTEQ3D for the PDFs above are shown in Figure 3.4.

Below 10 TeV, the differences are small (at or below the level of 5%). Above this, the GRV cross-section falls below that of CTEQ3D with the values being 10% smaller by 10 PeV. Above 1 PeV, the MRS D_′ cross-section becomes significantly larger (as expected from [103]) with an excess of 20% at the maximum energy of the simulation at 100 PeV. The differences between CTEQ3D and CTEQ5D are much smaller and only rise above the level of 5% close to the maximum simulation energy of 100 PeV.

These uncertainties will affect the calculation of event rates in several ways. The interaction rate near the detector is simply proportional to the cross-section. Additionally, absorption in the Earth (see the description of the event weights in Section 3.4) has an exponential term with the cross-section in the exponent. The energy of the outgoing muon will depend on the PDF and hence be affected by any energy dependence of the reconstruction. The contribution to the overall uncertainty is non-trivial and energy dependent so we shall return to this in Section 5.2 after a full detector simulation and muon reconstruction.

3.2.4 Overall systematic effects in simulating neutrino interactions

In the sections above, we have shown that LEPTO can reproduce the published cross-sections and kinematics in [103] to better than 5% in the main region of interest. We have shown that the contribution of Quasi-Elastic and Resonance events is small but not negligible and that the effect of the choice of interaction medium is less than 5%. These uncertainties will be neglected for the remainder of this thesis.

The dominant uncertainty from this section arises from the choice of PDF which affects the neutrino interaction cross-sections and the event kinematics in a non-trivial way. The effect of this, though relatively small in terms of the interaction cross-section below 1 PeV, cannot necessarily be neglected. Above 1 PeV, the uncertainty in the neutrino cross-section increases markedly. The effect of the choice of PDF will be investigated further after the muon reconstruction in Section 5.2.2.

3.3 High energy muon propagation

For neutrinos which interact outside the can, it is necessary to propagate the particles produced in the interaction to its surface before they are processed with the detector Monte Carlo. In practice, only high energy muons have a long enough range to reach the detector with 100 TeV muons able to travel many tens of kilometres. The method used to propagate muons and the approximations made in this tracking will then have an important effect on the number of muons seen at the detector.

3.3.1 Muon energy losses at high energies

There are a number of different processes by which high energy muons lose energy as they propagate through matter. The processes discussed here are taken from the MUM (MUons + Medium) muon propagation code which has been extensively checked against existing data and is numerically accurate to better than the level of uncertainty on the inputs [114]. We can divide the energy losses into the following categories (described fully in the MUM code and in [114]):

Ionisation The continuous energy loss of muons passing through a medium as relatively low energy transfers to atomic electrons ionise the material along the muon path. The

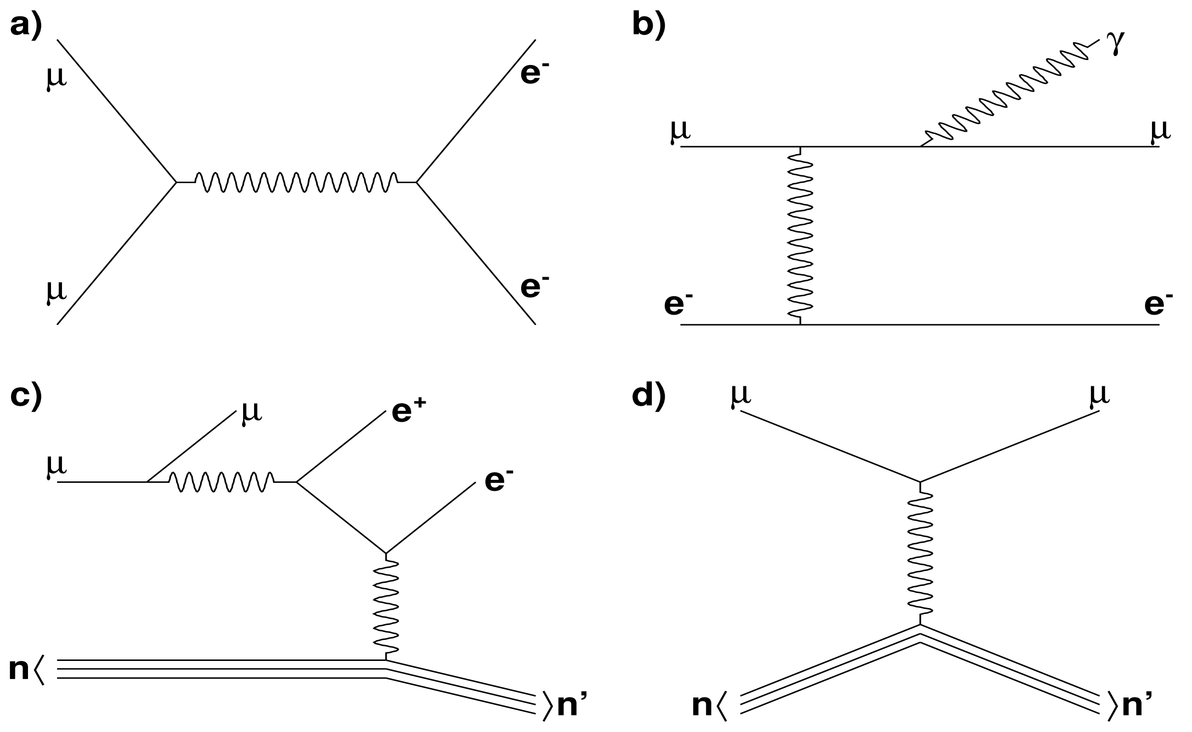

Figure 3.5: Muon energy loss processes in matter. Diagram a) shows muon scattering from atomic electrons (i.e. ionisation loss and knock on electrons), b) shows muon bremsstrahlung on atomic electrons, c) shows electron pair production and d) shows a photonuclear interaction with a general nucleon, n.

energy loss is calculated using the Bethe-Bloch formula and the basic process is shown in diagram a) in Figure 3.5.

Bremsstrahlung In the electric field of a nucleus or atomic electrons, muons can radiate high energy photons as shown in diagram b) of Figure 3.5.

Pair production A muon can radiate a virtual photon which, again in the electric field of a nucleus, can convert into a real e^+e^- pair. This process is shown in diagram c) of Figure 3.5.

Photonuclear interactions A muon can radiate a virtual photon which directly interacts with a nucleus in the muon propagation medium. The interaction is either electromagnetic or following the fluctuation of the photon into a quark-antiquark pair (i.e. a virtual vector meson). The basic interaction is shown in diagram d) of Figure 3.5.

Knock on electrons Muon interactions with electrons as shown in diagram a) in Figure 3.5 can produce free electrons with large enough energies to travel a significant distance (and produce Cherenkov light). These are termed knock-on electrons.

In the context of a simulation of muon propagation, these processes are usually divided into “continuous” and “stochastic” processes. The distinction is made purely for the purposes

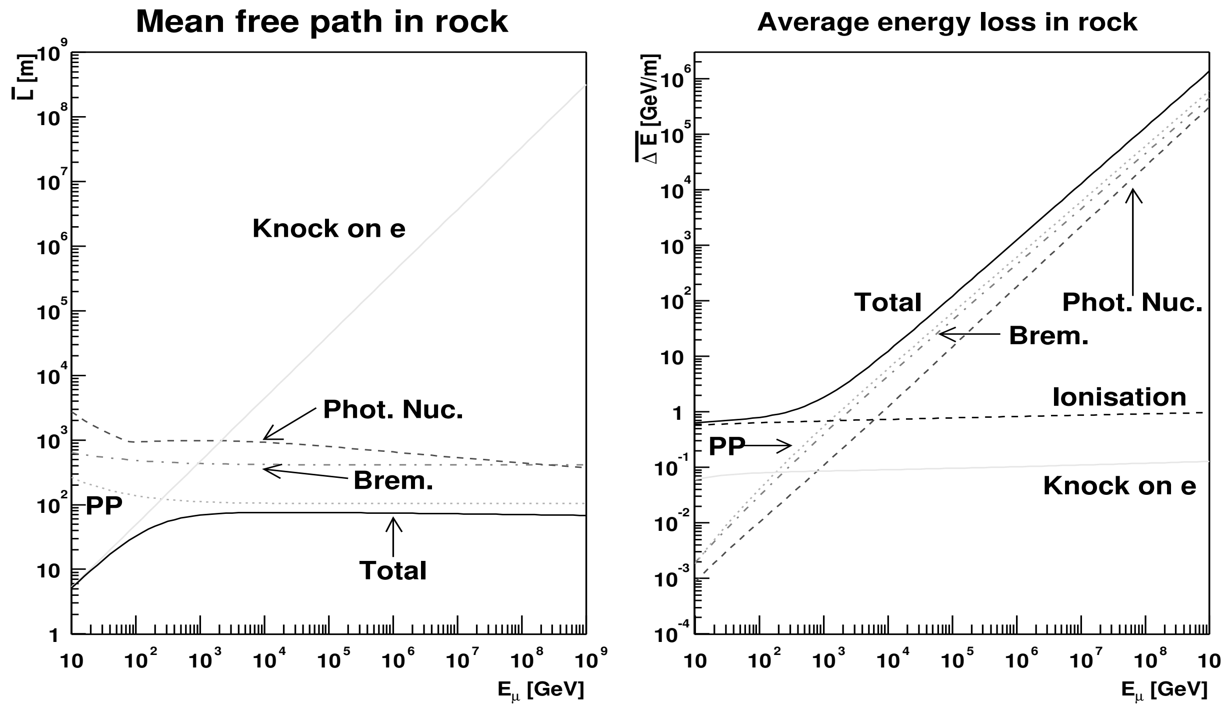

Figure 3.6: Mean muon interaction lengths (left) and energy losses (right) in standard rock for continuous and stochastic energy losses for the absolute and relative energy cuts of 10 MeV and 0.01. Continuous processes dominate the total energy loss at low energies and stochastic processes dominate at high energies.

of simulation[3] with a cut in both the absolute energy transfer (ΔE) and the relative energy transfer ($\frac{\Delta E}{E}$) being made. Only interactions with an absolute or relative energy transfer above these cuts are treated stochastically with the remainder being included with ionisation as the continuous energy loss. Based on a study of the effect of these cuts in [114], values of 10 MeV and 0.01 are chosen for the absolute and relative energy transfer cuts respectively for all the following simulations.

Muon interactions

The mean free paths between stochastic interactions and the average energy losses (in GeV per m) for muons propagating in standard rock with the cut levels above are shown in Figure 3.6. The values were extracted directly from the MUM code. Similar results are obtained for water.

Below 100 GeV, continuous energy losses (mainly ionisation) dominate and are (approximately) independent of energy. Hence, at low energies, the muon range is simply proportional to the energy. At higher energies, the stochastic processes dominate, particularly

[3] All processes, no matter how small the energy loss, are essentially stochastic at the microscopic level but simulating the propagation in such a manner would take a prohibitively long time.

Bremsstrahlung and pair production with interactions (with a relative energy transfer above 0.01) of order every 100 m and energy losses (approximately) proportional to the energy.

At very high energies, the photonuclear contribution becomes more important. Unfortunately, this is theoretically the least well understood of the above interactions and the uncertainties become large at these energies. In the version of MUM used here, the formula of Bezrukov and Bugaev in [115] has been used. This parameterisation may substantially underestimate the contribution of photonuclear interactions above 1 PeV to the total energy loss [116] and MUM is being developed to take account of this. However, due to the absorption of neutrinos in the Earth (see Section 3.4.2, page 74), the rate of events with muons above 1 PeV will be strongly suppressed and the uncertainty in the photonuclear interaction cross-section will therefore not be important for ANTARES.

Muon codes and muon multiple scattering

The MUM code has been chosen because of its proven [114] accuracy of simulation and speed. Historically, the much older PropMu code [109] has long been used in simulations of muon propagation. Recently, studies have shown significant numerical errors in PropMu [114, 117] failing to reproduce its own inputs at the level of 20% for the energy loss of muons between 20 GeV to 10 TeV. The PropMu code however does include muon multiple scattering which MUM does not. For ANTARES with a target angular resolution of a few tenths of a degree, this could be significant in the accuracy of the reconstruction of the neutrino direction for neutrino astrophysics. We will therefore evaluate both MUM and PropMu for use in the event generation in the following sections and later study the effects of these codes on event rates and angular resolutions in Chapter 5.

A third code, MUSIC [118], which is accurate and includes multiple scattering is also available but is much slower than the two above (the relative energy cut is much smaller) and is therefore not considered for the purposes of the event generation where speed is paramount. It is however used in the detector simulation described in Chapter 4 where accuracy over small distances and muon multiple scattering potentially become more important.

Matter density and water equivalent units

The principal difference between the results presented in Figure 3.6 for rock and those for water arises from the different densities of the two media (2.65 in g cm^{-3} for standard rock compared to approximately 1.0404 g cm^{-3} for sea water at a depth of 2.4 km) as the energy losses are simply proportional to the number of target nucleons per metre of muon track which in turn is proportional to the density of the medium.

The effect of the medium densities normally rescaled out by working in "water equivalent" (w.e.) units where we set the density of all materials to 1 in the simulations. We can then rescale the resulting water equivalent distances by $\frac{1}{\rho}$ to obtain the physical distances. This concept is used extensively in the sections below and in the event generation method described in Section 3.4 to take account of the densities of the different media.

3.3.2 Maximum muon ranges in rock and water

For muons of a given starting energy in a given medium, we can define a survival probability, P_{surv}, as a function of propagation distance, X. We apply a muon energy threshold $E_\mu^{min} = 0.16$ GeV (the threshold for Cherenkov light production of muons in water) below which muons are treated as though they have stopped. This choice is essentially equivalent to applying no threshold[4].

We then calculate this survival probability for a range of muon energies between 1 GeV and 1 EeV (10^9 GeV) as a function of the propagation distance by propagating 10^6 muons and recording the distance at which they are stopped. Sorting these distances then directly gives the distance after which specific fractions of the muons were stopped - i.e. it gives the survival probabilities.

The survival probabilities for muons of energies (in GeV) of 10^3, 3×10^3, 10^4, $\ldots$, 10^9 are shown in the upper figures in Figure 3.7 for rock and sea water as a function of the distance in water equivalent units. The simulation results from PropMu are shown as grey points and from MUM as black lines down to survival probabilities of 10^{-6} (the limit from the statistics in the simulation).

The interest in these simulations lies not in the survival probabilities themselves but with a parameterisation of the muon ranges calculated from them. In particular, we want to know the maximum distance a muon of a given starting energy will propagate in a given medium which will allow us to define an all encompassing volume around the detector for the event generation. As the stochastic muon energy losses are a randomly occurring process, the actual maximum range of any muon is extremely large[5]. Our main concern is that, by the limiting the size of the generation volume, we do not bias the resulting distribution of particles at the can. Hence, we define the maximum muon range, $R_{max}(E_\mu)$ as the distance within which a fraction $1 - P_{surv}$ of muons of a given starting energy are stopped. The optimum value of this fraction for defining the total event generation volume will be determined in Section 3.4.3.

The distances corresponding to survival probabilities of $10^{-1}, 10^{-2}, \ldots, 10^{-6}$ for muon energies between 1 GeV and 10^9 GeV are given for PropMu in rock and sea water and MUM in rock and sea water in Table B.3, Table B.4, Table B.5 and Table B.6 respectively in Appendix B. The results in these tables are interpolated in $\log_{10}(E_\mu)$ and $\log_{10}(R_{max})$ to give the function $R_{max}(E_\mu)$ for any of the above choices of P_{surv}.

The maximum muon ranges in rock and sea water for each of the above codes are shown in the lower plots of Figure 3.7 corresponding to a choice of P_{surv} of 10^{-3} (shown by the dashed line in the upper plots). At very high energies, PropMu gives shorter ranges. At lower energies (shown in the insets), the differences are smaller and depend on the medium.

---

[4]Muons in water lose approximately 0.25 GeV per m. Hence, a 0.16 GeV muon will travel roughly 60 cm which will be negligible compared to muon paths in the ANTARES simulations of the order of hundreds of metres or even kilometres.

[5]There is an extremely small but non-zero probability that a given muon will go an arbitrarily large distance without any stochastic interaction so the range will be determined by the ionisation loss only.

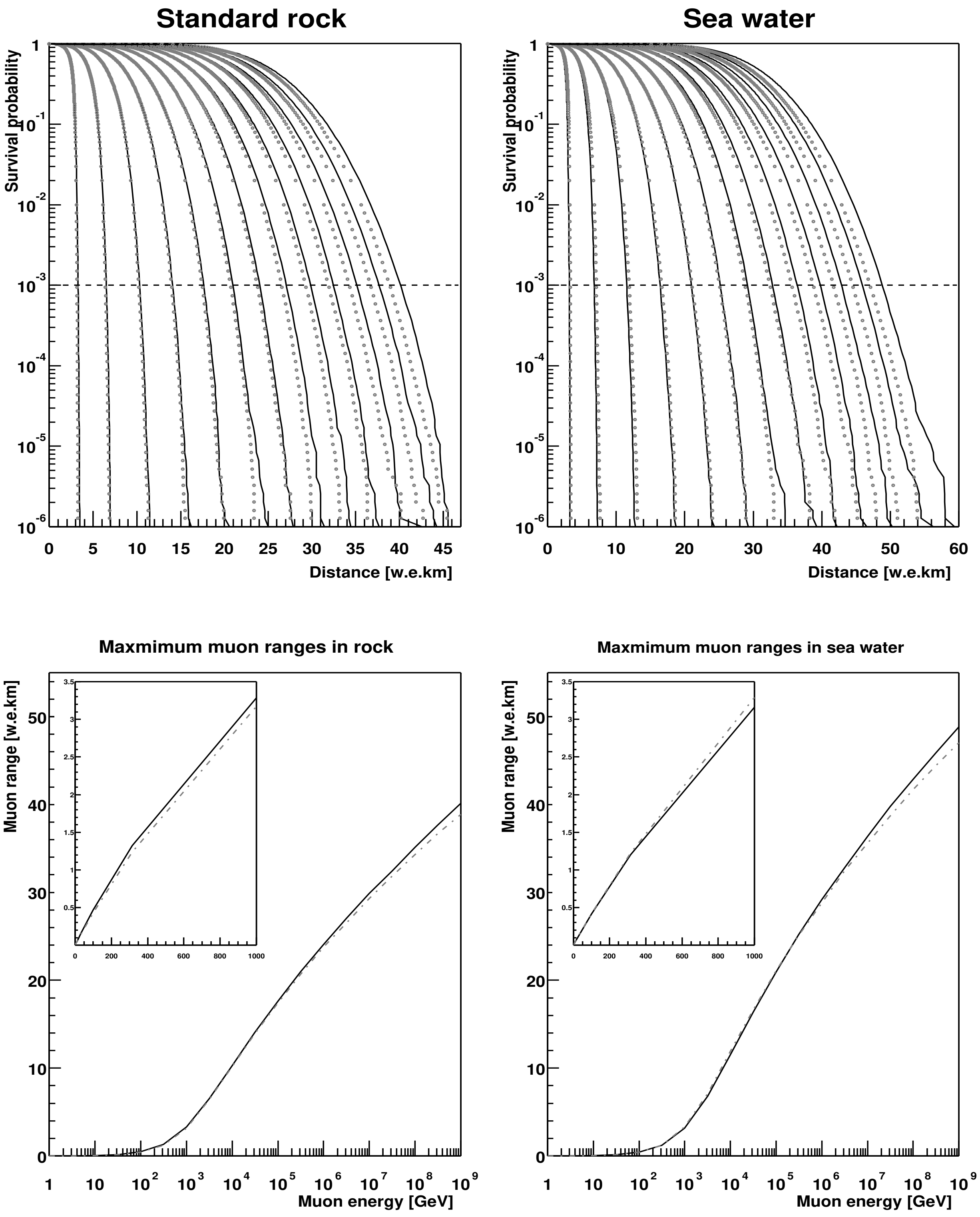

Figure 3.7: Muon survival probabilities for energies (in GeV) of 10^3, 3×10^3, 10^4, ..., 10^9 in standard rock and sea water using PropMu (grey points) and MUM (black lines). The ranges (in w.e.km) corresponding to a survival probability of 10^{-3} are shown in the lower plots for each medium.

As stated above, the interest in calculating and tabulating these maximum ranges is to define volumes for simulation which can contain all muons which could reach the detector (with an error less than the choice of $1 - P_{surv}$). In addition, it also allows fast decisions to be made on whether to simulate individual muons based on just an energy and distance without performing the full simulation of the muon energy losses. Both these techniques are used in the method described in Section 3.4.

3.3.3 Effective muon ranges

In addition to the maximum muon range above, it is also possible to define an "effective" range for muons with a given starting energy above a given energy threshold which is an average range taking into account fluctuations in the muon energy loss due to the stochastic nature of the muon interactions. The definition of the effective range is taken from [109]:

$$R_{eff}(E_\mu; E_\mu^{min}) = \int_0^\infty P_{surv}(E_\mu; E_\mu^{min}, X)dX \tag{3.7}$$

This could be calculated for a single muon propagation medium using the survival probabilities shown in Figure 3.7. However, muons reaching the ANTARES detector can propagate in both rock and water and the different target nuclei present different interaction cross-sections with a different energy dependence, even when working in water equivalent units (where all densities are set to 1). A simulation method which allows for the calculation of effective muon ranges in two media and the results of and fits to those simulations are discussed in detail in Appendix A.

The concept of effective muon ranges is not used directly in the event generation as a full simulation in the correct media is done for each event. However, it can be used to relate muon fluxes to neutrino fluxes and to calculate the detector efficiency as an "effective area". Some of the results of the simulations in Appendix A will be used in Section 5.4 to perform these calculations for ANTARES.

3.4 Event generation method

Using the tools described in the sections above, we now develop a method of generating neutrino interactions which satisfies the requirements described in Section 3.1.2. We choose a power law, E^{-X}, for the generation spectrum of the neutrino interactions (which we will refer to as the "interacting neutrino spectrum" in the following description). This can then be weighted to different neutrino fluxes to give the event rates for specific models.

Other approaches used in ANTARES [40, 102] can only generate events inside or outside the can, but not both and can involve reweighting events with a large variation in the weights assigned to individual events, limiting the statistical information which can be obtained from a particular sample[6]. The new approach described here generates events both inside and

[6] A large variation in the weights will mean that those events which contribute to the final sample with

outside the can in the correct proportions and reduces the number of factors which enter into the event weights.

3.4.1 Simulation scheme

The general simulation method is to define a volume around the detector which will contain all potentially observable neutrino interactions for the given energy range and simulate neutrino interactions within that volume using the tools described in Section 3.2. For those neutrino interactions outside the can, any muons produced are then propagated and stored if they reach the surface of the can using one of the muon codes discussed in Section 3.3. To get meaningful statistics after the muon propagation stage, say a few thousand muons at or within the can, it is typically necessary to simulate $\mathcal{O}(10^{10})$ neutrino interactions. Clearly, the simulation time required to completely process this number of events would be prohibitive in the extreme. A different approach is therefore needed which minimises the amount of detailed simulation required to account for each individual neutrino interaction.

Simulation algorithm

The largest possible muon energy in the simulation corresponds to the upper limit on the neutrino energies specified by the user, E_{max}. Hence, from the fits in Section 3.3.2, we can calculate the maximum muon ranges in both rock and water at this energy, $R_{max}(rock)$ and $R_{max}(water)$ respectively. No neutrino interacting further away from the detector than these distances in the appropriate medium can possibly produce a muon which will reach the detector. Hence we can use these distances to define our total simulation volume. Starting with this information, the full simulation then proceeds by the following method:

1. We define a cylindrical volume around the instrumented volume of the detector. The size depends on the range of zenith angles, θ_{min} to θ_{max}, in the simulation. For simulations containing just upward going events, the upper surface stops at the top of the can (as defined in Section 3.1.1). Otherwise, for simulations containing downward going events, it is $R_{max}(water) \times \cos\theta_{max}$ or the distance to the surface of the sea, whichever is smaller. In both cases, radially, it is $R_{max}(water)$ and downwards from the base of the can it is $R_{max}(rock)$. All the distances are in water equivalent units.

2. We divide the total interacting neutrino spectrum between E_{min} and E_{max} into equal bins in $\log_{10}(E_\nu)$ and calculate the number of events, N, to generate in each bin. For a bin i with energies E^i_{min} to E^i_{max}:

$$N^i(E^i_{min}, E^i_{max}) = N_{total} \times \frac{\int_{E^i_{min}}^{E^i_{max}} E^{-X} dE}{\int_{E_{min}}^{E_{max}} E^{-X} dE} \tag{3.8}$$

a large weight will dominate the final distribution and, hence, the statistical variations in that sample will correspond to this subset of events only.

3. For each energy bin, we can calculate a maximum range in rock and water using the maximum energy in that bin. We can then calculate a "scaled" generation volume for that bin in the same way we determined the total generation volume above. The number of events to generate in that scaled volume is then:

$$N^i_{scaled}(E^i_{min}, E^i_{max}) = P\left(N^i \times \frac{V_{scaled}}{V_{total}}\right) \tag{3.9}$$

   We have smeared the average number to generate in each bin by sampling from a Poisson distribution $P(\mu)$ with mean μ to preserve the statistical fluctuations between different energy bins.

4. Now, for each energy bin in turn:

   (a) We perform the numerical integration of the cross-section in LEPTO and initialise the generation for just this energy range. This helps to reduce numerical errors which are introduced if the energy range spans many decades.

   (b) Looping over the number of events to generate in this scaled volume, N^i_{scaled}:

      i. The energy of the interacting neutrino is sampled from the E^{-X} spectrum within the energy range of this bin.

      ii. The neutrino position is chosen from within the scaled volume. Using the distance downwards in the rock (when the vertex is in the rock) divided by the density of the rock, ρ_{rock}, gives the vertex position in "real" (i.e. not water equivalent) distances and ensures that there are $\frac{\rho_{rock}}{\rho_{water}}$ times as many interactions per unit volume in the rock compared to the water (the interaction rate in rock is proportional to ρ_{rock}).

      iii. Whether or not the vertex is inside the can is determined. If it is outside, the shortest distance from the neutrino vertex position to the can is calculated. If this distance is greater than the maximum muon range at that neutrino energy, no muon produced by this neutrino will ever reach the can and the event is rejected with no further processing.

      iv. The neutrino direction is sampled from an isotropic distribution. For events outside the can, we calculate whether the distance of closest approach of the neutrino direction to the can is greater than some user specified distance. If it is, the event is rejected. There are two extreme cases here:

         - At low energies, the muon and the neutrino directions are not closely correlated. Hence, testing on the neutrino direction for whether the muon will hit the can isn't necessarily a good test. However, low energy neutrinos must interact close to the can to produce a detectable muon so will pass this test provided the user specified distance is large enough.
         - At high energies, the neutrino and muon are essentially co-linear so, even though the neutrino could be a large distance away from the can, checking the neutrino direction is sufficient to determine whether the muon hits the can.

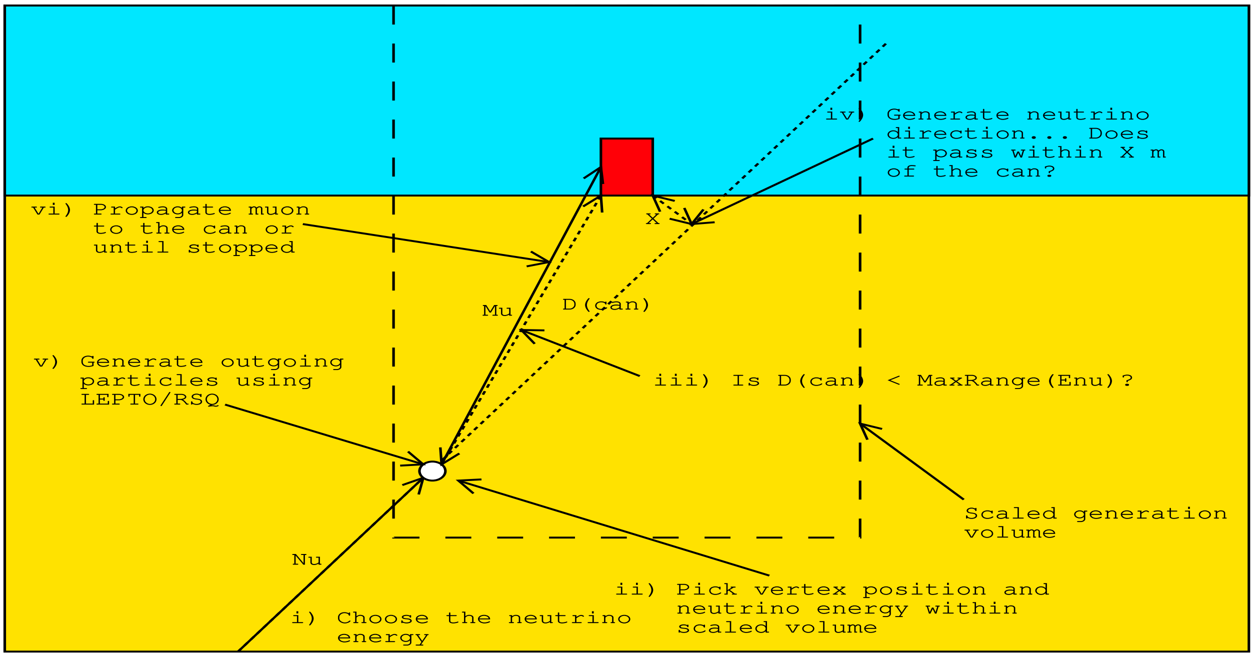

Figure 3.8: Schematic overview of the event generation algorithm.

In the intermediate region, both of these apply to some extent. The degree to which this selection biases the resulting distribution of events at the can and the most appropriate value of the cut distance will be investigated in Section 3.4.3.

v. For each event, we choose a channel (DIS,Resonant or Quasi-Elastic) according to the relative cross-sections. We then simulate the neutrino interaction using the appropriate code (as described in Section 3.2) to get the final state particles at the neutrino interaction vertex.

vi. For events inside the can, we record all these particles (position, direction, energy etc) for further processing. For events outside the can, we keep just the muons. If the muons' tracks intersect the can, they are propagated to the surface of the can using the chosen muon propagation code. Only if at least one muon reaches the can before being stopped is the event recorded.

vii. For those events which are kept, the "event weights" are calculated and all the event information written to disk. See Section 3.4.2 for a discussion of the event weights.

5. On completion of all the stages above, we have a record of every one of the $\mathcal{O}(10^{10})$ neutrino interactions which produced at least one particle at or inside the can.

A schematic overview of this method for a neutrino interaction outside the can is shown in Figure 3.8. We will evaulate the time savings made in each of the stages of the above method when determining the optimum values for the selection cuts in Section 3.4.3.

User inputs

For reference, we summarise the input parameters for the simulation method described above. For each simulation, the user must specify the following parameters:

- The range of neutrino energies, E_{min} to E_{max}, and zenith angles, θ_{min} to θ_{max}.
- The spectral index, $-X$, for the interacting neutrinos (i.e. the energies of neutrinos whose interactions are to be simulated are drawn according to E^{-X}).
- The number of neutrino interactions to generate.
- Whether we are simulating neutrinos or anti-neutrinos.

The following parameters can be altered (with the default values shown in square brackets, [...]). In future, if a parameter is not mentioned, it takes the default given here.

- The size of the can around the detector (as the distance beyond the outermost OMs of the instrumented volumes) [200 m].
- The neutrino flux model [Bartol] and prompt neutrino contribution [none] (see Section 3.4.2).
- The number of energy bins into which the total neutrino energy range is divided [10].
- Choice of Parton Distribution Function from either LEPTO or PDFlib [CTEQ3D].
- Muon code, multiple scattering and maximum range cut level ($1 - P_{surv}$ from Section 3.3.2). These choices will be discussed later in Section 3.4.3 and the effect of the different muon propagation codes on the detector performance will be discussed in Section 5.2 [MUM, cut at 0.1].
- The maximum allowed distance of closest approach of the neutrino direction to the can. Again, this choice will be discussed in Section 3.4.3 [500 m].
- The target medium - isoscalar (including standard rock) or water. Shown in Section 3.2 to be a difference of less than 4% in the cross-section and kinematic variables for all energies of interest [isoscalar].

A complete description of all these parameters and how they are implemented and used in the simulation code is given in [119].

3.4.2 Neutrino fluxes and event weights

The above method generates events for a user input power-law energy spectrum for the neutrino interaction rate. This is sufficient for calculating effective areas and volumes (see Section 5.4) as the generated neutrino energy spectrum can be divided out. However, it is sometimes desirable to be able to directly reweight individual events to a particular differential neutrino flux.

Weight derivation

To be able to derive the appropriate event weight, we need to define the following parameters (taken from the original ANTARES definition in [120]):

V_{gen} (m^3) The total generation volume (in water equivalent units in this case).

I_θ (sr) $= 2\pi \times (\cos(\theta)_{max} - \cos(\theta)_{min})$ The angular phase space factor depending on the specified range of $\cos\theta_\nu$. It is the integral of the solid angle between $\cos(\theta)_{min}$ and $\cos(\theta)_{max}$.

I_E The energy phase space factor depending on the input spectral index, X, for the neutrino interaction rate. If $X = 1$, $I_E = \ln(\frac{E_{max}}{E_{min}})$ otherwise $I_E = (E_{max}^{1-X} - E_{min}^{1-X})/(1-X)$. It is the integral of the generation spectrum between the minimum and maximum energies.

$\sigma(E_\nu)$ (m^2) The charged current neutrino interaction cross-section.

ρN_A (m^{-3}) The number of target nucleons per unit volume. Note that, as V_{gen} is in water equivalent m^3, the density is always 1. Otherwise, an "effective density" would be needed based on the fraction of events interacting in each medium.

$P_{Earth}(E, \theta)$ The probability of neutrino transmission through the Earth.

N_{total} The total number of generated events specified in the simulation inputs.

t_{gen} (s) The (arbitrary) time represented by the simulation. This will appear in the flux calculations below and eventually cancel.

Now, the events we generated correspond to a rate, Γ_ν^I, of interacting neutrinos (with units of GeV^{-1}sr^{-1}m^{-3}s^{-1}) with the following distribution:

$$\frac{d\Gamma_\nu^{\rm I}}{dE_\nu d\Omega dV dt} = \frac{E^{-X}}{I_E} \times \frac{1}{I_\theta} \times \frac{N_{total}}{V_{gen}} \times \frac{1}{t_{gen}} \tag{3.10}$$

Integrating this over the range of angles, energy, time and volume simulated then correctly gives the total number of generated events, N_{total}. The rate of interacting neutrinos depends on the incoming neutrino flux, ϕ_ν (per unit area dS), the target density and the neutrino cross-section. Hence, to convert from the above interaction rate to give the neutrino flux the events we generated correspond to, we divide the interaction rate by the target nucleon density and neutrino interaction cross-section:

$$\frac{d\phi_\nu}{dE_\nu d\Omega dS dt} = \frac{d\Gamma_\nu^{\rm I}}{dE_\nu d\Omega dV dt} \times \frac{1}{\sigma(E_\nu)\rho N_A} = \frac{E^{-X}}{I_E} \times \frac{1}{I_\theta} \times \frac{N_{total}}{V_{gen}} \times \frac{1}{t_{gen}} \times \frac{1}{\sigma(E_\nu)\rho N_A} \tag{3.11}$$

This is the flux of neutrinos arriving at the detector which is in turn just the flux of neutrinos arriving at the surface of the Earth times the probability of transmission through the Earth, $P_{Earth}(E_\nu, \theta_\nu)$, for a particular E_ν and θ_ν. Hence, the flux of neutrinos arriving at the Earth that we simulated is:

$$\frac{d\phi_\nu}{dE_\nu d\Omega dS dt} = \frac{N_{total}}{V_{gen}\ I_\theta\ I_E\ E^X\ \sigma(E_\nu)\ \rho N_A\ t_{gen}\ P_{Earth}(E_\nu, \theta_\nu)} \tag{3.12}$$

For a flux corresponding to a particular model:

$$\frac{d\phi_\nu^{model}}{dE_\nu d\Omega dS dt} \equiv \phi(E_\nu, \theta_\nu) \tag{3.13}$$

we must reweight the events in each interval $dE_\nu d\theta_\nu$ by the ratio of the two fluxes at that point. To obtain a rate of events per second (setting t_{gen} to 1) corresponding to a specific neutrino flux model described by $\phi(E_\nu, \theta_\nu)$, we take each of our sample of events in each interval $dE_\nu d\theta_\nu$ from the simulation are weight them by the ratio of the model neutrino flux to the generated flux. This then gives us the weight, W_{event}, with a flux independent part, $W_{generation}$, associated with each individual event for a particular model:

$$\begin{aligned} W_{generation} &= \left(\frac{V_{gen}\ I_\theta\ I_E\ E^X\ \sigma(E_\nu)\ \rho N_A\ P_{Earth}(E_\nu, \theta_\nu)}{N_{total}}\right) \\ W_{event} &= W_{generation} \times \phi(E_\nu, \theta_\nu) \end{aligned} \tag{3.14}$$

For convenience, we calculate $W_{generation}$ for each event during the generation phase. This allows for a range of different fluxes to be applied without recalculating all the individual elements of the weight. To obtain distributions or event rates corresponding to a particular model we then just multiply each event by its weight when filling histograms.

It should be noted that the neutrino flux ϕ is often specified as a power law. The index of this flux refers to the neutrinos arriving at the Earth and is different from the index, X, used in the definition of the weights above (the two are connected by the cross-section and the target density). In the following sections, we reweight events to an E_ν^{-2} neutrino flux which refers to that arriving at the Earth and corresponds to the the types of sources discussed in Section 1.3.2, page 15.

Atmospheric neutrino flux models

The principal neutrino signal in ANTARES will be that from "conventional" atmospheric neutrinos. There are a number of different calculations of the atmospheric neutrino flux depending on measurements of the primary cosmic ray flux and different interaction models in the atmosphere. A full discussion of these different fluxes and a code to calculate all of them is given in [121] and references contained therein. The main models of interest are Honda (HKKM) [122], Bartol [123] and Fluka [124] (only up to 100 GeV). The differential fluxes predicted by these models are shown in Figure 3.9.

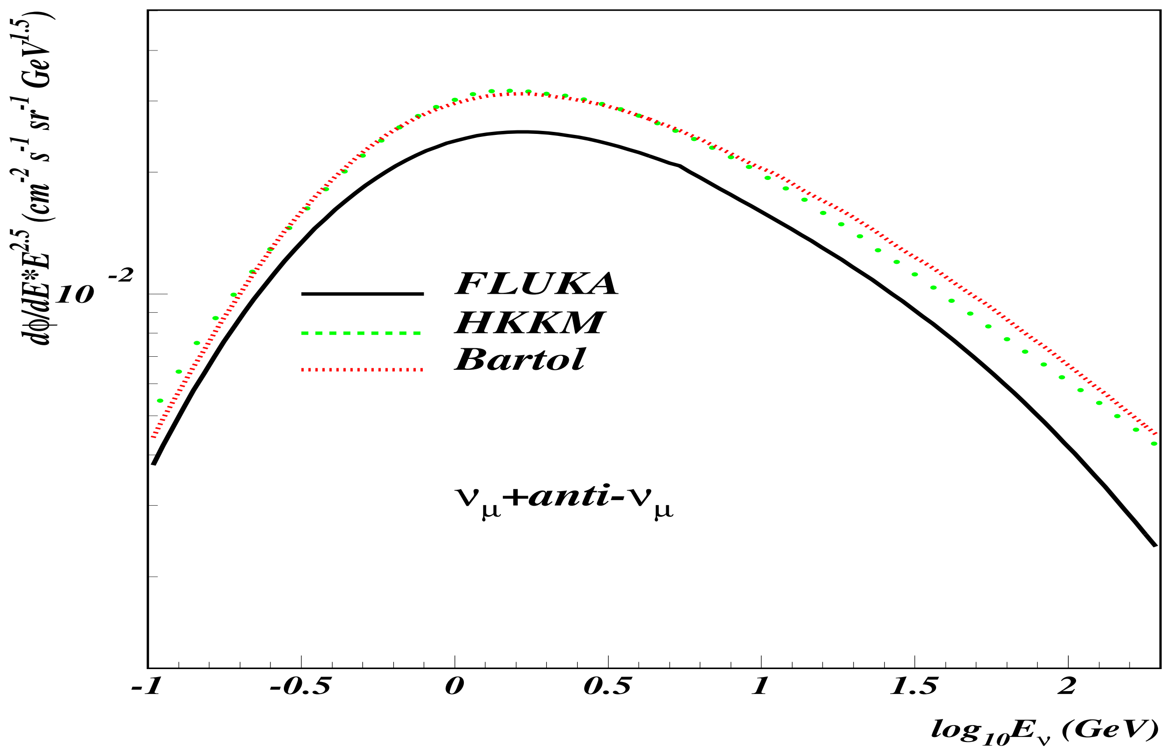

Figure 3.9: The angle averaged upward going muon neutrino and anti-neutrino differential flux (multiplied by a factor of $E^{2.5}$) predicted by the Honda [122], Bartol [123] and Fluka [124] groups (taken from [125]).

These calculations depend on the measured cosmic ray spectrum and extrapolation of hadronic interaction models to high energies. The overall uncertainty on the high energy atmospheric neutrino flux is estimated [125] to be of order 20% based on the uncertainties in the two inputs above. It should be noted that the close agreement between the Honda and Bartol flux calculations is a result of a cancellation between the differences in the primary cosmic ray spectrum used and the hadronic interaction models and that the actual uncertainty is much larger than the difference between these two models suggests.

In addition to the conventional neutrino flux produced by decaying pions and kaons in cosmic ray showers, there is the so-called "prompt" neutrino flux from the decay of charmed mesons which dominates the total flux above 10^5 GeV with a range of different predictions depending on the extrapolation of charm production cross-sections from accelerator energies. A review of these prompt fluxes is given in [126] where three general models of charm production are described:

QGSM Quark-Gluon string model

RQPM Recombination Quark Parton Model

pQCD Perturbative QCD

The code described in [121] includes the highest and lowest prompt neutrino fluxes from each of these three types of models as well as an independent prediction using pQCD (TIG [127]). This code is included in the program described above to allow the calculation of event rates (using the weights) for any combination of the above conventional and prompt atmospheric neutrino fluxes. The effect of different atmospheric neutrino flux models on the event rate will be discussed further in Section 5.2.4.

Neutrino absorption in the Earth

The probability of a neutrino being absorbed as it passes through the Earth depends on the density of matter along its path and the neutrino interaction cross-section. The integrated column density of the Earth, $\rho_l = \int_L \rho_{Earth}(r)dL$ (taken from the description in [103] and implemented for ANTARES by [40]) along some path L corresponding to a given zenith angle θ is shown in the left hand plots of Figure 3.10. The core of the Earth is clearly visible for the upward directions. The range of values at each angle for downward going events (where the column density is due to the water above the detector) is due to the variation in vertical position of the neutrino interactions.

The probability of transmission through the Earth is given by:

$$P_{Earth}(E_\nu, \theta_\nu) = e^{-N_A \times \sigma(E_\nu) \times \rho_l(\theta_\nu)} \tag{3.15}$$

This is shown in the right hand plot of Figure 3.10 as a function of neutrino energy and zenith angle. For neutrino directions close to vertically upwards ($\cos(\theta) = 1$), absorption in the Earth starts to be significant for neutrino energies above 10 TeV. Above 1 PeV, only neutrinos close to the horizontal remain unattenuated which strongly suppresses the neutrino flux above this energy. This effect will be seen again in the effective area presented in Section 5.4.3, page 143.

3.4.3 Verification of the optimisation cuts

In the above sections, we described a method of generating high energy neutrino events which relies on two main parameters to be efficient: the level at which the maximum muon ranges are defined (in terms of the fraction of muons which must be stopped to define the maximum range) and how close the neutrino direction must pass to the can to be likely to produce a muon at the can. In this section, we check that these cuts do not bias the distribution of events produced and obtain the optimal values.

The upper set of data points in the top plots of Figure 3.11 show the numbers of events at or within the can for atmospheric neutrinos and for a neutrino flux proportional to E^{-2} arriving at the Earth corresponding to a "typical" astrophysical source (both calculated using the event weights given in Eq. (3.14)). These are plotted as a function of X, the maximum muon range cut where X is defined by requiring $P_{surv} \leq 10^{-X}$. The second curves on each of the upper plots show the number of muons at the can generated per minute. The lower

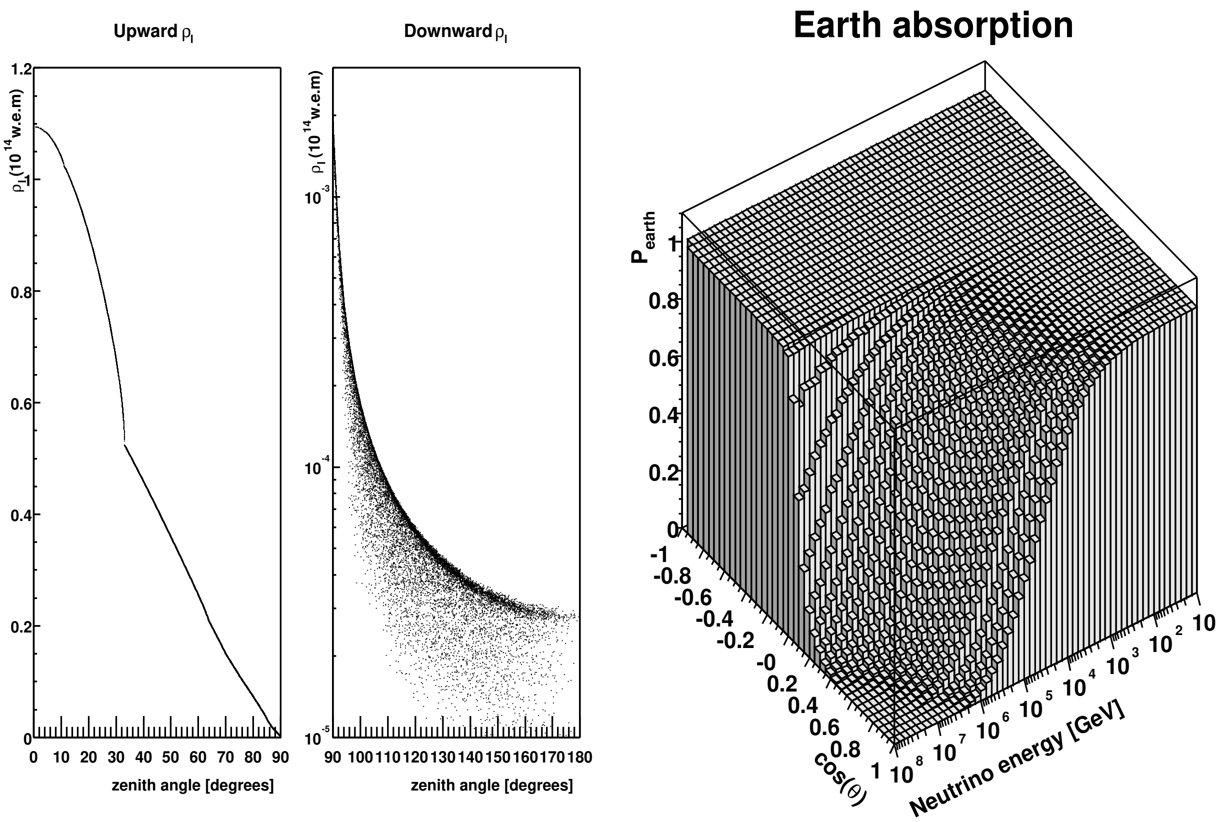

Figure 3.10: Line integrated column density of the Earth as a function of zenith angle (left). The spread for downward going neutrinos is from the range of depths for neutrinos in ANTARES. The transmission probability as a function of the energy and zenith angle of the neutrino (with $\cos(\theta) = 1$ being vertically upwards, i.e. from a path down through the Earth) is shown on the right.

plots show the muon energy distribution for cut levels of 10^{-1} and 10^{-6}. The two curves are completely consistent showing that not only is the total number of events consistent but also that the shape of the distributions is unchanged by setting the cut level at 10^{-1}. This level is also (obviously) the most efficient of those considered here so we choose this for all future simulations.

The plots in Figure 3.12 show the same information varying the maximum distance of closest approach between the muon direction and the can. Here, the algorithm is most efficient for a distance of 300 m (shorter than this and too many events are rejected, longer than this and too many events which can't reach the can are simulated). However, the aim here is to produce an unbiased simulation, not an optimally efficient one and we only achieve a constant number of events for distances greater than around 500 m and we therefore choose value this as the default for all future simulations. It can be seen from the lower plots in Figure 3.12 that the energy dependence for the cuts at 500 m and 1000 m is consistent for both atmospheric and E^{-2} neutrinos.

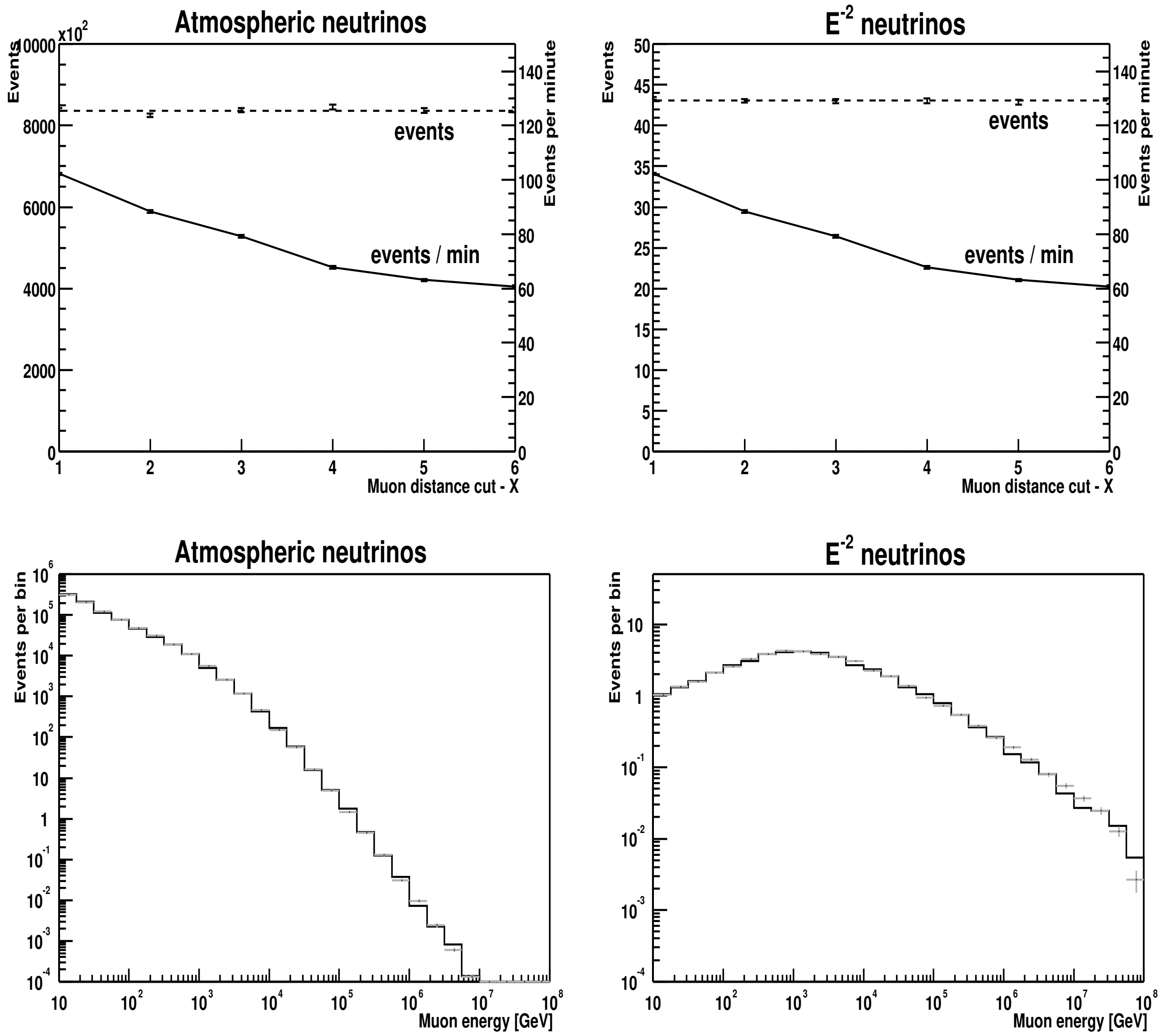

Figure 3.11: Number of muon events at or within the can as a function of the muon range cut ($P_{surv} \leq 10^{-X}$) for atmospheric and E^{-2} neutrinos. The dashed line shows the constant number of events with each muon range cut. The solid line shows the number of events generated per minute, representing the efficiency of the algorithm at each muon range cut. The lower plots show the rate of muons per year for cut levels of 10^{-6} (black) and 10^{-1} (grey) showing the consistency between the two sets of events.

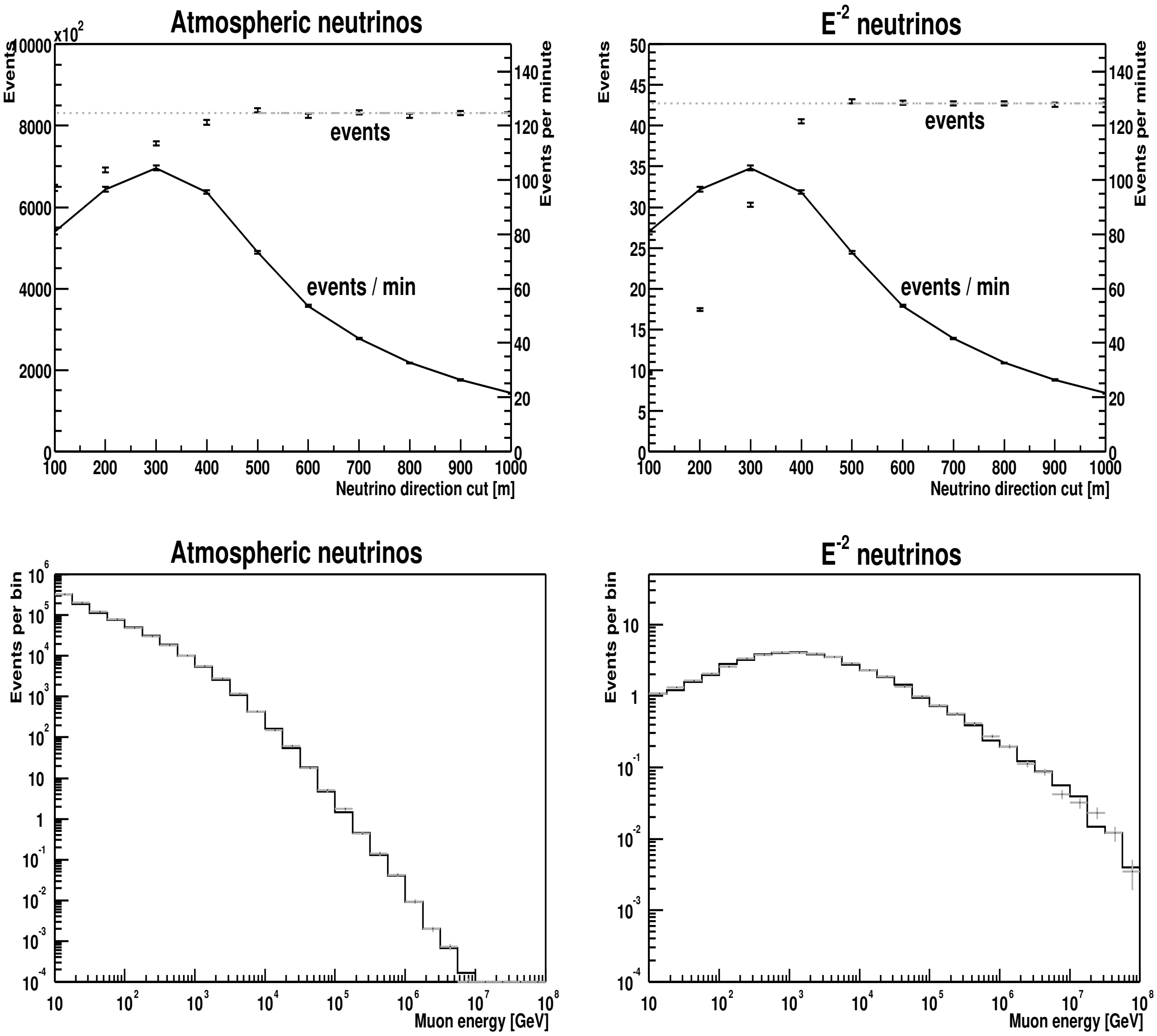

Figure 3.12: Number of muon events at or within the can as a function of the neutrino direction cut for atmospheric and E^{-2} neutrinos. The dotted line shows the asymptotic number of events reached when the neutrino direction cut exceeds 500 m. The lower plots show the rate of muons per year for cuts of 500 m (grey) and 1000 m (black) showing the consistency between the two samples.

In addition to optimising the values used in the selection cuts above, it is also important to quantify the increase in speed with each successive optimisation. In the event generation method described above, we successively apply the following cuts:

None (full simulation) The total generation volume is defined as described above. Each neutrino interaction is then fully simulated and any muons produced outside the can are propagated until they reach the can or are stopped.

10 scaled generation volumes The full energy range is divided into 10 bins and a "scaled" generation volume is defined for each energy range. Only a fraction of the total number of events in each energy bin are generated (according to Eq. (3.9)).

Maximum muon range cut Only neutrinos which interact at a distance less than the maximum muon range at the generated neutrino energy are simulated (as vertices further away cannot produce a neutrino which reaches the can). The optimal cut level in the maximum muon ranges of 10^{-1} is used.

Neutrino direction cut Only neutrinos whose directions pass within 500 m of the can (the optimal value obtained above) are simulated.

The overall time savings cannot be evaluated directly as the time required to perform the full simulation is prohibitive. However, we can estimate the time savings made by removing each successive optimisation in reverse order as follows:

Neutrino direction cut If we set the neutrino direction cut to be essentially infinite (i.e. much larger than the size of the generation volume), we can directly calculate the time savings made by making this selection cut with all the other optimisations in place.

Maximum muon range cut We can then disable the maximum muon range cut on the distance of the neutrino interaction vertex from the can and directly calculate the time savings (albeit with a reduced number of events) made by this cut. Note that we still need to use the maximum muon range to define the total generation volume.

10 scaled generation volumes We cannot perform a full simulation without the scaled generation volumes and the cuts above. Therefore, for each energy bin, as we know the fraction of the total number of events in that energy bin we actually simulated (from Eq. (3.9)) and if we assume that each event takes a constant amount of time to process[7], we can sum over the energy bins and find what fraction of the total number of events we actually simulated and hence estimate the overall time saving.

[7]This is a reasonable assumption as, although full simulations of higher energy events take increasing lengths of time, we only perform full simulations for those neutrinos interacting within the can and this fraction drops with increasing energy. For events outside the can, we only simulate the energy and direction of the produced muon. Therefore the simulation time does not necessarily increase with energy as would naively be expected.

Optimisation cut	Cumulative speed increase	Events per hour
None (full simulation)	1	0.06
10 scaled generation volumes	50	3
Maximum muon range cut	250	15
Neutrino direction cut	100000	6000

Table 3.3: Summary of the cumulative gains in simulation time compare to a full simulation with no scaled generation volume, no cut on the distance of the neutrino interaction from the detector and no cut on the neutrino direction. The number of events at the can (and hence to be processed in the detector simulation) generated per hour of simulation time is also shown.

The estimates of the time saved by each stage are summarised in Table 3.3. Of course, the exact savings for a particular simulation depend on the range and distribution of neutrino energies simulated. Here we have calculated the savings for a "typical" simulation of high energy neutrinos (corresponding to the HE production described in Appendix C and used in Chapter 5 to calculate the ANTARES detector performance).

From the results in Table 3.3, we can see that the overall gain in speed compared to the full simulation is about 10^5 meaning statistically significant numbers of events (even after reweighting as described in Section 3.4.2) can be obtained within a few hours. The largest gain is in the final cut on the neutrino direction with respect to the can as, for all neutrinos interacting more than a few hundred metres away from the detector, the solid angle subtended by the can is small. Once the scaled generation volumes are defined, the increase in speed in applying the maximum muon range cut is only a factor of five as the vast majority of neutrino interactions (in the full generation volume) which would be affected by this cut are never simulated.

Independent of the optimisation cuts described above and the length of the simulation, there is always a fixed time of around 3 minutes (excluded from the above estimates) required at the start of each simulation to initialise LEPTO.

3.4.4 Results and general discussion

There are several features of the distribution of events at or within the can arising from these simulations which can be understood with relatively general arguments about the generation method. This will aid in understanding the relative importance of various systematic effects in the event generator.

Surface and volume events

The distribution of muon energies for events at or within the can generated by the above algorithm is shown in Figure 3.13 weighted according to the default atmospheric neutrino flux model and for the version of the Waxman-Bahcall bound given in Eq. (1.10). The events interacting inside the can (volume events) are shown as a subset of the complete sample.

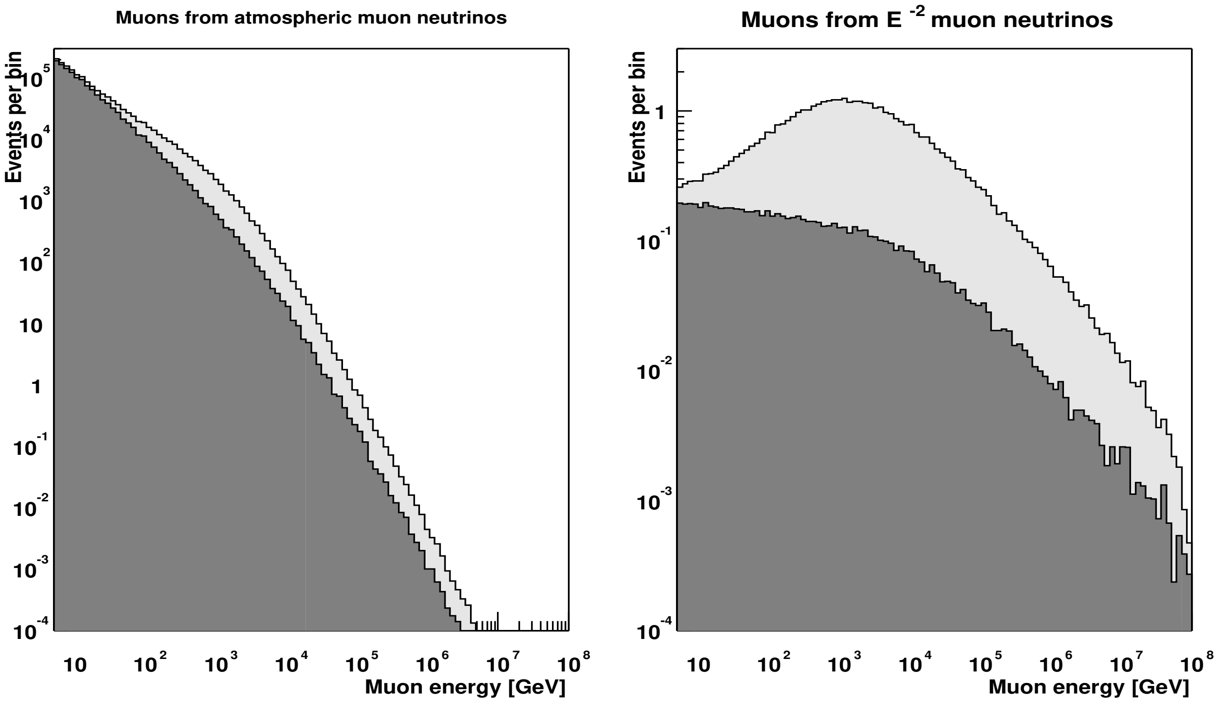

Figure 3.13: Distribution of muon energies at the can for atmospheric and E^{-2} neutrinos and anti-neutrinos. The events interacting within the can (volume events) are shown as a subset of the complete distribution in dark grey.

Two points are immediately clear: for a steeply falling flux like the atmospheric neutrino flux ($\sim E^{-3}$), events within the can (volume events) remain important at all observed muon energies; for a flatter E^{-2} spectrum, the contribution of events starting outside the can (surface events) is more important and peaks at around 1 TeV. The relative importance of the volume events in the steep spectrum can be understood as follows:

- To produce a muon of a given energy at the can, the interacting neutrino must start with a higher energy.
- For events starting outside the can, the muon will also lose energy as it propagates to the surface of the can. Hence, surface events require comparatively higher neutrino energies than volume events.
- For a very steep spectrum, there are fewer of these "even higher energy neutrinos" for a given muon energy compared to the volume events despite the much larger interaction volume. Hence, the volume events produce a more significant contribution.
- For a flatter spectrum, there are enough higher energy events produced in the very large interaction volume outside the can to contribute to and dominate the rate.

The result of this effect is that the volume within which ANTARES is sensitive to neutrino interactions is vastly increased for E^{-2} neutrinos compared to atmospheric neutrinos.

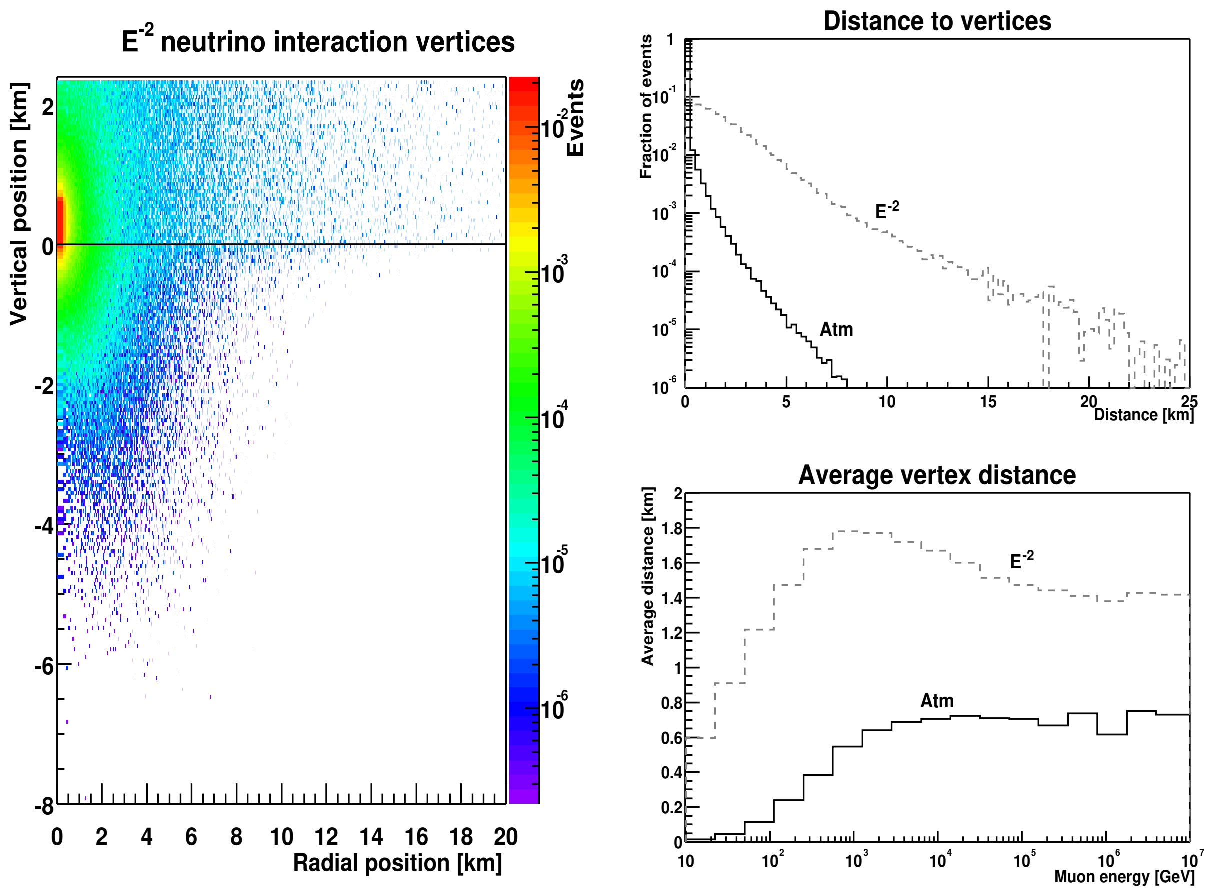

Figure 3.14: Location of the neutrino interaction vertices for events at the can and the distance the muon is propagated to get to the surface of the can for atmospheric (black solid) and E^{-2} (grey dashed) neutrinos.

Vertex position and muon propagation distance

The location of vertices in the generated sample and the distribution of distances from the can for atmospheric and E^{-2} neutrinos is shown in Figure 3.14. The left hand plot shows the relative densities of neutrino interaction vertices which produce at least one particle at the can. We can see events at the can interacting as much as 6 km away in rock and 20 km away in water (although at an extremely small rate).

The right hand plots show the overall distribution of distances from the can and the average distance as a function of energy. Clearly, the muons from E^{-2} neutrinos arrive much further away with the largest average distance around 1 TeV corresponding to the energy where the contribution of surface events is most important. This is significant because we would therefore expect a much larger dependence on the muon propagation code for the E^{-2} neutrinos compared to the atmospheric neutrinos as they will both lose more energy and be more likely to be affected by multiple scattering.

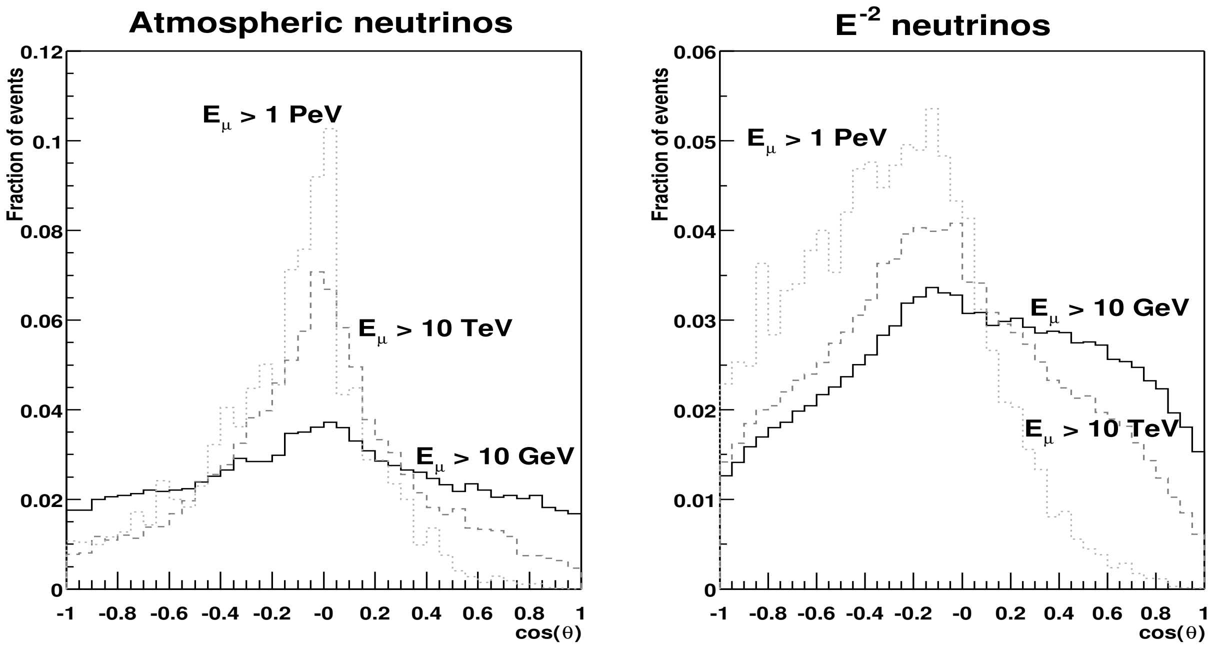

Figure 3.15: Neutrino angular distributions for atmospheric (left) and E^{-2} (right) neutrinos with muon energy thresholds of 10 GeV, 10 TeV and 1 PeV showing the effect of the absorption of neutrinos in the Earth on the observed distribution of muons.

Neutrino zenith angle distributions

The neutrino zenith angle distributions for atmospheric and E^{-2} neutrinos are shown in Figure 3.15 for three muon energy thresholds for muons at or within the can: 10 GeV, 10 TeV and 1 PeV. For the atmospheric flux, neutrinos close to the horizontal become favoured with higher thresholds as there is sufficient target material to produce an observable muon at the detector (which isn't the case for downward neutrinos) but not so much as to absorb all the neutrinos (which is the case for upward neutrinos).

For the E^{-2} neutrinos, the distributions are more strongly affected by the Earth absorption. As muons from an E^{-2} spectrum on average start further away from the can (Figure 3.14), they must be produced with by neutrinos with higher energies than the atmospheric neutrino spectrum and, therefore, have a higher probability of being absorbed in the Earth. As the muon energy threshold increases, the screening effect of the Earth's core becomes even more significant.

Muon multiple scattering in the generated sample

As discussed in Section 3.3.1, the MUM code accurately describes the energy losses of muons in matter (unlike PropMu) but only PropMu includes the muon multiple scattering. If the effect of the latter was small, we could safely use MUM for all future simulations.

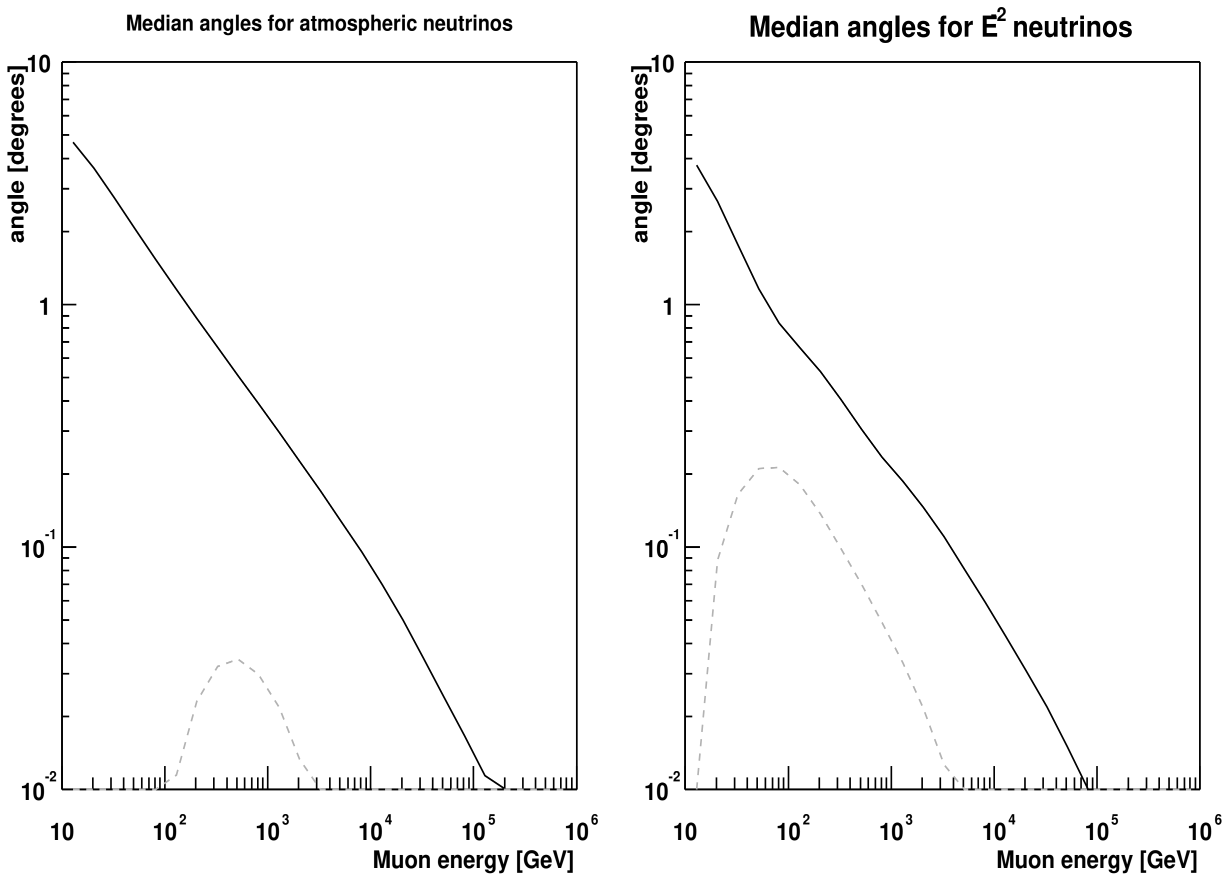

Figure 3.16: Medians of the distributions of muon directions at the can for the atmospheric and an E^{-2} neutrino flux. The solid line shows the median angle between the neutrino and the muon at the can. The dashed line shows the angle between the muon at the interaction vertex and the muon at the can (i.e. it just contains the muon scattering). At low energies, the majority of muons start within the can so the overall effect of multiple scattering is small. Even over many kilometeres, high energy muons only scatter through very small angles.

We define the measure of the correlation between two track directions in a sample of tracks as the median of the distribution of angles between the tracks (see Section 5.1.3). This ensures that we aren't dominated by a few events at large angles but get a measure of the overall distribution. The plots in Figure 3.16 show the median angles between neutrinos and muons at the can (solid) and between muons at the interaction vertex and muons at the can (dashed grey) simulated with PropMu.

The contribution of the muon multiple scattering is much larger for the E^{-2} events (for the same reasons as surface events being more important as discussed in Section 3.4.4) being about 20% of the neutrino-muon median between 30 GeV and 3 TeV. This will be significantly reduced once the angular resolution for the reconstruction of muons is added but the effect isn't necessarily sufficiently small that it can be neglected at this stage. Hence, we will investigate it further in Section 5.2.

3.5 Summary

In this chapter we have addressed several issues related to the generation and subsequent propagation of particles produced by neutrino interactions in and around the ANTARES detector.

- We have described and evaluated two tools (LEPTO and RSQ) which together can simulate the interaction of neutrinos in all relevant channels. We have checked the performance of these codes against published results and found an acceptable agreement (Section 3.2).
- We have evaluated two codes, MUM and PropMu, to simulate muon propagation. For each code, we have calculated and parameterised the maximum muon ranges for energies up to 1 EeV (10^9 GeV) (Section 3.3).
- We have developed a simulation method capable of simulating $\mathcal{O}(10^{10})$ neutrino interactions in a large volume surrounding the detector and propagating the resulting muons to the can. We have defined our default parameters and checked they do not bias the simulations (Section 3.4).

Based on these simulations, we have reached the following conclusions concerning the event generation method described in this chapter:

Neutrino interaction models

Both LEPTO [105] and RSQ [107] are suitable tools for generating neutrino interactions for ANTARES. LEPTO reproduces the results for the neutrino cross-sections and kinematic variables in [103] to better than 5% up to 10^7 GeV and only gets marginally worse by 10^8 GeV. The contribution of RSQ is small so any uncertainties there and in matching up the kinematic cuts at low energies between LEPTO and RSQ are negligible.

The choice of target medium is fixed by the simulation scheme. Choosing the wrong medium for a particular interaction introduces a maximum error of 4% in the cross-section and kinematic variables. For low energy studies, most of the detected neutrino interactions take place in water. At high energies, most of the detected muons originate from neutrino interactions in rock. If we choose the target medium in the simulation to correspond to the energy range where we expect the majority of our events (given the energy range and spectrum of the generation), we can further reduce this error.

The choice of Parton Distribution Function describing the distributions of momenta within the nucleon can have a large effect on the cross-sections at high energy. Below 1 PeV, interaction cross-sections from all tested modern PDFs agree to within 5%. Above this they diverge and may become an important uncertainty. This will be investigated further in Section 5.2.

Concentrating on the range of neutrino energies between 10 GeV and 1 PeV where the majority of neutrino interactions observed by ANTARES are expected, we can summarise the systematic errors on the simulated rate of events as follows:

Numerical inaccuracies in LEPTO (compared to [103])	$\leq 5\%$
Choice of target medium	$\leq 4\%$ (in the worst case)
Choice of Parton Distribution Function	$\leq 5\%$
Total (added in quadrature)	$\leq \mathbf{8}\%$

This overall error of 8% from the event generation stage should be compared to roughly a 20% uncertainty in the normalisation of the atmospheric neutrino flux. Additionally, as we will see in Section 5.3, the uncertainty arising from our relatively limited knowledge of the detector medium is significantly larger. Therefore, this overall uncertainty is acceptable at this stage.

Muon propagation codes

Ideally, we would like a fast code which accurately calculates muon energy losses and includes muon multiple scattering (a "3D code"). Unfortunately, no such code is currently available. Hence, we use both MUM [114] and PropMu [109] in future simulations. A "3D" version of MUM is currently under development [116] which will eventually be an ideal tool for these simulations.

Event generation method

The event generation method employs several efficient selections to make the full simulation of a very large number of events possible. These selections have been checked so they are as efficient as possible whilst still producing unbiased distributions of events. For the first time in ANTARES, this method allows for the generation of neutrino interactions both inside and outside the can over a wide range of energies from the same underlying generation code (and hence with the same systematic errors and uncertainties). By use of the event weights, it can be used to describe a range of different neutrino fluxes.

The results of this section and in particular those produced by the generation method described above will form the starting point for all the simulation and analyses described in the following sections.

Chapter 4

Detector Monte Carlo simulation and medium parameters

> In this chapter we describe in detail the previously existing ANTARES detector Monte Carlo code, KM3, which performs a simulation of the detector response to muons and electromagnetic showers including photon scattering in the water. We then extend this Monte Carlo to add the Cherenkov light produced by hadronic showers at the neutrino interaction vertex and find this to be an important contribution to the total light production for neutrino energies up to 10 TeV. We also justify our choice of can size in Chapter 3 at 200 m on the basis of light produced both by through-going muons and neutrino interactions in the can. We then define two scattering models and select a range of parameters in each to be simulated with this Monte Carlo in preparation for an investigation of the effect of scattering on the detector performance in Section 5.3. Finally, we develop a new simulation based on the above models to evaluate the effect of using the wavelength dependent group refractive index on the photon arrival times and find an effect larger than that from the PMT transit time spread and the electronics. We quantify this effect and add it as a correction to KM3.

In the previous chapter, we described a method of producing distributions of particles created by neutrino interactions both within and on the surface of the can surrounding the instrumented volume of the detector. The next stage is to simulate the production of Cherenkov photons by these particles and the detection of these photons by the PMTs.

A full Monte Carlo simulation where all particles (including the Cherenkov photons) are fully tracked as they pass through the detector is not computationally feasible given the large numbers of events which need to be simulated (mainly to understand the atmospheric muon background), the large distances involved (hundreds of metres across the ANTARES detector) and the large numbers of particles produced by individual muons (in high energy electromagnetic showers and in the $\sim 10^5$ Cherenkov photons per metre of charged particle track). Therefore, a different technique is needed. Historically, ANTARES has had two separate Monte Carlo codes adopting different approaches which can each only simulate some aspects of the events:

KM3 [128] Large "photon tables" are generated which parameterise the amount and arrival times of Cherenkov light detected by individual PMTs at different positions and orientations with respect to short muon track segments and electromagnetic showers.

These tables are used to simulate individual muons with Bremsstrahlung showers and to include the effect of photon scattering in the water. The contribution of Cherenkov light from charged hadrons is neglected.

Geasim [129] Performs a full tracking simulation of all particles except Cherenkov photons as they pass through the detector. It uses an analytical function to calculate the number of photons detected which assumes that there is no photon scattering and all light arrives directly in the Cherenkov cone.

For most of this chapter we concentrate on KM3 as photon scattering has an important effect on the final detector performance (see Section 5.3). We give a brief overview of how this calculation is performed and what external packages are used and describe an extension of this to include the hadronic shower contribution (using routines from Geasim). We also describe several different scattering models in Section 4.2 in preparation for an investigation of the effect of scattering on the ANTARES detector performance in Section 5.3.

Previously, both KM3 and Geasim incorrectly used the phase velocity at a fixed wavelength to calculate the propagation times of Cherenkov light from the track to the PMTs. In reality, the group velocity should be used and the wavelength dependence should be taken into account. Using a new simulation developed for this purpose, we quantify this effect and add it as a correction to the existing Monte Carlo code. This is discussed in Section 4.3.

The results presented in Chapter 5 use the results of these simulations to evaluate the systematic effects described in Chapter 3 and those due to the photon propagation medium and then to calculate the overall detector performance. In Chapter 6, the results are used to make the first estimation of the sensitivity of ANTARES to the detection of Dark Matter via its annihilations into neutrinos.

4.1 Detector Monte Carlo simulation

The requirements for a complete ANTARES detector Monte Carlo simulation mirror those for the event generator discussed in Section 3.1.2 as it must be able to handle the same set of events.

- It must track muons with energies up to tens of PeV and generate the Cherenkov light they produce.
- It must include electromagnetic showers from processes such as Bremsstrahlung in the muon energy loss as localised events along the track. These processes dominate the muon energy losses above a few TeV.
- The effect of the sea water on light propagation must be correctly modeled. This is important for two reasons:
  - For reconstructing the direction of upward going muon tracks from neutrino interactions, a good timing resolution is needed. Any scattering will smear the arrival times and degrade the angular resolution.

  - For the background of downward going muons from cosmic ray interactions, a large fraction of the Cherenkov light will fall on the back of the OMs, missing the photocathode. However, the photons which do scatter in the water back towards an OM will be detected and are hence comparatively more important in understanding (and rejecting) the background.

- For neutrinos which interacted inside the can, the light produced by the hadronic shower at the vertex must be included.

- The response of the ANTARES PMTs as a function of wavelength and incident angle must be included.

- The simulation must be fast enough to simulate a very large number of through-going muons from the cosmic ray background which are expected at a rate of $\sim 10^5$ per second.

As stated previously, the approach taken in KM3 is to build large tables which contain distributions of numbers of PMT hits and arrival times for generic types of events (e.g. one metre segments of muon tracks). The hit amplitudes and times for individual track segments for a particular event are then randomly sampled from these distributions so that each event is unique. This technique was originally implemented as described in [130] and forms the vast majority of the current ANTARES Monte Carlo, KM3 [128]. Aside from various technical developments, the modifications made to this package are the addition of the hadronic shower simulation (Section 4.1.5) and the inclusion of a wavelength dependent group velocity (Section 4.3).

4.1.1 General simulation scheme

There are three types of particles which need to be simulated:

Muons are characterised by long, approximately straight tracks continuously losing energy and emitting Cherenkov light. They also suffer stochastic losses which produce independent electromagnetic showers.

Electromagnetic (EM) showers are either produced by Bremsstrahlung photons from muons or by electrons at the neutrino interaction vertex. All their energy is deposited in a short distance (on the scale of the ANTARES detector) and can generally be considered point-like. They contain a large number of electrons and hence, statistically, showers of a similar energy all have similar properties.

Hadrons have complex decay chains and the amount of light they produce depends on the primary particle and its particular set of decays. In addition, they may produce muons in the final state which may travel a significant distance. Hence, they are not amenable to parameterisation in the same way electrons and muons are. They will be dealt with separately in Section 4.1.5.

For the muons and EM showers, the simulation then proceeds by the following general stages (the details of which will be discussed in the following sections):

1. A detailed simulation of a particular type of particle used to build tables of the hit amplitudes and arrival times for different distances and orientations of the PMTs. This is only performed once for each particle type and scattering model and consists of two stages:
   (a) A full simulation (including generating and tracking all secondary particles down to the Cherenkov threshold) is performed for either a section of the muon track or a full EM shower of a given energy. Photons are tracked according to a particular scattering model in the water and the positions, times, directions and wavelengths of photons crossing a number of spherical shells surrounding the parent particle are recorded.
   (b) For a set of zenith angle bins on each shell, each photon is weighted according to the probability of being detected for each of a set of different OM orientations with respect to the parent track or shower. This gives the number of hits in each bin and a weighted distribution of hit times from which an inverse cumulative distribution is built. These are the final photon tables.
2. For each generated event, muons are simulated in steps corresponding to the track segments in the photon tables and a list of EM showers (energy, position, direction and time) is built. For each of these steps / showers and for every OM in the detector, the number of detected photons and their arrival times is drawn from the photon tables to give the hits recorded for that individual event. These hits are then processed by a simulation of the detector electronics to give the final output of the simulation.

This is very much a generalised view of the simulation. There are several subtleties concerned with optimising the simulation which will be mentioned briefly below. A schematic overview of the whole process is shown in Figure 4.1.

4.1.2 Photon table generation

The photon tables must be generated on the basis of a detailed simulation of a particular type of particle. This is done using GEANT 3.21 [131] to track individual particles and develop showers up to the point of Cherenkov photon generation. The generated tables correspond to the following two classes of simulation:

- One metre lengths of muon tracks with energy losses below 0.3 GeV. This includes all secondary processes (knock on electrons for example) below this value. The muons are tracked in one centimetre steps and muon scattering is included.
- Electromagnetic showers (initiated by electrons) at energies of 100 MeV, 1 GeV, 10 GeV and 100 GeV. The tables from these simulations will be interpolated for individual showers in the final simulation.

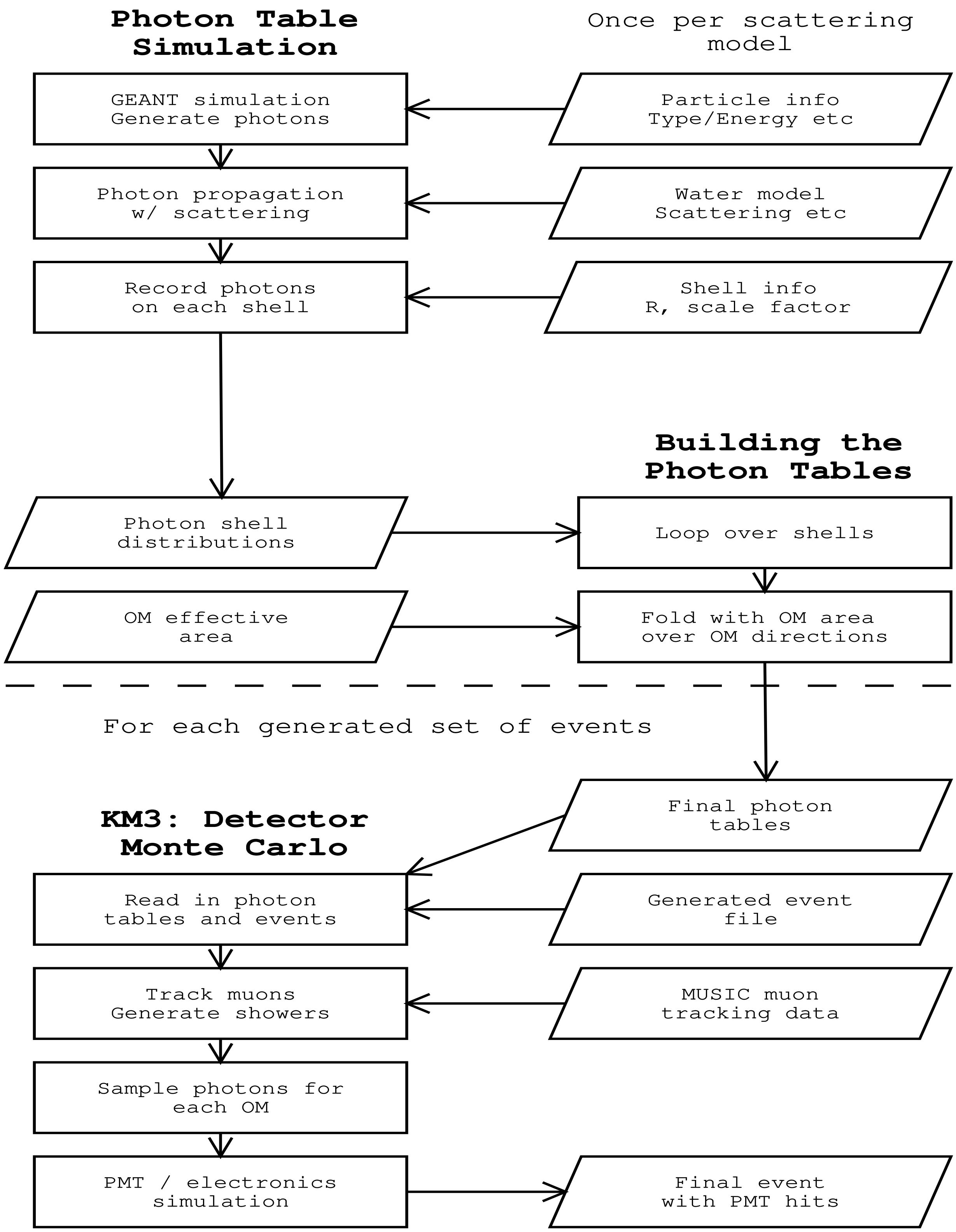

Figure 4.1: Schematic overview of the whole detector Monte Carlo simulation. The upper half is performed once for each photon scattering model. The lower half (the main detector Monte Carlo) is then performed for each set of input events using the photon tables.

All the photons produced by this simulation are then tracked individually. We define a number of spherical shells, typically 20, surrounding the origin of the simulation (i.e. the centre of the muon's track or the maximum of the shower). The shell radii run in steps of increasing size ranging from 2 m to 200 m. If we recorded all the photons crossing each shell, storing a statistically significant number of photons for the outer shell would require storing millions of photons for the innermost and therefore produce huge tables. For each shell, we therefore only record some fraction of the photons which actually cross it. This fraction is chosen to give $\sim$ 10000 photons on each shell and hence reasonable statistics at each distance.

Photon tracking algorithm

In the photon tracking, the refractive index of the medium is assumed to be fixed (i.e. neglecting the wavelength dependence). The phase velocity (instead of the group velocity) is used for calculating photon propagation times. Correcting for this error will be discussed in Section 4.3[1]. The individual photons are now tracked as they cross these shells according to the following method:

1. A wavelength is chosen from a Cherenkov ($\frac{1}{\lambda^2}$) spectrum between 300 nm and 600 nm.
2. A single absorption length is drawn from an $e^{-\frac{d}{\lambda}}$ distribution for each photon at the chosen wavelength λ.
3. A scattering length is drawn (at λ) and compared to the absorption length:
   - If the scattering length is longer, the photon is propagated to its point of absorption and stopped. The positions, directions, times and wavelengths of each shell crossing are recorded and labelled as "direct" photons.
   - Otherwise, the photon is propagated to the scattering point and a scattering angle is drawn from an appropriate angular distribution. The photon's direction is changed by this angle. The positions, directions, times and wavelengths of any shell crossings on the photon path segment before the first scattering are recorded and labelled as "direct" photons. Another scattering length is drawn and the process is repeated with all subsequent shell crossings recorded and labelled as "scattered" photons. This continues until the total path length exceeds the initially drawn absorption length.
4. The set of photon positions, directions, times and wavelengths on each shell is stored with direct and scattered photons being recorded separately.

The distinction between direct and scattered photons is important as it allows good statistics to be collected for both direct and scattered photons independently and for the bins

[1] At the time KM3 was written, it was generally assumed that the phase velocity should be used for Cherenkov photon propagation and this assumption (which isn't easily extractable from the KM3 code) persists. The wavelength dependence was neglected as it allows the simulation of non-scattered Cherenkov photons to be optimised. This point is discussed further in Section 4.3.4.

in which the photon tables are built to be optimised. Gaining good statistics in the photon tables is important as they are to be sampled from many times in simulating individual muons and this will therefore avoid biasing the statistical errors of simulation results with a particular set of photon tables.

Building the photon tables

We then have a large number of photons recorded for each spherical shell for each type of event. We bin the data in the zenith angle θ with respect to the muon track direction or the shower axis. For direct hits, there is only one bin (all the photons arrive at the same point[2]). For scattered hits, there are 20 bins in $\cos(\theta)$, 6 below (closer to the track axis) the Cherenkov angle and 14 above. For the direct photon muon tables, we subtract the photon propagation time corresponding to direct Cherenkov light from the recorded arrival times. For the other tables (scattered photons from muons and the electromagnetic shower tables) we subtract the direct photon propagation time to the centre of that bin in $\cos\theta$. This allows the time distributions to be built around $t = 0$ with a known offset depending only on the distance which is added for individual track segments or showers in the final Monte Carlo.

OM effective area

Now, for each bin in $\cos\theta$ on each shell, we weight the flux of photons by the OM effective area as a function of wavelength and angle (taken from [132] and tabulated for normal incidence in Appendix B in Table B.10). The measured effective area of the OM for an angle of incidence θ with respect to the PMT axis is a combination of the absorption in the OM glass sphere, absorption in the optical gel, the quantum efficiency (QE) and the collection efficiency (CE) of the PMT (see Figure 2.4, page 45 in Section 2.3 and [92]):

$$A_{eff}^{PM}(\lambda,\theta) = A_{geom}^{Photocathode}(\theta) \times QE(\lambda) \times CE \times P_{transmission}^{glass}(\lambda,\theta) \times P_{transmission}^{gel}(\lambda,\theta) \quad (4.1)$$

This is done for a number of different OM orientations (θ_{OM}, ϕ_{OM}) with respect to the normal direction of each bin in $\cos\theta$ on each shell. A schematic view of the simulation geometry is given in Figure 4.2. Note that the angle ϕ_{OM} is required as, for bins away from the Cherenkov angle, different amounts of light will be seen depending on whether the OM is pointing towards the Cherenkov cone or not. We then have the number of detected photons and the distribution of their arrival times (with the known offset) for each shell radius, in each zenith angle bin for each OM orientation (θ_{OM}, ϕ_{OM}) with respect to the shell normal. These distributions are stored for the next stage of the simulation.

[2]Unfortunately, this is the same optimisation that makes adding the effect of a wavelength dependent refractive index to this simulation non-trivial as this gives a range of Cherenkov angles dependent on the wavelength. For this reason, this correction is added as an extra time spread to the final hits.

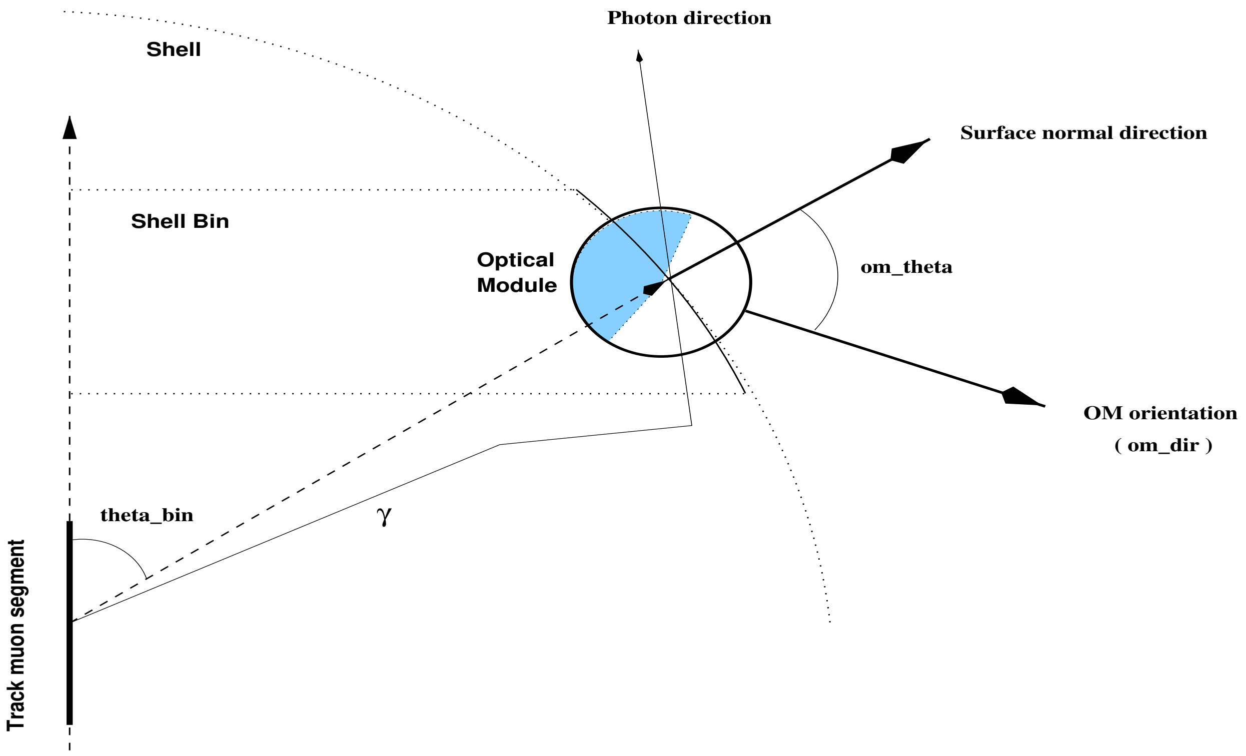

Figure 4.2: A schematic diagram of the geometry used to generate the photon tables. The OM direction (θ_{OM}, ϕ_{OM}) is defined with respect to the normal shell normal in each bin in $\cos\theta$.

4.1.3 Muon tracking and shower simulation

The events input to KM3 are in the form of a list of muon tracks with a given starting position, direction, energy and time. For each muon, its energy losses are calculated in 1 m steps using MUSIC [118]. For steps with energy loss above 0.3 GeV (the cut-off for storing photons for the "muon" tables above), the excess is taken to represent a Bremsstrahlung initiated electromagnetic shower at a random point along the track section with a starting energy corresponding to the extra energy loss above 0.3 GeV. An electron with the appropriate time and energy is added to the list of particles in the event. When the muon is stopped or leaves the can, tracking stops. This produces a list of muon track segments and electrons of various energies.

Sampling from the muon tables

For the muons the propagation time for direct Cherenkov photons is calculated (using the group velocity at a wavelength of 460 nm which corresponds to the maximum sensitivity of the ANTARES OMs) for each OM in the detector. Then the number of photons and arrival time spread (with respect to the direct time) is sampled from the photon tables, interpolating in the photon propagation distance for both the scattered and direct photons and in the relative photon-OM direction.

Sampling from electromagnetic shower tables

For electrons, the situation is a little more complicated as there is a wide range of shower energies (as opposed to a very narrow range for minimum ionising muons). The shower is not centred at its starting point but some distance along the shower axis dependent on the energy. In the generation of the photon tables and in sampling the hit amplitudes and times, the origin for the photon tables is set at a distance d_{max} (corresponding to the shower maximum for a starting energy E_e) from the starting point of the electron:

$$d_{max} = 0.9 \times \left(\frac{1 + \log_{10}(E_e \text{ [GeV]})}{\rho_{water} \text{ [g cm}^{-3}\text{]}} \right) \tag{4.2}$$

The form of this function and the constants are empirical fits to GEANT simulations [128]. Provided the energy dependence is correct, the exact numerical values are not critical as both the photon tables and the shower origin in the simulation are offset by the same amount. This process ensures that the shower is at the centre of the shells in the photon table generation and that the shower maximum is located correctly in the final Monte Carlo. The average number of photons seen on any OM is assumed to be proportional to the shower energy and is scaled accordingly by interpolating or extrapolating from the photon tables.

It is worth noting that the electromagnetic shower tables store the number and time distributions of photons averaged over many showers. Therefore, fluctuations in individual showers are lost in the resampling from the photon tables. However, as the number of photons detected from an individual shower is small (due to the low density of PMTs), fluctuations in the shower shape are unlikely to affect the reconstruction of muon tracks.

PMT Transit Time Spread

The efficiency of the OM is taken into account in building the photon tables above. However the Transit Time Spread (TTS) is not included (in part to allow it to be changed without rebuilding the photon tables). It is added at this stage by smearing each hit time by the TTS of the PMT. This has been assumed to be gaussian with a width (σ) of 1.3 ns (based on early measurements of ANTARES PMTs shown in [1]) and that value is used consistently throughout the simulations described here.

Optical background noise

There are many potential sources of background noise in the ANTARES PMTs when they are operated in the deep ocean. These include after-pulsing in the PMTs, electronics noise both in the raw PMT signal itself and in the digitisation electronics and high voltage breakdown. However, these are all dominated by a background of random PMT hits from potassium-40 decays and bioluminescent organisms as described in Section 2.3.3. In these simulations, a constant rate of 60 kHz per PMT of randomly occurring hits is assumed corresponding to the highest baseline of the measurements taken at the ANTARES site [133].

The potassium-40 hits recorded in each event must extend far enough (in time) outside the region of the hits caused by the muons and showers to affect the reconstruction in the same way as an infinite window of potassium-40. A buffer of 500 ns around the hits produced by the tracked particles is chosen for this purpose.

Digitisation scheme

The ANTARES front end electronics (ARS) was discussed in Section 2.3.2. There are currently two choices for modeling this electronics in the ANTARES software:

No waveform A simple simulation where no waveforms are generated. Each ARS integrates all hit amplitudes for 25 ns after the first hit on a tube is received. It is then dead for 250 ns. The two ARS chips operate independently with control passed to the second chip when the first is busy.

Full simulation A full simulation of pulse shapes from PMTs with all the discriminator thresholds and waveform generation included. Individual pulses are separated by fitting separate pulse shapes to waveforms.

For the former, this implies that two hits closer than 25 ns cannot be separated. With the fitting in the later, this is reduced to 10 ns [94] and the timing error associated with the fitting is less than 0.7 ns. The difference between the two methods after reconstruction and selection (see Section 5.1) was found to be negligible [94] for high energy muons[3].

In all the simulations and analysis which follows, we apply the "no waveform" simulation, neglecting any timing error and taking the worse double hit resolution of 25 ns.

4.1.4 Muon simulation results

Using the ANTARES detector geometry described in Section 2.3, we calculate the distribution of detected photons as a function of the distance of closest approach of the muon to each hit OM. This is shown in Figure 4.3 for muon energies of 1 TeV, 10 TeV, 100 TeV and 1 PeV. There is a continuous background rate of 60 kHz on each PMT from potassium-40 decays. The contribution from the minimum ionising muon and the electromagnetic showers is shown separately.

The number of generated muons and fraction of hits from muons and electromagnetic showers are shown in Table 4.1. We can see from Figure 4.3 and Table 4.1 that, at 1 TeV, there are more Cherenkov photons from the muon than from the electromagnetic showers. Above this, the shower contribution begins to dominate. The numbers of Cherenkov photons from the bare muon stays almost constant at all energies (as it should as any energy loss above a certain threshold is put into showers). The number of photons from showers scales

[3]The main interest in the waveforms is partly diagnostic and in case of unusual signals. It is also intended to be used to aid the reconstruction of hadronic showers both with and without muons which is not considered in this thesis.

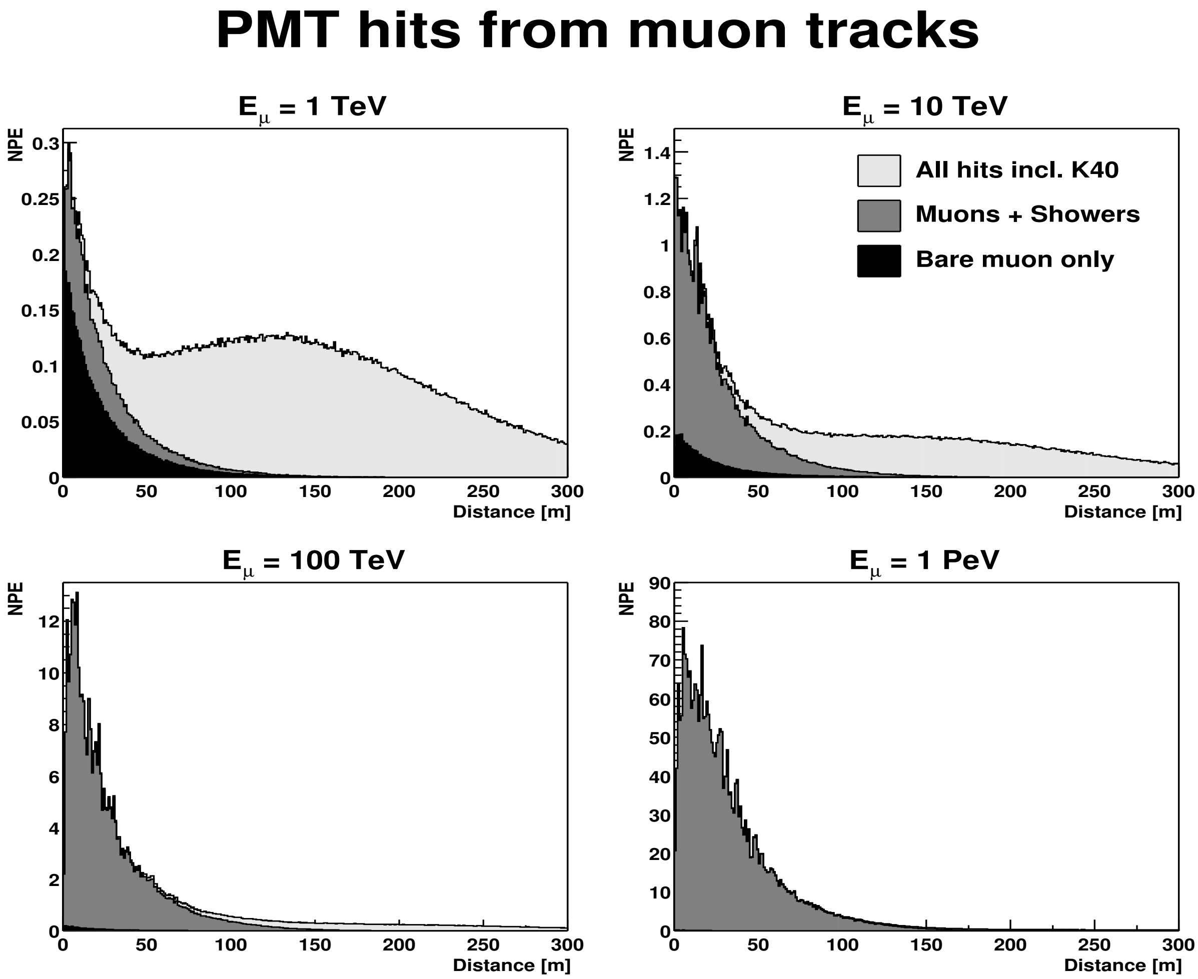

Figure 4.3: Number of detected Cherenkov photons per OM as a function of the **distance of closest approach** of the muon track to the hit OM. The total number of detected photons (including potassium-40) is shown in light grey. The hits from muons and EM showers are shown in medium grey and those from just the "bare muon" are in dark grey. The vertical scale is number of photoelectrons per event per 1m distance. The rate of potassium-40 hits per event increases with energy as higher energy events last for a longer time.

Muon Energy	Events Generated	Detected photons per event (% of total)		
		Muons+Showers	Bare Muons	EM Showers
1 TeV	40000	7.39 (22.4)	4.29 (13.0)	3.1 (9.4)
10 TeV	20000	35.7 (49.1)	4.48 (6.2)	31.2 (43.0)
100 TeV	10000	350 (85.3)	4.49 (1.1)	345.6 (84.2)
1 PeV	5000	2831 (97.0)	4.29 (0.2)	2827 (96.8)

Table 4.1: Numbers of detected photons for through-going muons. The total amount of light from the muons is shown as "Muons + EM showers" and then divided into bare muons and electromagnetic showers. The percentages of the totals are shown in brackets with the missing fraction being due to potassium-40.

roughly with energy as expected which indicates only having four electron photon tables is sufficient. In all cases (between 1 TeV and 1 PeV), the distributions excluding potassium-40 are of a similar shape, peaking close to the track and falling off quickly. Approximately 80% of the hits are within 50 m of the track and 95% are within 100 m. Our choice of a 200 m can is therefore reasonable[4].

4.1.5 Hadronic shower simulation and results

As noted above, the hadronic component of the neutrino interaction products will also produce charged particles giving off Cherenkov light. However, the fluctuations in the shower development are such that it is not possible to trivially build photon tables for hadronic showers in the same manner as for electromagnetic showers. The photon tables themselves represent an "average shower" (or, more correctly, an average of a large number of possible showers) and hence these fluctuations would be lost.

We stated in Section 4.1 that photon scattering is important for simulating muons with long tracks both in terms of the accuracy with which their direction can be reconstructed and for understanding the atmospheric muon background. In contrast, on the scale of ANTARES, showers are essentially point like and, certainly for charged current muon neutrino interactions, there is little interest in reconstructing the shower direction[5]. In addition, the particles themselves are not necessarily strongly aligned with the neutrino and muon direction and hence directional information about the source on an event by event basis is lost in the statistical fluctuations.

For these reasons, we neglect scattering in the simulation of the Cherenkov light produced by the hadronic shower and use the alternative GEANT based ANTARES Monte Carlo, Geasim [129, 131] which performs a full hadronic shower simulation but has no mechanism to include scattering. Hence, whilst it is not suitable for simulating high energy muons, it is well suited for just hadronic showers. The approach is to apply this Monte Carlo to just the shower particles at the neutrino vertex (ignoring muons) and add the extra PMT hits from this component to the output of KM3.

The number of PMT hits produced as a function of the distance from the interaction vertex for a range of neutrino energies for events within the can is shown in Figure 4.4 (recall that, for interactions outside the can, the hadronic shower is not simulated). For these events, the hadronic shower component is always significant and becomes more so at higher energies. However, the fraction of events which interact within the can (based on the generation method described in Section 3.4) decreases with energy and therefore becomes less significant in the overall sample. The percentage of events interacting in the can and the percentage of the non-background light produced by the hadronic shower for that fraction of events is shown in Table 4.2.

[4] At very high energies or looking for very high energy showers, a larger can may be necessary to include all the Cherenkov light which could affect the reconstruction.

[5] Looking at fully reconstructing electromagnetic showers or neutral current interactions is another case entirely and more thought would have to be put into the needs for a hadronic shower simulation

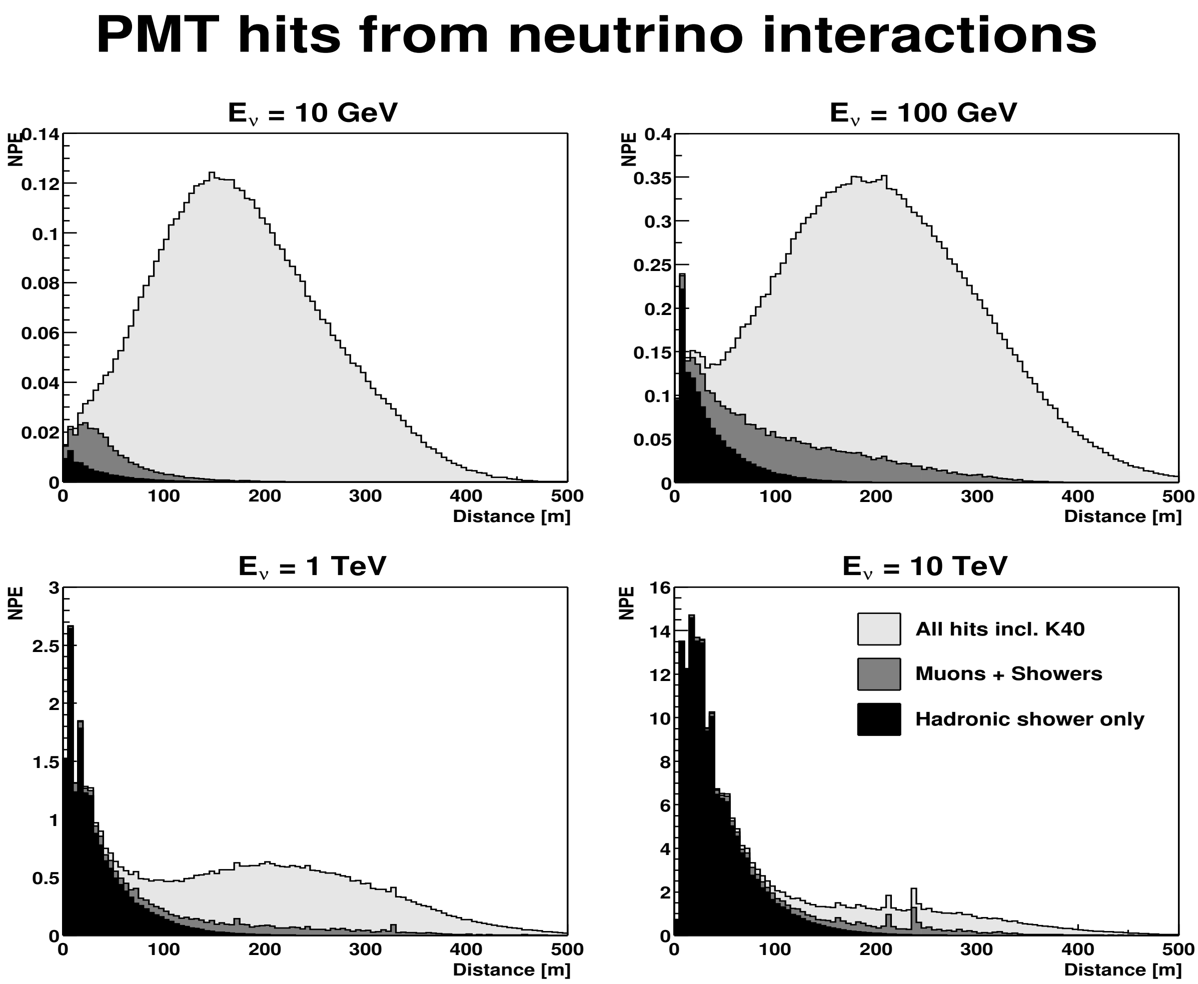

Figure 4.4: Origin of Cherenkov light generated in KM3 and Geasim as a function of the **distance of the OM from the neutrino interaction vertex** for events in the can. The total number of detected photons per OM (including potassium-40) is shown in light grey, those produced by all particles in medium grey and those produced by just the hadronic shower component of the interaction vertex in dark grey.

Neutrino energy	Percentage of generated events in the can	Percentage of non-background light from showers for events in the can
10 GeV	94.4 %	28.0 %
100 GeV	65.3 %	42.0 %
1 TeV	21.7 %	79.3%
10 TeV	8.7 %	88.7 %

Table 4.2: Hadronic shower contribution to Cherenkov light production. The second column shows the percentage of events in the generated sample which interact in the can (and hence have their hadronic showers simulated). The third column shows the percentage of non-background photons which originate from the hadronic shower.

Even at low energies (10 GeV), the contribution of the hadronic shower to the total light output is around 30%. It is likely the inclusion of vertex showers will aid the identification of events (and hence improve the overall event rate), especially at low energies where relatively few photons are detected. The effect on the angular resolution is less clear as the light is localised at one point on the track.

At high energies (above 10 TeV), only a small fraction of events interact close enough to the detector (i.e. within the can) for the hadronic shower to be visible. These events are in any case more likely to be reconstructed even if the shower light is neglected so the effect of the shower should be much less significant. The final effect on the detected events will be discussed in Section 5.2.1 where a maximum neutrino energy for which the time consuming hadronic shower simulation is important will be determined.

Finally, we can see from Figure 4.4 that the vast majority of light from hadronic showers is seen within 100 m of the neutrino interaction vertex at all energies (the light from muons and electromagnetic showers is seen from further away as the muons will propagate large distances through the detector). This justifies our choice of 200 m for the can size for simulating the hadronic shower in neutrino interactions.

4.2 Scattering models and photon absorption

The simulation method described above allows for the simulation of different scattering models. The current choice of scattering models for ANTARES is based on theoretical expectations and early measurements at the ANTARES site. This section briefly discusses the underlying models and the choices of parameters for the scattering models simulated. These models will be used in Section 5.3 to investigate the effect of these different scattering models on the ANTARES muon reconstruction.

4.2.1 Theoretical and empirical models

A great deal of work has been done and is still in progress within the ANTARES Collaboration on modeling and measuring the optical properties of water in ANTARES (see [97, 98, 134, 135]). In these analyses, scattering has historically been divided into two components with separate scattering lengths and angular distributions which are then combined to give overall models; the implementation in KM3 follows this assumption.

Scattering angular distributions

The first of the two types of scattering is Rayleigh (R) scattering in pure sea water [136] with the angular distribution:

$$\frac{dN_R}{d\Omega} = 0.06225 \times (1 + 0.835 \cos^2 \theta) \tag{4.3}$$

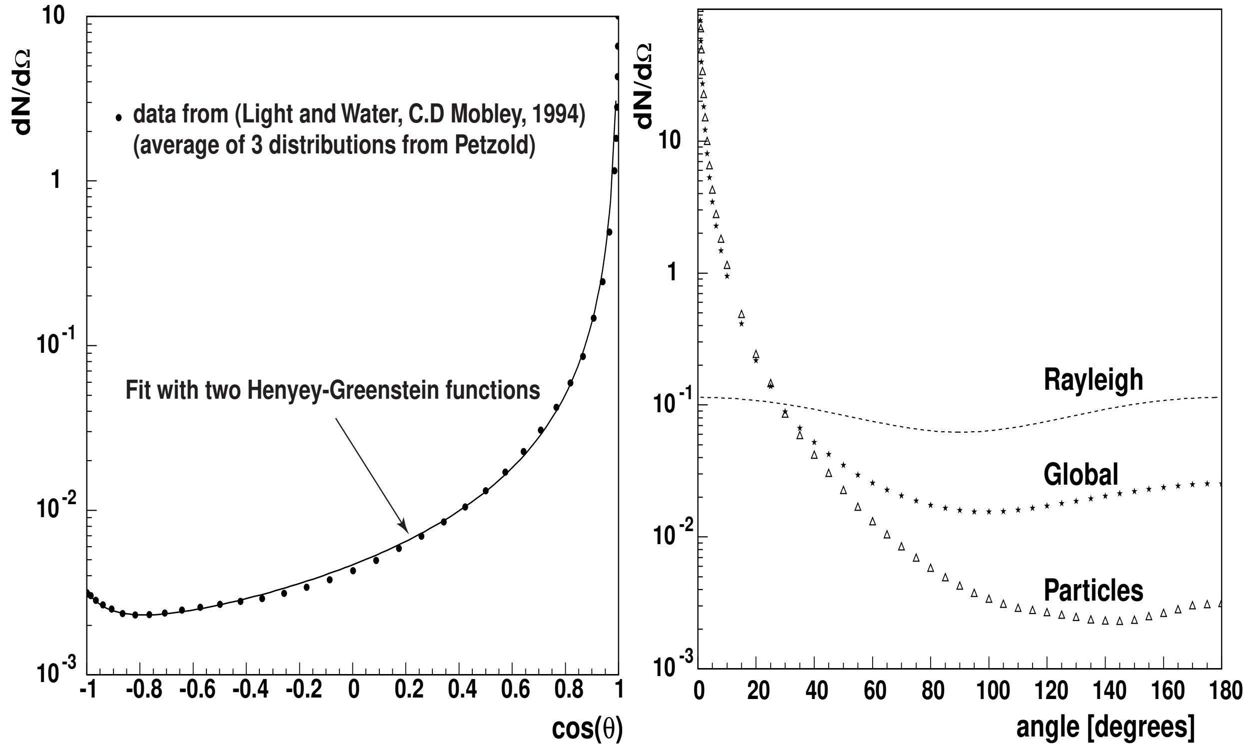

Figure 4.5: Angular distribution of scattered photons based on the data in [137] (left) and in combination with Rayleigh scattering (right) assuming a 20% particle contribution (taken from [134]).

where the factor 0.835 (as opposed to the more usual 1) in the above expression arises because of the anisotropy of the water molecule. The second component is the so-called "particle" scattering from small sedimentary particles and microscopic organisms. Two possible models are considered:

- The first is based on measurements by Petzold [137] of the angular distribution of scattered light in water with a high particle load at a wavelength of 514 nm as shown in Figure 4.5 (and tabulated in Table B.9 in Appendix B). The data itself is the average of 3 similar measurements with very different particle densities and is taken to be "typical" of particles scattering in water. The particle scattering is strongly forward-peaked with an average $\cos\theta$ of 0.924. It should be noted that there is no direct evidence that this is a valid model for the ANTARES site and care must be taken in interpreting results derived using it.

- The second model is based on the Henyey-Greenstein function:

$$\frac{dN_{HG}}{d\Omega} = \frac{1}{4\pi}\frac{1-g^2}{(1+g^2-2g\cos\theta)^{\frac{3}{2}}} \tag{4.4}$$

  where g gives the average $\cos\theta$ of the function. This is an approximate description of "Mie" scattering (scattering from particles with a size greater than $\sim \frac{\lambda}{20}$ [136]). This description is more flexible as it allows for a range of different values of $\langle\cos\theta\rangle$

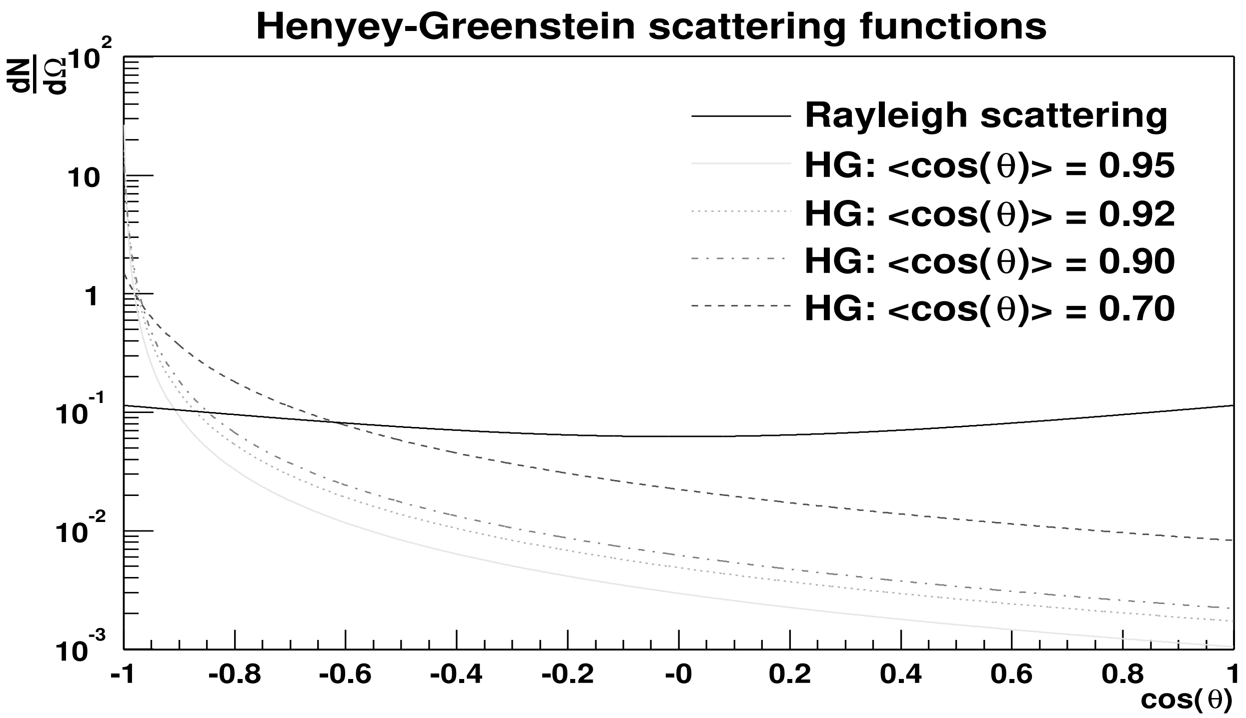

Figure 4.6: Angular scattering functions for particles using the Henyey-Greenstein function with average $\cos\theta$ of 0.95, 0.92 (close to the Petzold data), 0.9 and 0.7.

to be tested. It also has the advantage that it can be inverted analytically for Monte Carlo sampling. The form of the Henyey-Greenstein function is shown in Figure 4.6 for a range of $\langle\cos\theta\rangle$. For specific choices of $\langle\cos\theta\rangle$, a linear combination of two Henyey-Greenstein functions can be fitted to the Petzold data as shown in Figure 4.5. However, in general, we vary $\langle\cos\theta\rangle$ in this model to study the effect of different scattering angular distributions.

Scattering lengths

The overall scattering length, λ_{scat}, which is used in the photon propagation algorithm described in Section 4.1.2 is given by a combination of the Rayleigh and particle scattering:

$$\frac{1}{\lambda_{scat}} = \frac{1}{\lambda_{Rayleigh}} + \frac{1}{\lambda_{particle}} \tag{4.5}$$

The scattering lengths used as inputs for the simulations are usually specified at a single wavelength (e.g. corresponding to specific measurements). The wavelength dependence of the scattering lengths is taken from the empirically derived model of Kopelevich [136]:

$$\frac{1}{\lambda_{scat}} = 0.0017\left(\frac{550}{\lambda_\gamma}\right)^{4.32} + 1.34\, v_s \left(\frac{550}{\lambda_\gamma}\right)^{1.7} + 0.312\, v_l \left(\frac{550}{\lambda_\gamma}\right)^{0.3} \tag{4.6}$$

where λ_γ is the photon wavelength (in nm) and v_s and v_l are the volume concentrations of "small" and "large" particles respectively[6] in ppm. The first term is the wavelength dependent Rayleigh scattering length in water and the remaining two make up the particle contribution.

Overall models

There are two slightly different scattering models implemented in KM3. This situation arose from the uncertainty over the best model to describe early measurements of scattering at the ANTARES site [134, 138].

P Models using the data in [137] (Figure 4.5) for the "particle" angular distribution. The probability of a particular scattering being a Rayleigh scatterer is η.

M Models using a combination of two Henyey-Greenstein functions to give the strongly forward-peaked particle contribution and a smaller back-scattering component representing Rayleigh scattering. This gives an "overall" scattering function:

$$\frac{dN}{d\Omega}(\theta) = \alpha\frac{dN_{HG}}{d\Omega}(g_1, \theta) + (1-\alpha)\frac{dN_{HG}}{d\Omega}(g_2, \theta) \tag{4.7}$$

The overall $\langle\cos\theta\rangle$ can then be expressed for the two overall models above (recalling that $\langle\cos\theta\rangle_{Rayleigh} = 0$) in terms of the probabilities for each different type of scattering:

$$\langle\cos\theta\rangle_P = (1-\eta) \times \langle\cos\theta\rangle_{particle} \tag{4.8}$$

$$\langle\cos\theta\rangle_M = \alpha \times g_1 + (1-\alpha) \times g_2 \tag{4.9}$$

The above models give an overall average $\cos\theta$ dependent on the parameters η for P or α,g_1 and g_2 for M. In [139] the concept of "effective scattering length" is introduced for models where the average $\cos\theta$ of the scattering function is close to 1.

$$\lambda_{eff} = \frac{\lambda_{scat}}{1 - \langle\cos\theta\rangle} \tag{4.10}$$

It is noted in [139] that, although this is a purely artificial parameter, for models where $\langle\cos\theta\rangle \sim 1$ the observed photon distributions should be degenerate for models with the same λ_{eff}. The derivation of this degeneracy in [139] is only valid in the limit where the photon scatters many times before being detected. Neither of the above two condition are necessarily true for ANTARES and we shall comment on the usefulness of this parameter in Section 5.3.

[6] The exact definition of "small" and "large" isn't important in this context. They can just be considered as free parameters in the model which are fitted to existing data.

Model	λ_{scat} [m]	$\langle\cos(\theta)\rangle$	λ_{eff} [m]	Parameters			
P1	40.8	0.77	175		$\eta = 0.17$		$v_s = v_l = 0.01$
P2	52.0	0.77	223		$\eta = 0.17$		$v_s = v_l = 0.0075$
M1	52.0	0.77	226	$\alpha = 1$	$g_1 = 0.77$	$g_2 = 0.0$	$v_s = v_l = 0.0075$
M2	22.3	0.90	223	$\alpha = 1$	$g_1 = 0.90$	$g_2 = 0.0$	$v_s = v_l = 0.0196$
M3	4.7	0.98	220	$\alpha = 1$	$g_1 = 0.98$	$g_2 = 0.0$	$v_s = v_l = 0.1$
M4	40.8	0.90	397	$\alpha = 0.985$	$g_1 = 0.92$	$g_2 = -0.6$	$v_s = v_l = 0.01$
M5	8.0	0.98	400	$\alpha = 1$	$g_1 = 0.98$	$g_2 = 0.0$	$v_s = v_l = 0.0575$
M6	52.0	0.90	506	$\alpha = 0.985$	$g_1 = 0.92$	$g_2 = -0.6$	$v_s = v_l = 0.0075$
N	∞	–	–				

Table 4.3: Scattering models used in the study of the effect of the water properties on the performance of ANTARES. η is the parameter of the "P" model. α,g_1,g_2 are the parameters of the "M" model. v_s and v_l specify the scattering lengths from the Kopelevich model in Eq. (4.6). All scattering lengths are in metres and at a wavelength of 466 nm.

4.2.2 Choice of scattering models

Measurements of the water properties of the deep ocean are extremely difficult and different methods often produce conflicting results. There is therefore some uncertainty over what scattering model to chose to represent the ANTARES site. There are two general reasons this choice of model is important to ANTARES:

- The sensitivity of the reconstruction to each of the different parameters of the scattering models and how well this needs to be measured is important in choosing a site (for a future km^3 project for example) and in optimising experiments to measure these parameters.
- We need to know how well we understand the performance of ANTARES, i.e. what are the systematic errors on the angular resolutions and efficiencies arising from the uncertainties in our knowledge of the water properties.

At the time this study was performed, the only analysis of measurements of the water properties at the ANTARES site was that of Palanque-Delabrouille (PD) [97, 134] which assumed a strongly forward-peaked particle scattering angular distribution (based on the data of Petzold shown in Figure 4.5). PD found an effective scattering length at 466 nm of around 260 m with an overall scattering length of order 50 m.

The range of scattering models chosen based on this analysis is summarised in Table 4.3. All the scattering lengths are specified in metres at a wavelength of 466 nm (corresponding to the blue data in [97]). The positions of the models in Table 4.3 are plotted in the $\lambda_{scat}-\langle\cos\theta\rangle$ plane in Figure 4.7. The best fit model of PD is P2 (taking the March '99 data from [97]). In addition to the scattering models above, there is a model with no scattering at all, simply referred to as "N" in the following descriptions.

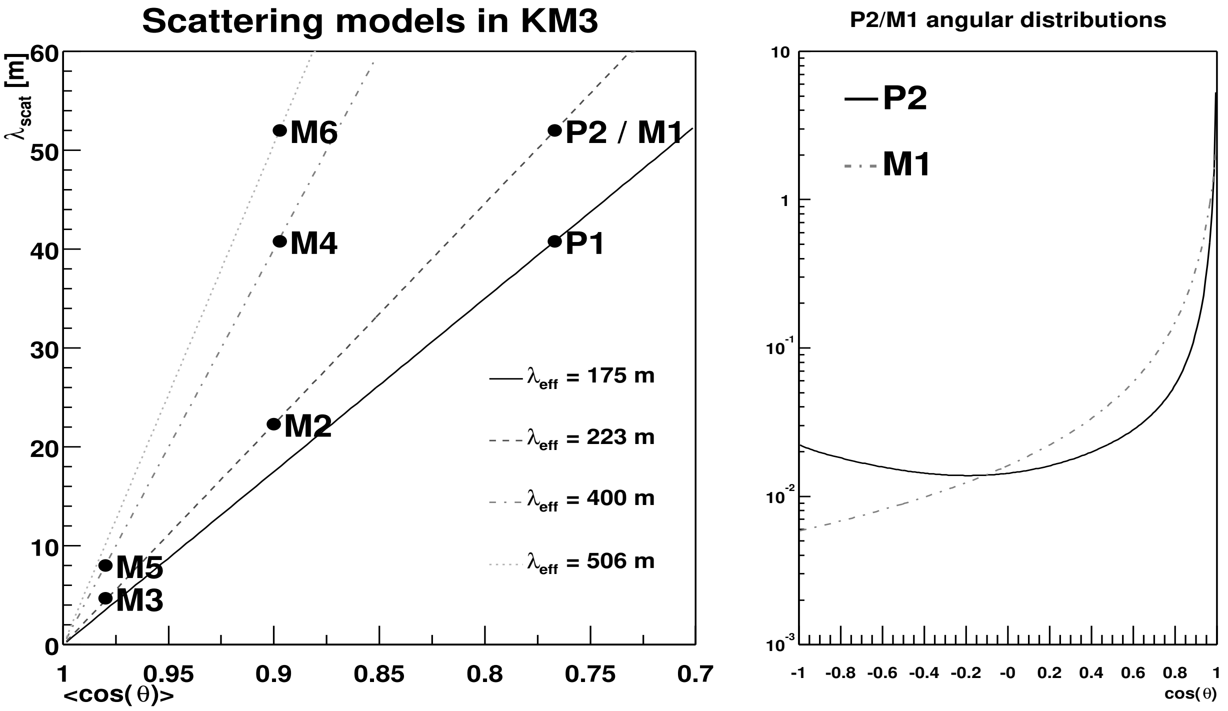

Figure 4.7: Scattering models of Table 4.3 in parameter space $\langle\cos\theta\rangle$, λ_{scat} and λ_{eff}. The overall angular distributions for the overlapping points P2 and M1 are shown on the right.

Recently, very preliminary results from an improved analysis of data at 374 nm by Schuster (WS) [98] have suggested that models with $\langle\cos\theta\rangle \sim 0.55$ (compared to 0.924 assumed by PD) are favoured by the experimental data. Whether this is also the case at 466 nm (in the region where the majority of photons are observed) is not clear from the current measurements though, in combination with the measurements of Petzold at 514 nm, it does suggest that there is some (currently unknown) wavelength dependence of $\langle\cos\theta\rangle$.

WS also gives overall scattering lengths of order 75 m when the $\langle\cos\theta\rangle$ is left free which is significantly longer than the 20 to 25 m scattering lengths reported by PD for the same data (the exact result for PD depends on the assumptions made in the analysis). For comparison, WS has also performed an analysis where the $\langle\cos\theta\rangle$ is fixed to that used by PD. In this case, overall scattering lengths of order 30 m are found. Though this is in rough agreement with the results of PD, it also highlights a strong correlation between $\langle\cos\theta\rangle$ and the scattering lengths and therefore calls into question the results of PD at 466 nm where the angular distribution is assumed but not measured[7].

Given the current uncertainty over the water properties at the ANTARES site, it is impossible to draw quantitative conclusions about the systematic effect of the water properties on the detector performance. In Section 5.3, we will restrict ourselves to making general statements about the effect of the water properties on the performance. It is not

[7]Several other issues with the calibration and analysis of PD have also been raised in [140] which further call into question these results.

possible to improve on this situation and obtain quantitative estimates of the systematic uncertainties without a better understanding of the existing experimental measurements at the ANTARES site and an additional measurement of the scattering angular distribution at a range of wavelengths, both of which are beyond the scope of this thesis.

4.2.3 Photon absorption at the ANTARES site

All the models described in Section 4.2.2 share a common description of the absorption of photons at the ANTARES site. The absorption length at 466 nm is fairly well constrained by individual measurements [97] though some annual and seasonal differences are seen. The value used in all the simulations performed here is within the range of measured values and corresponds to an absorption length of 60 m at the reference wavelength of 466 nm.

The wavelength dependence of the absorption length in all the ANTARES detector Monte Carlos has been taken from [91] and then rescaled to correspond to the measured absorption length at 466 nm. This is shown in Figure 4.9, page 114 in Section 4.3. The maximum value of 60 m is close to 466 nm and it falls off to 20 m by 375 nm (corresponding to the UV measurements in [98]) and 550 nm.

4.2.4 Effect on the expected arrival times

The important parameter for the reconstruction of muon tracks in ANTARES is the arrival time at each PMT with respect to the time direct Cherenkov light would have arrived for a given track. This is referred to as the arrival time delay.

In the absence of scattering, with no optical background and a negligible PMT TTS it would be possible to accurately define the track parameters for a given set of PMT hits[8]. Scattering in the water is one of the things which will degrade the performance of the detector by reducing the numbers of photons near zero time delay and increasing the spread in arrival times for those which are close to zero.

The plots in Figure 4.8 show the arrival time delays, calculated including the PMT TTS and after the electronics simulation. The curves show the delays for through-going muons at 1 TeV for the favoured model P2, the models where only one of the parameters (angular distribution, $\langle\cos\theta\rangle$ or λ_{scat}) differs from P2 and for the model N where there is no photon scattering.

The "no scattering" model has the largest number of photons in the peak of the distribution as expected and we would anticipate that this model will give the best detector performance. However, it is not realistic to neglect scattering, so we can instead use this to give us an upper limit on the performance for all scattering models.

With reference to the P2 model, we can see the effect of each of the different parameters in the shape of the arrival time delay distributions:

[8]Some sets of hits have two compatible tracks which are related by a rotation of twice the Cherenkov angle. In this case, the hit amplitudes could be used to separate the two possible solutions.

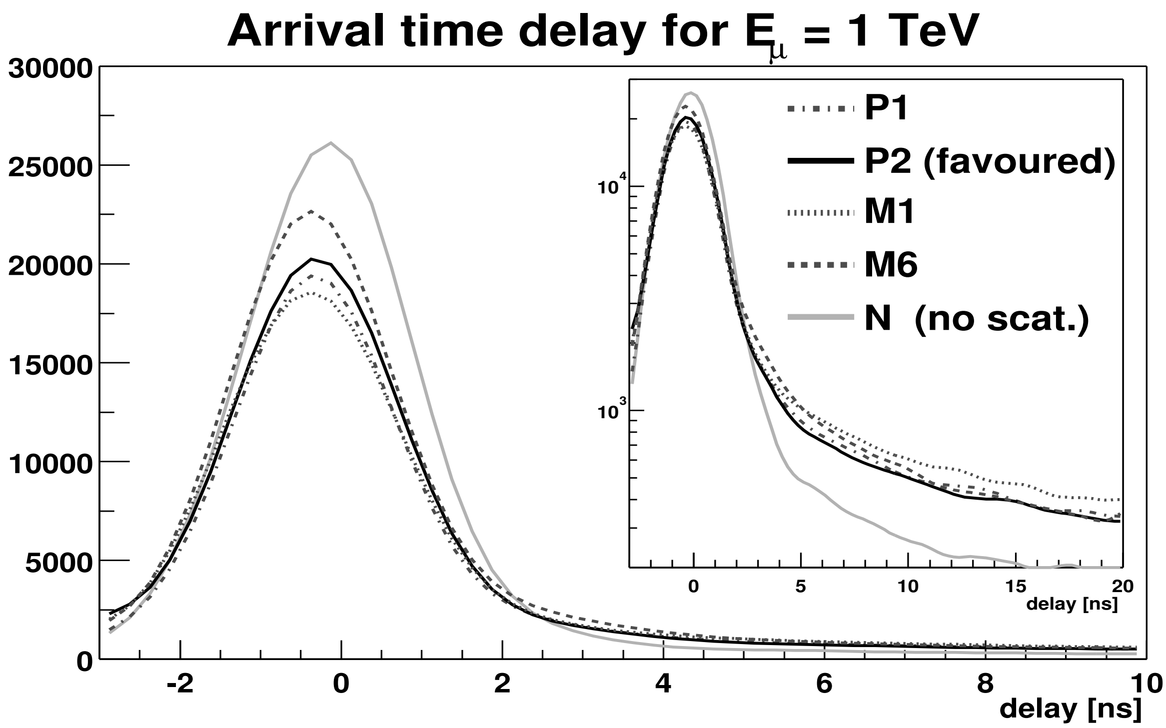

Figure 4.8: Arrival time delay for different scattering models for 1 TeV through-going muons. The favoured model (P2) is shown in black. The model with the same $\langle\cos\theta\rangle$ and λ_{scat} (M1) is shown as a light grey dotted line. Changing λ_{scat} to 40 m (P1) is shown as a medium grey dash-dotted line. Changing $\langle\cos\theta\rangle$ to 0.9 (M6) is shown as a dark grey dashed line. The model N is shown in very light grey. The slight shift of the peak to negative delays is the effect of the electronics recording the time of the first hit where several arrive close together.

- Making λ_{scat} shorter (P1) reduces the number of photons in the peak.

- More forwarded peaked scattering and hence a longer effective scattering length (M6) increases the number of photons in the peak but makes it wider.

- Changing the angular distribution to remove the back scattered component but with the same $\langle\cos\theta\rangle$ (M1) gives fewer photons in the peak but more with a delay greater than 10 ns. P2 has either has very forward-peaked scattering (leaving the photon very close to the peak) or back scattering (in which case the photon is essentially lost). Photons that scatter in M1 pick up a larger time delay than those subject to the particle (forward-peaked) scattering in P2 and therefore are more likely to be observed with a time delay greater than 10 ns.

These effects are all intuitively understandable in terms of the properties of the scattering models. Their effects on the reconstruction will be investigated further in Section 5.3 to identify the most important components of the scattering models in this respect.

4.3 Arrival time spread from a wavelength dependent refractive index

Historically, ANTARES and other similar experiments (e.g. [81, 83]) have calculated the propagation times of Cherenkov photons using the phase velocity. The ANTARES Monte Carlos use a value of the phase velocity (and hence the refractive index, n_p) corresponding to a wavelength of around 460 nm. As pointed out in [141], using the phase velocity is incorrect.

The speed of light pulses in matter of angular frequency $\omega = 2\pi\nu$ and wavenumber $k = \frac{2\pi}{\lambda}$ is given by the group velocity, defined as:

$$v_g = \frac{d\omega}{dk} \tag{4.11}$$

Using the relations:

$$\omega = \frac{ck}{n(\omega)} \Rightarrow \frac{d\omega}{dk} = \frac{c}{n^2}\left(n - k\frac{dn}{dk}\right) \tag{4.12}$$

$$k = \frac{2\pi}{\lambda} \Rightarrow \frac{d\lambda}{dk} = -\frac{\lambda^2}{2\pi} \tag{4.13}$$

we can write the group velocity as:

$$v_g = \frac{c}{n}\left(1 + \frac{\lambda}{n}\frac{dn}{d\lambda}\right) \tag{4.14}$$

We can define a "group refractive index" as[9]:

$$n_g(\lambda) = \frac{n}{1 + \frac{\lambda}{n}\frac{dn}{d\lambda}} \tag{4.15}$$

The calculated error in arrival times with respect to a muon track due to the incorrect use of the phase refractive index for photon propagation in AMANDA was found to be of order 2 ns compared to a phototube jitter of order 10 ns [142] and hence not significant. For ANTARES, where the overall timing resolution is intended to be of order 1 ns [90], this correction will be important. In addition, as $\frac{dn}{d\lambda}$ is usually negative for water in the optical region, the wavelength dependence of n_g will be stronger than that of n_p and cannot necessarily be neglected.

In the remainder of this section, we develop a special Monte Carlo simulation to evaluate the offset and spread in arrival times due to using a wavelength dependent refractive index and add it to the main ANTARES detector Monte Carlo.

[9]The definition given in [141] is the first order expansion of this result. The expansions are equivalent provided $\lambda\frac{dn}{d\lambda} \ll n(\lambda)$ which holds for all reasonable models of refractive indices in water.

Parameter	Value
n_0	1.31405
n_1	1.779×10^{-4}
n_2	-1.05×10^{-6}
n_3	1.6×10^{-8}
n_4	-2.02×10^{-6}
n_5	15.868
n_6	0.01155
n_7	−0.00423
n_8	−4382
n_9	1.1455×10^{6}

Table 4.4: Fit parameters for the Quan and Fry refractive index curve.

4.3.1 Refractive indices in water

The choice of refractive index model is critical to understanding the spread in arrival times due to the dispersive nature of light propagation. A study of available models of the refractive index of seawater in the literature on the subject has been made for ANTARES in [143]. The conclusion of this study was that, for the range of wavelengths of interest (300 nm to 600 nm), the most suitable model was that of Quan and Fry [144] who perform a 10 parameter empirical fit to all available experimental data for the refractive index of sea water. This fit is of the form:

$$n(S,T,\lambda) = n_0 + (n_1 + n_2T + n_3T^2)S + n_4T^2 + \frac{n_5 + n_6S + n_7T}{\lambda} + \frac{n_8}{\lambda^2} + \frac{n_9}{\lambda^3} \tag{4.16}$$

The values of each of these parameters are shown in Table 4.4. The ranges of validity for these values are $0\ °C < T < 30\ °C$, $0 < S < 35$ ‰ and 400 nm $< \lambda <$ 700 nm. They are stated to reproduce the available data to within the experimental errors (at the level of 1.5×10^{-5}).

The measured values of the salinity and temperature at the ANTARES site [145] are $S = 38.44$ ‰ and $T = 13.1\ °C$. The temperature is within the quoted range but the salinity lies slightly outside. In addition, we want to use Eq. (4.16) for wavelengths down to 300 nm. We can justify the extrapolation of this model as the dependence of Eq. (4.16) on the salinity is small and the absorption and PMT efficiency (see Figure 4.9) limit the contribution of photons below 400 nm.

These fits also neglect any pressure dependence of the refractive index. A fit to available data at different pressures was performed in [143] and the dependence was found to be 1.4×10^{-5} bar^{-1}. Taking the values of salinity and temperature above and substituting them in Eq. (4.16) gives refractive indices dependent on pressure, p, (in bars) of:

$$n(\lambda, p) = 1.3201 + 1.4 \times 10^{-5} \times p + \frac{16.2566}{\lambda} - \frac{4382}{\lambda^2} + \frac{1.1455 \times 10^6}{\lambda^3} \tag{4.17}$$

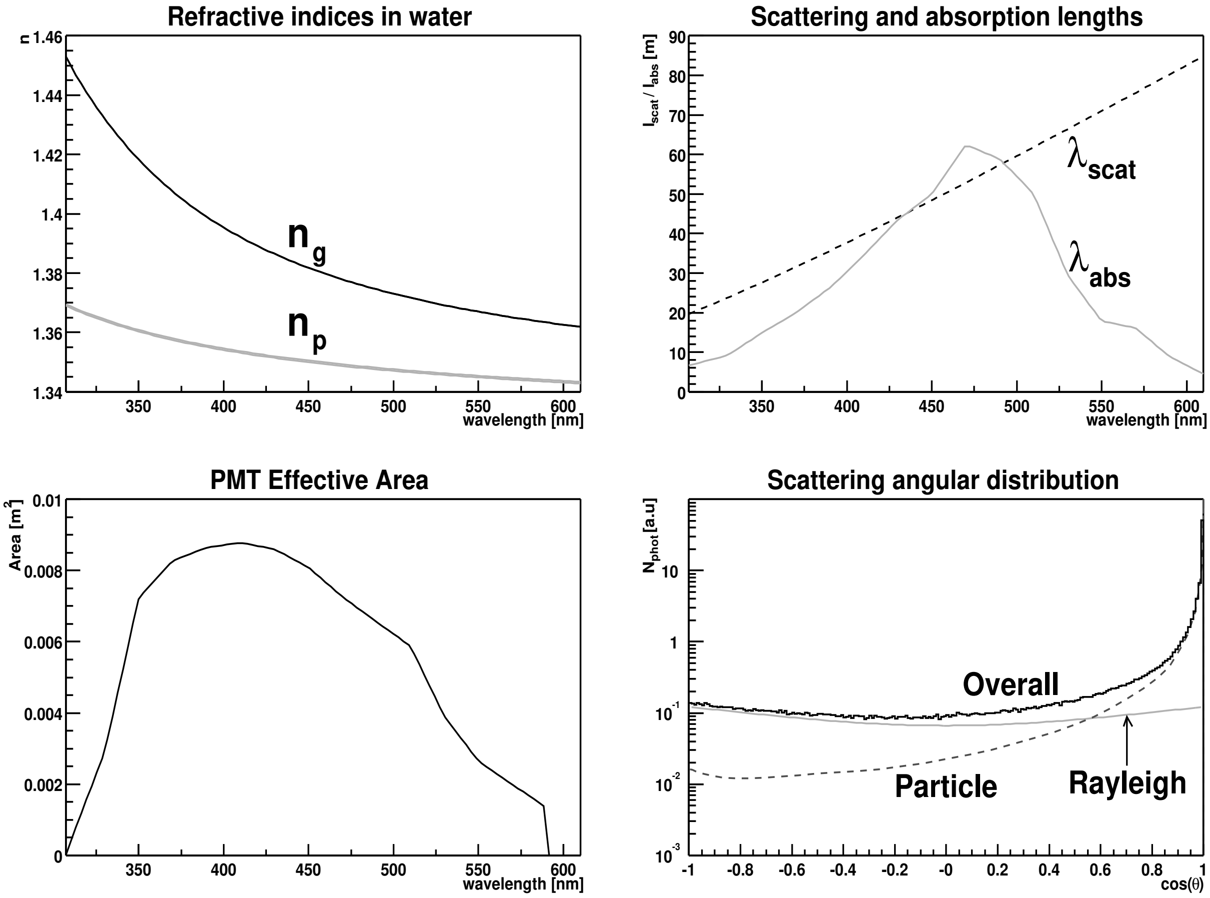

Figure 4.9: Refractive indices (top left), absorption and scattering lengths (top right), PMT efficiency (bottom left) and scattering angular distributions (bottom right) for the dispersion simulation. The scattering angular distribution curves show the shape of Rayleigh and particle scattering and the histogram shows the overall distribution of scattered photons.

Both the phase and group refractive indices are shown in Figure 4.9. Over the range of pressures corresponding to the instrumented volume of the ANTARES detector, 200 to 240 bars, the pressure dependence causes a uniform shift in the refractive index of 0.00056, a percentage change of less than 0.05% (it is smaller than the width of the lines in Figure 4.9). Hence, we choose a pressure of 240 bars and neglect the pressure dependence.

Both the temperature and salinity dependences are small and the values stated above were found to be comparable to 30 year old measurements in the Gulf of Lyon [145]. Hence, we use the measured values of temperature and salinity, assuming they will remain consistent with the values at the ANTARES site, neglecting any further dependence on both temperature and salinity on the grounds of the size of the effect and the long term stability of the values.

For future reference, we calculate the values of both the phase and group refractive indices at a wavelength of 460 nm (approximately the most sensitive wavelength of the ANTARES OMs). This gives $n_p(460\text{ nm}) = 1.3499$ and $n_g(460\text{ nm}) = 1.3797$ (the errors are smaller than the last quoted digit [144]).

4.3.2 Photon propagation simulation

There are several components to a simulation of photon propagation in water to evaluate the spread in arrival times at an ANTARES PMT for light with a Cherenkov spectrum. For the purposes of this evaluation, a photon propagation algorithm has been implemented based on the description in Section 4.1.2 to propagate light generated from a point-like section of Cherenkov light emitting track.

Absorption and scattering models

The absorption length profile is identical to that used in KM3. The choice of scattering model corresponds to the favoured model from [97] labelled P2 in Table 4.3, page 108. The wavelength dependences of both the absorption and scattering lengths are shown in the top right plots of Figure 4.9. Note that the maximum of the absorption length is around 460 nm which was the reference wavelength for the refractive indices above. The angular distributions of Rayleigh and particle scattered photons are shown in the bottom right plot of Figure 4.9 corresponding to a relative fraction of Rayleigh scattering (η) of 0.17. The curves show the functional form of the distributions, the histogram shows the overall distribution of sampled photons.

OM efficiency

The OM efficiency is also taken directly from KM3 (as the effective area of the OM from Eq. (4.1), page 97). It is tabulated for normal incidence in Table B.10 in Appendix B. It is shown in the bottom left plot of Figure 4.9.

4.3.3 Results and discussion

As stated above in Section 4.2.4, the interesting parameter for muon reconstruction is the arrival time delay with respect to direct Cherenkov light. As the reconstruction must calculate the delays at a fixed wavelength[10], the wavelength dependence of the refractive index will increase the spread in the time delays and could therefore have an effect on the detector performance. Using the photon propagation simulation described in this section, we can evaluate the delays with respect to photons with a wavelength of 460 nm as a function of photon propagation distance. In the next section, we will use this spread in arrival times to adjust the detector Monte Carlo simulation.

The two plots in Figure 4.10 show the mean and RMS spread in arrival times when using the phase and group refractive indices to calculate photon propagation times in the simulation and the delay in the analysis. In both cases here, there is no scattering in the water model used to allow us to isolate just the effect of the wavelength dependence of the refractive index.

[10]There is no wavelength information in the output of the PMTs so a fixed, central wavelength must be assumed to calculate time delays in the reconstruction.

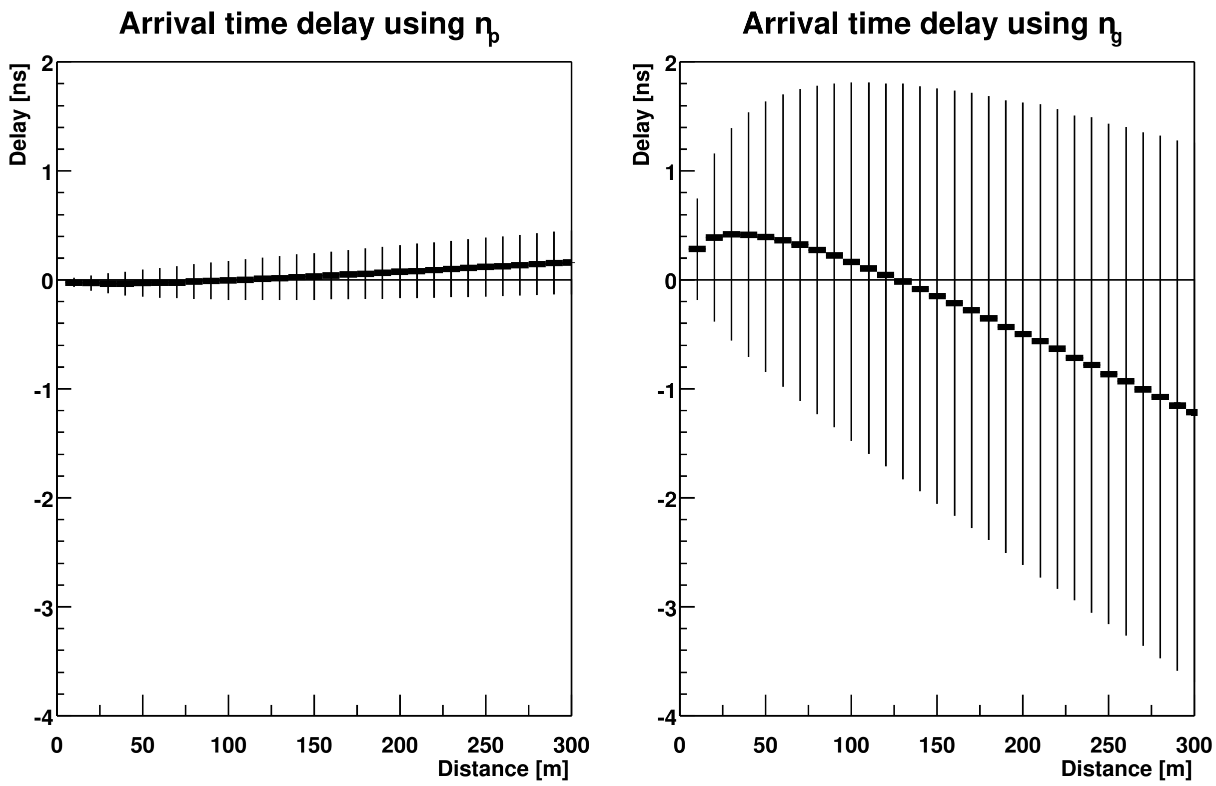

Figure 4.10: Mean arrival time delays relative to direct Cherenkov light at 460 nm using the phase (left) and group (right) velocity in the photon propagation simulation and in calculating the delays. The mean of the distribution is shown as the thick line and the error bars show the RMS spread about this mean.

Previous calculations of this effect for ANTARES [145] incorrectly used the phase velocity and concluded that this effect was significantly smaller than the PMT TTS and could safely be neglected. This conclusion is consistent with the left hand plot in Figure 4.10. Both the offset and the spread are consistently within 0.4 ns of the reference value at 460 nm.

The right hand plot in Figure 4.10 shows the realistic case where the Cherenkov angle depends on the phase refractive index and the photon propagation time is calculated using the group refractive index. Here the effect is much larger (due to the much stronger dependence of n_g on wavelength compared to n_p). The offset of the average from the expected value varies between +0.4 ns (at around 40 m) to -1 ns (at around 300 m) beyond which virtually no photons are detected. The spread is 0.5 ns even at 10 m away from the track, by 40 m it is 1.1 ns and by 100 m it is 1.6 ns. Beyond this, the effect is even larger.

We now perform simulations of photon propagation including the effect of scattering (using the model P2) with and without dispersion and compare this to our simulations without scattering. The shapes of the delay distributions from these simulations at 40 m and 140 m are shown in Figure 4.11. Aside from being non-gaussian and dependent on distance it is clear that, near to the direct Cherenkov peak, the dispersion dominates the

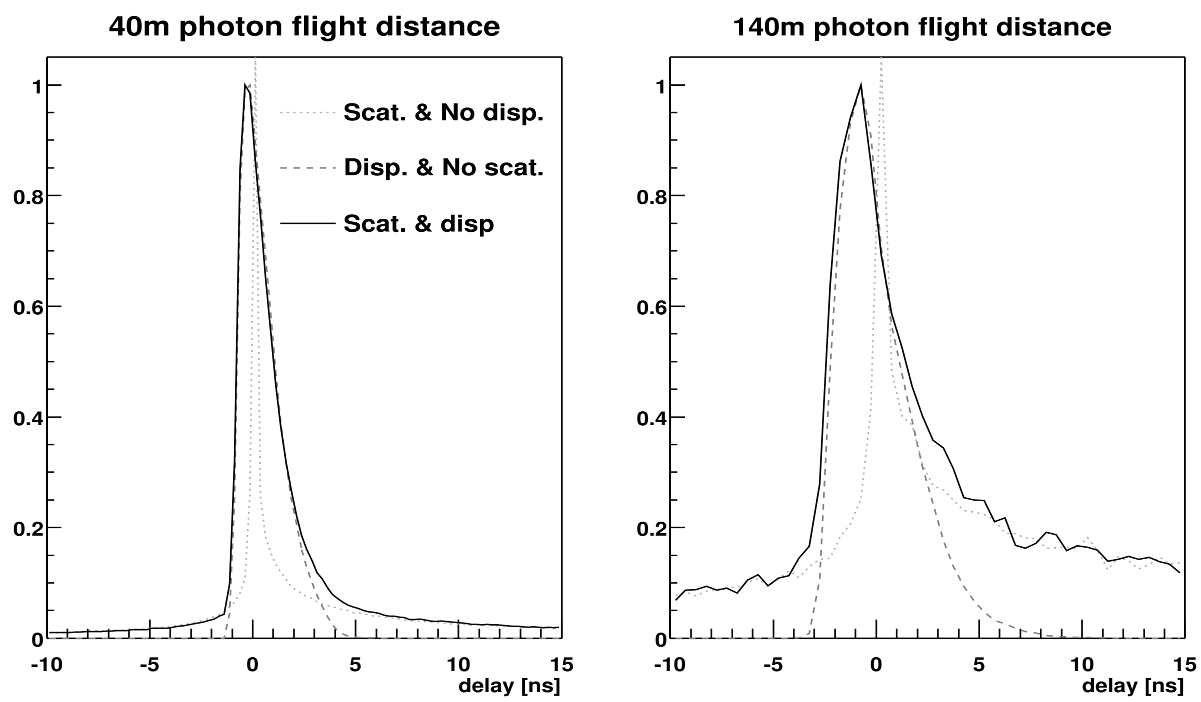

Figure 4.11: Arrival time delays at 40 m and 140 m from the generation point. The light grey dotted curve shows the old simulation which just includes scattering. The dashed line shows the effect of the dispersion without scattering. The black solid line shows the overall effect including both scattering and dispersion.

shape of the delay and, outside this region scattering dominates. This is important as it allows us to assume that the two effects are reasonably independent[11].

4.3.4 Application to the detector MC

We are interested in using the results of these simulations to apply a correction[12] to KM3 (and Geasim). KM3 already includes scattering so the only additional correction is that from a "no scattering" simulation (shown by the dashed curves in Figure 4.11). We saw in the previous section that scattering and dispersion are reasonably independent. In addition, it is only photons which arrive close to zero delay for which this spread is important and this region is dominated by the direct photons. For both these reasons, it is sufficient to take the dispersion in a model without scattering to parameterise the arrival time spread.

[11]This is not necessarily obvious as the scattering (particularly the Rayleigh scattering) is strongly wavelength dependent. The particular scattering model used will affect the wavelength distribution of the photons arriving close to zero delay and hence affect the spread in arrival times from the refractive index. However, for this case, it appears not to be important.

[12]In KM3, a distinction is made between direct and scattered photons to improve the speed of the simulation. The assumption made is that all direct photons arrive "on time" and therefore this spread cannot be trivially included directly in the photon tables. Hence, we can only include this effect as a correction after the main simulation.

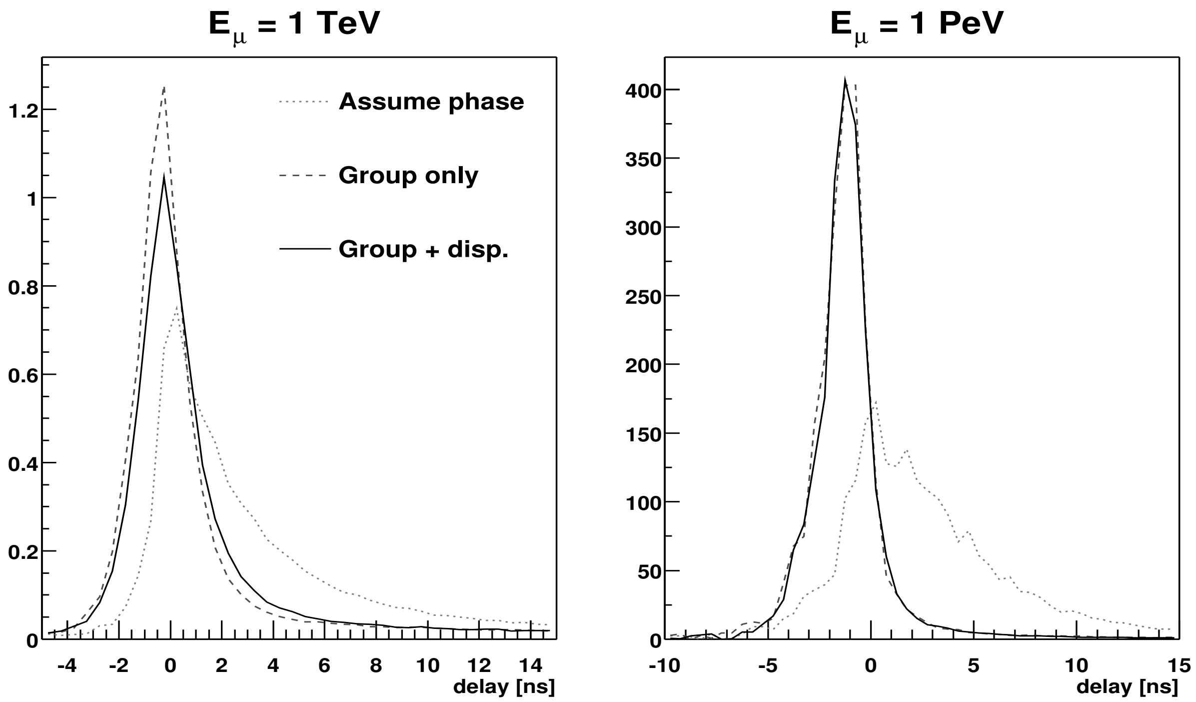

Figure 4.12: Arrival time delays for muons of initial energies 1 TeV and 1 PeV using the group velocity to calculate the photon propagation time. The light grey dotted curve shows the delays calculated by mistakenly using the phase velocity. The dark grey dashed curve shows the delay without dispersion and the solid black curves shows the final simulation using the group velocity including dispersion.

Histograms corresponding to the arrival time spread with dispersion but without scattering at distances at 10 m intervals from 5 m to 295 m (direct photon propagation distance) are recorded from the photon propagation simulation described above. In KM3, the group refractive index is set to the reference value at 460 nm given in Section 4.3.1, page 113. For each detected photon in KM3, the arrival time is smeared by sampling from the histogram closest to the direct Cherenkov photon propagation distance for that PMT and the muon track. Conceptually, this approach is very similar to how scattering itself is included in KM3.

The arrival time delays, calculated including the PMT TTS and after the electronics simulation and with the scattering model P2 for muons of energies 1 TeV and 1 PeV are shown in Figure 4.12. In all cases, the group velocity is used in calculating photon propagation times in the simulations. The dotted curve shows the time delays which would be obtained if the phase velocity was mistakenly used in their calculation. The effect of the dispersion is much smaller than the phase-to-group correction.

At both energies, the width of the peak of the arrival time delay distribution is dominated by the PMT TTS. At 1 TeV, comparing the dashed curve to the solid black curve, we can see a slight widening of the peak. More significantly, the photons which cause this widening are removed from the peak, reducing its height by around 20% which could have a significant effect on the performance. At 1 PeV, the effect is much less significant as the width of the peak is dominated by the shower light and the time integration in the electronics (when many photons arrive at a single PMT, the recorded time in any 25 ns window is that of the first hit only).

It is clear from the above that a wavelength dependent group velocity needs to be used to calculate photon propagation times for Cherenkov light produced in the ANTARES Monte Carlos. Using the results of the simulation described in this section, we have added this effect and it will be used in all the simulations whose results are presented in Chapter 5 and Chapter 6.

4.4 Summary

In this chapter the methods used to simulate the detector response to muons, electrons and hadrons have been described. In particular:

- We have described KM3, the existing algorithm for simulating muons and electromagnetic showers caused by Bremsstrahlung photons (Section 4.1). We have also defined the OM effective area, the TTS of the PMTs and the optical background noise and the digitisation scheme used in all following simulations (Section 4.1.2).
- We have modified Geasim and combined it with KM3 to add the light produced by hadronic showers into a simulation including scattering for the light produced by muons for the first time in ANTARES (Section 4.1.5).
- We have defined two overall scattering models based on theoretical and empirical considerations and selected a set of points spanning the parameter space around the experimentally favoured value at the ANTARES site for further investigation (Section 4.2).
- We have implemented the scattering algorithms and scattering models described in Section 4.1 and Section 4.2 and a model of the wavelength dependence of the refractive index in water to simulate the arrival time spread of Cherenkov light (Section 4.3) and then added this effect to the ANTARES Monte Carlo codes (Section 4.3.4).

In this chapter, we have used these simulations to show that the vast majority of light is seen from less than 200 m of the muon track (in the case of muons entering the can, Section 4.1.4) or within 200 m of the neutrino interaction vertex (for interactions inside the can, Section 4.1.5) thus justifying our choice of can size in the generation of events (see Section 3.1.1).

In terms of the arrival times of photons at individual PMTs with respect to the expected time for direct Cherenkov light (arrival time delays), we have shown that the changes in the shapes of these distributions can be understood in terms of the parameters of the chosen scattering models. This will be important in understanding the effect of the medium on the detector performance (Section 5.3).

Finally, using an independent simulation, we have shown that (correctly) using the group velocity instead of the phase velocity to calculate photon propagation times and including the effect of the wavelength dependence is entirely necessary given the timing resolution of ANTARES. We have also shown that, at the level of accuracy required, this spread in arrival times and scattering are independent. Using tables extracted from these simulations, we have implemented this effect in the ANTARES Monte Carlo codes and, in Chapter 5, will provide the first determination of the performance of ANTARES including this effect.

Chapter 5

The ANTARES detector performance

In this chapter we use one of the existing ANTARES reconstruction algorithms to evaluate several potential sources of systematic errors on the performance of ANTARES. Based on a limited Monte Carlo sample, the selection cuts reduce the misreconstructed background of atmospheric muons to a negligible level. The systematic errors from the event generation are below the level of 5% below 1 PeV (and only exceed that above 1 PeV for a neutrino flux from a specific point source). The water properties have a significant effect on the detector performance and further measurements at the ANTARES site are required to properly quantify this effect. We then describe several methods of presenting the efficiency of ANTARES as effective volumes and effective areas with the emphasis on developing methods that are model independent and apply to the whole range of neutrino energies relevant to ANTARES. Using these methods we find an effective area greater than 30000 m^2 for neutrino energies above 100 TeV and about 20000 m^2 for an E_ν^{-2} neutrino spectrum. The angular resolution above 100 TeV is 0.15° and 0.23° for an E_ν^{-2} neutrino spectrum.

The previous two chapters described methods used to generate particles produced by neutrino interactions around the detector and to simulate the response of the detector to these events. In doing this, several potential sources of systematic errors were highlighted which will affect our ability to predict the performance of ANTARES in various ways. In this chapter we evaluate these systematic effects on the event rate and angular resolution of ANTARES for a range of neutrino energies using the current "best" reconstruction and analysis method available within ANTARES which is described briefly below.

The presentation of the performance of ANTARES in a manner which is independent of the generated events (and hence can be understood without reference to individual simulations or models) is also discussed. Several previously neglected subtleties in these presentations are covered and used to describe two new ways of presenting the performance of ANTARES. The performance is then evaluated using these methods for the favoured set of simulation models with reference to the systematic errors calculated previously.

5.1 Reconstruction and analysis methods

A great deal of work has been done by the Collaboration in developing the current reconstruction algorithms used in ANTARES (see [146, 147] for an overview) and that work is still ongoing. The method described here is that with the best performance which has been demonstrated to reject the vast majority of the current Monte Carlo sample of atmospheric muons. Only a brief overview of the components of the reconstruction are given. More details can be found in [147].

5.1.1 "Triggering"

The exact details of the real ANTARES trigger and online data filtering is still under investigation [90] and the electronics scheme to control it is general enough to allow for a wide range of possibilities depending on the experimental conditions and physics requirements.

At the level of the reconstruction software, it is clear that some prefiltering is needed given the large number of events[1] to be processed and the relatively high noise rates. The "trigger" described here is a software filter which has been constructed based on very general requirements for the reconstruction and estimates of the conditions at the ANTARES site. It has been in use in ANTARES for several years and describes a reasonable minimum trigger condition under normal conditions[2] [148].

This trigger is based on local coincidences of PMT hits within the triplets of OMs on each storey of each string. First, all hits with an amplitude of less than 0.5 photoelectrons (pe) are ignored. Then, a PMT hit is said to be in local coincidence if it is within $\pm$ 20 ns of another hit on a different tube in the same group of three Optical Modules. This is required as the high background rate on each tube (typically $\sim$ 60 kHz) means that isolated hits alone cannot be used to identify events. In contrast, the coincidence rate (from randomly overlapping potassium-40 hits) is less than one per 2 μs window containing each event over the whole detector.

For an event to pass this minimal trigger, the following requirements must all be satisfied:

- There must be at least 2 local coincidences of the type above.
- There must be at least 2 strings with local coincidences. This ensures that there is some 3D information to begin the fit with.
- There must be at least 5 OMs which have been hit. The position and direction of the track has 5 parameters (x,y,z,θ,ϕ) so 5 hits in different positions are the absolute minimum required.

The information about the local coincidences is retained as a starting point for the track reconstruction, giving those PMT hits which are most likely to have originated from a muon track.

[1] What defines an event in the continuous data stream received from the detector is another question. Here it is taken to describe independent Monte Carlo events. In reality, events will be extracted from 10 μs time-slices of the data based on clusters of causally connected hits [90] although the exact details of this process have not yet been made available in the reconstruction software.

[2] i.e. Not in bioluminescence burst phases

5.1.2 Reconstruction and selection

The reconstruction aims to take a set of PMT hits (forming an event) and reconstruct the best set of track parameters (position, direction and time) which are compatible with those hits. The method used to obtain the results presented here and Chapter 6 is fully described in [149, 150]. It begins with a simple straight line fit through the local coincidences identified above which is then used to filter some of the potassium-40 background from the event. This fit is then refined firstly by an iterative scan of the track parameter space and finally by a maximum likelihood fit based on the arrival time delays with respect to direct Cherenkov light from a given candidate track.

The set of reconstructed events will not only include upward going muons created by neutrino interactions but also downward going atmospheric muons from cosmic ray interactions. Some of these atmospheric muons will be misreconstructed as upward going. Though the probability of misreconstructing a downward going muon as upward going is low, the large excess of these events over the atmospheric neutrino sample means they can significantly pollute the final data sample. Hence, it is necessary to apply some further restrictions, referred to here as selection cuts, to exclude this background.

The selection cuts applied here are those documented in [150]. They are derived from a comparison of the Monte Carlo samples of background and signal events available and have been shown [146] to reject all of the current ANTARES sample of single muons[3] corresponding to $\sim$ 24 hours worth of simulated data. From the sample of multiple muons, corresponding to $\sim$ 9 days of data with a primary energy threshold above 2 TeV, two events were misreconstructed as upgoing ($\sim$ 80 events per year) with both of these close to the horizon. This is small compared to the expected rate of atmospheric neutrinos ($\sim$ 2000 events per year, see Section 5.2.4) and we will therefore assume we can neglect the background contribution of atmospheric muons. However, further Monte Carlo need to be performed in this area with larger data samples.

5.1.3 Angular resolution and efficiency

Before starting on various estimates of systematic effects in the simulations, it is worth commenting on the presentation of these results and what this is intended to achieve. The aim is to present an estimate of the uncertainty in final results way which is independent of any neutrino flux model and can be understood and applied (where necessary) in the context of future (i.e. model specific) studies.

The full presentation of the efficiency of the detector will be discussed in Section 5.4. For the examination of generator effects (Section 5.2) and photon propagation medium effects (Section 5.3) we present the efficiencies as a ratio of the number of events for different models as a function of neutrino energy. Where necessary, this could then be reweighted to a particular neutrino flux for specific models.

[3]The existing background production was divided into events which produce only one muon at the can generated using a fast parameterisation and a full simulation of cosmic ray interactions where only events with multiple muons at the can were kept which allows for a higher primary energy threshold.

It is also useful to define the angular resolution, the error in the reconstructed track direction. If we used the mean error for this purpose, the quoted value would be dominated by a relatively small number of very badly reconstructed events. Therefore, we define the angular resolution as the median of the distribution of the errors in reconstruction. We shall comment further on this definition (compared to, say, quoting 1σ errors) in Section 5.4.5.

To obtain the statistical error on the angular resolution, we use the bootstrap method [151]. The distribution of the angular error in the reconstructed track direction is resampled to create a large number of new distributions containing an equivalent number of events to the original and we calculate the median error for each of these distributions. The RMS of these medians gives the statistical error on the original angular resolution. For this method to give reliable answers, the original distribution has to be representative of the underlying distribution (i.e. in the limit of very high statistics). For the results presented in this Chapter, the distributions which are resampled generally contain several thousand events and our estimates of the statistical errors are therefore robust.

To study astrophysical and terrestrial neutrino fluxes, we are interested in determining the accuracy with which the direction of a given neutrino can be determined. Therefore, the neutrino flux model independent method of expressing this is the neutrino angular resolution as a function of neutrino energy. Again, this can be reweighted for a given source spectrum if required to determine the distribution of reconstructed neutrino directions for a given source.

5.2 Systematic errors from event generation models

In Chapter 3, several aspects of the event generation were discussed. Different target media and parton distribution functions lead to different calculations of the neutrino cross-sections and interaction kinematics. Two different muon propagation codes were discussed which affect the muon energies seen at the detector and the direction of the muon with respect to its parent neutrino. Different models of the atmospheric neutrino flux were described which will affect the overall event rate. In addition to the uncertainties in the event generation, the (correct but previously neglected) inclusion of the hadronic shower in the detector Monte Carlo will affect the event rate at some level. We can now determine at what level and over what range of neutrino energies these effects are important.

For all the results in this chapter and in Chapter 6, we have made two large productions of simulated data. These will be referred to as “Low Energy (LE)” (5 GeV to 100 TeV with an E^{-2} spectrum for the interacting neutrinos, close to the atmospheric neutrino spectrum) and “High Energy (HE)” (5 GeV to 100 PeV with a flatter, $E^{-1.35}$ spectrum to give good statistics at high energies). The angular distribution of the neutrinos in each of these productions is isotropic and covers the entire sky. The exact properties of each production are described in detail in Appendix C.

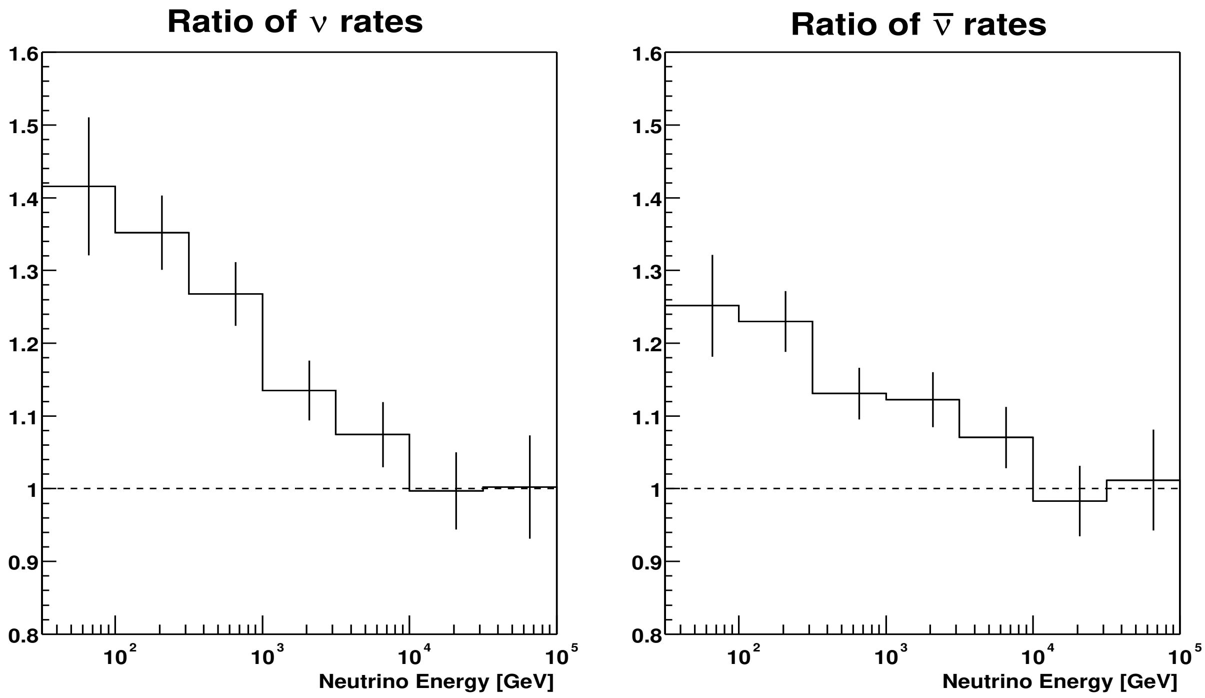

Figure 5.1: The ratio of the numbers of selected events with and without the hadronic shower simulation showing the increase in the event rate due to its inclusion. The errors are purely statistical.

5.2.1 Hadronic shower simulation

The first effect we investigate is that of the hadronic shower on the overall event rate. As discussed in Section 4.1.5, the hadronic shower will produce a significant amount of light at all energies but the fraction of events which interact close enough to the instrumented volume for the hadronic shower to be visible will decrease with energy. Therefore, there will be an energy above which (the time consuming) simulation of the hadronic shower is no longer necessary.

Using the LE sample, we calculate the ratio of selected events for otherwise identical simulations with and without the hadronic shower for neutrino energies up to 100 TeV. The results are shown in Figure 5.1.

Firstly, we can see that the results are different for neutrinos and anti-neutrinos. As seen in Figure 3.2 in Section 3.2.2, the mean inelasticity is smaller for anti-neutrinos compared to neutrinos. Therefore, the muon energy (given by $E_\mu = (1 - y)E_\nu$) will be larger. This supports the result seen in Figure 5.1 where the hadronic shower is less significant for anti-neutrinos because it contains a smaller fraction of the initial neutrino energy.

Secondly, we see that there is essentially no increase in the event rate for neutrino (or anti-neutrino) energies above 10 TeV. In all future simulations extending to higher neutrino energies (i.e. the HE production), we only include the hadronic shower contribution in the detector Monte Carlo for neutrinos with energies below 100 TeV which conservatively takes into account the above result.

The effects discussed above are not a systematic error as such as it is clear that including the Cherenkov light from the hadronic shower is the correct approach (and is the one adopted here). It does show however that the energy up to which it is important is higher than previously thought and cannot be neglected for any of the physics studies in ANTARES.

5.2.2 Parton distribution functions and neutrino cross-sections

In Section 3.2.3 we saw the differences in the neutrino and anti-neutrino cross-sections which arose for different choices of the Parton Distribution Functions (which differ in the assumptions they make in extracting the quark distribution functions from DIS data). As discussed in Section 3.4.2, there are three ways in which the different PDFs contribute to the final event rate:

- The event kinematics at the interaction vertex will differ, giving a different distribution of muon energies for a given neutrino energy.
- The neutrino cross-section at the interaction vertex will differ, giving different numbers of muons for a given neutrino flux.
- The absorption in the Earth will differ as the neutrino cross-section differs, giving different neutrino fluxes at the detector for a given neutrino flux arriving at the Earth.

We generate the same total number of events (with parameters identical to the HE production) for each PDF and run these through the detector Monte Carlo simulation and reconstruction described previously. As the neutrino cross-section and Earth absorption only enter the calculation of the event rate as a weight (the method in Section 3.4 starts with an interacting neutrino spectrum), we can separate the effect of the interaction kinematics, the interaction cross-section and the absorption in the Earth.

In Figure 5.2 we plot the ratios of selected events for each alternative PDF compared to those for our reference PDF of CTEQ3D. The top plots in Figure 5.2 show the results without any weights applied and hence just show the effect of the interaction kinematics. At all energies (in the range 300 GeV to 100 PeV considered here) the ratio is generally within 5% and any differences are dominated by the statistical fluctuations in the available sample.

The middle plots in Figure 5.2 show the ratios of selected events weighted by the neutrino cross-section for each PDF. Here we see the effect of the different cross-sections shown in Figure 3.4, page 63, giving higher interaction rates at high energies for MRS D_-' and lower rates for GRVDIS. For energies below about 1 PeV the differences are generally within about 5% and again are dominated by the statistical fluctuations in the high energy sample.

In the bottom plots of Figure 5.2 we show the ratio of final event rates weighted by both the interaction cross-section and the probability of absorption in the Earth (which in turn

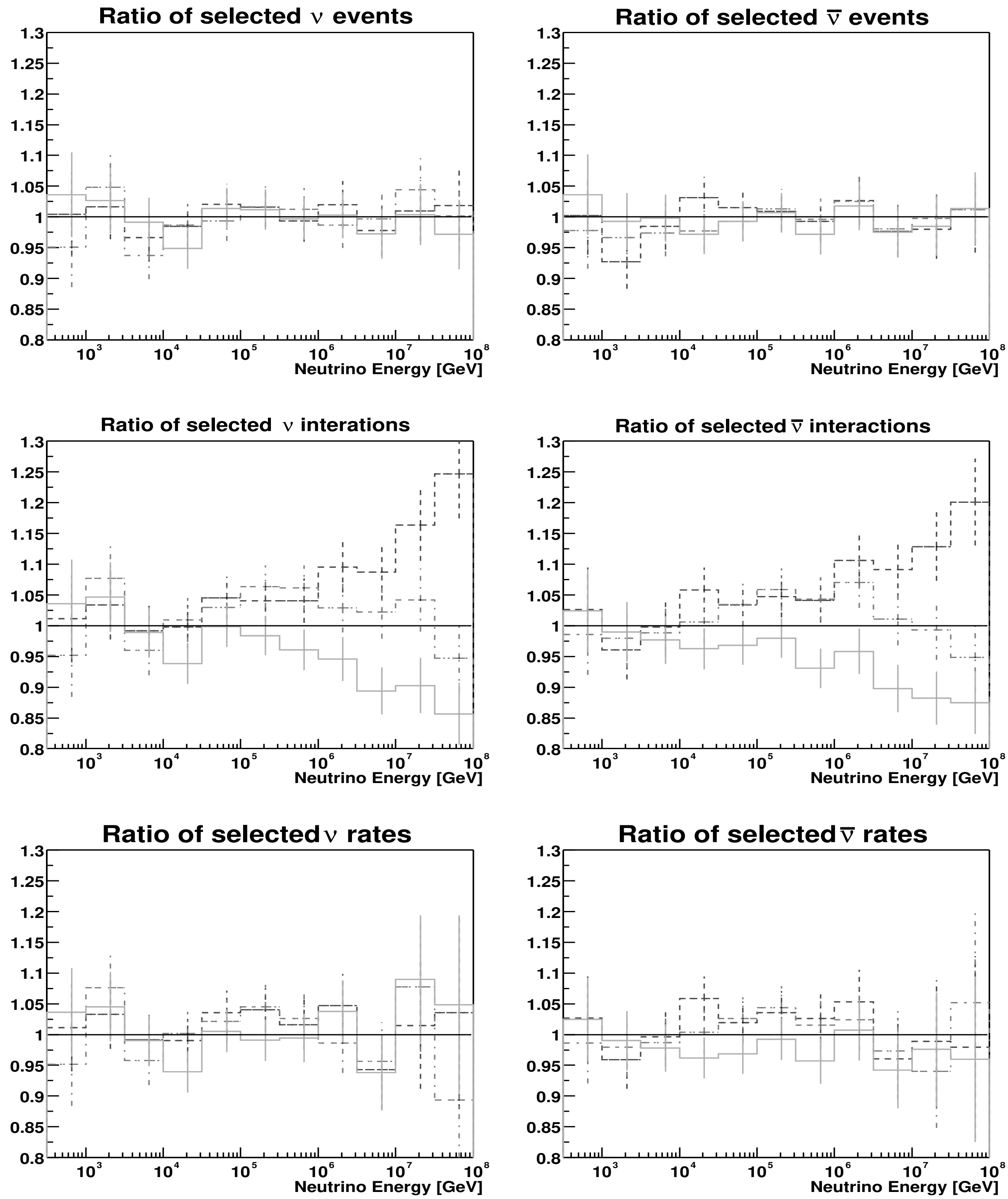

Figure 5.2: Ratio of selected events with different PDFs with respect to CTEQ3D. The top plots show the ratio of selected events (comparing different interaction kinematics). The middle plots show the ratio of events weighted by the cross-section (comparing different interaction rates). The bottom plots show the ratio of final event rates including the cross-section and Earth absorption. The dashed line is MRS D_′, the dash-dot line is CTEQ5D and the grey dotted line is GRVDIS.

depends on the cross-section and the neutrino zenith angle). Here we are averaging over an isotropic neutrino distribution corresponding to a diffuse flux of neutrinos. We can see that the difference between the PDFs is much smaller than would naively be expected from the cross-sections shown in Figure 3.4. As the cross-section increases, the interaction rate at the detector increases but so does the probability of absorption in the Earth. These two effects do, to some extent, cancel out and reduce the differences between different PDFs in the energy range studied here to the level where the differences are consistent with the statistical fluctuations in the sample.

Based on the results in Figure 5.2, we can see that the systematic uncertainty arising from the choice of PDF in the event generation is generally less than 5% for neutrino energies below 1 PeV. Furthermore, our reference choice of CTEQ3D is in the centre of the range of PDFs studied. These systematic errors can therefore be neglected. Above 1 PeV, the differences in the cross-sections increase and more care must be taken over the systematic errors. Averaging over an isotropic neutrino distribution means the change in interaction rate near the detector is cancelled to some extent by the changed absorption in the earth giving systematic errors again less than 5%. In Section 5.4, we calculate the detector performance averaging over an isotropic flux so we can neglect this systematic error for all neutrino energies in this case. Only in the unlikely case of specific point sources from which neutrinos mainly above 1 PeV are detected is this systematic error likely to exceed 5%.

As a final point to this discussion, we have tried to estimate the systematic uncertainty on the predicted event rate arising from uncertainties in the neutrino cross-section and event kinematics. There are two sources of uncertainty: those from different models used to extract the PDFs and those from uncertainties in the fits to each model. Here we have concentrated on the first kind and, as we saw in Section 3.2.3, the extreme models here can be distinguished from the data (MRS D_-' slightly overestimates existing data). Therefore, the range of cross-sections considered here should be larger than that due to the second kind of uncertainty and hence provide a good estimate of the systematic error.

5.2.3 Muon propagation code

As discussed in Section 3.3.1, two different muon propagation codes are available in the ANTARES event generation. The first, PropMu, has been shown to have inaccuracies in the calculation of the muon energy loss of order 20% in the energy range 20 GeV to 10 TeV (which is the most interesting for the majority of neutrino interactions observed in ANTARES). It does, however, include the multiple scattering of the muon between the neutrino interaction vertex and the can. The second, MUM, is numerically accurate to better than uncertainty on the theoretical inputs (i.e. a few percent) but does not include the muon multiple scattering in its simulation of muon propagation[4].

We saw in Figure 3.16, page 87, that the angular deviation with respect to the neutrino direction caused by multiple scattering can be a large as 20% (for neutrino energies close

[4]These muon codes are only used in the event generation stage of the simulation and therefore only affect the muon fluxes observed at the detector. The detector Monte Carlo uses a different and much slower code for muon propagation within the can, MUSIC, which is both accurate and includes multiple scattering.

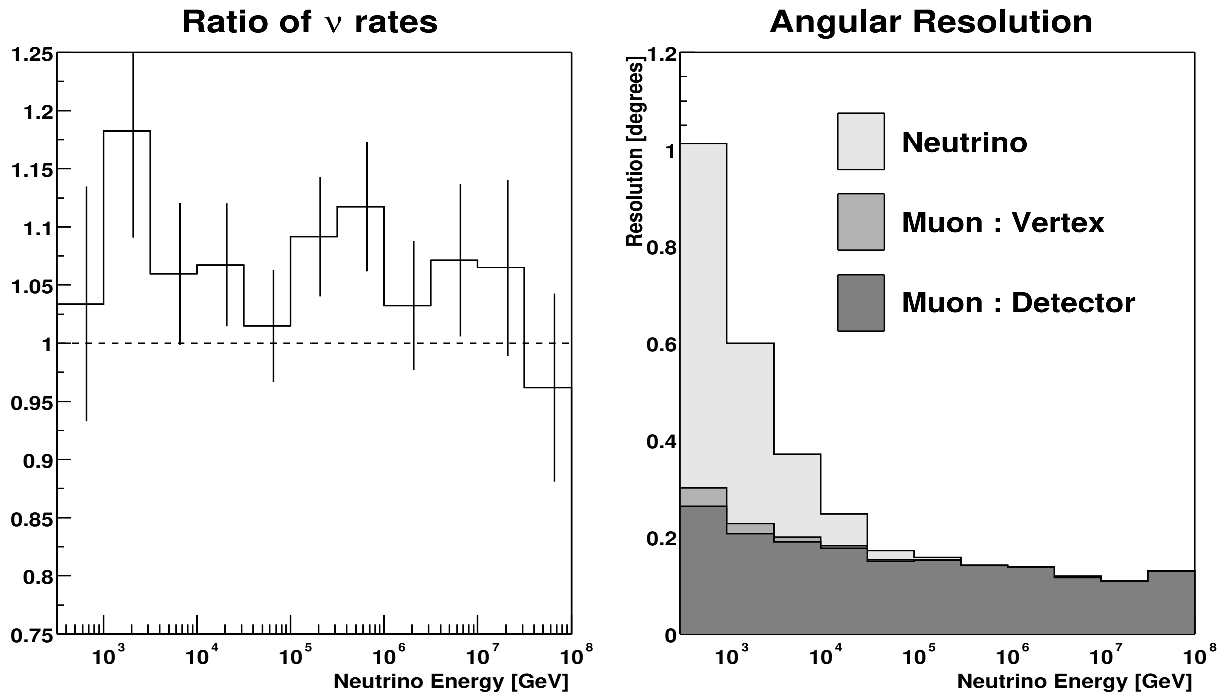

Figure 5.3: Ratio of neutrino event rates for PropMu compared to MUM showing an overestimation of the event rate of order 10% when using PropMu. The right hand plots show the angular resolution for the reconstructed track with respect to the muon entering the detector, the muon at the interaction vertex and the initial neutrino.

to 1 TeV) of the total difference between the neutrino and the muon in the detector. This difference will be less significant after a full detector simulation and muon reconstruction.

In Figure 5.3, the left hand plot shows the ratio of selected events as a function of muon energy for PropMu divided by MUM. On average, there are between 5% and 10% more events in each neutrino energy bin when using PropMu compared to MUM (in Figure A.3, page 188, we can see PropMu gives longer effective muon ranges and therefore, for a given neutrino energy, will give more muons arriving at the detector and with higher energies). If we used PropMu instead of MUM in calculating the event rate, we would overestimate the number of events by up to 10%.

The right hand plot in Figure 5.3 shows the angular resolution with respect to the muon as it enters the detector, the muon at the interaction vertex and with respect to the initial neutrino. We can see that at high energies, we are clearly dominated by the quality of the reconstruction itself at between 0.1° and 0.2°. At low energies, the angle between the neutrino and muon at the interaction vertex becomes the dominant contribution. For the range of neutrino energies between 300 GeV and 10 TeV, we can see the separate contribution of the muon multiple scattering. At most, this gives a 5% contribution to the total neutrino angular resolution for neutrino energies around 1 TeV. Below 300 GeV, the neutrino-muon angle is by far the most significant contribution to the angular resolution.

The contribution of multiple scattering is always less than 5% and is only important at this level for neutrino energies around 1 TeV. It can therefore be neglected in the simulations of muon propagation without affecting the results. The effect of the inaccuracies in PropMu is larger (up to 10%) and is important over the whole range of neutrino energies simulated. Given the two simulation codes available in the event generation, we therefore choose MUM[5] for future studies and neglect muon multiple scattering.

5.2.4 Neutrino flux models

As discussed in Section 3.4.2, there are several different models for the atmospheric neutrino flux. We divided the total flux into two components, conventional (from the decay of pions and kaons) and prompt (from the decay of charmed mesons), and described a range of models for each. For low energy studies such as the Dark Matter analysis described in Chapter 6, the uncertainties in conventional fluxes are most relevant. At high energies, such as searches for diffuse astrophysical sources where a large fraction of the low energy atmospheric neutrino background is removed by cutting on the reconstructed energy, the variation in the prompt neutrino fluxes dominates.

In the left hand plot of Figure 5.4 we show the atmospheric neutrino ($\nu + \overline{\nu}$) rate for neutrino energies up to 100 TeV with the Honda, Bartol and Fluka atmospheric neutrino fluxes. The Fluka calculation is only valid up to 100 GeV. Above this, the Honda model is used, hence the close agreement between the two. The difference between the overall event rates itself is small at the level of $\sim$ 7%. This is a comparable level to several of the other uncertainties in the simulation and analysis (see Chapter 3, Section 5.3 and the rest of this section). However, when looking for effects in the distortion of the atmospheric neutrino energy distribution (in the oscillation analysis for example), such a difference may be significant and the inclusion of a full range of neutrino flux models in the event weights is critical.

The right hand plot of Figure 5.4 shows the range of the prompt neutrino contributions to the total rate for neutrino energies up to 100 PeV. The lowest value is that calculated with no prompt neutrinos. The largest value is generally the highest prediction from the RQPM model (see Section 3.4.2) with the other models lying somewhere in the shaded range. With the highest prompt neutrino flux, the event rate is increased by around 60 events per year compared to the rate with just the conventional flux.

The neutrino ($\nu_\mu + \overline{\nu}_\mu$) event rate corresponding to the diffuse flux limit in Eq. (1.10) is also shown. A full analysis of diffuse neutrino fluxes and potential limits which could be set is a subject in itself and depends on many factors including the reconstruction of the muon energy which is not discussed here. However, it is clear that the sensitivity of ANTARES to such a diffuse flux above the atmospheric neutrino background is strongly dependent on the prompt neutrino flux and that this would be a dominant source of uncertainty in such an analysis.

[5] MUM is also still being developed and extensively tested and is a better structured and documented code making it easier to work with.

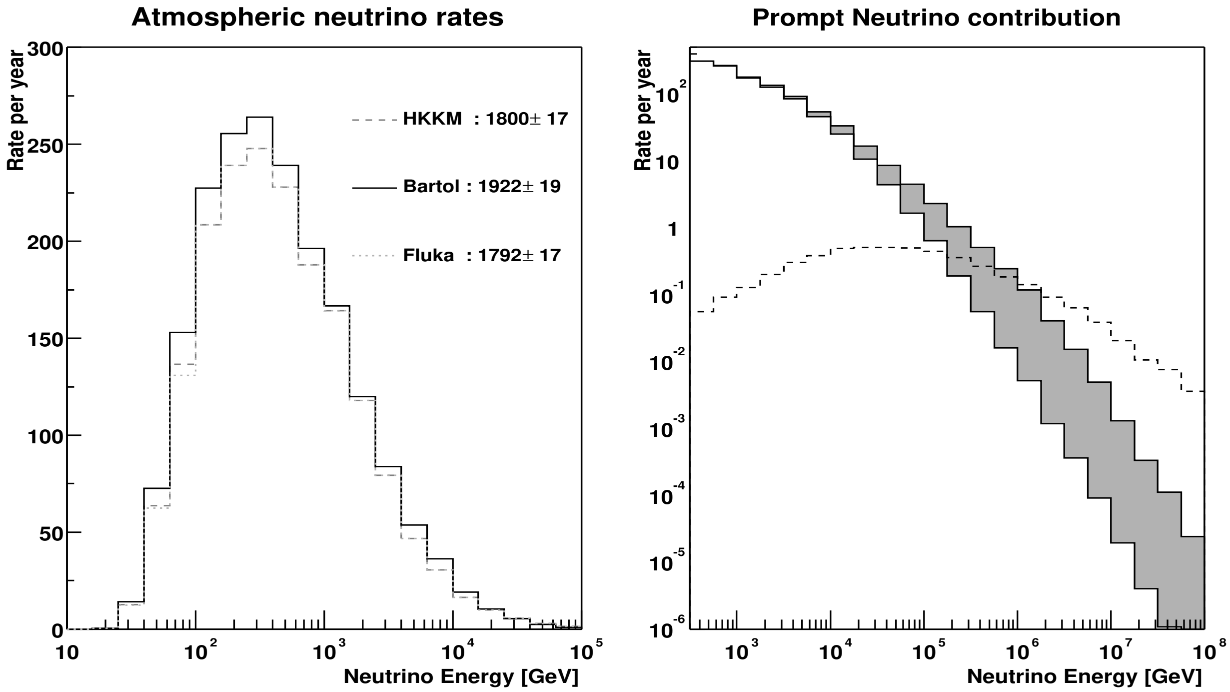

Figure 5.4: The rate of atmospheric neutrinos for different conventional fluxes (left) and prompt fluxes (right). The event rate per year for the conventional fluxes is shown in the left hand plot. The right hand plot shows the range of event rates between the extreme models for the prompt neutrino contribution. The dashed curve shows the rate assuming ν_μ and $\overline{\nu}_\mu$ fluxes at the diffuse flux limit given by Eq. (1.10).

5.2.5 Summary of systematic effects from the event generation

In this section we have investigated the effect of the hadronic shower and the choice of Parton Distribution Function on the rate of selected events in ANTARES. We have also investigated the effect of muon multiple scattering on the neutrino angular resolution for different neutrino energies. Finally, we considered different models of both conventional and prompt atmospheric neutrino fluxes on the overall event rate. We can summarise the conclusions drawn from these simulations as follows:

- The hadronic shower has a significant (up to 40%) effect on the event rate for neutrino energies up to 10 TeV and should not be neglected. In our final analyses in Section 5.4 and Chapter 6, we shall include this effect for neutrino energies up to 100 TeV.

- The range of PDFs considered gives smaller differences compared to our reference choice of CTEQ3D than would be expected from just the effect of the neutrino cross-sections on the interaction rate near the detector. This is due to the increased absorption of neutrinos in the Earth which compensates for the increased neutrino interaction rate near the detector as the cross-section increases. Our reference choice of PDF, CTEQ3D is fairly central in the range of considered models and the spread of event rates once all effects are taken into account is generally less than 5%. We therefore keep this as our reference model for future studies.

- The error introduced by using (the inaccurate) PropMu in the event generation is between 5% and 10% for a wide range of neutrino energies. The underestimation of the angular resolution by neglecting muon multiple scattering is at most 5% of the total neutrino angular resolution for neutrinos around 1 TeV and generally much smaller at other energies.
- The different atmospheric neutrino flux models give a difference in the total event rate of around 7%. Where this is important in setting limits in Chapter 6, we shall use the largest of the predictions, the Bartol flux. The extremes of the prompt neutrino flux contribution give a range of values of about 3% for the event rate. This will only have an important impact if the low energy neutrino contribution is removed by some selection criteria (as would be the case for a diffuse flux or high energy analysis).

All the systematic effects above have either been accounted for in the simulations (in the case of the hadronic shower) or are each less than 5% over the energy range of interest for ANTARES. Once the hadronic shower is included, the remaining uncertainty is less than 8% as discussed in Section 3.5 and will be neglected in the presentation of results below in Section 5.4 and Chapter 6.

5.3 The effect of the water properties

In Section 4.2, a range of different scattering models spanning some of the potential parameter space (see Table 4.3, page 108) relevant to ANTARES were described. For each of the different scattering models we can calculate the numbers of events detected and the angular resolution (for the same initial HE event generation sample) as a function of neutrino energy to get an estimate of the dependence on each of the parameters compared to the reference model P2.

5.3.1 Event rates

In Figure 5.5 we show the ratio of the selected event rates for various water models compared to that for P2. For each case we sum the contribution of neutrinos and anti-neutrinos according to their relative cross-sections (i.e. we assume that our source has an equal flux of neutrinos and anti-neutrinos). Similar results are obtained for ν and $\overline{\nu}$ in any case as the only difference between the two is in the muon energy produced at the interaction vertex and this difference is small.

Before looking at the effect of each of the individual parameters of the water models, we first consider the model which does not include any photon scattering, shown by the dashed curve in the central figure of Figure 5.5. The largest effect is seen at low energies where 60% more events are seen compared to P2. Even at high energies, the difference of 20% is still

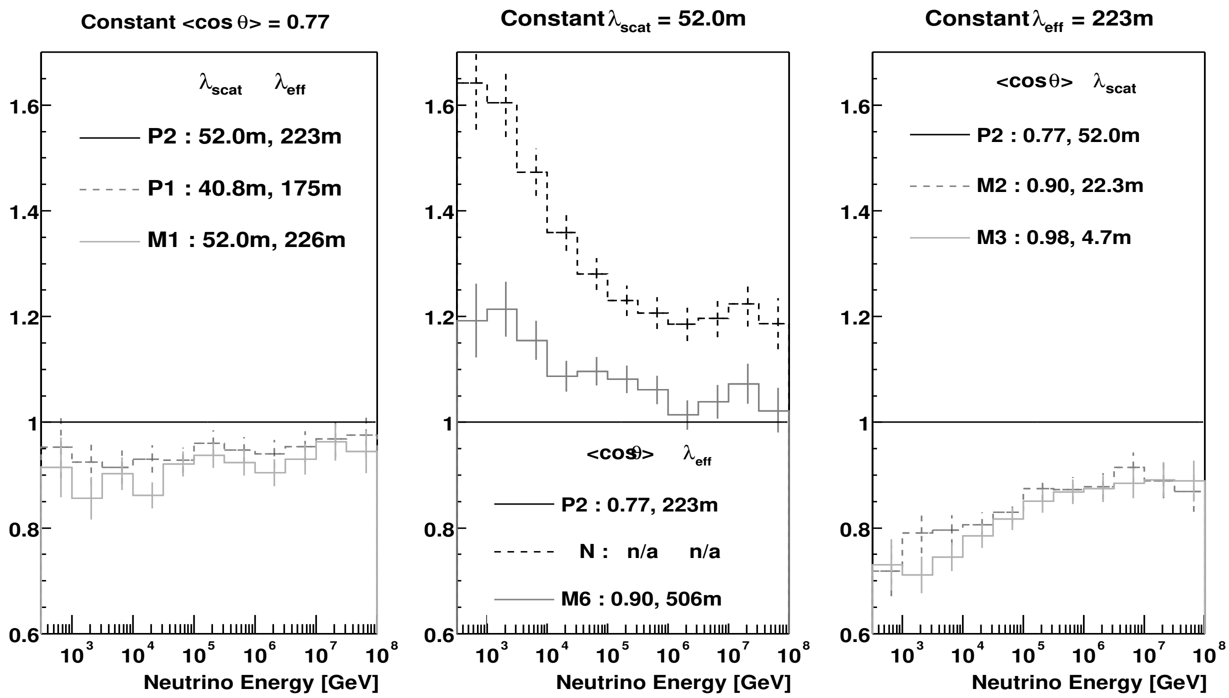

Figure 5.5: Relative event rates for different waters models with respect to the favoured model P2 holding one parameter constant in each case.

significant. Therefore, the inclusion of scattering in the simulation of the Cherenkov light produced by high energy muons is essential for all physics studies in ANTARES[6].

Constant $\langle\cos\theta\rangle = 0.77$

The left hand plot in Figure 5.5 shows models where the overall $\langle\cos\theta\rangle$ is fixed at 0.77 and the scattering length is varied from 52.0m (P2) to 40.8m (P1) or where the form of the angular distribution is varied (M1 - as shown in Figure 4.7, page 109).

A shorter scattering length (for the same angular distribution) will mean that fewer photons reach the PMTs without being scattering and hence the number of photons close to zero arrival time delay will be reduced. We would therefore expect a shorter scattering length to lead to a reduced rate of reconstructed events. From the results in Figure 5.5, we can see that reducing the scattering length by around 10 m (20% of the total) causes the event rate to be reduced by between 5 and 10%.

If we change the shape of the angular distribution to give a less forward-peaked particle scattering contribution and no Rayleigh scattering (M1 compared to P2), there are two competing effects on the overall event rate: fewer photons will scatter through large angles

[6]Up until this study, it was believed within ANTARES that it was possible to neglect scattering for the low energy events.

and be completely lost in the background noise but those that do scatter will be delayed more. In Figure 5.5, we can see that the rate of events for M1 is around 10% less than that for P2. This suggests that it is only the direct and very forward-scattered photons which have a small enough time delay to be useful in the reconstruction.

Constant $\lambda_{scat} = 52.0m$

Aside from the model without scattering (N), the central plot in Figure 5.5 shows models where the value of λ_{scat} is fixed at 52.0 m and the $\langle\cos\theta\rangle$ is varied from 0.77 (P2) to 0.9 (M6). At high energies (above 10 TeV), the differences are below 10% with the more forward-peaked model having the higher event rate. At lower energies, the effect is larger with differences up to 20%. Again, this suggests that it is only the direct and very forward scattered photons which affect the reconstruction.

Constant $\lambda_{eff} = 223m$

The final plot in Figure 5.5 shows the ratios of event rates for models with the same effective scattering length (P2, M2 and M3). As discussed in Section 4.2, [139] asserted that models with the same λ_{eff} should be degenerate provided $\langle\cos\theta\rangle$ is "close enough" to 1. This assertion is only valid if photons are scattered many times before being detected (and hence for ANTARES, the scattering lengths are much shorter than the dimensions of the detector).

We can see from the final plot of Figure 5.5 that the models M2 ($\lambda_{scat} = 22.3$ m, $\langle\cos\theta\rangle = 0.90$) and M3 ($\lambda_{scat} = 4.7$ m, $\langle\cos\theta\rangle = 0.98$) are approximately equivalent, suggesting that $\langle\cos\theta\rangle > 0.9$ ensures that λ_{eff} is sufficient to specify the model. However, compared to P2, there is approximately a 20% difference with fewer events for shorter scattering lengths indicating that the degeneracy in λ_{eff} does not apply for $\langle\cos\theta\rangle = 0.77$.

5.3.2 Angular resolution

In Figure 5.6 we show the angular resolution for neutrinos energies of ~ 1 TeV (300 GeV to 3 TeV) and ~ 100 TeV (30 TeV to 300 TeV) as a function of the three parameters of the water models discussed previously. The dashed lines in each case show the range of angular resolution (within the statistical errors) for the water model without scattering.

The general dependence on each of the parameters for the set of water models studied is similar at 1 TeV and 100 TeV, though the angular resolution itself is larger at 1 TeV as it is dominated by the angle between the neutrino and the muon at the neutrino interaction vertex (see the final presentation of the angular resolution in Figure 5.11, page 153). The effect of the water properties is more significant at higher energies where the quality of the reconstruction dominates the angular resolution and we shall therefore concentrate on the high energy results in the following discussion.

If we consider the models with a scattering length longer than 40 m (P1,P2,M1,M4,M6), the angular resolutions at 100 TeV range from 0.22° to 0.25° including the statistical errors (a

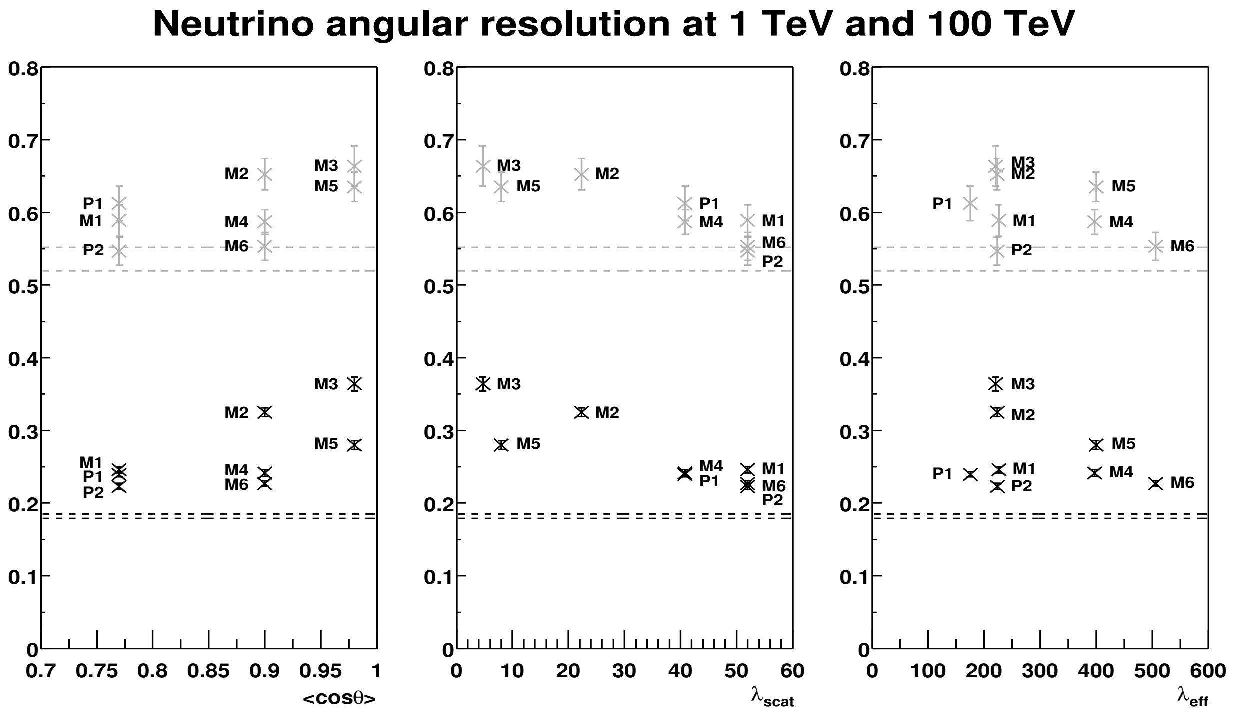

Figure 5.6: Neutrino angular resolution as a function of $\langle\cos\theta\rangle$, λ_{scat} and λ_{eff} for 1 TeV (top) and 100 TeV (bottom) neutrinos. The horizontal lines show the angular resolution (within the statistical errors) for the water model with no scattering. The parameters for each of the models are given in Table 4.3, page 108 and shown in Figure 4.7, page 109.

spread of 7% about the central value). These models have $\langle\cos\theta\rangle = 0.77$ and $\langle\cos\theta\rangle = 0.90$ suggesting that there is no strong dependence on $\langle\cos\theta\rangle$ in this range.

The other models, all with scattering lengths shorter than 25 m (M2,M3,M5) have significantly higher angular resolutions, even compared to models with the same $\langle\cos\theta\rangle$ (M2 compared to M4 and M6). As with the relative rates of events above, this suggests that the important parameter is the scattering length as, once a photon is scattered through anything other than a very forward angle, its time delay is too large to be useful in reconstructing the track parameters. This is confirmed by the central plot in Figure 5.6 which shows a reasonable strong correlation of the angular resolution with the scattering length.

5.3.3 Summary and conclusions

From the sections above, we have seen the effect of adjusting the scattering lengths and $\langle\cos\theta\rangle$ of the scattering angular distribution with respect to our reference model P2. Using these results, we can make the following very general statements:

- Scattering should not be neglected in any of the simulations of muons where we are trying to measure accurately the muon direction.

- A 20% change in the overall scattering length from 52 m to 40 m reduces the event rate by between 5 and 10% at all neutrino energies.

- Modifying the angular distribution while keeping $\langle \cos\theta \rangle$ constant can change the event rate by around 10%.

- The angular resolution is most strongly correlated to to overall scattering length.

- The effective scattering length proposed by [139] is not sufficient to describe the water properties at the ANTARES site.

We can qualitatively explain the differences with the hypothesis that it is the amount of light at or very close to zero time delay (with respect to direct Cherenkov light) which is important in the reconstruction. This light corresponds to direct Cherenkov light and just the very forward-peaked part of the scattering angular distribution.

The current uncertainty in the water properties at the ANTARES site discussed in Section 4.2.2, page 108, mean it is not yet possible to draw quantitative conclusions about the ANTARES detector performance from these results. The very recent measurement by Schuster at 374 nm [98] of a much less forward-peaked angular distribution than had previously been assumed would certainly affect the results if the same is true close to 460 nm (where ANTARES is most sensitive). This can be seen in the comparison of P2 and M1. Schuster also finds very different scattering lengths to those of Palanque-Delabrouille [97] on whose results this study was based. Given the correlation of the scattering length to the angular resolution (central plot in Figure 5.6) and the effect on the number of events detected (P1 compared to P2), this will also introduce a significant uncertainty on calculations of the detector performance.

From the above we can see that the water properties have a significant effect on both the number of events which ANTARES will detector and the angular resolution with which they can be reconstructed. With the current measurements, the systematic error due to the water properties cannot easily be estimated but it is clearly larger than any of the effects discussed in Section 3.2 or Section 5.2. This situation will not be improved until there is an accurate measurement of both the angular distribution and the scattering lengths at the ANTARES site.

5.4 ANTARES Detector performance

The previous two sections have been concerned with evaluating relative effects (i.e. ratios of event rates for different neutrino energies or changes in the angular resolution) resulting from particular choices made at the event generation or detector Monte Carlo stages of the simulation. Whilst this adds to our understanding of the important parameters for ANTARES, in isolation these results do not allow us to make quantitative predictions concerning the efficiency of the ANTARES detector for individual types of neutrino source.

In this section we take the reconstruction and selection discussed in Section 5.1 and apply it to the "high energy" production described in Section 5.2. We describe several methods of presenting the performance of ANTARES in a way which is independent of any neutrino flux model using the outputs of these simulations. These results can then be used in further analyses or for comparison with other experiments.

The emphasis of this section is mainly on describing calculational methods which can be used as intermediate stages in a full analysis of some class of neutrino sources. However, the quantities obtained by these methods are conventionally used to summarise the detector performance and at the end of this section we shall present the overall detector performance using some of the methods described here.

Effective Volumes The volume of a 100% efficient detector for observing neutrinos that interact within that volume which would obtain the same event rate as ANTARES for a given neutrino interaction rate (depending on the flux, target medium and interaction cross-section).

Effective Areas for Neutrinos The area of a 100% efficient surface for detecting through-going neutrinos which would observe the same event rate as ANTARES for a given neutrino flux.

Effective Areas for Muons The area of a 100% efficient flat surface for detecting through-going muons which would observe the same event rate as the ANTARES detector for a given muon flux (through a flat surface at the centre of the ANTARES detector).

Though the methods described in this section are general, their application is mainly concerned with high energy neutrinos typical of astrophysical sources and the results presented here reflect this. In Section 5.4.3 we present the effective area for neutrinos which can be used as a calculational tool for investigating sets of neutrino flux models and present some sensitivities to different power law neutrino fluxes. In Section 5.4.4 we present an effective area for muons as a function of neutrino energy which is then used to calculate the effective area for an E_ν^{-2} spectrum which is a figure of merit to compare with other experiments. Finally, in Section 5.4.5 we present the angular resolution at high energies, critical for the identification of astrophysical point sources.

5.4.1 Choice of simulation parameters

From the studies of various systematic effects above, we have concluded the following points about simulation requirements for high energy neutrinos:

- The inclusion of the Cherenkov light produced by the hadronic shower is essential for neutrino energies up to 10 TeV. Conservatively, we include it for energies up to 100 TeV for these final simulations.

- The choice of Parton Distribution Function affects the overall event rates (once the effect of the absorption in the Earth is included) at less than the 5% level (below 1 PeV or for a isotropic flux above this energy). Our reference choice of CTEQ3D is representative of the set of models studies and we continue using it as our reference choice for these simulations.
- Our best choice of muon propagation code in the generation stage is MUM (based on the careful studies in [114]) and we use that for the simulations here. The effect on the angular resolution of neglecting the muon multiple scattering is only important around 1 TeV at a level of less than 5% (and is much smaller at other energies). We therefore neglect this effect for this analysis.
- We use the water model (P2) discussed in Section 4.2.2. The uncertainty in the water properties at wavelengths most relevant for Cherenkov light detection in ANTARES mean that the systematic effects of this choice cannot be evaluated without further measurements at these wavelengths.

5.4.2 Presentation of effective areas and effective volumes

As we will see below, different methods of presenting the detector efficiency are suitable for different neutrino and muon energy ranges. It is important to choose the correct method of presentation to give results which are comparable with other experiments and can be used sensibly to calculate event rates.

As seen in Figure 3.13, page 84, the relative numbers of events which arrive as muons on the surface of the detector or are seen as neutrino interactions within the instrumented volume depends on both the neutrino spectrum and the observed muon energy. It does not necessarily make sense to talk about a sensitivity to a muon flux (i.e. an effective area for muons) when the majority of observed events interact within the instrumented volume. However, we can use the effective muon range, as defined in Section 3.3.3, to convert effective volumes to effective areas to give a universally applicable presentation of the effective area which is the overall aim of this section.

Effective volumes

Our starting point for these calculations is the effective volume of the detector as defined above which includes the efficiency of the reconstruction and the selection described previously. The aim is to calculate a quantity which, when multiplied by a neutrino interaction rate per unit volume, gives an event rate. Therefore, we take the distribution of selected events (binned in neutrino energy and zenith angle in this case) and divide by the number of events per unit volume that we generated (recalling that our generation volume was defined to be large enough to contain all potentially visible neutrino interactions by using the maximum muon range).

In Section 3.4 we described the generation of events with a power law index, $-X$, for the energy of the interacting neutrinos and with an isotropic angular distribution. Therefore, the number of generated events, $N_{generated}$, in some energy bin E_1 to E_2 and angular bin $\cos\theta_1$ to $\cos\theta_2$ is just:

$$N_{generated}(E_1 < E_\nu < E_2, \cos\theta_1 < \cos\theta_\nu < \cos\theta_2) = \frac{\cos\theta_2 - \cos\theta_1}{\cos\theta_{max} - \cos\theta_{min}} \times \frac{\int_{E_1}^{E_2} E^{-X} dE}{\int_{E_{min}}^{E_{max}} E^{-X} dE} \times N_{total} \quad (5.1)$$

where E_{min} and E_{max} are the minimum and maximum neutrino energies in the event generation, $\cos\theta_{min}$ and $\cos\theta_{max}$ are the smallest and largest values of $\cos\theta_\nu$ in the event generation and N_{total} is just the total number of simulated neutrino interactions. Note that we can not obtain this from the output of the event generation as only those events which reach the can are written to the output file.

The generation volume, $V_{generation}$, is identical for all neutrino energies and zenith angles and is calculated as part of the event generation (in water equivalent units). Therefore, the generated number of neutrino interactions per unit volume is $N_{generation}$ divided by $V_{generation}$ (in water equivalent units). We can then divide the number of selected events (in the same energy and angular bins) by this quantity to obtain the effective volume:

$$V_{eff}(E_\nu, \theta_\nu) = \frac{N_{selected}(E_\nu, \theta_\nu)}{N_{generated}(E_\nu, \theta_\nu)} \times V_{generation} \quad (5.2)$$

As in the calculation of the number of generated events above, E_ν refers to neutrino energies in the range $E_1 < E_\nu < E_2$ (and similarly for the range in θ_ν). Given this effective volume, we could take a neutrino flux, ϕ_ν, for a given theoretical model and calculate the neutrino interaction rate per unit volume based on some parameterisation of the neutrino interaction cross-section, σ, and using the knowledge that the target density, ρ, is 1000 kg m^{-3} in water equivalent units (and using Avogadro's number, N_A) as follows:

$$N_{observed} = \int V_{eff}(E_\nu, \theta_\nu)(\rho N_A)\sigma(E_\nu)\frac{d\Phi_\nu}{dE_\nu d\theta_\nu} dE_\nu d\theta_\nu \quad (5.3)$$

However, we have the information on the neutrino cross-sections available in the event generation so it makes more sense to include this in the expression of the detector efficiency.

Neutrino effective areas

From Eq. (5.3) above, it is clear that we can combine the effective volume with the target nucleon density, (ρN_A), and the energy dependent neutrino cross-section, $\sigma(E_\nu)$, to produce a quantity which, when multiplied by a differential neutrino flux and integrated gives a rate of observed events. This quantity is an effective area corresponding to neutrino fluxes (arriving at the detector):

$$A_{eff}^{\nu\,\text{(detector)}} = V_{eff} \times (\rho N_A) \times \sigma(E_\nu) \quad (5.4)$$

One additional complication is the absorption of neutrinos in the Earth as described in Section 3.4.2. In Eq. (3.15), page 78, we defined the probability of transmission through the Earth, P_{Earth}, in terms of the neutrino cross-section and the line integrated column density corresponding to a particular neutrino zenith angle. Multiplying the above effective area by $P_{Earth}(E_\nu, \theta_\nu)$ will then give us an effective area for neutrinos arriving at the (opposite) surface of the Earth:

$$A^{\nu}_{eff}(E_\nu, \theta_\nu) = V_{eff}(E_\nu, \theta_\nu) \times (\rho N_A) \times \sigma(E_\nu) \times P_{Earth}(E_\nu, \theta_\nu) \tag{5.5}$$

As we will see in Section 5.4.3, this quantity is mainly useful as a calculational tool for quickly calculating the event rate for different neutrino flux models. We shall apply this method again in Chapter 6 in the prediction of the sensitivity of ANTARES to the indirect detection of Dark Matter.

Previous ANTARES definition of effective area

Historically in ANTARES, the performance of the detector has been expressed as a surface effective area as a function of the muon energy. In the following section we shall argue that this presentation does not apply when considering medium and low energies and provide an alternative unified calculation. However, for reference, we will define the surface effective area and we will then compare it with our proposed calculation in Section 5.4.4.

The cylindrical can presents an area which depends on the zenith angle, θ:

$$A_{can}(\theta) = 2rh\sin\theta + \pi r^2 \cos\theta \tag{5.6}$$

where r is the radius of the can and h is the height of the can. If we have a number of muons arriving on the surface of the can, $N_{generated}$, with an energy, E_μ, and a zenith angle, θ_μ, the effective area is then defined by dividing the number of selected events by the incident muon flux:

$$A^{surface}_{eff}(E_\mu, \theta_\mu) = \frac{N_{selected}(E_\mu, \theta_\mu)}{N_{generated}(E_\mu, \theta_\mu)} \times A_{can}(\theta_\mu) \tag{5.7}$$

Note that there is an implicit assumption in this that all the muons at a given energy E_μ are incident on the surface of the can and that none are produced within it. We have seen in Figure 3.13, page 84, that the extent to which this is true depends on both the muon energy and the original neutrino flux. Furthermore, it will also depend on the size of the can chosen to define the volume for the full detector Monte Carlo simulation. Whilst there is a range of muon energies for which this assumption is valid (e.g. between 1 TeV and 1 PeV for an E_ν^{-2} neutrino spectrum as shown in Figure 3.13, page 84), it is not universally applicable.

Muon effective areas

In this section, we will derive an effective area expressing our sensitivity to a muon flux which is applicable over the full range of neutrino energies in ANTARES. The starting point for this calculation is the relationship connecting a neutrino flux, ϕ_ν, to the muon flux, ϕ_μ, it produces deep underground or underwater [44]:

$$\phi_\mu(E_\mu^{min},\Theta) = \int_{E_\mu^{min}}^{\infty} P_\nu(E_\nu, E_\mu^{min}) P_{Earth}(E_\nu,\Theta)\, \frac{d\phi_\nu}{dE_\nu}(E_\nu,\Theta) dE_\nu \tag{5.8}$$

where:

- $\phi_\mu(E_\mu^{min},\Theta)$ is the integral muon flux above some energy threshold E_μ^{min} from a particular direction given by Θ.
- $P_\nu(E_\nu, E_\mu^{min})$ is the probability that a neutrino of energy E_ν on a trajectory through a detector produces a muon above an energy threshold, E_μ^{min}, at the detector.
- $P_{Earth}(E_\nu,\Theta)$ is the probability of neutrino transmission through the Earth in a particular direction.

The product of the differential neutrino flux at the surface of the earth and the probability of transmission through the Earth give the neutrino flux at the detector. The first item, $P_\nu(E_\nu, E_\mu^{min})$, depends on the differential neutrino cross-section in the produced muon energies and the effective muon range, R_{eff} (as defined in Eq. (3.7), page 70, and with a full calculation described in Appendix A):

$$P_\nu(E_\nu, E_\mu^{min}) = (\rho N_A) \int_0^{E_\nu} \frac{d\sigma_\nu}{dE_\mu}(E_\mu, E_\nu) R_{eff}(E_\mu, E_\mu^{min})\, dE_\mu \tag{5.9}$$

where $\frac{d\sigma_\nu}{dE_\mu}(E_\mu, E_\nu)$ is the differential cross-section for a neutrino of energy E_ν to produce a muon in the energy range E_μ to $E_\mu + dE_\mu$. This equation represents the probability of a neutrino interacting per unit distance ($\rho N_A \times \sigma$) multiplied by the distance, R_{eff}, over which it could have been produced and still be detected on a hypothetical flat surface at the ANTARES detector.

We want to define a method which will allow us to combine both surface and volume events in the overall efficiency whilst allowing us to express our sensitivity to a muon flux which is the preferred method of comparison between different experiments in this field. To do this, we need to derive a quantity which we can combine with a muon flux to get an event rate. Taking Eq. (5.8) and Eq. (5.9), we can calculate the differential flux of muons produced by a particular differential neutrino flux:

$$\frac{d\phi_\mu}{dE_\nu} = (\rho N_A) \frac{d\phi_\nu}{dE_\nu} \int_0^{E_\nu} \frac{d\sigma_\nu}{dE_\mu} R_{eff}(E_\mu) dE_\mu \tag{5.10}$$

For clarity, we have omitted the directional dependence and set the muon energy threshold to zero (as was the case in the maximum muon range calculations of Section 3.3.2). We also omit the probability of absorption in the Earth. This can be added to convert between neutrino fluxes at the surface of the Earth and the detector as required. Now, $\frac{d\sigma_\nu}{dE_\mu}$ is just the total neutrino cross-section for a neutrino of energy E_ν times the probability, $\frac{dP_\mu}{dE_\mu}$, of producing a muon in the interval dE_μ. We can then write the above equation as:

$$\frac{d\phi_\mu}{dE_\nu} = (\rho N_A)\sigma_\nu(E_\nu)\frac{d\phi_\nu}{dE_\nu}\int_0^{E_\nu}\frac{dP_\mu}{dE_\mu}R_{eff}(E_\mu)dE_\mu \tag{5.11}$$

The integral is then just the average effective muon range in the neutrino energy interval $E_\nu \to E_\nu + dE_\nu$ where the average is taken over the muons produced at the neutrino interaction vertices. Returning to Eq. (5.3), we can replace the differential neutrino flux by the differential muon flux:

$$N_{observed} = \int \frac{V_{eff}(E_\nu)}{\langle R_{eff}(E_\nu)\rangle}\frac{d\phi_\mu}{dE_\nu}dE_\nu \tag{5.12}$$

where $\langle R_{eff}(E_\nu)\rangle$ is the average effective muon range. The first term in the integral is a quantity with dimensions of area which, when multiplied by a differential muon flux passing through a flat surface at the ANTARES detector and then integrated over neutrino energy, will give the same event rate as ANTARES (for the same original neutrino flux). It is, by definition, the effective area for muons:

$$A_{eff} = \frac{V_{eff}(E_\nu)}{\langle R_{eff}(E_\nu)\rangle} = \frac{N_{selected}(E_\nu)}{N_{generated}(E_\nu)} \times \frac{V_{generation}}{\langle R_{eff}(E_\nu)\rangle} \tag{5.13}$$

In Eq. (5.12), all the information on the detector sensitivity (to a neutrino interaction rate from a particular neutrino flux) is contained within the effective volume. The above calculation then converts the neutrino flux in Eq. (5.3) to the muon flux it would produce on a flat surface at the ANTARES detector. The effective area in Eq. (5.13) can then be considered as the area of an equivalent "flat" detector at the ANTARES site which would observe the same number of events.

Note that despite being an effective area with respect to a muon flux, the above is expressed as a function of neutrino energy. Whilst the quantity $\frac{d\phi_\mu}{dE_\nu}$ is well defined (it is the total flux of muons produced by neutrinos with energies in the range $E_\nu \to E_\nu + dE_\nu$), it is not the most obvious way of describing a differential muon flux. However, it is the most suitable for these calculations for the following reasons:

- As we are trying to describe the full energy range of ANTARES including neutrino energies where the event is completely contained within the instrumented volume, there is no single surface on which all the muons are incident and therefore no unique definition for the muon energy in the muon flux[7]. Therefore, we cannot express our effective area as a function of the muon energy in the detector.

[7]For any event, one could choose the muon energy at the interaction vertex, at the point of closest

- When using neutrino energies, calculating the efficiency from the number of selected events is relatively simple as the initial distribution is known from the inputs to the event generation and it is universal and independent of whether the events are surface or volume events in the actual output of the generator. To use the muon energy, one must use the surface and volume events separately and combine them with the appropriate normalisation. This is a non-trivial process and is discussed at some length in [152].

- Following the discussion in [44], the effective area is defined with respect to a specific neutrino spectrum and then multiplied by a total flux to give an event rate. The determination of an energy dependent effective area is an intermediate stage in the calculation. Here, we can simply calculate the differential muon flux above (using Eq. (5.11)) to reweight the energy dependent effective area to correspond to a particular neutrino flux. Expressing the effective areas this way gives the easiest path to the actual effective area (corresponding to the definition in [44]) for a total muon flux on a single surface.

Keeping these points in mind, in the next sections we shall calculate the effective areas for neutrinos and muons as a function of neutrino energy to express the efficiency of ANTARES in a manner which is suitable for use both in comparing different reconstruction methods, systematic effects, etc. and for calculating effective areas corresponding to a particular neutrino flux. We shall perform this second stage of the calculation for our reference E^{-2} neutrino flux.

5.4.3 Effective areas for neutrinos

Following the discussion above, we now present the effective area for neutrinos for ANTARES using the selection and reconstruction described in Section 5.1. Here, we present these effective areas to illustrate certain features of the ANTARES detector and then use them to make a rough estimatation of the sensitivity of ANTARES to known point sources with different power law spectra. The concept of neutrino effective areas is used again in Chapter 6 to calculate the detector efficiency with respect to Dark Matter annihilation.

Effective areas for ANTARES

In Figure 5.7, we plot the effective area for upward going neutrino fluxes arriving at the surface of the Earth (i.e. including the Earth absorption) for an isotropic flux (to show the average efficiency) and for neutrinos in the zenith angle ranges $0° \leq \theta \leq 30°$, $30° \leq \theta \leq 60°$ and $60° \leq \theta \leq 90°$ (to show the effect of the Earth absorption at different zenith angles).

approach to the centre or on crossing some arbitrary surface within the instrumented volume. Each of these would differ depending on the starting point of the muon and its starting energy. This choice cannot be made consistently for both surface and volume events. At high energies when the majority of observed muons interact outside the can, the muon energy can be uniquely defined as that at the can surface. This relies on the fact that the muon energy loss inside the can is small compared to its total energy.

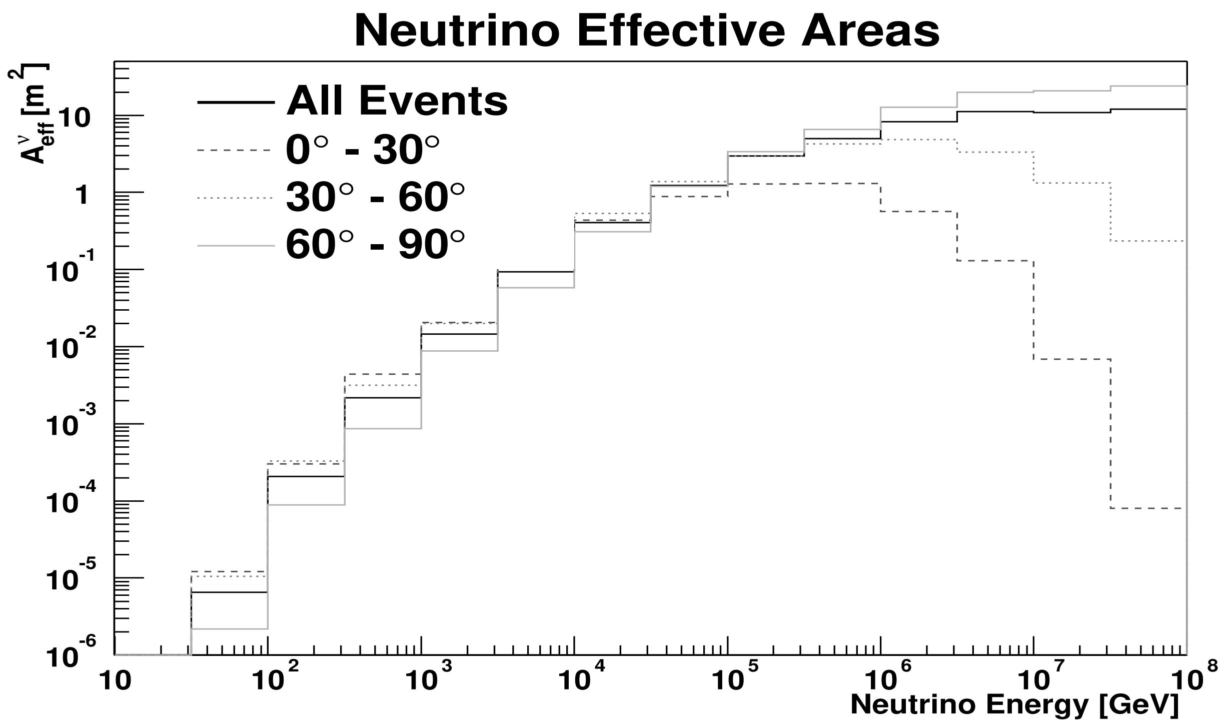

Figure 5.7: Effective areas for neutrinos fluxes at the surface of the Earth for an isotropic flux (solid line) and zenith angle ranges of $0° \leq \theta \leq 30°$, $30° \leq \theta \leq 60°$ and $60° \leq \theta \leq 90°$. Similar results are obtained for anti-neutrinos.

We can see from Figure 5.7 that the effective area for all upgoing neutrinos (the solid black histogram) increases steadily up to about 1 PeV. Above this energy, the curve becomes flatter as the increasing neutrino cross-section at the interaction vertex and the Earth absorption cancel out. This is the same effect seen in the discussion of the different PDFs in Section 5.2.2.

Looking at the three different ranges of zenith angles, at low energies we can see that the detector is relatively more efficient for neutrinos arriving closer to the vertical. At these angles, the detector volume is longer and therefore presents a greater length for observing muon tracks from neutrino interactions.

At higher energies, we would expect the reverse of this to be true where the larger surface area gives the higher efficiency (as more neutrinos interact outside the instrumented volume). This will be somewhat offset by still having a longer detector in the vertical direction to observe light from the muon track[8]. Before this reversal is complete, the effect of the Earth absorption begins to dominate. For near vertical ($0° \leq \theta \leq 30°$) neutrinos, the efficiency (for neutrinos arriving at the surface of the Earth and hence including the effect of the Earth absorption) is significantly reduced and above 1 PeV it decreases rapidly. For neutrinos in the zenith angle range $30° \leq \theta \leq 60°$, this only starts to become important above 1 PeV. At the very highest energies, virtually all of our efficiency is close to the horizontal.

[8]For the 10 string ANTARES detector used here, the transverse dimension is only of order 100 m and so it is still possible that a horizontal high energy muon will not be reliably reconstructed.

Sensitivity to power-law neutrino fluxes

We can use the effective areas for neutrinos calculated above to estimate the sensitivity of ANTARES to different power-law neutrino fluxes. A full analysis of this sensitivity is beyond the scope of this thesis as it requires a knowledge of specific source spectra and a full study and optimisation of the signal and background. However, we can gain an approximate understanding of the sensitivity of ANTARES to a known point source (but with an unknown neutrino energy spectrum) as follows:

- We (somewhat arbitrarily) look for neutrinos reconstructed with a direction within one degree of a known source position. As we shall see from the angular resolution in Section 5.4.5, this means at least half the neutrinos above 300 GeV from any source will be contained within the search cone. For the simulations performed here, this means we calculate the effective area for muon tracks reconstructed within one degree of the neutrino direction.

- Whilst a specific version of this analysis would have to be performed for a known point source, here we average over all zenith angles and therefore calculate the "typical" sensitivity of ANTARES. In this, we assume the source is below the horizon (and hence visible to ANTARES) for 50% of the year.

- We saw in Section 5.2.4 that, with this reconstruction and selection, ANTARES expects of order 1900 atmospheric neutrino events per year (neglecting any contamination from atmospheric muons which we stated was small compared to the atmospheric neutrino rate). In a 1° cone below the horizon for half the year, this gives a rate of background events per year in the search cone of:

  $$\Gamma_{background} = 1900 \times 0.5 \times (1 - \cos(1^\circ)) = 0.145 \text{ yr}^{-1} \tag{5.14}$$

  Note that, with this one degree cone, the rate of background events is small and there would therefore not be significant gains in sensitivity by using a smaller (i.e. optimised to maximise the significance of the signal over the background) cone around the known source direction.

- Using the method of Feldman and Cousins [153], we can estimate the sensitivity (defined as the average upper limit that would be obtained by an ensemble of experiments with the expected background and no true signal) to power-law neutrino fluxes with different spectral indices and different low energy cut-offs. We estimate the upper limit on the number of signal events by taking the results from Table XII of [153] corresponding to a detection at 99% CL. For the background rate from atmospheric neutrinos above, this will give upper limits of 4.9 events for one year and 1.7 events per year for three years of observation.

Now, we calculate the neutrino effective area as above with the additional restriction that the reconstructed track direction is within one degree of the neutrino direction (which will reduce the effective area slightly at lower energies). We can then reweight this effective area (in m^2) as a function of neutrino energy to different power-law differential neutrino fluxes with index X and with some low energy cut-off E_{min}:

$$\langle A^{\nu}_{eff} \rangle = \sum_i A^i_{eff} \times \frac{\int_{E^i_{min}}^{E^i_{max}} \Theta(E - E_{min}) E^{-X} dE}{\int_{E_{min}}^{E_{max}} E^{-X} dE} \text{ m}^2 \tag{5.15}$$

where the index, i, refers to the different energy bins in the effective area (as shown in Figure 5.7) and $\Theta(x)$ is 1 for $x \geq 0$ and 0 otherwise (i.e. a step function). This average effective area will therefore depend on both the spectral index and the low energy limit of the spectrum. For a differential neutrino flux of the form:

$$\frac{dN_\nu}{dE_\nu} = A \times E^{-X} \text{ GeV}^{-1}\text{cm}^{-2}\text{s}^{-1} \tag{5.16}$$

where A is a normalisation constant with units of GeV$^{\text{X}-1}$cm^{-2}s^{-1}, we can evaluate the upper limit on A (which is essentially the differential neutrino flux limit for a power law neutrino flux with index X) as:

$$\text{UL(A)} = \frac{2 \times \Gamma_{limit}}{\langle A^{\nu}_{eff} \rangle} \times \frac{1}{\int_{E_{min}}^{E_{max}} E^{-X} dE} \times \frac{1}{10^4 \times F_{syr}} \tag{5.17}$$

where Γ_{limit} is the upper limit on the number of signal events from above, the factor 2 is due to the fact we can only observe a source, on average, for 50% of the time and F_{syr} is the number of seconds in one year. The factor 10^4 is to convert from m^2 to cm^2.

In Figure 5.8, we show the sensitivity to power law neutrino fluxes. The left hand plot shows the sensitivity to an E_ν^{-2} neutrino flux which is cut-off at some neutrino energy[9]. Clearly, in the limit of such a flux extending to below the most sensitive energies of ANTARES, we would expect the sensitivity to the differential flux to remain constant which it does. The overall sensitivity of ANTARES to E_ν^{-2} neutrino fluxes is only affected by this cut-off if it is above 10 TeV (and this is generally true for a range of different power-law indices as discussed in Appendix B.4).

The sensitivity to an E_ν^{-2} neutrino flux can be compared to the Waxman-Bahcall limit in Eq. (1.10) which places a limit on the diffuse high energy flux with an E_ν^{-2} spectrum of $\sim 10^{-8}$ GeVcm^{-2}s^{-1}sr^{-1}. If we optimistically assume the actual flux is at this limit and it all comes from a known single point source (i.e. a single source produces the high energy cosmic ray spectrum above 10^{19} eV), this would give a point source flux (integrating the above over solid angle) of $\sim 10^{-7}$ GeVcm^{-2}s^{-1} which is at the limit of the ANTARES sensitivity, even with three years' observation.

The right hand plot in Figure 5.8 shows the upper limit a differential neutrino flux (which should be interpreted as the upper limit on the normalisation constant at 1 GeV - A from Eq. (5.16)) with a neutrino energy cut-off at 10 GeV. We can see from this that the sensitivity

[9]The rationale behind this cut-off is to account for models which are not a pure power-law and to give a quantitative evaluation of the sensitivity of ANTARES above different neutrino energy thresholds.

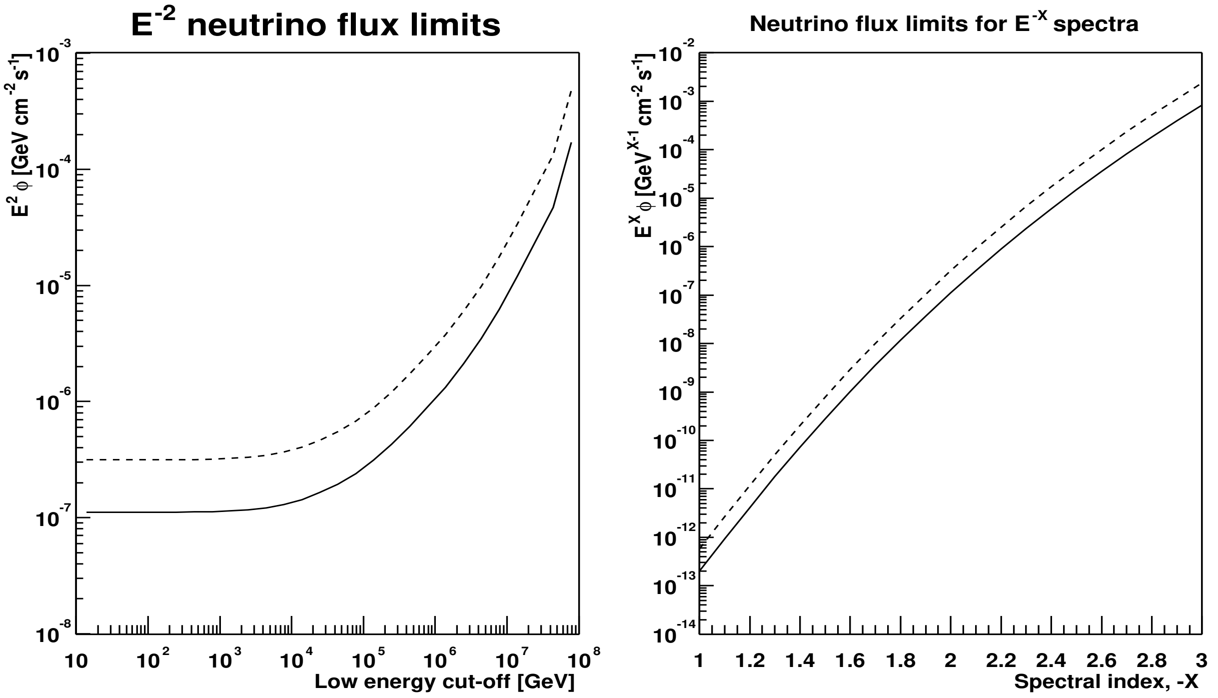

Figure 5.8: Differential neutrino flux limits in a search for a known point source. The left hand plot shows the sensitivity for a source producing an E_ν^{-2} flux of neutrinos with a varying lower energy limit on the neutrino energy. The right hand plot shows the sensitivity to a power-law neutrino flux with index -X (above 10 GeV) in terms of the normalisation constant at 1 GeV. In both cases, the dashed line represents the sensitivity after one year of observation, the solid line after three years.

is strongly dependent on the spectral index of the source (as expected given the strong energy dependence of the neutrino cross-section). Using the information contained in these plots, it should be possible to estimate the ANTARES sensitivity for a range of different neutrino flux models.

Summary

In the above, we have seen that we can express the efficiency of the ANTARES detector as an effective area for neutrinos. This includes all the effects of the neutrino cross-section, muon propagation and reconstruction efficiency and can be combined directly with a neutrino flux at the surface of the Earth to give an event rate. We have also seen that the effect of the Earth's absorption only becomes important at 100 TeV and, above this energy, depends on the neutrino zenith angle.

We have estimated the sensitivity of ANTARES to a "known" point source with a power law neutrino flux for a range of different spectral indices and low energy cut-offs in the power law spectrum. Comparing the sensitivity to an E_ν^{-2} neutrino flux to the Waxman-Bahcall limit in Eq. (1.10), we can see that the prospects for discovering high energy sources of neutrinos (at least for sources subject to this limit) are not promising. It should also be noted that the more sources that are studied in this way, the lower the significance of the detection of a single source with this method becomes (as there is an increased probability of the background around one source in the sample fluctuating upwards by this amount).

In this section, we have made a rough estimate of the sensitivity of ANTARES to high energy neutrinos. In Chapter 6, we will perform a more detailed calculation in terms of the sensitivity of ANTARES to the annihilation of Dark Matter. In the following section, we consider a different method of presenting the ANTARES detector performance - the effective area for muons.

5.4.4 Effective areas for muons

In this section we take the effective area for muons defined in Eq. (5.13) and use it to calculate the detector efficiency as a function of neutrino energy. We will then reweight this effective area to our reference E_ν^{-2} neutrino spectrum to obtain a result which can be used in further calculations and compared to other experiments.

Effective areas for ANTARES

The following method is used to actually calculate the effective area (binned in neutrino energy):

1. We calculate the distribution of generated events according to Eq. (5.1) and then divide the distribution of selected events by this. This gives an “efficiency” (number of selected events per generated event in each bin).

2. This efficiency is then multiplied by the total generation volume in water equivalent units to give the effective volume according to Eq. (5.2). Working in water equivalent units at all times removes the complication of having media of different densities around the detector.

3. The average muon range for the events in each of the neutrino energy bins is calculated from the generated sample (using the results of the simulations in Appendix A).

4. The effective volume is then divided (on a bin by bin basis) by the average effective muon range to give the overall effective area.

The description above can be applied to different zenith angle bins. For simplicity, we have averaged over an isotropic neutrino flux (corresponding to a diffuse flux or randomly located selection of point sources). For comparison, we calculate the effective area from the previous definition in ANTARES according to Eq. (5.7), also averaging over an isotropic neutrino flux. These effective areas are plotted in Figure 5.9.

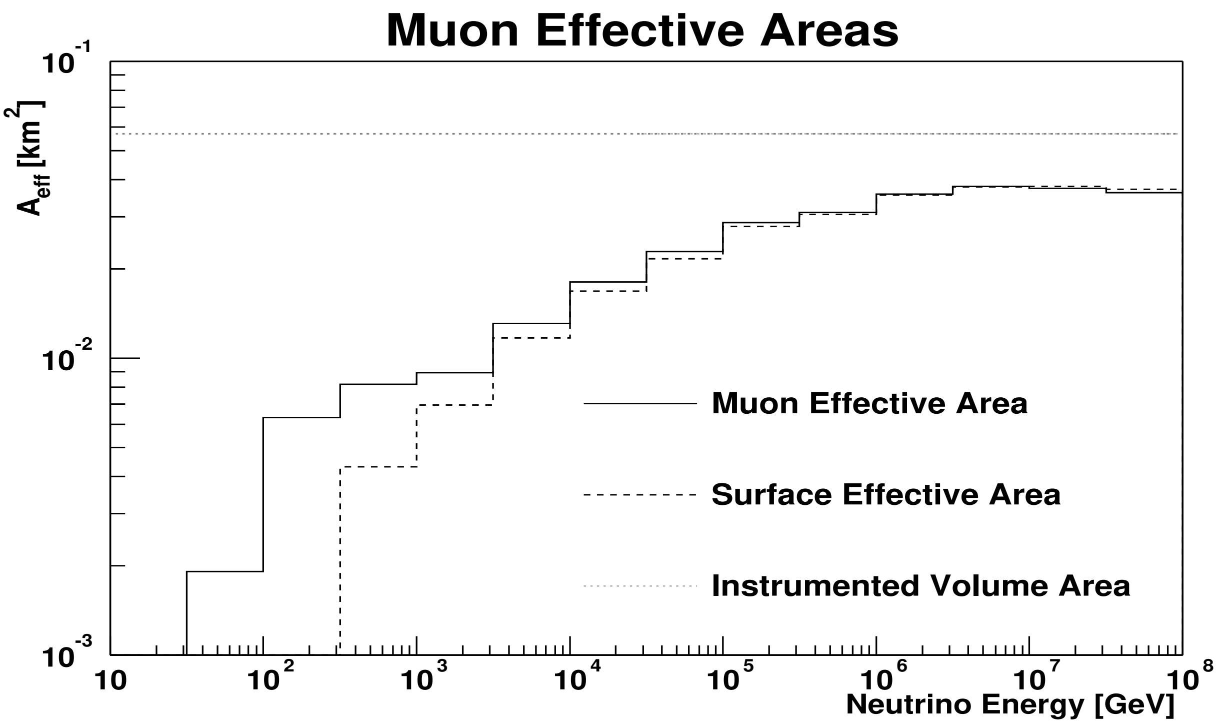

Figure 5.9: The total effective area for muons (solid) and the previous ANTARES definition (dashed) corresponding to just events arriving on the surface of the can. The horizontal dotted line shows the geometric area of the instrumented volume (averaged over zenith angle).

Discussion

We can see from Figure 5.9 that the effective area approaches 35000 m^2 for neutrino energies around 1 PeV. Above this, the effective area appears to be constant which may indicate that our can is not large enough. However, because of absorption in the Earth and steeply falling neutrino fluxes typical of astrophysical sources, the muon flux over 1 PeV is very small and this is unlikely to have a significant effect on the overall event rate for our reference choice of an E_ν^{-2} spectrum. For sources where the dominant contribution is from neutrinos above 1 PeV, the choice of can size may have to be reconsidered.

For neutrino energies above 3 TeV, the contribution of events which arrive on the surface of the can (given by the previous ANTARES definition of effective area) is greater than 90% and above this energy, this is a reasonable approximation to the total effective area (although how close it is still depends on the energy and the can size). For neutrino energies below 1 TeV, over half the events interact within the can and the previous ANTARES definition of effective area is not a good description of the efficiency. To include neutrinos in this lower energy range (which will be important for virtually all neutrino flux models), it is essential to use the method described here to calculate the effective area for muons.

Reweighting to an E_ν^{-2} neutrino flux

The actual definition of the "effective area" needed by phenomonologists to calculate event rates for specific models or used to compare different experiments (as defined in [44] and elsewhere) should correspond to a specific neutrino flux. Therefore, we would like to average the muon effective area in Figure 5.9 using the muon flux corresponding to a particular neutrino flux model. As a generic example of this procedure, we choose an E_ν^{-2} neutrino flux and will then use it to calculate the event rate corresponding to the diffuse flux limit of Waxman and Bahcall in Eq. (1.10), page 19.

To calculate the differential muon flux, $\frac{d\phi_\mu}{dE_\nu}$ in neutrino energy for an E_ν^{-2} neutrino spectrum, we use Eq. (5.11). The quantity $\frac{dP_\mu}{dE_\mu}$, the fraction of muons in an energy interval dE_μ for a given neutrino energy, is easily extractable from the event generator described in Section 3.2 (it is just the distribution of $1 - y$ from the interaction kinematics). The effective muon ranges are obtained from the fits described in Appendix A. Though the fits in Appendix A correspond to a general combination of two different media for muons arriving at the ANTARES detector, given the other uncertainties in the simulations and the approximate nature of effective area calculations, here we shall just evaluate the reweighted effective areas assuming all the propagation is either in rock or in water.

One additional choice is that of the muon energy threshold which enters into the definition of the effective muon ranges. A higher muon energy threshold implies shorter muon ranges and therefore a larger effective area (from Eq. (5.13), page 142). However, the corresponding muon flux used to calculate an event rate would also be lower (Eq. (5.11), page 142) so, provided the choice of threshold is made consistently, the event rates (for muons above threshold) will be unaffected. In presenting an effective area alone, it is therefore important to quote a muon energy threshold with an effective area as it will affect both the numerical values and future calculations. In this section, we present results corresponding to an energy threshold of 0 GeV. Using an energy threshold of 10 GeV which is often quoted as a benchmark figure for ANTARES gives results which differ by less than 1% from those presented here so, for astrophysics studies of high energy neutrinos, the choice of threshold is relatively unimportant.

The left hand plot in Figure 5.10 show the calculated differential muon flux (from Eq. (5.11) as described above) for neutrinos propagating entirely through rock. The distribution is normalised to one as we are going to use it (and the corresponding distribution for anti-neutrinos) to average the effective area. The right hand plot shows this normalised muon flux and the effective area from Figure 5.9 (both in grey and rescaled to fit on the plot). The product of these two quantities gives the effective area weighted by an E_ν^{-2} neutrino spectrum.

The results in Table 5.1 give the averaged effective areas and the integrated muon fluxes corresponding to Eq. (1.10), page 19, under the simplifying assumptions that all the propagation is either in rock or water. The event rates calculated from these quantities are then given. The corresponding values obtained by using the event weights from Section 3.4.2, page 74, by directly weighting the selected sample of events are 2.6 events per year (for neutrinos) and 2.2 events per year (for anti-neutrinos).

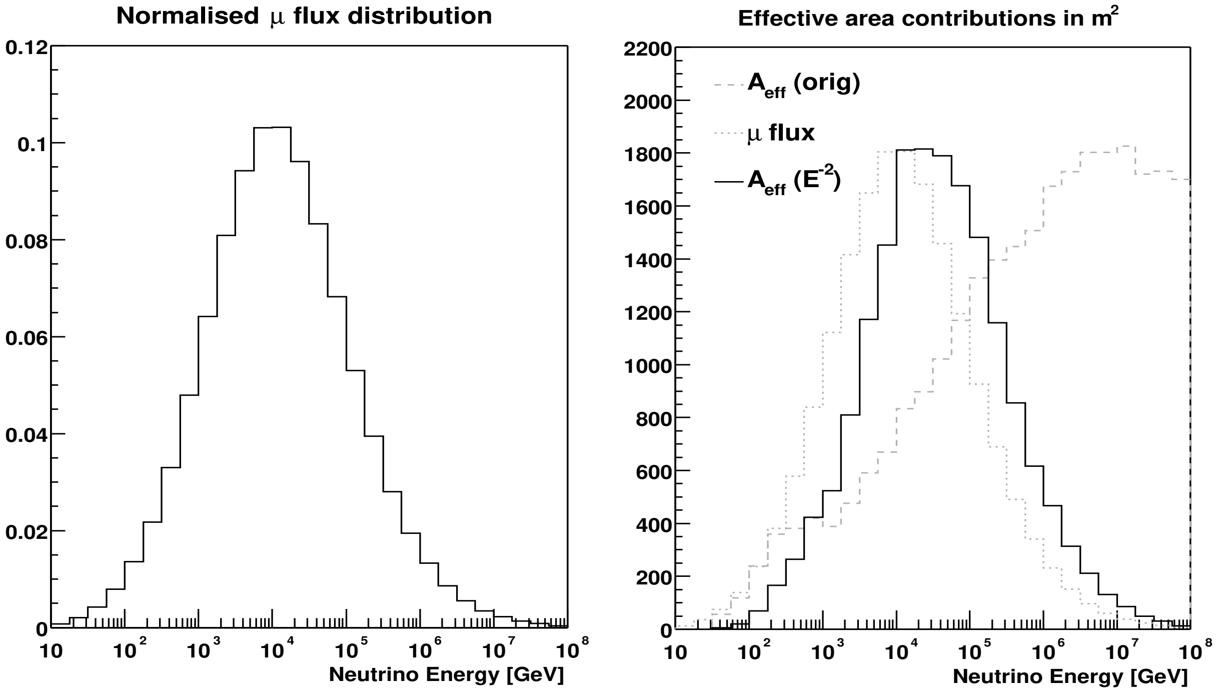

Figure 5.10: The left hand plot shows the normalised muon fluxes assuming propagation in rock. The solid histogram in the left hand plot is the muon effective area averaged over an E_ν^{-2} flux. The dashed histogram shows the effective area from Figure 5.9 ($\mathrm{A_{eff}}$(orig)) and the dotted histogram shows the muon flux from the left hand plot. These last two are both rescaled to fit on the plot.

Given the approximate nature of all these effective area calculations (the coarse binning neutrino energy, the averaging over an isotropic neutrino flux, the simplification of the treatment of the different media using the muon ranges), the agreement between the event rates calculated here and those obtained by using the event weights is good. The effective areas agree to within a few percent for the different choices of muon propagation medium.

Summary

In the sections above we have discussed the calculation of the effective area for muons as a function of neutrino energy (and in principle direction as well) and shown how to average this over a given neutrino flux. We have stated that the difference between a 0 GeV and 10 GeV energy threshold is small and that the effective areas for different (assumed) muon propagation media only differ by a few percent. We have also shown that there is good agreement between event rates predicted using these effective areas and those calculated directly from the event weights.

In this section, the emphasis has been on describing the calculation of the effective areas using the information from the event generation (Section 3.2) and the effective muon ranges

Medium Particle	Effective area (E^{-2}) $[m^2]$	Integrated ϕ_μ (Eq. (1.10)) $[m^{-2}]$	Event rate (Area) $[yr^{-1}]$
Rock : ν	17400	1.33×10^{-4}	2.3
Water : ν	17900	1.47×10^{-4}	2.6
Rock : $\overline{\nu}$	18600	1.02×10^{-4}	1.9
Water : $\overline{\nu}$	19100	1.14×10^{-4}	2.2

Table 5.1: Averaged muon effective areas for neutrinos and anti-neutrinos in rock and water. The integrated muon flux from Eq. (1.10) and the expected event rate calculating the effective areas and integrated fluxes. The corresponding values using the event weights are 2.6 yr^{-1} (neutrinos) and 2.2 yr^{-1} (anti-neutrinos).

(a detailed calculation of which is described in Appendix A). The power of describing the detector efficiency as an effective area can be seen as follows: consider an astrophysical (neutrino flux) model for some set of sources in the sky. Using the effective area as shown in Figure 5.9 (extended to include the directional dependence), one can average over the source spectrum and then proceed to calculate event rates for individual or sets of sources. This process can be repeated many times for different sources models and distributions. All this is possible without reference to the original sample of Monte Carlo events[10]. The method described in this section gives the machinery necessary to calculate such an effective area.

5.4.5 Muon and neutrino angular resolution

In the sections above we calculated the detector efficiency. It is equally important (certainly for astrophysics studies) to know the accuracy with which the neutrino (i.e. source) direction is reconstructed. This is the angular resolution and is defined in Section 5.1.3 as the median of the distribution of angles between the reconstructed track and the original neutrino.

In Figure 5.11, we plot the angular resolution for (anti-)neutrino and muons as a function of the neutrino energy. In terms of studying individual point sources, the important curve is the neutrino angular resolution where the limiting value at high energies[11] is 0.15°. We can see from Figure 5.11 that, for neutrino energies greater than 100 TeV, the angular resolution is limited by the quality of the reconstruction. Below this energy, the angle between the neutrino and the muon at the interaction vertex becomes important and dominates the overall angular resolution below 1 TeV.

In the right hand plots of Figure 5.11, we show the distribution of errors on the reconstructed track direction corresponding to an E_ν^{-2} spectrum (which will have the distribution of neutrino energies in the reconstructed sample shown in the right hand plot of Figure 5.4). This is the distribution of events one would expect to reconstruct around a point source

[10] Reprocessing the Monte Carlo events is a time consuming to process in any case and would potentially not be available (for an author outside the Collaboration for example).

[11] In terms of the reconstruction of the muon direction, we are limited at low energies by the amount of light produced by the muon and therefore the number of points we can include in our likelihood fit. At high energies, when we have sampled points along the whole muon track, we are limited by the size of the detector and the timing resolution. Therefore, the angular resolution reaches a constant value at high energies.

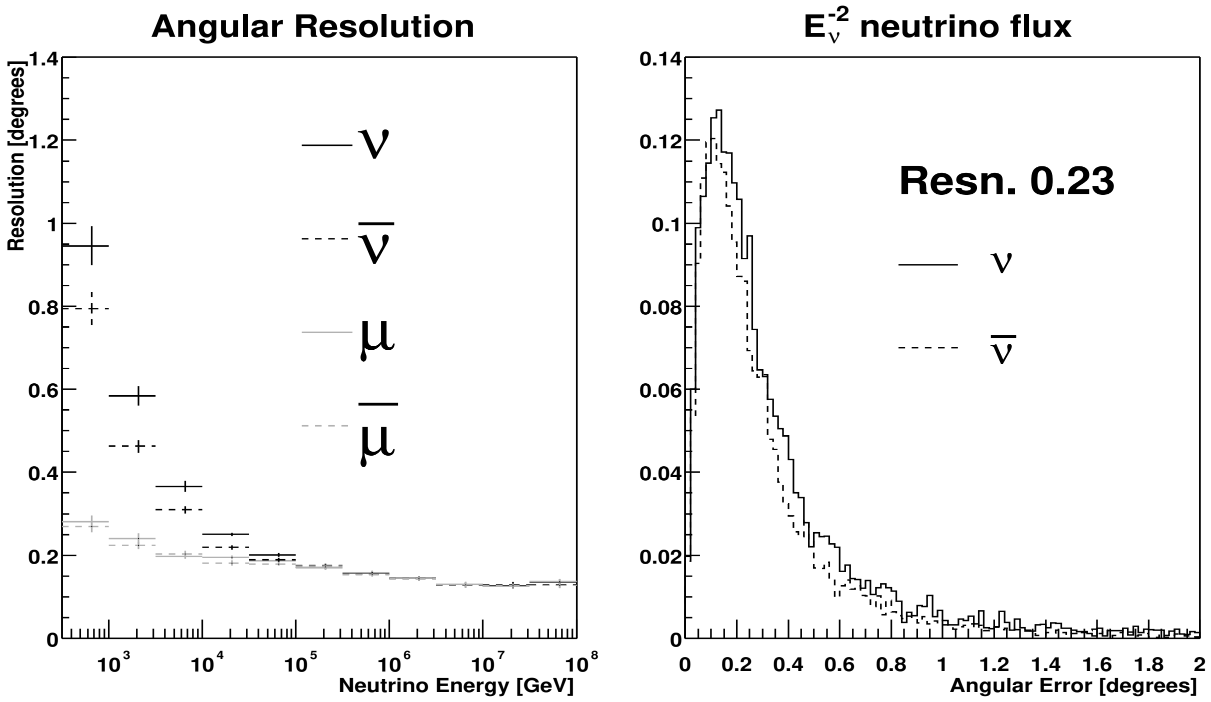

Figure 5.11: ANTARES angular resolution for neutrinos and muons as a function of neutrino energy (left) and the distribution of angular errors in the reconstruction for an E^{-2} neutrino source of neutrinos and anti-neutrinos (right). The resolution for an E^{-2} source is $\sim 0.23°$.

with an E_ν^{-2} neutrino spectrum. The median of the distributions for both neutrinos and anti-neutrinos is about 0.23° (with a negligible statistical error) and this can be taken as the angular resolution for a "typical" astrophysical neutrino source. This compares with a value of around 3° for AMANDA B10 [83] over a wide range of neutrino energies for their point source analysis and ANTARES would therefore expect to have greatly reduced backgrounds in any point source search compared to AMANDA.

In Section 5.1.3, we defined the angular resolution as the median error in the reconstructed track direction. We can perform the calculation as above but defining the angular resolution as the angle with respect to the neutrino (i.e. source) direction containing 68% (1σ) or 90% of the selected events. Defining the angular resolution as the angle containing 68% of the selected events, we obtain 0.25° at high energies and 0.75° for an E^{-2} neutrino spectrum. Increasing this to 90% gives 0.6° at high energies and 20° for an E^{-2} spectrum (due to the long tail of poorly reconstructed muons seen in the right hand plot of Figure 5.11). Even the relatively small increase from the median to 68% gives a large increase in the angular resolution with only a marginal gain in the number of signal events reconstructed within the angular resolution. The median therefore better represents the capabilities of the ANTARES detector in terms of searching for point sources of high energy neutrinos and is therefore conventionally used to define the angular resolution.

5.5 Summary

In this chapter we have discussed several aspects of the data analysis in ANTARES in terms of understanding the systematic errors which arise from the simulation methods employed and in calculating the expected performance of the detector. In particular:

- We have briefly described the reconstruction method used in this chapter. The results presented in this chapter have been obtained with a set of selection cuts which has been shown to reduce the atmospheric muon background in the sample of upward going muons to a negligible amount (Section 5.1).
- We have investigated several potential sources of systematic errors in both the rate of reconstructed events and the angular resolution arising from assumptions made in the event generation and detector Monte Carlo simulation and shown we can correct for them or they are smaller than 5% in the energy range of interest to ANTARES and can therefore be neglected (Section 5.2).
- We have investigated the effect of different models of photon propagation in water on the detector performance. We have shown that both changes in the scattering lengths and angular distribution have a significant effect on the performance of ANTARES (Section 5.3).
- We have derived two methods of presenting the efficiency of the ANTARES detector as an effective area which are applicable to the full range of neutrino energies in ANTARES. We have used the effective area for muons to calculate number of events for an E_ν^{-2} spectrum and shown that it is approximately consistent with that obtained using the event weights (Section 5.4).

From the various studies described above, we can draw the following conclusions about the performance of ANTARES:

Systematic effects from the event generation

The Cherenkov light from the hadronic shower has a significant (up to 40%) effect on the rate of reconstructed events for neutrino energies up to 10 TeV. It is therefore important to include it in all Monte Carlo simulations of the detector and this has been done for all the final simulations here using the method developed in Section 4.1.5.

Above 1 PeV, the neutrino interaction cross-sections for different PDFs differ by more than 5% in both directions from our reference choice of CTEQ3D. However, for an increased cross-section (for example) the competing effects of increased interaction rates near the detector and increased absorption in the Earth tend to cancel each other out. This leaves us much less sensitive to our choice of PDF than we otherwise might be. Only for specific point sources (i.e. from a specific direction) where the most significant contribution to the event rate is from neutrinos above 1 PeV are we sensitive to the choice of PDF. In general, for neutrino energies between 10 GeV and 1 PeV (where the majority of observed neutrino interactions are anticipated), the overall uncertainty from the event generation is that from Section 3.5 of $\leq 8\%$.

In terms of muon propagation code, the underestimation of the muon energy losses in PropMu gives an overestimation of the expected event rate of between 5% and 10% over a wide range of energies. In contrast, the maximum effect of muon multiple scattering on the angular resolution is less than 5% and is only this important around 1 TeV. This justifies our choice of MUM (which simulates the muon energy losses accurately but does not include the multiple scattering) for the muon propagation code in the event generator.

We also investigated the effect of different models of both conventional and prompt atmospheric neutrino fluxes. In terms of the overall rate, the two main models in the energy range of interest to ANTARES (Bartol and Honda) are very similar and, where it is important in estimating the atmospheric neutrino background in Chapter 6, we shall use the larger of the two predictions. By contrast, the different prompt neutrino flux calculations can differ by up to an order of magnitude above 100 TeV and will have a significant effect on any diffuse flux analysis which aims to just select events at high energies.

Effects of the water properties

We have shown that both the rate of detected events and the angular resolution are sensitive to the properties of the photon propagation medium in ANTARES and it is not realistic to neglect scattering in any simulation of muons passing through the ANTARES detector. A 10 m change in the scattering length and changes in the angular distribution (changing the $\langle \cos\theta \rangle$ from 0.77 to 0.9 or changing the shape with the same $\langle \cos\theta \rangle$) can each give up to a 10% change in the event rate and the angular resolution. Whilst these effects can be qualitatively understood in terms of the effect of the water properties on the amount of light arriving close to the time of direct Cherenkov light, the current uncertainty on the water properties at the ANTARES site precludes drawing quantitative conclusions about the systematic effects of the water properties. This uncertainty is potentially much larger than the 10% changes seen above and currently dominates the overall systematic error. Further measurements of the angular distributions and scattering lengths at the ANTARES site are required to improve this situation.

ANTARES detector performance

Using the methods described in Section 5.4.2 we have presented the efficiency (as effective areas for neutrinos and effective areas for muons) and angular resolution of ANTARES. The effective area for muons uses the effective muon range to include the contribution from events which interact both outside and inside the can, the latter of which are important for neutrino energies below 3 TeV. The previous method in use in ANTARES (i.e. quoting surface effective areas only) did not take account of this contribution. We then demonstrated a method by which the effective area for a particular neutrino flux can be calculated and applied this to the diffuse neutrino flux limit of Waxman and Bahcall (Eq. (1.10), page 19) giving event rates which were in good agreement with those calculated directly using the event weights.

The emphasis of these calculations was in developing the methods to calculate these effective areas and apply them usefully to specific models. However, we can also make general statements about the performance of ANTARES for this reconstruction and selection using these results:

- The sensitivity of ANTARES to neutrinos from a known point source with an E_ν^{-2} spectrum (i.e. the sensitivity to $E_\nu^2 \frac{dN_\nu}{dE_\nu}$) is of order 10^{-7} GeVcm^{-2}s^{-1}. Even with this very rough, unoptimised analysis, this is somewhere between the sensitivities of AMANDA-B10 and AMANDA-II [84].
- The effective area (for muons) of ANTARES at high neutrino energies is:
$$A_{eff}(E_\nu \geq 100\, TeV) \sim 30000 \text{ m}^2 \tag{5.18}$$
- Averaging over an E_ν^{-2} neutrino flux, the effective area of ANTARES for muons is:
$$A_{eff}(E_\nu^{-2}) \sim 20000 \text{ m}^2 \tag{5.19}$$
This can be compared[12] to $\sim$ 13000 m^2 for AMANDA-B10 [83] and approximately 30000 m^2 for AMANDA-II [84].
- The neutrino angular resolution at high energies is:
$$\Theta_{\nu-\mu}(E_\nu \geq 100\, TeV) \simeq 0.15^\circ \tag{5.20}$$
and for an E_ν^{-2} neutrino source:
$$\Theta_{\nu-\mu}(E_\nu^{-2}) \simeq 0.23^\circ \tag{5.21}$$
In both cases, the statistical error is negligible. This angular resolution is significantly better than that reported for AMANDA-B10 [83] where the limiting value is 3° at high energies.

These calculations give the expected performance of ANTARES in specific circumstances (i.e. in the high neutrino energy limit or to an E_ν^{-2} neutrino flux). These numbers can be compared to other experiments (and comparisons with AMANDA show that, in terms of efficiency, ANTARES is somewhere between AMANDA-B10 and AMANDA-II but with a much improved angular resolution). The proposed km^3 experiment, ICECUBE, would be expected to improve on this performance by well over an order of magnitude.

More importantly than the results given above, the methods developed in this chapter allow for the performance of ANTARES to be computed and parameterised accurately in a number of different ways and applied to virtually any neutrino analysis. In the next chapter, we shall apply the concepts of effective volumes and effective areas for neutrinos to a specific situation: the calculation of the expected sensitivity of ANTARES for the indirect detection of Dark Matter.

[12]The effective areas for AMANDA are presented for different muon energies and zenith angles. To obtain a comparable number, we take the effective area for 10 TeV muons, which is a typical muon energy at the detector for an E_ν^{-2} neutrino spectrum, and average over zenith angles.

Chapter 6

ANTARES sensitivity to Dark Matter

> In this chapter we develop an analysis using the concept of effective areas and effective volumes presented in Section 5.4 and apply it to the results of the simulations developed in Chapter 3 and Chapter 4. We predict the sensitivity of ANTARES for the indirect detection of Dark Matter and make the first calculation of anticipated upper limits on neutrino and muon fluxes for the Sun and the Galactic Centre corresponding to one and three years of observation. The expected limits are found to be competitive with current published limits after just one year of observation and improve on these by up to a factor of 5 for WIMP masses above 100 GeV, probing muon fluxes as small as a few hundreds km^{-2} yr^{-1}.

In Chapter 5 we have applied the best of the current ANTARES reconstruction algorithms to the results of the simulations described in Chapter 3 and Chapter 4 and presented results in a general way which can be applied to a range of different analyses. In this chapter, we apply some of those methods (effective volumes and effective areas for neutrinos) to predict the sensitivity of ANTARES for the indirect detection of Dark Matter.

In Section 1.4 we described a possible Dark Matter candidate, the neutralino (χ), as the Lightest Supersymmetric Particle (LSP) in some extensions of the Standard Model. We also discussed how these particles can become gravitationally bound and thus concentrated at the centre of massive bodies leading to a significant increase in the annihilation rate over that in "free space". In this chapter we use predictions of the energy distributions of neutrinos from the annihilation of these particles at the center of the Sun and of the Galaxy[1] (shown in Figure 1.10, page 30) to predict the sensitivity of ANTARES for different neutralino masses and compare this to other experiments. For this analysis, we adopt the following strategy:

- We take effective volumes calculated using the reconstruction and selection described in Section 5.1 as a function of neutrino zenith angle and energy. We apply additional cuts to the effective volumes to correspond to a small solid angle (defining a cone with an opening angle θ_{cone}) with a range of different sizes around the initial neutrino direction (Section 6.1.1).
- Both the Sun and Galactic Centre have a distribution of zenith angles during the course of 1 year (Section 6.1.2). We average the effective volumes above over this distribution of zenith angles (Section 6.1.3).

[1] Others in the ANTARES Collaboration [70, 154] are performing analyses for neutralino annihilation at the centre of the Earth using a different reconstruction code dedicated to low energies.

- We convert the effective volume to an effective area for neutrinos using the neutrino cross-section information from the event generation (Section 6.2.1).

- We use the neutrino energy distributions for neutralino annihilation into different channels to reweight these effective areas as a function of neutrino energy to effective areas as a function of neutralino mass (Section 6.2.2).

- Using the event weights described in Section 3.4.2, we calculate the atmospheric neutrino rate in the same size solid angle as each effective volume above whilst tracking the source for one year (Section 6.3).

- We can then predict our expected limits on the neutrino flux using the neutrino effective area and the background estimates for a range of neutralino masses. For each mass, we choose the cone size which gives the best limits (Section 6.4.2).

- Finally, for direct comparison with other indirect detection experiments, we convert these neutrino flux limits to muon flux limits (Section 6.4.3) using flux ratios derived from the widely used DarkSUSY code [63].

As stated above, the final stage of this analysis is to convert our neutrino flux limits to muon flux limits for comparison with other experiments. An alternative would be to set directly the muon flux limits on the basis of the (simulated) data. However, this introduces a range of complications. For the neutrino energies of interest, the ANTARES detector is not "thin" - i.e. the majority of detected neutrinos are ones which are contained within the instrumented volume rather than those which arrive at the surface of the detector as a flux of muons. This is in contrast to other experiments who set such limits. There is no single surface within the ANTARES detector on which all the muons are incident and hence we cannot directly extract a muon flux from our simulations. In addition, we need to be able to convert an efficiency in terms of event properties into one for different neutralino masses. Whilst differential neutrino and muon fluxes are easily obtainable (from DarkSUSY), those for muons at a neutrino interaction vertex are not.

The "natural" method of expressing the desired limits for ANTARES is therefore as a limit on the neutrino interaction rate (i.e. via expressing the efficiency as an effective volume) as that is what is observed. The conversion of this to a neutrino flux limit using the neutrino cross-section is then well defined. However, we still want to compare to other experiments. Therefore, we take published conversion factors for neutrino fluxes to muon fluxes to modify our limits accordingly.

Although there are a wide range of model predictions as seen in Section 1.4.4 and it is therefore difficult to draw quantitative conclusions about the nature of Dark Matter and indeed the parameters of supersymmetry, we can still compare our results to these predictions to see what impact we make on these models. A further conversion to allow for comparison to direct detection experiments is possible but is highly model dependent (see [155] for a detailed discussion). It has been performed for the results of this analysis in [70, 156] and we shall briefly comment on this aspect as well.

6.1 Effective volumes for neutrinos from the Sun and Galactic Centre

The first stage in this analysis is to calculate the effective volume of ANTARES for neutrinos with energies up to 1 TeV (which is the highest mass neutralino we shall consider here). For this, we use the "low energy" production from Chapter 5 (described in Appendix C) which includes scattering with the reference model P2 (see Section 4.2) and the hadronic shower contribution (see Section 4.1.5). We use the definition of effective volume from Eq. (5.2), page 139:

$$V_{eff}(E_\nu, \theta_\nu) = \frac{N_{selected}(E_\nu, \theta_\nu)}{N_{generated}(E_\nu, \theta_\nu)} \times V_{generation} \tag{6.1}$$

The effective volume is calculated in 10 equal upward going bins in $\cos\theta$ and 20 equal bins in $\log_{10}(E_\nu)$ between 10 GeV and 1 TeV. In addition to the selection used in Chapter 5, an extra cut is applied which requires the reconstructed muon direction to be within a specific angle θ_{cone} of the neutrino direction. This last cut will later correspond to selecting events within a specified angle of a known source in the sky (i.e. the Sun or Galactic Centre). This cone size is varied from 0.1 degrees to 10 degrees in 0.1 degree steps. The effective volumes are calculated for neutrinos and anti-neutrinos separately as they have different cross-sections and will therefore contribute differently to the overall efficiency for a given total neutrino flux.

6.1.1 Effective volumes for different selection cones

We have a range of possible cone sizes surrounding the source, the final choice of which will depend on the neutralino mass (higher masses produce higher energy neutrinos where the neutrino and muon directions are more strongly correlated). Larger cone sizes will contain more of the signal from the source but will also contain more background. Whereas the background will increase roughly as θ^2_{cone} (for small θ_{cone}), the amount of signal will depend on the distribution of reconstructed muon directions with respect to the parent neutrino.

The plots in Figure 6.1 show the effective volumes averaged over an isotropic distribution of upgoing neutrinos for cone angles of 10, 3 and 1 degrees (similar results are obtained for anti-neutrinos). For a cone size of 10 degrees, there is virtually no reduction in the effective volume over the whole range of neutrino energies for which events are selected. For a 3 degree cone, the difference is largest at low energies where both the angular resolution of the muon reconstruction is worst and the neutrino-muon angle at the interaction vertex is largest. For a cone of 1 degree, there is a significant reduction in the efficiency at all energies as this is typically smaller than the neutrino-muon angle. We therefore expect our optimum cone size, which will depend on the background as well as the signal efficiency, to lie within the two extremes of this range. How this optimum is determined will be discussed in Section 6.4.1.

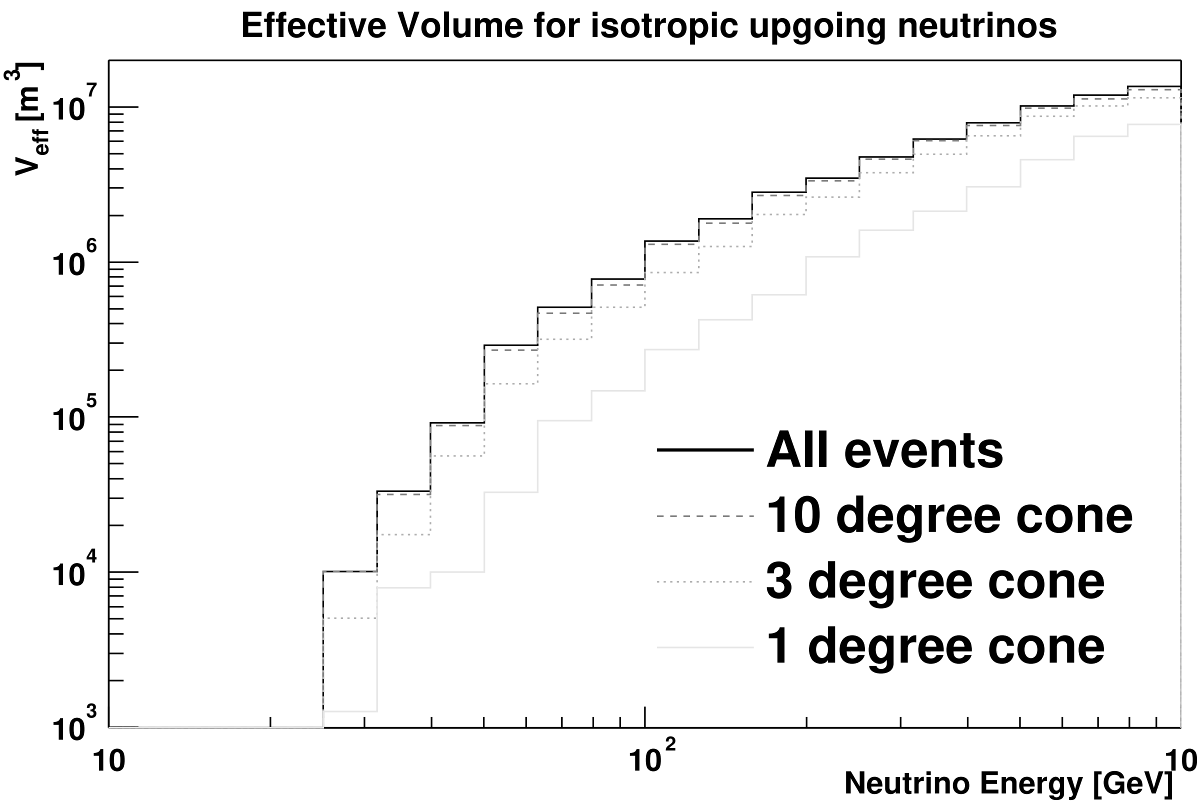

Figure 6.1: Effective volumes for isotropic upgoing neutrinos corresponding to cones of size 10, 3 and 1 degrees around the parent neutrino direction. The effective volume with no cone is shown in solid black.

6.1.2 Zenith angle position of the Sun and Galactic Centre

The distribution of Sun and Galactic Centre zenith angles throughout one year (chosen to be 2005 to correspond to the first full year of operation of ANTARES) has been calculated using the standard astronomical co-ordinate and geometry routines in SLALIB [157]. The values as a function of the local zenith angle at the ANTARES site have been provided by [158] and are shown in Figure 6.2 for angles below the horizon.

The data in the table are used in the following sections to weight zenith angle dependent efficiencies to correspond to the particular zenith angular distribution of the Sun or Galactic Centre. The last line in the table shows the total fraction of a year which the given source is visible to ANTARES.

Note that in everything that follows we assume that the detector is cylindrically symmetric and we neglect any azimuthal dependence of the detector efficiency. A recent study of this [159] for high energy (1-10 TeV) neutrinos has found a weak azimuthal dependence (due to the shape of the detector) but with very poor statistics. In addition, it is not clear that the same would be true at lower energies where the events are more likely to be completely contained within the instrumented volume. A detailed study of this would also require an

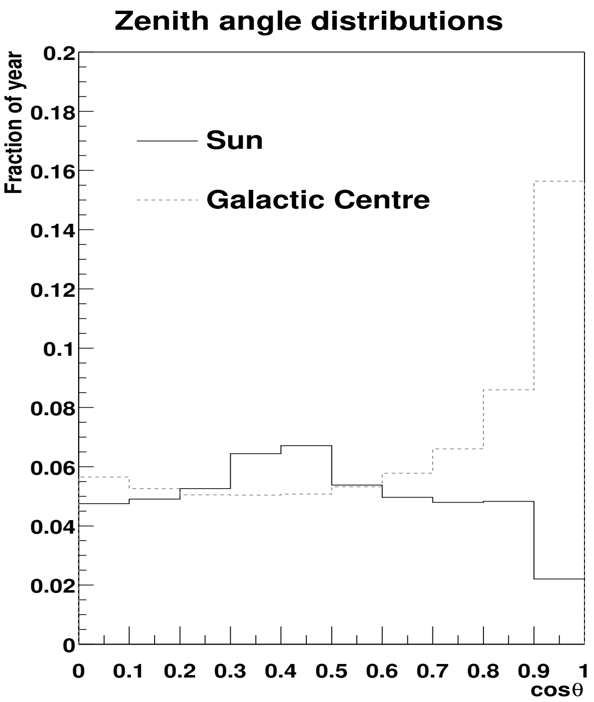

$\cos\theta$ (low)	$cos\theta$ (high)	f_{Sun}	f_{GC}
0.0	0.1	0.0475	0.0565
0.1	0.2	0.0490	0.0526
0.2	0.3	0.0526	0.0505
0.3	0.4	0.0644	0.0504
0.4	0.5	0.0671	0.0507
0.5	0.6	0.0538	0.0532
0.6	0.7	0.0496	0.0578
0.7	0.8	0.0479	0.0660
0.8	0.9	0.0483	0.0859
0.9	1.0	0.0221	0.1564
0.0	1.0	0.5023	0.6800

Figure 6.2: The fraction of the year spent by the Sun and the Galactic Centre in local zenith angle bins at the ANTARES site. The bottom line in the table shows the fraction of the year the source spends below the horizon (and is therefore visible to ANTARES).

order of magnitude better statistics in the Monte Carlo simulation than that used here so we neglect this effect but note it as a possibility for future improvements of this analysis.

6.1.3 Effective volumes for each source

We take the effective volumes calculated as a function of neutrino energy and zenith angle above and sum over the zenith angle bins weighting by the data in Figure 6.2:

$$V_{eff}^{Sun/GC} = \sum_{i=1}^{10} V_{eff}^{i} \times f_{Sun/GC}^{i} \tag{6.2}$$

This gives the effective volume corresponding to neutrinos in the same $\Delta\cos\theta = 0.1$ bins as the Sun or Galactic Centre as seen from ANTARES over the course of one year. Note that as $\sum f_{Sun} \sim 0.5$, we have taken into account that the Sun is only visible (to ANTARES) for approximately half the year (and similarly for the Galactic Centre).

6.2 Neutrino effective areas

In the previous section we described the calculation of the effective volume corresponding to various cone sizes whilst tracking a moving source. We want to be able to use these efficiencies to be able to set limits on the sensitivity of ANTARES to the indirect detection of Dark Matter as a function of neutralino mass. Initially, we set limits on the neutrino flux and therefore want to express our efficiency in terms of an effective area for neutrinos.

6.2.1 Conversion of effective volumes to effective areas

We can apply the method described in Section 5.4.2 to convert the effective volumes above to an effective area for neutrinos by multiplying each bin by the neutrino cross-section at that energy and the target nucleon density (i.e. using Eq. (5.5), page 140). We do this separately for neutrinos and anti-neutrinos to take account of the different cross-sections.

The above calculation gives us effective areas which can be multiplied by a (differential) neutrino flux to give an event rate. The information about the neutrino and anti-neutrino cross-sections is contained within the effective areas. In the potential Dark Matter signal, neutrinos and anti-neutrinos are produced in equal quantities and hence their fluxes at the ANTARES detector are the same. Therefore, the rate of events (Γ_{DM}) due to neutrino flux from Dark Matter annihilation (ϕ_{DM}) would be:

$$\Gamma_{DM} = A^{\nu}_{eff} \times \frac{1}{2}\phi_{DM} + A^{\overline{\nu}}_{eff} \times \frac{1}{2}\phi_{DM} = \frac{1}{2}\left(A^{\nu}_{eff} + A^{\overline{\nu}}_{eff}\right) \times \phi_{DM} \tag{6.3}$$

We can therefore just take the average of the effective areas for neutrinos and anti-neutrinos and multiply them by the total $\nu + \overline{\nu}$ flux to get the event rate. We take this average for each of our cone sizes.

6.2.2 Effective areas as a function of neutralino mass

The above calculation gives effective areas as a function of neutrino energy. We saw from the description in Section 1.4.4 that a range of different neutrino energy distributions were possible depending on the annihilation channel of the WIMPs. We defined "hard" and "soft" energy distributions (discussed in Section 1.4 with the distributions for a neutralino mass of 130 GeV shown in Figure 1.10, page 30) corresponding to the highest and lowest energy neutrino distributions respectively (i.e. "hard" is a relatively flat spectrum with a significant contribution at high energies whereas "soft" is steeply falling). The hard channel is annihilation into W^+W^- (above the $M_\chi = M_W$ threshold for this process) or $\tau\tau$ (below this threshold). The soft channel is always annihilation in $b\overline{b}$ quarks.

An additional distinction between neutrinos from the Sun and the Galactic Centre was also made in Section 1.4.4. The column density of matter between the centre of the Sun (where the neutralinos annihilate) and the outside is non-negligible. Neutrinos from this source will have their spectrum distorted as higher energy neutrinos (which have higher cross-sections) will be preferentially absorbed.

Our actual efficiency (i.e. effective area) for a particular model will depend on the particular set of branching ratios for WIMP annihilation that nature selects. However, by

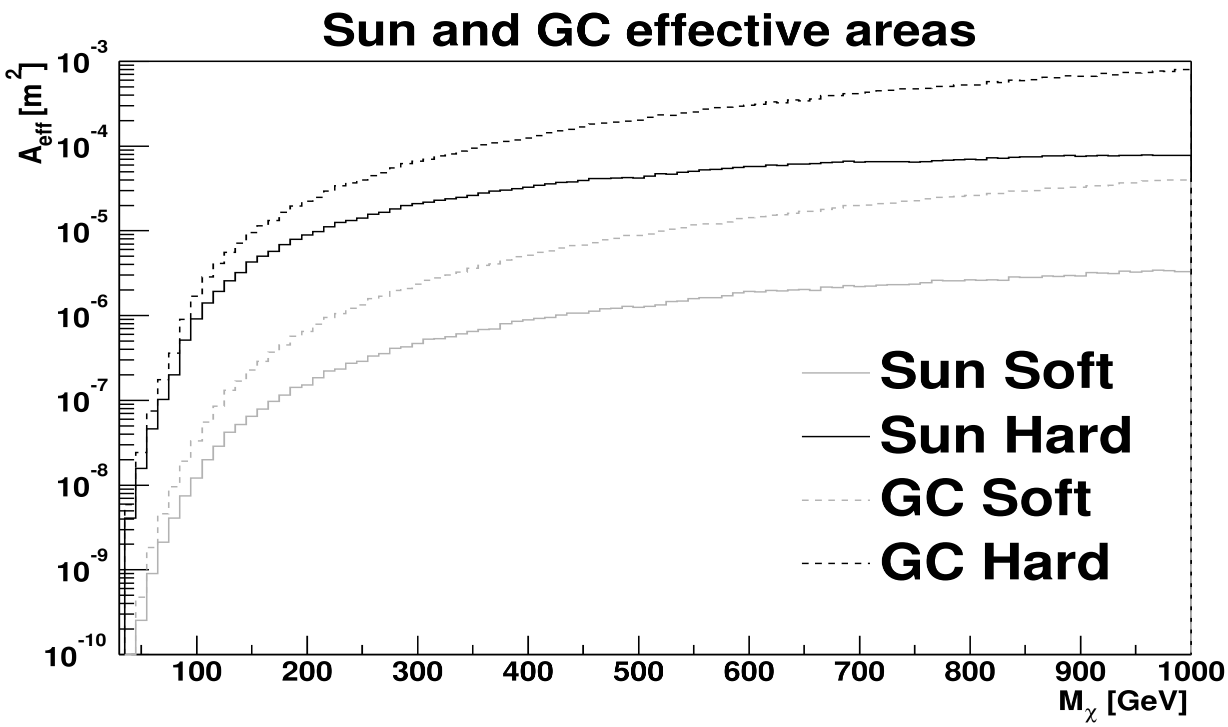

Figure 6.3: Effective areas for neutrinos as a function of neutralino mass for hard and soft spectra from the Sun and Galactic Centre for a cone size of 3°.

taking the two extremes (within the realm of Standard Model physics), we can be sure that the actual efficiency will lie somewhere between the two. This will be seen in the presentation of the final limits where a range of values is given for any individual neutralino mass.

To convert the effective areas above to a function of the neutralino mass for each value of θ_{cone}, we take the normalised "hard" and "soft" differential neutrino distributions (which are given in 50 equal energy bins from 0 to M_χ) and calculate the weighted average of the effective area:

$$A_{eff}(M_\chi) = \frac{1}{\sum N_i} \times \sum_{i=1}^{50} N_i \times A_{eff}(E_\nu) \tag{6.4}$$

where N_i is the number of entries in the hard or soft neutrino distribution, for a neutralino mass M_χ, in bin i which has a central neutrino energy E_ν. The results of this process are shown in Figure 6.3 for a cone size of 3°.

Several effects are immediately clear. Firstly, for both the Sun and Galactic Centre the variation of the hard and soft effective areas with mass are similar although the absolute values differ by around two orders of magnitude in each case. The difference can be easily understood in that higher neutralino masses give higher energy neutrinos which are easier to detect both because of their larger interaction cross-section and the longer ranges of the muons they produce.

The second effect is that of the absorption of neutrinos in the Sun. Due to the large column density of matter, the fraction of high energy neutrinos leaving the Sun is reduced. This causes the effective areas for solar spectra to be much flatter at higher values of M_χ than those from the Galactic Centre as there is no gain in efficiency from producing higher energy neutrinos as an increasing fraction of them are unable to escape the source. Therefore, we would expect the limits for neutrinos from the Sun to improve much more slowly with neutralino mass than those for the Galactic Centre.

Finally, the effective areas for the Galactic Centre are generally higher than those for the Sun, even at low neutralino masses where the effect of the neutrino absorption is relatively small. This is because the Galactic Centre is visible for a greater fraction of the year than the Sun (68% compared to 50%). Given all these points, we would therefore expect significantly better limits for the Galactic Centre, especially for high neutralino masses.

6.3 Atmospheric neutrino backgrounds

The calculations above give us the effective areas as a function of neutralino mass corresponding to a particular source for two extreme annihilation channels. In order to predict the sensitivity of ANTARES to that signal, we also need an estimation of the background in the same cone tracking each source. The selection used has been shown to identify almost all of the available ($\sim$ 9 days) sample of downward going atmospheric muons which are misreconstructed as upgoing. Therefore, we assume we can neglect this contribution to the background[2].

The remaining background is that from atmospheric neutrinos (taken here to mean neutrinos + anti-neutrinos). This is irreducible in the sense that both the direction and structure of the events are identical to the signal (i.e. they are upward going muon neutrino interactions). We discussed a range of different neutrino flux models in Section 3.4.2 and calculated the annual event rate in Section 5.2.4. If we compare the two calculations presented there (ignoring Fluka as it uses the Honda flux over most of the interesting range), they differ by $\sim$ 100 events in a total of nearly 2000. This difference is relatively small in any case and, to be conservative, we take the larger of the two predictions, the Bartol neutrino flux, for our background estimations.

Figure 6.4 shows the rate of selected atmospheric neutrino events per year as a function of zenith angle. To calculate the rate of background events per year, R_{cone}, within θ_{cone} of a source we multiply the ratio of the cone solid angle to that in one zenith angle bin (of size 0.1 in $\cos\theta$) by the rate of events in each zenith angle bin i, R^i, summed over the source distribution, $f^i_{Sun/GC}$.

$$R_{cone} = \left(\frac{1}{0.1 \times 2\pi}\int_{\cos\theta_{cone}}^{1} d\cos\theta d\phi\right) \times \left(\sum_i R^i f^i_{Sun/GC}\right)$$

[2]Even if a small number of atmospheric muons are reconstructed as upgoing, the chance of them coinciding with the cone surrounding either the Sun or Galactic Centre is small. This remains true provided the number of misreconstructed atmospheric muons is small compared to the atmospheric neutrino signal.

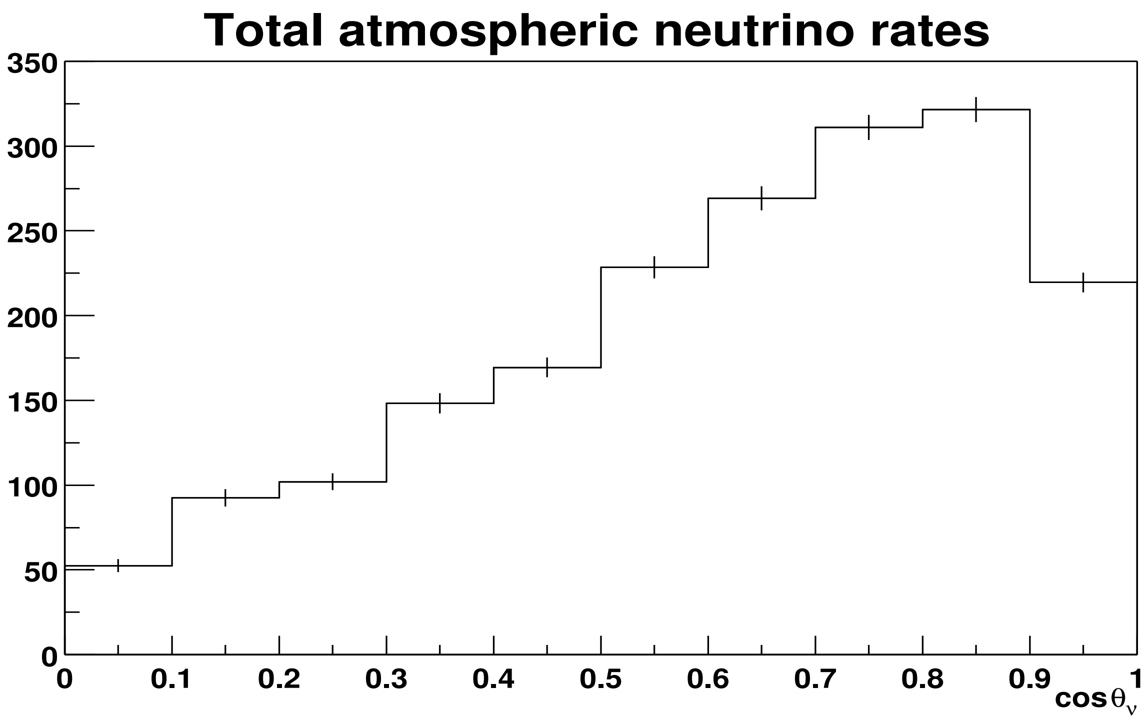

Figure 6.4: Atmospheric neutrino and anti-neutrino rates per year as a function of zenith angle. The errors shown are statistical. The total number of events per year in this sample is 1915 ± 19. The form of the distribution is a result of the shape of the ANTARES detector (∼350 m tall and only ∼180 m in diameter).

$$= \frac{1 - \cos\theta_{cone}}{0.1} \times \sum_i R^i f^i_{Sun/GC} \tag{6.5}$$

The results of this calculation are shown in Table 6.1 for selected values of θ_{cone}. For values of θ_{cone} less than about 2.5 degrees, we expect roughly one or fewer background events per year. Even for angles up to 5 degrees, we expect less than 5 events per year. Given an angular resolution of order 1 degree (including the angle between the muon and neutrino at the interaction vertex), we would expect our optimum values of θ_{cone} to lie within this range.

6.4 Predicted flux limits as a function of M_χ

From the sections above we have an estimate of the signal efficiency and expected background in cones of varying sizes tracking both the Sun and Galactic Centre across the sky. In this section we use these results to predict the limits ANTARES could set for the indirect detection of Dark Matter for 1 and 3 years of observation. As many of the predictions for the expected neutrino fluxes from WIMP annihilation are small compared to current experimental limits, we perform this analysis under the assumption that what we observe is consistent with the predicted atmospheric neutrino background.

θ_{cone} [degrees]	Rate per year tracking the Sun	Rate per year tracking the GC
0.1	0.0014	0.0021
0.5	0.0359	0.0530
1.0	0.144	0.212
2.0	0.574	0.848
3.0	1.291	1.908
4.0	2.295	3.392
5.0	3.586	5.299
7.5	8.062	11.91
10.0	14.32	21.16

Table 6.1: Atmospheric neutrino rates per year in a cone of angle θ_{cone} in the direction of the Sun and of the centre of the Galaxy.

6.4.1 Method of setting limits

It is clear from the numbers in Table 6.1 that our expected rate of background events is relatively small and the fluctuations will be determined by Poisson statistics. The method used here is that proposed by Feldman and Cousins [153] for exactly this situation. This method gives a unified approach for setting both confidence limits and intervals where the choice between the two is not based on the data and does not give unphysical intervals or empty sets.

We want to calculate an upper limit on the signal (i.e. on the number of observed events as a result Dark Matter annihilation) for a known[3] background rate. We want the "average" upper limit - i.e. that which would be obtained from a collection of many experiments and analyses like the one described here. For this we use the 90% confidence limits given in Table XII of [153] (see Appendix B.3 for a fuller discussion on how this data is used).

We can now determine the rates of events per year from Dark Matter annihilation in the Sun and Galactic Centre which we can exclude at 90% confidence corresponding to 1 and 3 years of operation of ANTARES where the expected background is observed. This is shown in Table 6.2 for the same values of θ_{cone} as in Table 6.1.

When the cone size is very small (less than 1 degree), we have essentially no background and the limit is roughly that we would get for observing zero events and excluding a downward fluctuation in the signal at 90% confidence. In this limit, our sensitivity will increase linearly with exposure time. In this case we are said to be "signal limited" in our ability to set limits. At the other extreme, when the background is large, our ability to detect or exclude a signal will increase roughly with the square root of the observation time (as the characteristic size of the statistical fluctuations in the background is of order $\sqrt{t_{obs}}$). This is seen (approximately) in the change in the limits for cone sizes of 10 degrees. This can be described as being "background limited" in the setting of limits. In reality, we will probably lie somewhere between these two extremes. This is important as it determines our ability to

[3]Known from Monte Carlo studies here. In the analysis of real data, the rate can be determined by looking "off source" in equivalent sized cones to that used in the analysis.

θ_{cone}	Excluded rate of signal events at 90% confidence			
[degrees]	Sun : 1 year	Sun : 3 years	GC : 1 year	GC : 3 years
0.1	2.44	0.81	2.44	0.81
0.5	2.47	0.84	2.48	0.86
1.0	2.56	0.93	2.62	0.99
2.0	2.92	1.25	3.15	1.41
3.0	3.48	1.59	3.88	1.81
4.0	4.09	1.95	4.58	2.27
5.0	4.66	2.32	5.28	2.73
7.5	6.20	3.26	7.26	3.87
10.0	7.83	4.20	9.23	5.01

Table 6.2: Upper limits on the rate of observed events per year from Dark Matter annihilation at 90% confidence for 1 and 3 years of observations. The observation is assumed to be consistent with the expected background.

improve our sensitivity by extending the observation time and will impact on how quickly we can compete with other experiments in the field.

The analysis described above gives a calculation of the neutrino effective area as a function of neutralino mass for a range of different cone sizes. The effective area multiplied by a neutrino flux will give us an event rate. Hence, we can determine the neutrino flux corresponding to each of the event rate limits above:

$$A_{eff} \times \phi_{DM} = \Gamma_{DM} \Rightarrow \phi_{DM} = \frac{\Gamma_{DM}}{A_{eff}} \tag{6.6}$$

where Γ_{DM} is the limiting Dark Matter event rate from Table 6.2.

Finally, we apply the method above to the effective areas and background estimations corresponding to each of the values of θ_{cone} in 0.1° degree steps between 0.1 and 10. For each value of M_χ, we select the cone size which gives the best (i.e. lowest) limit. In the analysis of real data, we would use the optimum cone size determined from these Monte Carlo studies to set limits at each neutralino mass.

6.4.2 Neutrino flux limits at the ANTARES detector

Applying the method above to the signal and background estimates from the Sun and Galactic Centre gives an upper limit on the neutrino flux from neutralino annihilation assuming that the observations are consistent with no signal. Our limits are expressed as a range at each neutralino mass corresponding to values between those obtained for the extreme hard and soft annihilation channels. These limits are shown in Figure 6.5 for one and three complete years of observations with ANTARES.

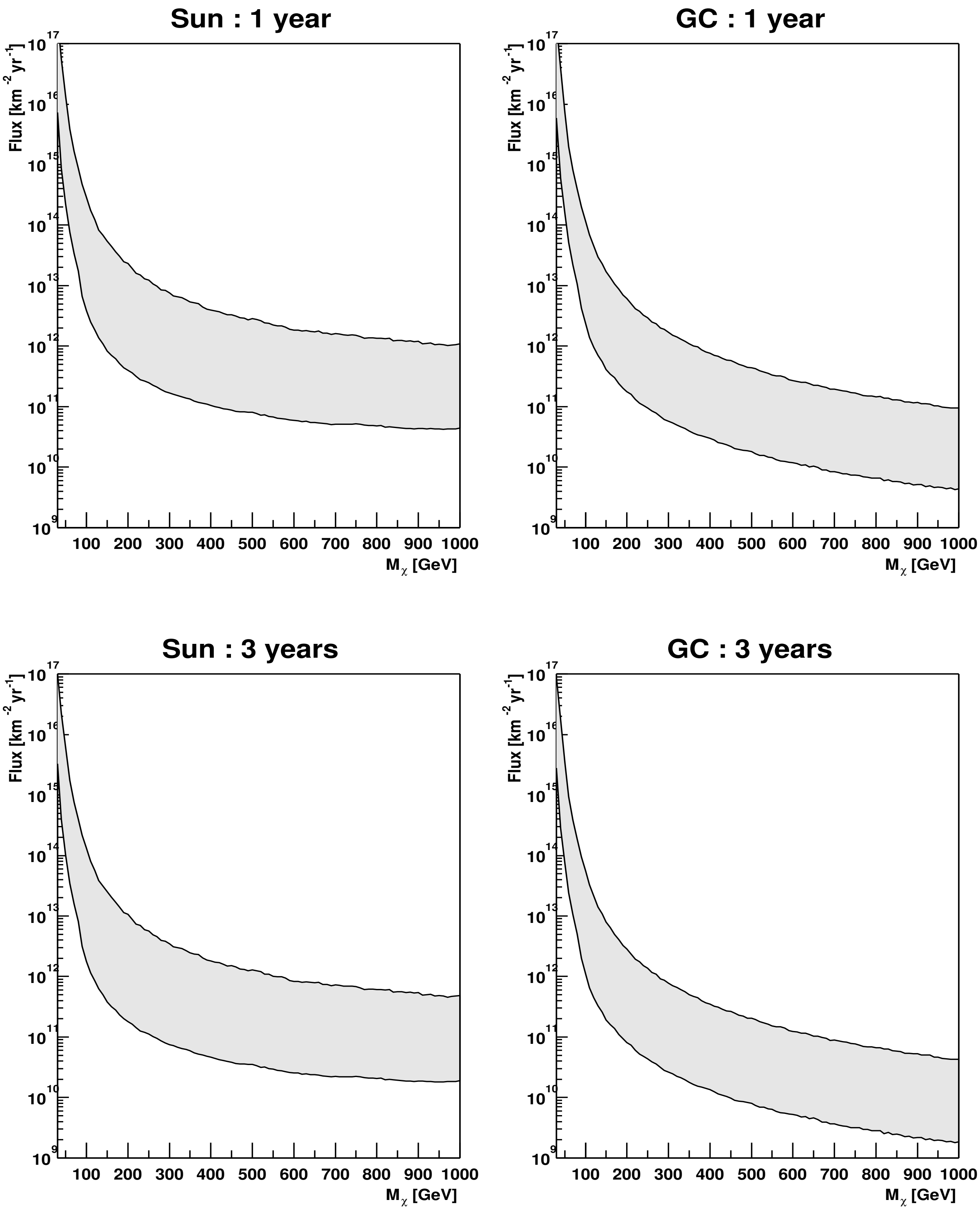

Figure 6.5: Upper limits on the neutrino flux which can be set in one and three years of observation in ANTARES assuming that the observed event rate is due to the atmospheric neutrino background alone.

Discussion of neutrino flux limits

We can see from Figure 6.5 that the range of values between the hard and soft channels for any given neutralino mass is quite large (as expected from the effective areas seen in Figure 6.3). A large part of this is due to the strong variation with energy of the neutrino interaction cross-section. We shall see in Section 6.4.3 that, once this factor is removed in calculating the muon flux limits, this difference is much smaller.

We can also see that the neutrino flux limits for the Galactic Centre continue to fall as the neutralino mass increases whereas the solar limits are much flatter. This is due to the softening of the neutrino spectrum from the Sun as discussed previously in Section 6.2.2. There is a steep rise in the lower limit for neutralino masses below 100 GeV. This steep rise is mainly the effect of the energy threshold of the muon reconstruction which can be seen in the effective volume essentially dropping to zero for neutrinos below about 30 GeV as shown in Figure 6.1.

We can see from the results in Figure 6.5 that, over a large range of neutralino masses, we are sensitive to neutrino fluxes below the maximum predictions for the Sun of around 10^{12} km^{-2}yr^{-1} shown in Figure 1.9, page 29, showing that there is some overlap between experimental sensitivity and the predictions of some supersymmetric models shown in Figure 1.9. To allow us to compare with both experimental predictions and other experimental limits simultaneously, we shall postpone a detailed comparison until we have calculated the muon flux limits.

Choice of optimum cone size

We stated previously that we expected our optimum cone size to be of order a few degrees. The plots in Figure 6.6 show the variation of the best θ_{cone} for different neutralino masses for soft and hard annihilation channels in the Sun and the variation of the limits with θ_{cone} for three values of M_χ.

From the left hand plots of Figure 6.6, we can see that our optimum cone size at high masses is about 3° for the soft channel and 2° for the hard. The optimum cone size increases toward lower masses as the average muon-neutrino angle at the interaction vertex increases. The largest value in either case is below 5°. This means we are in the limit where the number of background events remains relatively small and any approximations in the calculation of the background, where we assume that the cone is completely contained with one zenith angle bin at any one time[4], are negligible.

We can also see differences between the optimum cone size for 1 and 3 years of observation. If our ability to set limits was background limited, we would expect the best value of θ_{cone} to remain unchanged. However, we are closer to being signal limited than background limited and hence we can obtain better limits for 3 years observation by sacrificing a small amount

[4] This assumption is implicit in Eq. (6.5) where we calculate the rate of events in a zenith angle bin by taking the ratio of solid angles of the cone and the bin. This approximation is further justified in the right hand plots of Figure 6.6 where the dependence on θ_{cone} at large angles is relatively weak.

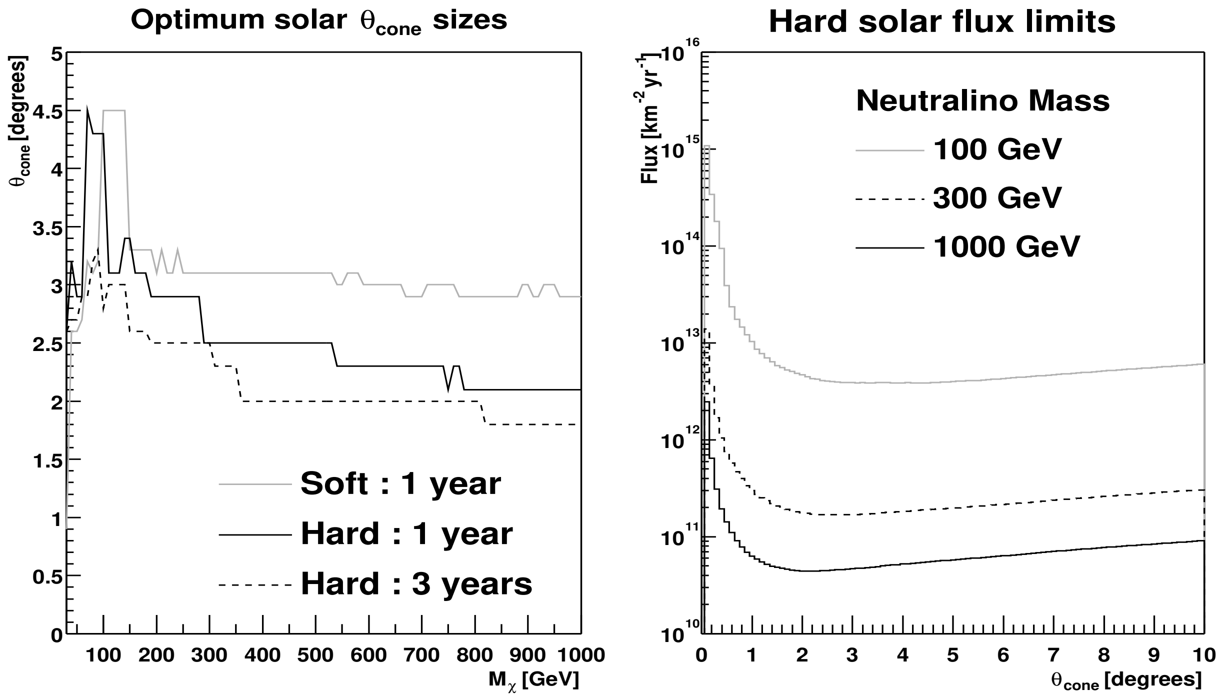

Figure 6.6: The optimum cone size as a function of neutralino mass for the Sun and the variation in limiting event rate for neutralino masses of 100 GeV, 300 GeV and 1 TeV. Similar results are obtained for the Galactic Centre.

of the signal to keep the background in this regime where we gain linearly in sensitivity with observation time.

The right hand plots in Figure 6.6 show the variation of the one year hard neutrino flux limits as the angle θ_{cone} is varied for neutralino masses of 100 GeV, 300 GeV and 1 TeV. We can see that the limits worsen rapidly if the cone size becomes too small as we start excluding significant amounts of the signal. This depends on the neutralino mass but occurs roughly at an angle of 1 degree.

For larger angles, we capture essentially all the signal and become limited by the amount of background we include within our cone. This variation is much weaker than that at smaller angles. This effect is potentially much more important as it means our results are relatively robust to effects which could worsen the angular resolution of the reconstruction such as a mis-reconstruction of the detector alignment or string distortion or a degradation in the performance of the electronics for example.

Summary

In this section we have calculated our anticipated limits on the neutrino flux from neutralino annihilation at both the centre of the Sun and the Galaxy and shown that, for the Sun, they are within the range of some of the theoretical predictions. Whilst this is the most useful expression of these limits for ANTARES, it makes comparison with other experiments difficult. Therefore, in the next section, we discuss a method of converting these neutrino flux limits into the more common muon flux limits.

A second result of this section is that, once the size of the cone surrounding the source is sufficiently large to contain the majority of the selected signal, we are not very sensitive to its exact size. This ensures that this analysis is robust against degradation of the angular resolution and our results would remain essentially unchanged if the cone size was fixed at, say, 5 degrees. Furthermore, we do not have to rely on the Monte Carlo estimate of the atmospheric neutrino background as we can obtain it from "off-source" measurements.

6.4.3 Muon flux limits at the ANTARES detector

As discussed previously, the "natural" expression of the detector efficiency in ANTARES for low energy events which are mostly contained within the instrumented volume is an effective volume or, equivalently, an effective area for neutrinos. However, other experiments setting these kind of limits publish their results as a limit on the observed muon flux. Therefore, we would like to convert our results to muon flux limits to allow a direct comparison.

Neutrino to muon flux conversion

We take the widely used DarkSUSY code [63] which calculates both neutrino and muon fluxes for particular neutralino annihilation channels. The ratio of these two fluxes is then the conversion factor we need. We calculate these fluxes with no energy threshold for the muons which gives us results which are comparable to other experiments (who quote either zero or very low muon energy thresholds in their results). These fluxes are publicly available and it therefore would be very easy to check or modify this conversion without repeating the whole analysis chain and without reference to any additional (not publicly available) code. In addition, this method ensures that a comparison of our muon and neutrino flux limits is consistent with respect to the flux predictions that DarkSUSY makes.

General discussion

The neutrino to muon flux conversion factors are shown as a function of neutralino mass and for hard and soft spectra in Figure 6.7. These numbers can be understood as giving the number of muons per neutrino on a surface at the depth of the detector. As with the effective areas in Figure 6.3, we can see the effect of the high energy neutrino attenuation in the Sun.

Applying these conversion factors to the neutrino flux limits shown in Figure 6.5 then gives the predicted muon flux limits shown in Figure 6.8 which ANTARES would be able to set for both the Sun and Galactic Centre after 1 and 3 years of observation. Figure 6.8 also shows the most recent published results from Super-Kamiokande [160], MACRO [78, 161] and Baksan [77] (for the Sun only).

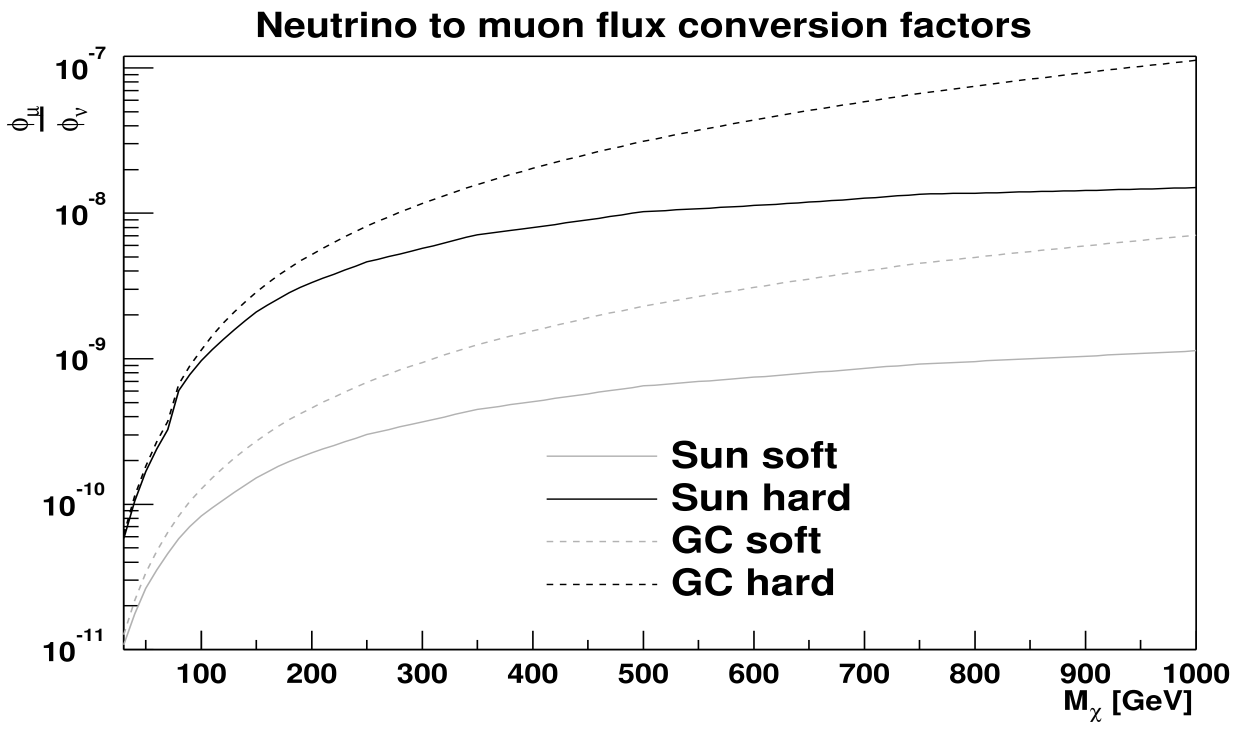

Figure 6.7: Neutrino to muon flux conversion coefficients extracted from DarkSUSY as the ratio of fluxes for hard and soft spectra at each neutralino mass.

The range of values between the hard and soft limits for each case is much narrower than for the neutrino flux limits in Figure 6.5 as these limits do not include the variation in energy of the neutrino cross-section (as they are limits for fluxes of muons). There is still a range of values for each neutralino mass as the reconstruction and selection efficiency are themselves functions of the muon energy and there is a non-negligible muon energy threshold for ANTARES. This is almost certainly much less true for MACRO, Super-Kamiokande and Baksan where the energy threshold is small (of order 1 GeV) and they are less sensitive to the details of the neutrino energy distribution. Their limits are therefore shown here as single lines.

The clear loss of sensitivity for neutralino masses below about 100 GeV is a result of the muon energy threshold in the reconstruction. However, even after just one full year of observation, ANTARES would be able to set competitive limits with other experiments in the field for neutralino masses above about 100 GeV although how competitive these limits would be would depend on the (model dependent) assumptions about the branching ratios of the annihilations.

As we saw above, for optimum cone sizes of between 2 and 5 degrees giving less than 5 background events per year, we are close to the region where we are limited by the size of the signal flux and not the fluctuations in the background. Therefore, we would expect a significant improvement in extending the observation time.

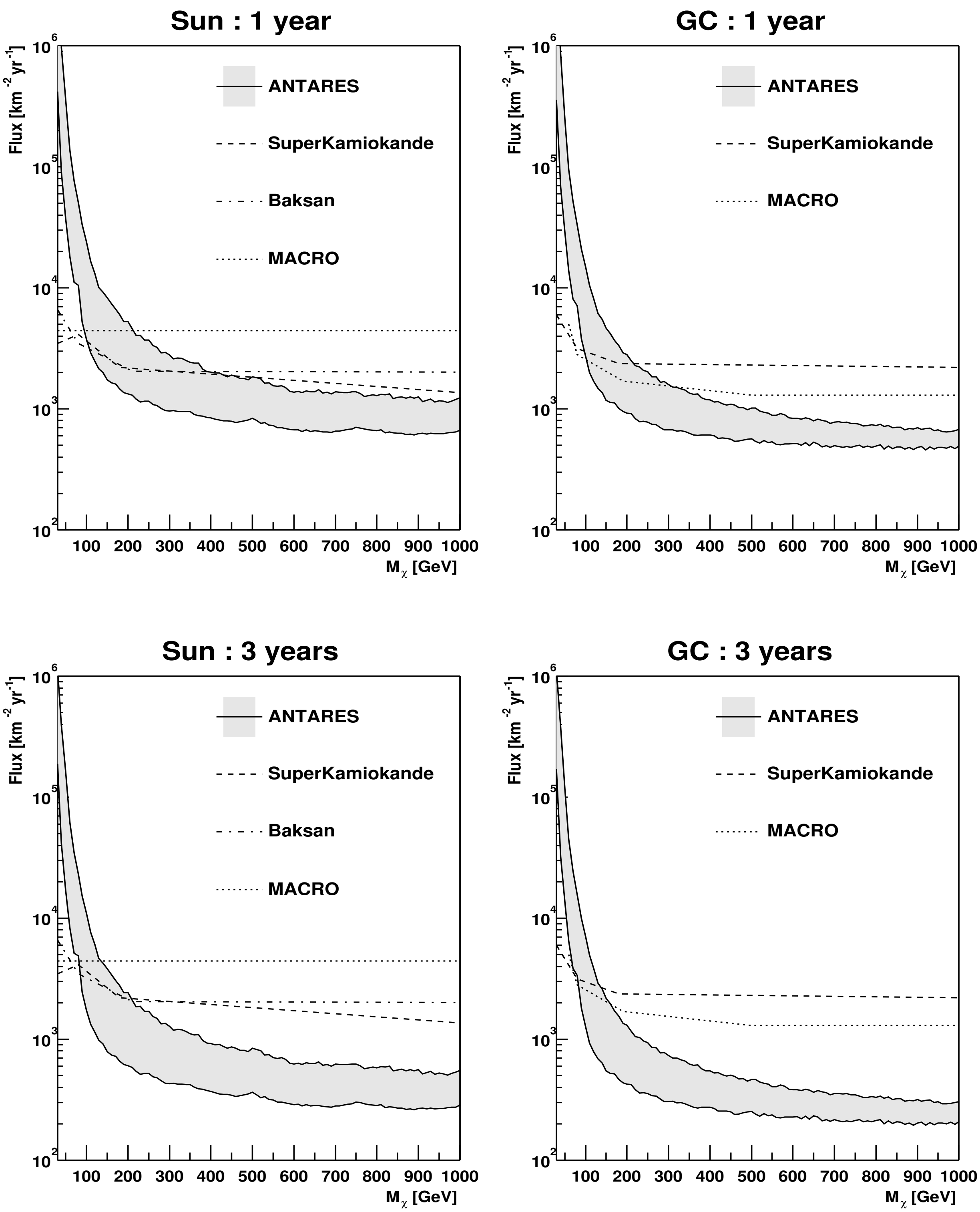

Figure 6.8: Anticipated limits on the muon flux at the ANTARES detector for the indirect detection of Dark Matter after 1 and 3 years of data taking as a function of neutralino mass. The published limits for Baksan (15 years), MACRO (4 years) and Super-Kamiokande (3 $\frac{1}{2}$ years) are also shown.

3 year muon flux limits

In the first instance, ANTARES is intended to take data for 3 years starting in 2005. The anticipated limits after this length of time are shown in the lower plots in Figure 6.8. We can see that, even with the very conservative assumption that all the annihilations branch into the soft channel, for neutralino masses above 200 GeV for the Sun and 150 GeV for the Galactic Centre, ANTARES will be able to set the world's best limits. Neither Baksan or MACRO are taking more data and Super-Kamiokande are in the process of rebuilding their detector so their limits for this analysis are unlikely to improve on this timescale. AMANDA and ICECUBE are unable to see the Sun or the Galactic Centre with any great efficiency as they are in areas of the sky dominated by the atmospheric muon background. Depending on the branching ratios of a particular model, we can potentially extend this reach down to around 100 GeV with this analysis and probe muon fluxes at the level of 300 km^{-2} yr^{-1} for the Sun and 200 km^{-2} yr^{-1} for the Galactic Centre.

6.4.4 Comparison to mSUGRA model predictions

We can take the muon flux limits for the Sun calculated above and compare them to muon fluxes derived (using the same neutrino to muon flux conversion factors as for the limits above) from the neutrino fluxes predicted by [69, 156] and shown in Figure 1.9, page 29. This will allow a direct comparison of our anticipated limits and those published by other groups to models over a wide scan of the mSUGRA parameter space. The scan is taken with $40 < m_0 < 3000$ GeV, $40 < m_{\frac{1}{2}} < 800$ GeV, $\tan\beta$ of 10 and 50 and with $A_0 = 0$ and $\mu > 0$ (see [69] for more details). Each point in this scan yields a value for the neutralino mass, M_χ, and a prediction of the integral muon flux. These points are shown in Figure 6.9 along with the ANTARES 3 year hard annihilation channel limit and the MACRO, SuperKamiokande and Baksan limits.

We can see from the left hand plot in Figure 6.9 that ANTARES will be sensitive to at least some models where the relic density is compatible with that favoured by the CMB measurements in [58]. ANTARES will also be sensitive to models with a lower relic density which can still be accommodated by the CMB measurements provided neutralinos aren't the only constituents of Cold Dark Matter.

The right hand plot in Figure 6.9 shows the dominant annihilation channel in each region of parameter space. The ANTARES sensitivity we have plotted corresponds to neutralinos annihilating to pairs of W bosons. We can see that the majority of models to which we are sensitive annihilate into pairs of W or Z bosons (which have a similarly hard spectrum to W pairs) and would therefore be subject to the sensitivity shown. In models where the annihilation is into bottom quarks, not only is our sensitivity worse (it is the upper end of the range shown in Figure 6.8), the muon flux predictions are also significantly lower. Hence, we have virtually no sensitivity to these models.

It is also possible to compare muon flux limits to direct detection (WIMP-nucleon scattering) experiments such as [162, 163, 164]. For each point in the parameter space scan, a prediction of the WIMP-nucleon scattering cross-section (which is how direct detection

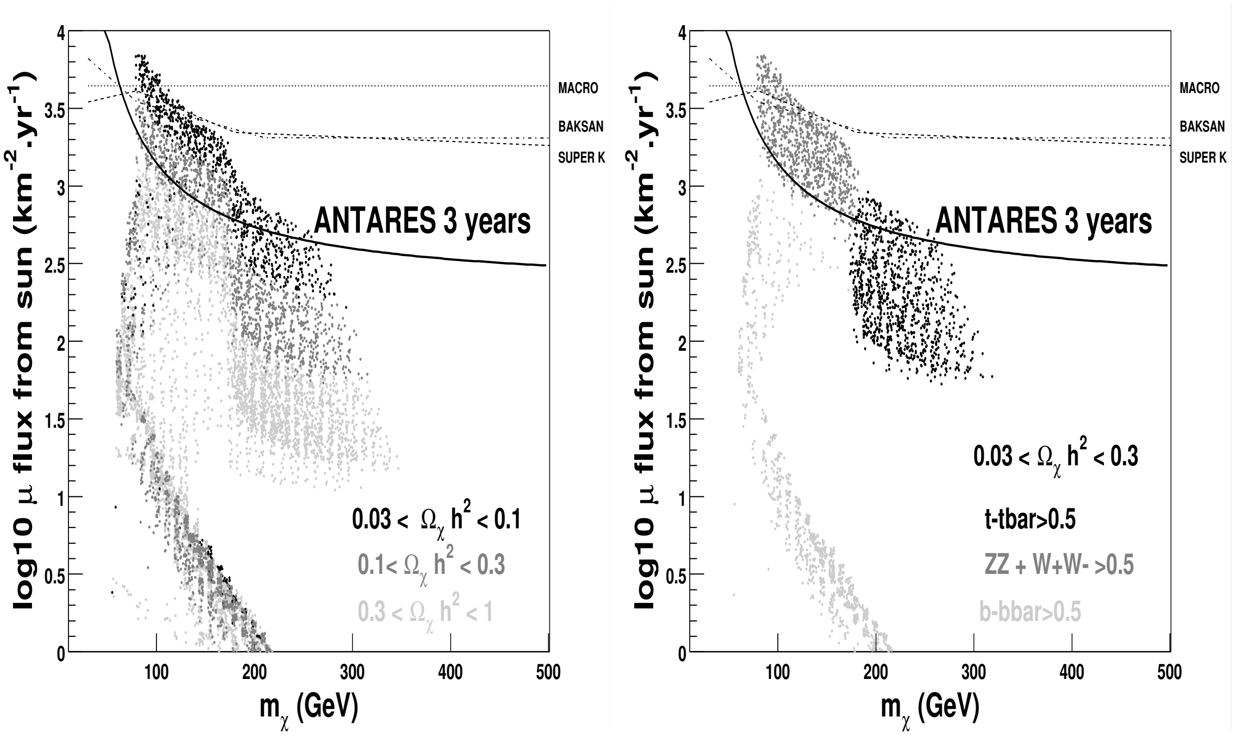

Figure 6.9: Predictions of the integral muon flux for different neutralino masses, M_χ over the mSUGRA parameter space. The expected experimental sensitivity for hard neutralino annihilations after three years of observation is also shown along with the MACRO, SuperKamiokande and Baksan limits. The left hand plot shows the points grouped by relic density, the right hand plot shows the points grouped by dominant annihilation channel.

experiments typically express their limits) can also be made. For reference, we compare ANTARES to the expected sensitivity of EDELWEISS II [165] (which will produce results on a similar timescale to ANTARES) as being representative of the next generation of direct detection experiments.

The left hand plot of Figure 6.10 shows the predicted muon fluxes and (spin-independent) WIMP-nucleon scattering cross-section. The points are grouped according to the sensitivities of ANTARES and EDELWEISS II. There are some points at which only one experiment is sensitive and some where both are sensitive showing both the complementarity and the redundancy offered by indirect and direct detection techniques. Of course, there is also a large region where neither experiment is sensitive due to the wide range of possible parameters in the mSUGRA parameter space scan.

The right hand plot in Figure 6.10 shows the same scan points grouped depending on how close they are to the expected EDELWEISS II sensitivity. Here we can see that a large part of the region to which ANTARES is sensitive is not covered by EDELWEISS II, again showing the complementarity of the two techniques.

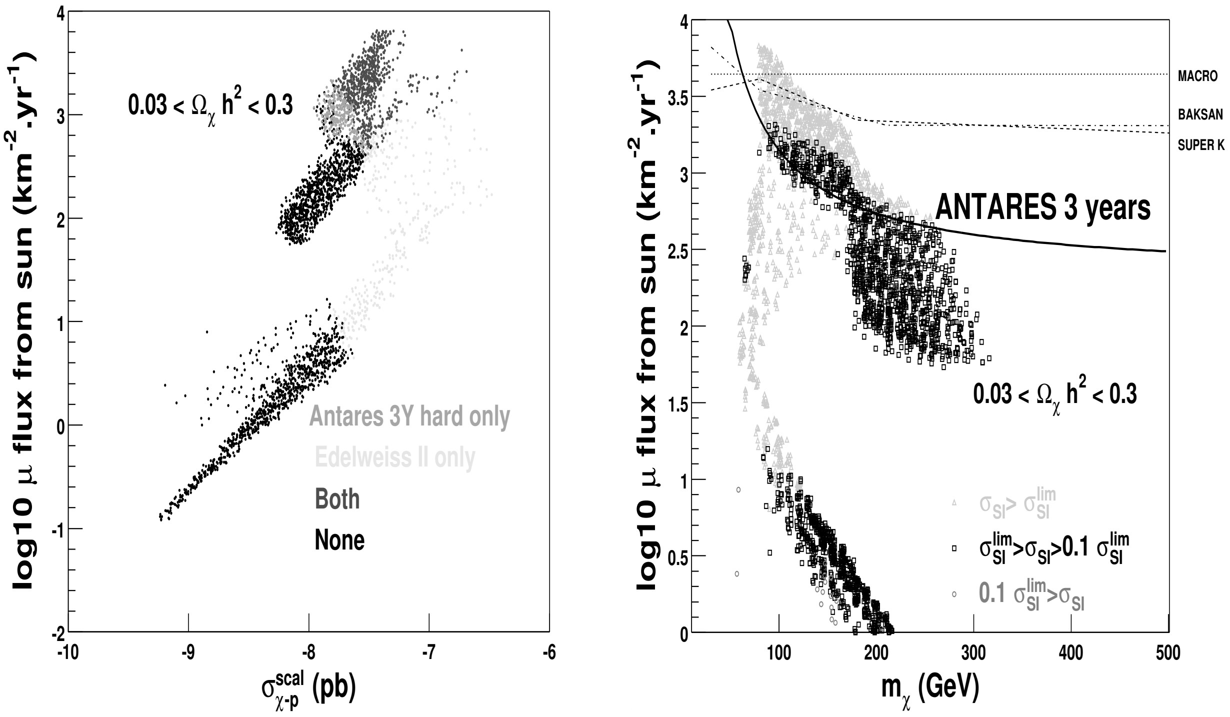

Figure 6.10: Predictions of integral muon fluxes compared to the spin-independent WIMP-nucleon scattering cross-section. Both the direct relationship between the two (left) and the sensitivity of ANTARES compared to the expected EDELWEISS II sensitivity (right) are shown.

6.4.5 Areas for future improvement

This analysis was the first attempt in ANTARES at predicting our sensitivity to the indirect detection of Dark Matter. It was undertaken in parallel with a study of the sensitivity to Dark Matter annihilation at the centre of the Earth [154]. There are several areas in which this analysis can be improved in the future:

- For both the analysis of neutralino annihilation at the centre of the Sun and the Galaxy, we have a source with a known direction. In the analysis above we have not used this information in the reconstruction. This ensures that we avoid any bias in the reconstruction of the backgrounds which could affect the estimated event rates. However, we could imagine that carefully using the directional information to improve the reconstruction efficiency in the direction of the signal could lead to improved limits.

- The reconstruction here was developed primarily for high energy neutrinos - specifically those from astrophysical sources. Whilst there is still a useful efficiency for muon energies down to about 30 GeV, further improvements could be made by lowering this threshold and improving the efficiency in the energy range between 30 and 100 GeV. Work is in progress within ANTARES to use the analysis for the neutrino oscillation study which includes events confined to a single string for this purpose.

- As mentioned above, the azimuthal dependence of the detector efficiency is neglected in this analysis. This is not expected to have a large effect on the final results but should still be investigated.

The analysis described above is the starting point for future studies of the sensitivity of ANTARES for the indirect detection of Dark Matter. We have shown that competitive limits can be set in a relatively short length of time and that this is a promising area for future study.

6.5 Summary

In this chapter we have developed a complete analysis chain to determine the expected sensitivity of ANTARES for the indirect detection of Dark Matter from both the Sun and Galactic Centre. This analysis uses both the results of the simulation methods described in Chapter 3 and Chapter 4 and the reconstruction and analysis methods described in Chapter 5. The analysis described here takes account of the following:

- The detector Monte Carlo simulation includes both the effect of scattering and the hadronic shower contribution to the Cherenkov light production (Chapter 4). This is the first analysis in ANTARES to include both of these effects simultaneously.
- The reconstruction and analysis used here has been shown to reduce the number of atmospheric muons misreconstructed as upgoing to the level of ~ 80 per year (albeit based on a relatively limited sample of events). This is small compared to the number of selected atmospheric neutrinos and is the best selection available in ANTARES in this respect.
- We have taken into account the position of the sources over one year (Section 6.1.2) for both the signal efficiency and background estimates.
- We have used two extremes for the distribution of neutrino energies produced by the annihilation of neutralinos into Standard Model particles (Section 1.4.4). The actual neutrino energy distribution (and hence our predicted limits) for any set of branching ratios must lie between these extremes.
- We have estimated the atmospheric neutrino background using the Bartol flux which is the largest of those considered in Section 5.2.4.
- We have considered a range of cone sizes tracking the source within which we calculate our signal efficiency and expected background. The optimal value (i.e. that which gives the best limit) has been selected independently for each neutralino mass (Section 6.4.1).
- We applied the widely used method of [153] to set upper limits on the neutrino fluxes from Dark Matter annihilation for a process described by Poisson statistics in the presence of background (Section 6.4.1 and Section 6.4.2).

- We presented our final results as a limit on the muon flux for direct comparison with other experiments, converting our neutrino flux limits using ratios of muon to neutrino fluxes calculated with the DarkSUSY code (Section 6.4.3).

The final results presented in Section 6.4.3 allow for a direct comparison with other experiments that have published similar limits. We have shown that, even with one year of observation, we can set competitive limits for both the Sun and the Galactic Centre for neutralino masses above 100 GeV. For three years of observation, our expected limits extend well below those published by current experiments (which are unlikely to improve significantly in the future). We will be able to improve on the published limits for both the Sun and Galactic Centre. For the Sun, we are able to improve on the existing limits from above 100 GeV (assuming a hard annihilation channel) to above 200 GeV (assuming a soft annihilation channel) and probe muon fluxes at the level of 300 km^{-2} yr^{-1}. For the Galactic Centre, we can improve on the existing limits from above 100 GeV (hard) to above 150 GeV (soft) and probe muon fluxes at the level of 200 km^{-2} yr^{-1}.

Compared to the predictions made by [69, 156] for different points in mSUGRA parameter space, we have seen that ANTARES is only sensitive to those models where the dominant neutralino annihilation channel is into gauge bosons. For these models however, ANTARES is sensitive to a range of neutralino masses between 100 and 300 GeV with a cosmologically interesting relic density. Using predictions of muon fluxes and WIMP-nucleon scattering cross-sections, we have compared our limits with the direct detection sensitivity of EDELWEISS II. For different regions of parameter space, there is both complementarity and redundancy between the two techniques though, in both cases, a large range of models remain inaccessible.

The results presented in this chapter are a starting point for future analyses. Work is in progress to improve the low energy efficiency of the reconstruction and hence improve the limits below 100 GeV and to perform a similar analysis for the detection of Dark Matter annihilation at the centre of the Earth. Further improvement can also be expected in all of these analyses if the directional information of the source is used in the reconstruction. We have shown that this is a promising area for future study where ANTARES is able to make a significant impact on our understanding of the Dark Matter problem.

Chapter 7

Summary, conclusions and future prospects

The ANTARES neutrino telescope is currently being constructed and deployed at a site 2.4 km deep in the Meditteranean. It is aiming to detect neutrinos from astrophysical sources, Dark Matter annihilation and to make a measurement of the oscillations of atmospheric neutrinos. An important part of this process is to develop simulations to allow us understand the raw data the experiment produces, to develop and optimise both the hardware and software used in the experiment and to develop analyses to make predictions for different theoretical models and so we are ready to test their validity with the experimental data.

7.1 Simulation methods

The simulation methods developed in Chapter 3 allow for the simulation of neutrino interactions and muon propagation for energies up to 100 PeV in a manner which produces complete, minimally biased, distributions of all particles which arrive at the ANTARES detector (without the artificial distinction between neutrinos interacting inside and outside the can). In Chapter 3 and Section 5.2 we showed that the systematic errors arising from these simulations are small (less than 8%) over the vast majority of the energy range of interest for ANTARES.

The detector Monte Carlo described in Chapter 4, KM3, includes the effect of photon scattering in the water. In Section 5.3 we showed firstly that it is important to include scattering in the simulations and then that differences in the water properties can have a significant effect on the ANTARES detector performance (both the efficiency and the angular resolution). Further measurements of the water properties at the ANTARES site are needed to fully understand these effects and, without this, it is going to be difficult to quantify the influence of the water properties in any published results.

Both the Cherenkov light from the hadronic shower for neutrinos interacting near the detector and the effect of the wavelength dependence of the refractive index are important and we have added these to KM3. We saw in Section 5.2 that the inclusion of the Cherenkov light produced by the hadronic shower is important for neutrino energies up to 10 TeV and is therefore relevant for all the physics studies in ANTARES.

7.2 ANTARES detector performance

In Section 5.4 we defined an effective area which correctly includes both the volume and surface events and is valid over the full range of energies seen in ANTARES (as opposed to the surface effective area used previously in ANTARES which we have shown to significantly underestimate the sensitivity for neutrino interactions below 3 TeV). This calculation makes use of effective muon ranges for which a full simulation including the effects of the different media around the ANTARES detector is described in Appendix A. We found effective areas around 20000 m^2 for an E_ν^{-2} neutrino flux. It should be noted that effective areas are defined for a particular neutrino flux and that the energy-dependent effective areas (such as that in Figure 5.9) are intermediate stages in the calculation. The above result (or at least similar results obtained using the same method) is that which should be taken as describing the general performance of ANTARES. This efficiency lies somewhere between that of AMANDA-B10 and AMANDA-II.

We calculated the angular resolution of ANTARES (defined as the median of the distribution of angles between the reconstructed muon track and the parent neutrino). At high energies, this approaches 0.15°. However, as for the effective areas, our figure of merit should be a comparison for a particular neutrino spectrum. We found an angular resolution of 0.23° for our reference choice of an E_ν^{-2} neutrino flux. This is significantly better than that the value of $\sim 3°$ quoted for AMANDA and shows an advantage of building a neutrino telescope in water where the effect of photon scattering is much smaller than in ice[1].

The analysis method described in Chapter 6 allows for limits to be set for the sensitivity to neutrinos produced by the annihilation of Dark Matter at the centre of the Sun and of the Galaxy and the results presented here are the first predictions of these limits for ANTARES. After three years of observation, ANTARES can improve on the current experimental limits for neutralino masses greater than somewhere between 100 GeV and 200 GeV (depending on the branching rations for particular models). In the most optimistic case of a high mass WIMP and “hard” annihilation channels, we are sensitive to muon fluxes at the level of a few hundred km^{-2} yr^{-1}, a factor of five better than current experiments.

With this analysis, we can begin to probe some regions of the supersymmetric parameter space with neutralino masses in the range 100 to 300 GeV and make both complimentary and redundant searches for neutralinos compared to direct detection experiments. Not only is this encouraging in itself, indirect searches for neutralino annihilation in both the Sun and near the Galactic Centre are areas in which ANTARES a capable of something AMANDA and ICECUBE are not (as both the Sun and Galactic Centre remain at or above the horizon as viewed with a neutrino telescope at the South Pole).

[1] This, of course, isn’t the only important factor. Ice has a longer absorption length and very low background levels giving a potentially higher efficiency for an otherwise identical detector.

7.3 Prospects for the future

The construction of ANTARES is the beginning of a new era in the development of neutrino telescopes being deployed in the deep ocean with the eventual aim being to scale up to a km^3 detector capable of making detailed measurements of some of the proposed astrophysical neutrino fluxes. The contents of this thesis contribute to both our ability to understand the performance of ANTARES and in the search for Dark Matter. Whilst we have made the best use of the knowledge currently available, there are still a range of issues to be addressed:

- The accuracy of both the simulation of high energy neutrino interactions and high energy muon propagation, especially above 1 PeV, is still an open question which relies on the extrapolation of various aspects of Standard Model physics (for example, the extrapolation of PDFs to predict high energy neutrino cross-sections) which could be affected by new physics beyond the Standard Model.
- The understanding of the optical properties of the water at the ANTARES site, especially at the most important wavelengths around 460 nm is a large contribution to the uncertainty in these simulations. Only with further careful measurements at the ANTARES site (either with a dedicated instrument or using the ANTARES experiment itself as a detector), will this understanding improve.
- In this thesis, we simulated the optical background as random PMT hits with a constant rate corresponding to the baseline of the measurements discussed in Section 2.3.3. The question of the optical background in terms of the bioluminescent bursts both on the rate of PMT hits and correlations between different areas of the detector is still open and, although some preliminary measurements have been made, more detailed studies of dead times and the effect on the reconstruction are needed.
- The full trigger logic is currently missing from the simulation chain and whilst preliminary results obtained in developing this logic show a small effect on the rate of "physics" events, more detailed studies applied to a range of different analyses are needed.
- The rejection of atmospheric muons (which has only been demonstrated on a small sample of Monte Carlo events) will be a significant challenge. Work is underway to produce and analyse a more statistically significant sample of events corresponding to one month of "real" data.
- For the Dark Matter analysis, there are a number of aspects missing from this, the first real estimate of the sensitivity of ANTARES. For example, the azimuthal detector efficiency and the reconstruction of low energy events using single lines can be added and this is all work for the future.

Given all the points above, the real test for simulations and analyses described here still remains and will only be fully addressed with the data still to be taken with ANTARES in the coming years. Only then will the potential of these deep ocean neutrino telescopes begin to be seen and applied to the problems of neutrino astrophysics and Dark Matter.

Appendix A

Effective muon ranges

In Section 3.3.3, page 70, we defined the effective muon range in terms of muon survival probabilities. We used this effective muon range in Section 5.4, page 136, to calculate the overall effective area for ANTARES. For the level of accuracy required in Section 5.4, the effective muon ranges calculated in a single medium (either rock or water) were sufficient. However, in principle, different muon energy losses in rock and water will have an effect on the ranges for muons which reach the ANTARES detector, depending on the muon direction and its entry point on the can.

In this appendix we describe a simulation method which calculates the effective muon ranges for particles propagating through a general combination of rock and water where the water is at the end of the muon path (corresponding to muons arriving at the ANTARES detector). We then fit a functional form to these ranges so these results can be used in further calculations. The results used in Section 5.4 correspond to the limits of the results presented here when all the propagation is in either rock or water.

A.1 Effective muon range simulation

The effective muon range is defined in Eq. (3.7), page 70, as the integral of the survival probabilities, P_{surv} as a function of muon propagation distance, X. We can write this integral as a sum over discrete bins, i, at increasing distances from the muon starting point. If each bin has width ΔX and the survival probability for muons reaching bin i is P^i_{surv}, we can write the effective muon range as:

$$R_{eff}(E_\mu) = \int_0^\infty P_{surv}(E_\mu, X)dX \simeq \sum_i P^i_{surv}\Delta X \tag{A.1}$$

Now, consider a linear simulation path with a total length of D, divided into a number of bins, each of width ΔX, as shown in Figure A.1. Consider a general bin, i: if we propagate a number of muons, N^i_{gen}, all starting in bin i with the same initial energy, and record the number of muons, N^i_{rec}, which reach the end of the simulation path, the fraction of the generated sample which is recorded will be the survival probability for muons propagating

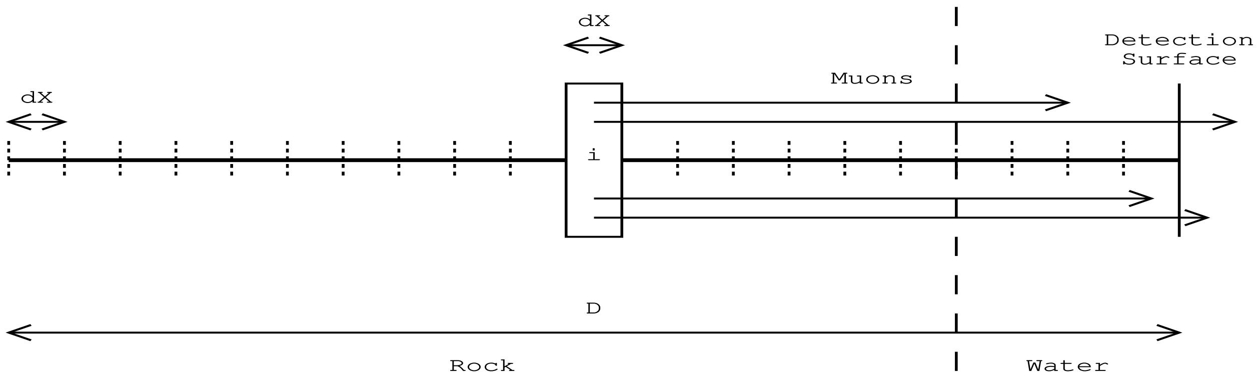

Figure A.1: The simulation geometry for the effective muon range simulation. A path of length D is divided into a number of bins. Muons are propagated from each bin to the end of the path and the fraction reaching the end are recorded for each bin, i, to give the survival probability as a function of distance.

over the distance from bin i to the end of the path. This is the same survival probability for bin i as that in Eq. (A.1) above and we can therefore write the effective muon range as:

$$R_{eff} \simeq \sum_i \frac{N^i_{rec}}{N^i_{gen}} \Delta X \tag{A.2}$$

If we repeat this process for all bins, i, and start the same number of muons, N^i_{gen}, in each bin, we can write the above equation in terms of the total path length, D, and the total number of generated muons, N_T:

$$R_{eff} \simeq \sum_i N^i_{rec} \times \frac{\Delta X}{N^i_{gen}} \simeq \frac{D}{N_T} \sum_i N^i_{rec} \tag{A.3}$$

where $\frac{\Delta X}{N_{gen}}$ and $\frac{D}{N_T}$ are both the inverse of the number of muons per unit distance which, as the same number of muons were started in each bin, must be equivalent. Now if we divide the simulation path in Figure A.1 into rock and water where the water is at the end of the path, we have the effective range (i.e. the average propagation distance) for muons arriving at the ANTARES detector (where the distance in water is fixed by the muon direction and the entry point on the can).

We can use this result to develop a simulation to calculate the effective muon ranges for different distances of muon propagation in water (corresponding to different entry points and angles for muons at the detector):

1. A linear path is defined with the origin at the rock-water interface. The length of the path, D, is (conservatively) chosen to be 1.5 times the maximum muon range as calculated above in Section 3.3.2, page 68. All calculations are performed in water equivalent units.

2. A number of reference points for recording muons are defined. The first of these corresponds to the rock-water interface (at the origin of the simulation path). The remainder are at 20 equal steps along the path in water to correspond to a range of different entry points on the can. As the simulation is run, the numbers of muons passing each of these reference points will be counted.

3. For a large number of muons all with the same starting energy:

   (a) A point is randomly chosen along the path defined above. If this point is in the rock, the muon is propagated to the rock-water boundary and, assuming the muon survives, the number of muons at this point is incremented by 1.

   (b) The muon is propagated to each of the reference points defined above or until it is stopped. For each reference point it reaches, the number of muons at that point is incremented by 1.

4. We then divide the number of muons at each reference point by the total number generated and multiply by the total length of the simulation path to give the effective range for each distance in water.

The random sampling of the starting point of each muon in the simulation performs the sum over i in Eq. (A.3) and we therefore have a calculation of the effective muon range for each of the chosen muon propagation distances in water. To obtain the results presented below, the above simulation is run using both PropMu and MUM for muon energies in equal steps of 0.5 in $\log_{10}(E_\mu)$ from 10 GeV to 1 EeV. An additional simulation is performed at 200 GeV to provide more information in the region where stochastic energy losses become important (see Figure 3.6, page 66).

A.2 Results in a single medium

The effective ranges in each medium as a function of the starting muon energy are shown, for MUM, in the left hand plot of Figure A.2. The right hand plot in Figure A.2 shows the ratio of the effective range in water to the effective range in rock for both PropMu and MUM as a function of energy. At low energies, the range in water is shorter[1], at high energies, it is longer with the change over between 100 GeV and 1 TeV.

At low energies, ionisation loss dominates (see Figure 3.6). Very crudely, from the formulae in the appendix of [114], this is because ionisation losses are proportional to $\frac{Z}{A}$ which is higher in water ($\frac{10}{18}$) than in rock ($\frac{11}{22}$), giving shorter ranges. On the basis of this argument, one would expect ranges in water to be approximately $\frac{11}{22} \times \frac{18}{10} \simeq 0.9$ of those in rock which is close to what we see in Figure A.2 for MUM.

At high energies, the stochastic processes dominate, in particular Bremsstrahlung and direct pair production. These are both interactions with charged nucleons which are proportional to the value of Z^2 in the medium which is larger in rock (11^2 compared to 10^2).

[1] Note that everything here is in water equivalent units where the effective density of each medium is unity and hence, all density effects cancel

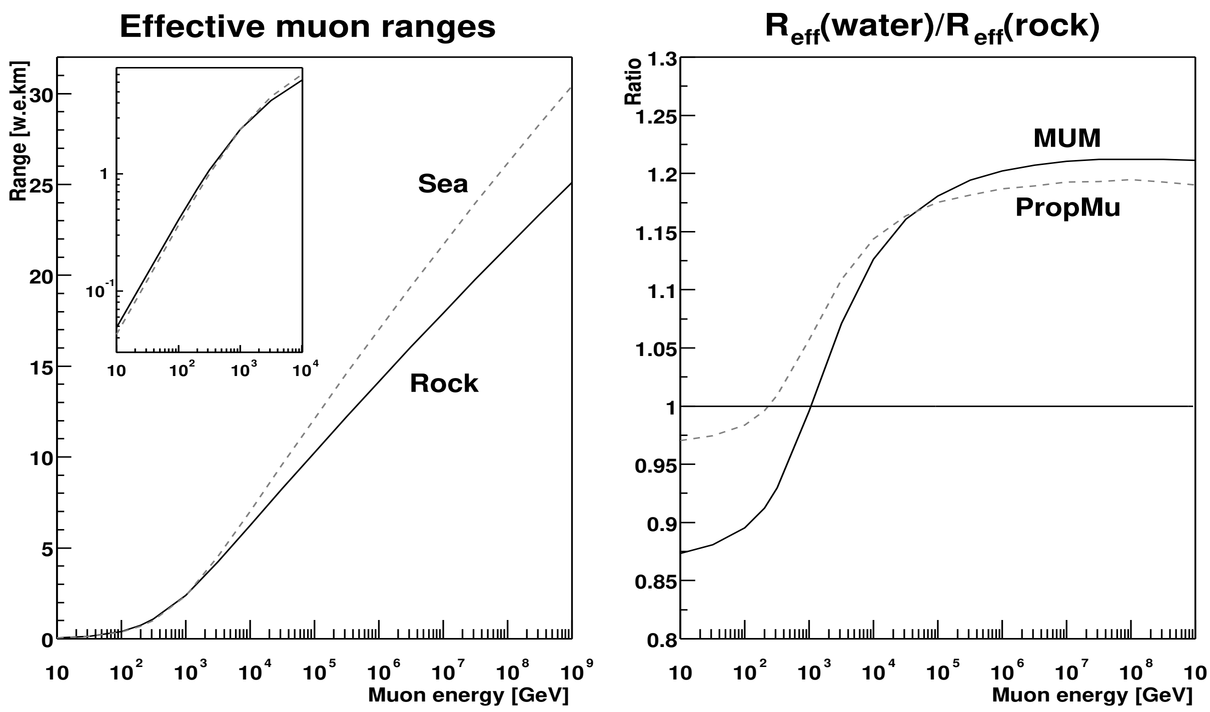

Figure A.2: Effective muon ranges in rock and sea water using MUM (left). The ratios of the range in rock to the range in water are shown in the right hand plot for MUM and PropMu.

Again, crudely, one would expect ranges in water to be longer by approximately $(\frac{11}{10})^2 \simeq 1.2$ which is close to what is found in both cases.

A.3 Results and fits for a general combination of two media

The simulations described above produce tables of data with the effective muon range as a function of the starting energy and the distance the muon traveled in water, X. For each energy, we perform a five parameter fit (P_1 ... P_5) as a function of the distance in water. We (empirically) determine the form of this fit function based on very general statements about the form of the effective muon ranges.

When the propagation distance in water is significantly less than the muon range, the different muon energy losses in rock and water are important and we would expect some slow continuous change over between the range in rock and the range in water as the distance changes. It is also possible for a muon with an initial energy above the point where the ranges in rock and water are the same ($\sim$1 TeV for MUM from the right hand plot of Figure A.2) to spend its entire path in the medium with the higher energy loss and hence it is possible that the muon range could be shorter than that for rock or water alone for some values of X. This behaviour can most simply be described by a quadratic function of X.

When the distance in water significantly exceeds the range of the muon, all the paths of muons reaching the reference point will be entirely in water so the effective range will be just that in water alone. As the muon energy losses are essentially random, this will not be a sharp division but will be approached asymptotically as X increases.

To include both these effects, we separate the function describing the effective range, $R_{eff}(X)$, into two parts, R^1_{eff} and R^2_{eff}, depending on the value of X. Below, some value of $X = P_3$, we have:

$$R^1_{eff}(X \leq P_3) = P_4 \times X^2 + P_5 \times X + P_2 \tag{A.4}$$

Above this value, we construct a function which tends asymptotically to the range in water alone at large X and match the value and gradient to that of R^1_{eff} at $X = P_3$:

$$R^2_{eff}(X \geq P_3) = R^1_{eff}(P_3) + (P_1 - R^1_{eff}(P_3)) \times \tanh\left(R'^1_{eff}(P_3) \times \frac{X - R^1_{eff}(P_3)}{P_1 - R^1_{eff}(P_3)}\right) \tag{A.5}$$

where each of the parameters has the meaning:

P_1 is the effective range in water.

P_2 is the effective range in rock.

P_3 is the distance corresponding to the change over between R^1_{eff} and R^2_{eff}.

P_4 **and** P_5 are the quadratic and linear parameters respectively which describe the change over in importance between rock and water.

$R'^1_{eff}(P_3)$ is the gradient of R^1_{eff} at P_3.

We then fit each of the simulated energies with this function to get a table of the variation of each of these parameters with muon energy. The results of these fits for each code for 100 GeV, 1 TeV and 10 TeV muons are shown in Figure A.3 and the variation of the fit parameters with energy is shown in Figure A.4.

All the results are then tabulated (see Appendix B, Table B.7 for PropMu and Table B.8 for MUM for the complete results) and interpolated in $\log_{10}(E_\mu)$ and $\log_{10}(P_1...P_3)$ and linearly in P_4 and P_5 to get a final function $R_{eff}(E_\mu, X)$. The complete set of original data at each energy along with the values of $R_{eff}(E_\mu, X)$ obtained from this interpolation are shown in Appendix B in Figure B.1.

A.4 Discussion

Using the results shown in Figure A.3, we can try and understand the different variations in the effective muon ranges with distance in terms of the basic processes of muon energy loss.

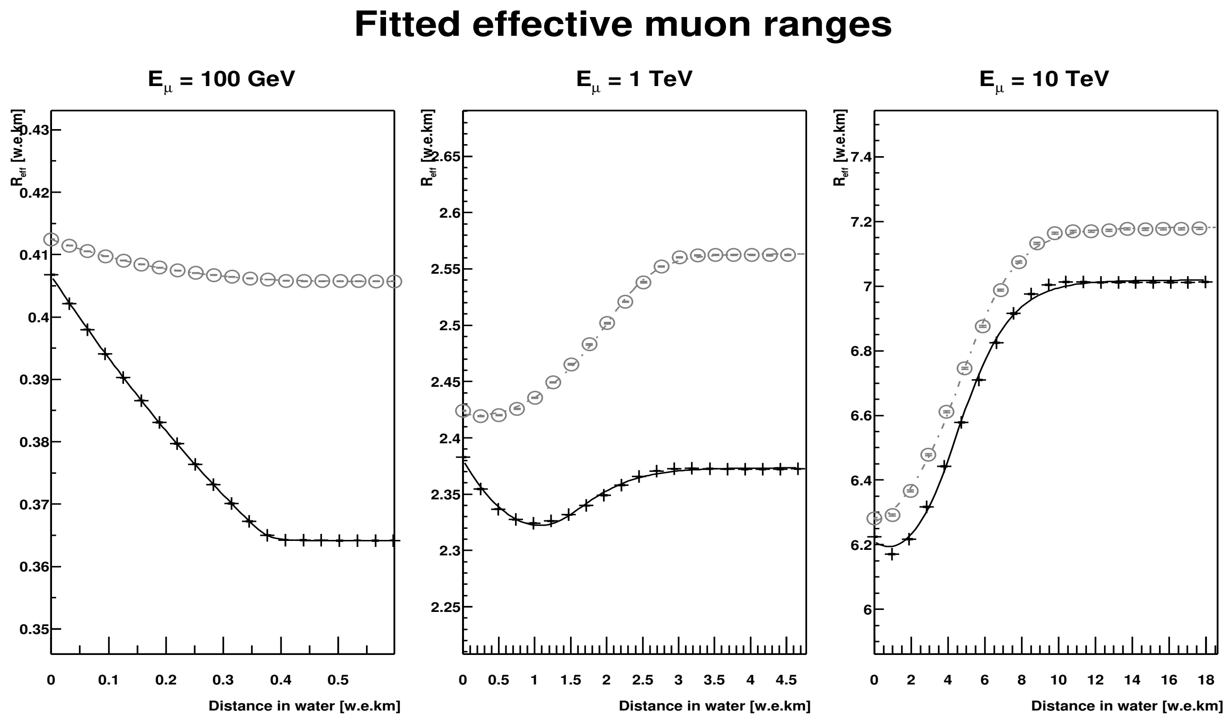

Figure A.3: Fitted effective muon ranges as a function of the length of the muon path in water for 100 GeV, 1 TeV and 10 TeV muons for MUM (black +) and PropMu (grey O). For the form of the fitting function, see the text.

For reference, we shall concentrate on the results from MUM although similar features are present in the PropMu results.

100 GeV: Ionisation losses dominate and the energy loss per metre is constant. Hence, the ranges in both rock and water are well defined (all the muons travel the same distance). Therefore, the change over from rock to water as the distance in water changes is just linear between the two extreme values.

1 TeV: As the muon energy increases, the stochastic energy loss processes become important and the longer range changes over from rock to water. The muon always starts in rock and ends in water. Hence, for some intermediate value of the distance in water, the muon will always be in the medium with the higher energy losses and hence produce a range shorter than either the range in rock or water.

10 TeV: For the majority of the muon track, it is in the region where the stochastic processes dominate so we see a shorter range in rock than water. Due to the random nature of the stochastic processes, the transition between rock and water as X increases is not well defined and therefore the muon range asymptotically approaches that in water, only reaching its final value when X is significantly larger than the effective muon range.

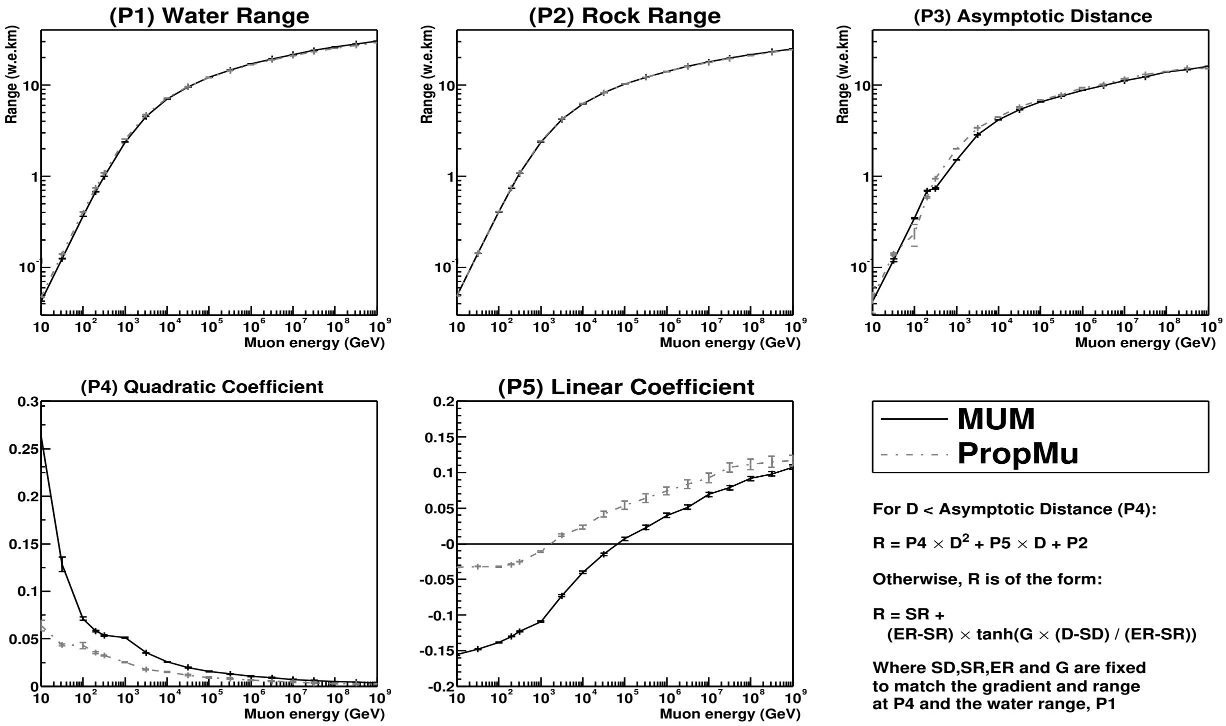

Figure A.4: The 5 fit parameters (see text) as a function of energy for the muon effective range fits. These results are interpolated to produce the final fit function.

The values of the effective ranges in rock and water and the shortest effective range (where it isn't one of the preceding two) are shown in Table A.1. The final column shows the size of the variation in ranges between the two media as a fraction of the range in water.

From Table A.1, we can see that below 200 GeV, the differences in the ranges in rock and water are generally greater than 10%. In the intermediate range of energies, as the longest range changes from rock to water, the differences are smaller than this but, from the energies sampled here, are greater than 2.5%. At high energies, the differences rise again up to a maximum of 18% (consistent with the expectation based on the simple arguments for effective ranges in a single medium).

Finally, from Figure A.3, we can see the differences between MUM and PropMu in the effective ranges in the different media. The differences are most significant at low energies in water suggesting that the known inaccuracies in PropMu arise from the description of the continuous energy losses in water.

A.5 Summary

The simulations and fits described here have given us a single function (based on tabulated data) from which we can calculate the effective muon range at any energy up to 1 EeV in rock, water or any combination of both to correspond to muons arriving at the ANTARES

Energy (GeV)	R(water) (w.e.km)	R(rock) (w.e.km)	Min. (w.e.km)	$\lvert\frac{\Delta R}{R}\rvert$
1.000×10^1	0.0425	0.0486	-	0.144
3.162×10^1	0.1253	0.1422	-	0.135
1.000×10^2	0.3642	0.4066	-	0.116
2.000×10^2	0.6764	0.7408	-	0.095
3.162×10^2	0.9989	1.0740	-	0.075
1.000×10^3	2.3734	2.3804	2.3223	0.024
3.162×10^3	4.5140	4.2031	4.1655	0.077
1.000×10^4	7.0183	6.2099	6.1944	0.117
3.162×10^4	9.5820	8.2299	8.2276	0.141
1.000×10^5	12.1108	10.2246	-	0.156
3.162×10^5	14.5894	12.1847	-	0.165
1.000×10^6	17.0154	14.1156	-	0.170
3.162×10^6	19.3860	16.0185	-	0.174
1.000×10^7	21.7019	17.8779	-	0.176
3.162×10^7	23.9728	19.7177	-	0.177
1.000×10^8	26.1667	21.5253	-	0.177
3.162×10^8	28.3205	23.2975	-	0.177
1.000×10^9	30.4165	25.0343	-	0.177

Table A.1: Effective muon ranges in water and rock and the shortest possible range in a combination of both. The final column gives the range of effective muon ranges at that energy as a fraction of the range in water.

detector. We can qualitatively understand the form of this function in terms of the muon energy losses in each individual medium.

This function can be used to calculate overall effective areas or the event rate corresponding to a particular neutrino flux given an effective area as described in Section 5.4, taking into account the different media around the detector. However, in Section 5.4, we used just the values of these fits at $X = 0$ (rock) and $X \rightarrow \infty$ (water) as the differences between the media were small given the accuracy required in the calculation and the other uncertainties in the simulations.

Appendix B

Tabulated data and detailed results

This appendix contains detailed results obtained from some of the various simulations described in this thesis. In addition, we tabulate some of the numbers extracted from various papers for reference.

B.1 Event generation tables

There are two sets of tables corresponding to the event generation stage of the simulations described in Chapter 3. Firstly, there are the extracted values of the neutrino cross-sections and kinematic variables and secondly tables relating to the simulations and fits for muon propagation.

B.1.1 Neutrino interactions

For comparison between the values extracted from LEPTO in Section 3.2 and those published in [103] (referred to as Gandhi in the tables), the neutrino and anti-neutrino charged-current cross-sections for eight energies between 10 GeV and 10^8 GeV are given in Table B.1. The corresponding values for the mean inelasticities are given in Table B.2.

Energy (GeV)	σ_{ν}^{CC} (Gandhi)	σ_{ν}^{CC} (LEPTO)	$\sigma_{\overline{\nu}}^{CC}$ (Gandhi)	$\sigma_{\overline{\nu}}^{CC}$ (LEPTO)
10^1	0.777×10^{-41}	0.839×10^{-41}	0.368×10^{-41}	0.415×10^{-41}
10^2	0.697×10^{-40}	0.720×10^{-40}	0.349×10^{-40}	0.370×10^{-40}
10^3	0.625×10^{-39}	0.638×10^{-39}	0.338×10^{-39}	0.350×10^{-39}
10^4	0.454×10^{-38}	0.456×10^{-38}	0.292×10^{-38}	0.296×10^{-38}
10^5	0.196×10^{-37}	0.194×10^{-37}	0.162×10^{-37}	0.164×10^{-37}
10^6	0.611×10^{-37}	0.598×10^{-37}	0.582×10^{-37}	0.570×10^{-37}
10^7	0.176×10^{-36}	0.168×10^{-36}	0.174×10^{-36}	0.166×10^{-36}
10^8	0.478×10^{-36}	0.443×10^{-36}	0.477×10^{-36}	0.443×10^{-36}

Table B.1: Neutrino charged-current cross-sections from [103] and integrated in LEPTO.

Energy (GeV)	$<y>_\nu$ (Gandhi)	$<y>_\nu$ (LEPTO)	$<y>_{\overline{\nu}}$ (Gandhi)	$<y>_{\overline{\nu}}$ (LEPTO)
10^1	0.483	0.462	0.333	0.330
10^2	0.477	0.474	0.340	0.348
10^3	0.472	0.476	0.354	0.366
10^4	0.426	0.420	0.345	0.343
10^5	0.332	0.320	0.301	0.295
10^6	0.273	0.283	0.266	0.268
10^7	0.250	0.247	0.249	0.249
10^8	0.237	0.228	0.237	0.226

Table B.2: Mean inelasticities for neutrino charged current interactions from [103] and sampled from LEPTO.

B.1.2 Muon propagation

The maximum muon ranges in Section 3.3.2 are obtained by interpolating on the distances at which the muon survival probability falls below a certain level for a range of energies. These distances for 6 different survival probability levels (corresponding to the muon range cut levels described in Section 3.4.3) are given for PropMu: Table B.3 for rock and Table B.4 for sea water and for MUM: Table B.5 for rock and Table B.6 for water.

The five parameters extracted at each simulated energy from the fits to the effective muon range in Appendix A.3 are given for PropMu in Table B.7 and for MUM in Table B.8. The fits themselves for the effective muon range as a function of the distance in water at each simulated energy are shown in Figure B.1 for both PropMu and MUM.

Energy (GeV)	10^{-1}	10^{-2}	10^{-3}	10^{-4}	10^{-5}	10^{-6}
1.000×10^0	4.95	4.95	4.95	4.95	4.95	4.95
3.162×10^0	16.33	16.33	16.33	16.33	16.33	16.33
1.000×10^1	49.11	49.11	49.11	49.11	49.11	49.11
3.162×10^1	145.40	145.40	145.40	145.40	145.40	145.40
1.000×10^2	429.16	429.16	429.16	429.16	429.16	429.16
3.162×10^2	1210.96	1228.94	1235.38	1235.38	1235.38	1235.38
1.000×10^3	2936.16	3066.48	3167.45	3216.25	3247.43	3263.62
3.162×10^3	5531.34	5997.77	6392.78	6597.97	6758.96	6887.31
1.000×10^4	8366.43	9321.16	10183.80	10650.75	11009.81	11292.50
3.162×10^4	11092.52	12517.85	13890.90	14659.53	15207.23	15492.10
1.000×10^5	13664.38	15521.72	17360.02	18384.85	19113.50	19947.57
3.162×10^5	16105.35	18329.06	20604.40	21873.08	22983.18	23396.46
1.000×10^6	18436.98	20963.31	23623.28	25163.45	26533.22	27559.41
3.162×10^6	20638.12	23468.21	26392.48	28108.01	29401.53	29904.04
1.000×10^7	22793.97	25856.52	29123.27	31045.60	32404.11	33203.98
3.162×10^7	24855.93	28130.67	31708.83	33993.84	35698.50	36335.40
1.000×10^8	26821.94	30292.84	34082.38	36353.00	38332.75	40170.75
3.162×10^8	28746.83	32412.29	36467.85	39058.01	40907.24	42688.42
1.000×10^9	30595.68	34427.07	38625.15	41224.94	43535.16	45464.25

Table B.3: Muon ranges in rock for PropMu as a function of survival probabilities for calculating maximum muon ranges

Energy (GeV)	10^{-1}	10^{-2}	10^{-3}	10^{-4}	10^{-5}	10^{-6}
1.000×10^0	4.78	4.78	4.78	4.78	4.78	4.78
3.162×10^0	15.80	15.80	15.80	15.80	15.80	15.80
1.000×10^1	47.65	47.65	47.65	47.65	47.65	47.65
3.162×10^1	141.48	141.48	141.48	141.48	141.48	141.48
1.000×10^2	419.75	419.75	419.75	419.75	419.75	419.75
3.162×10^2	1210.40	1224.90	1224.90	1224.90	1224.90	1224.90
1.000×10^3	3080.70	3200.81	3289.50	3327.82	3348.19	3348.19
3.162×10^3	6144.41	6657.18	7082.06	7290.21	7476.19	7648.21
1.000×10^4	9640.95	10794.18	11834.51	12351.80	12826.55	13074.34
3.162×10^4	13025.97	14816.31	16563.42	17543.25	18367.92	18606.73
1.000×10^5	16225.94	18562.22	20938.23	22332.12	23440.12	24036.42
3.162×10^5	19216.31	22015.58	24937.91	26615.21	27997.56	28896.17
1.000×10^6	22057.19	25267.38	28636.51	30644.32	32138.09	33022.49
3.162×10^6	24771.37	28338.72	32259.66	34638.56	36508.99	38240.19
1.000×10^7	27355.83	31222.68	35392.41	38034.71	39793.32	41858.14
3.162×10^7	29830.46	33938.31	38503.46	41349.46	43770.35	45189.73
1.000×10^8	32206.97	36555.28	41426.67	44450.85	46635.84	47911.52
3.162×10^8	34488.17	39067.87	44193.66	47500.71	49621.53	51017.57
1.000×10^9	36640.39	41417.12	46753.04	50231.97	52861.54	53893.97

Table B.4: Muon ranges in water for PropMu as a function of survival probabilities for calculating maximum muon ranges

Energy (GeV)	10^{-1}	10^{-2}	10^{-3}	10^{-4}	10^{-5}	10^{-6}
1.000×10^0	4.79	4.79	4.79	4.79	4.79	4.79
3.162×10^0	16.10	16.10	16.10	16.10	16.10	16.10
1.000×10^1	48.65	48.65	48.65	48.65	48.65	48.65
3.162×10^1	152.55	155.15	156.42	156.44	156.44	156.44
1.000×10^2	448.68	460.08	468.74	472.16	473.93	474.09
3.162×10^2	1240.22	1286.09	1323.55	1341.13	1352.14	1355.25
1.000×10^3	2942.79	3122.34	3275.44	3352.97	3412.56	3457.09
3.162×10^3	5510.11	6024.76	6484.40	6726.67	6877.17	6941.45
1.000×10^4	8353.34	9341.57	10267.15	10792.95	11137.82	11467.80
3.162×10^4	11103.25	12583.17	14014.26	14814.60	15449.70	15878.88
1.000×10^5	13724.60	15636.15	17546.08	18624.73	19364.23	20018.44
3.162×10^5	16219.60	18500.35	20855.96	22137.57	23597.17	24647.33
1.000×10^6	18610.59	21198.75	23908.38	25464.79	26751.00	27670.05
3.162×10^6	20910.78	23816.07	26932.10	28778.64	30210.66	30974.92
1.000×10^7	23144.08	26296.62	29677.02	31803.14	33445.69	34217.62
3.162×10^7	25316.28	28707.16	32285.67	34546.99	36135.99	37288.07
1.000×10^8	27409.43	31019.88	34946.99	37401.57	39218.42	40129.14
3.162×10^8	29463.19	33287.43	37442.94	40044.24	42439.47	43871.25
1.000×10^9	31460.08	35456.82	39888.72	42607.88	44638.56	45550.19

Table B.5: Muon ranges in rock for MUM as a function of survival probabilities for calculating maximum muon ranges

Energy (GeV)	10^{-1}	10^{-2}	10^{-3}	10^{-4}	10^{-5}	10^{-6}
1.000×10^0	4.11	4.11	4.11	4.11	4.11	4.11
3.162×10^0	13.95	13.95	13.95	13.95	13.95	13.95
1.000×10^1	42.47	42.47	42.47	42.47	42.47	42.47
3.162×10^1	133.99	136.08	137.06	137.09	137.09	137.09
1.000×10^2	398.80	408.06	414.95	417.75	418.39	418.40
3.162×10^2	1135.56	1172.17	1201.10	1213.47	1220.76	1224.19
1.000×10^3	2874.75	3025.80	3153.55	3214.84	3257.47	3268.96
3.162×10^3	5838.89	6339.72	6776.10	6993.10	7145.46	7261.23
1.000×10^4	9390.10	10479.24	11479.95	12010.74	12407.38	12612.47
3.162×10^4	12922.90	14648.06	16325.64	17268.31	18064.68	18432.75
1.000×10^5	16268.59	18562.22	20845.38	22178.91	23177.68	23834.72
3.162×10^5	19433.00	22221.83	25069.74	26755.94	28157.25	28950.09
1.000×10^6	22449.68	25653.71	29000.80	30937.12	32687.37	34624.23
3.162×10^6	25325.62	28898.80	32638.49	34921.26	36660.63	38670.51
1.000×10^7	28076.30	31960.24	36189.28	38693.66	40550.84	41685.00
3.162×10^7	30738.31	34931.73	39527.56	42267.83	44514.34	45660.45
1.000×10^8	33301.21	37757.23	42635.35	45680.41	48330.34	49526.77
3.162×10^8	35770.93	40463.18	45646.77	48917.00	51499.16	54495.43
1.000×10^9	38165.40	43084.38	48574.68	52129.09	55924.24	57952.22

Table B.6: Muon ranges in water for MUM as a function of survival probabilities for calculating maximum muon ranges

Energy (GeV)	P1 (water)	P2 (rock)	P3 (asymp. dist)	P4 (x^2)	P5 (x)
1.000×10^1	0.0474	0.0488	0.0463	0.06387	−0.03301
3.162×10^1	0.1400	0.1436	0.1413	0.04373	−0.03194
1.000×10^2	0.4057	0.4124	0.2349	0.04283	−0.03205
2.000×10^2	0.7508	0.7534	0.5901	0.03557	−0.02881
3.162×10^2	1.0926	1.0930	0.9461	0.03244	−0.02522
1.000×10^3	2.5633	2.4214	2.0044	0.02531	−0.01076
3.162×10^3	4.7333	4.2576	3.4006	0.01787	0.01212
1.000×10^4	7.1816	6.2700	4.4534	0.01517	0.02348
3.162×10^4	9.6525	8.2717	5.7535	0.01175	0.04151
1.000×10^5	12.0696	10.2552	6.8513	0.00925	0.05418
3.162×10^5	14.4237	12.1817	7.8014	0.00811	0.06389
1.000×10^6	16.7212	14.0687	9.3561	0.00633	0.07429
3.162×10^6	18.9575	15.9230	10.1906	0.00533	0.08342
1.000×10^7	21.1407	17.6979	11.6777	0.00454	0.09249
3.162×10^7	23.2552	19.4521	13.1087	0.00340	0.10712
1.000×10^8	25.3426	21.1339	14.0563	0.00307	0.11149
3.162×10^8	27.2924	22.8379	15.3683	0.00253	0.11506
1.000×10^9	29.2222	24.5130	15.1846	0.00245	0.11654

Table B.7: Effective muon range fit parameters for PropMu.

Energy (GeV)	P1 (water)	P2 (rock)	P3 (asymp. dist)	P4 (x^2)	P5 (x)
1.000×10^1	0.0425	0.0486	0.0424	0.26301	−0.15565
3.162×10^1	0.1253	0.1422	0.1201	0.12857	−0.14792
1.000×10^2	0.3642	0.4066	0.3478	0.07124	−0.13838
2.000×10^2	0.6764	0.7408	0.6927	0.05818	−0.13014
3.162×10^2	0.9989	1.0740	0.7354	0.05353	−0.12311
1.000×10^3	2.3734	2.3804	1.5175	0.05114	−0.10905
3.162×10^3	4.5140	4.2031	2.8453	0.03526	−0.07286
1.000×10^4	7.0183	6.2099	4.1517	0.02558	−0.04006
3.162×10^4	9.5820	8.2299	5.3549	0.01977	−0.01477
1.000×10^5	12.1108	10.2246	6.5433	0.01561	0.00694
3.162×10^5	14.5894	12.1847	7.6020	0.01300	0.02298
1.000×10^6	17.0154	14.1156	8.7873	0.01052	0.03996
3.162×10^6	19.3860	16.0185	9.8487	0.00902	0.05148
1.000×10^7	21.7019	17.8779	11.1719	0.00713	0.06928
3.162×10^7	23.9628	19.7177	12.3073	0.00613	0.07864
1.000×10^8	26.1667	21.5253	13.9148	0.00487	0.09167
3.162×10^8	28.3205	23.2975	14.8482	0.00431	0.09820
1.000×10^9	30.4165	25.0343	16.1445	0.00361	0.10748

Table B.8: Effective muon range fit parameters for MUM.

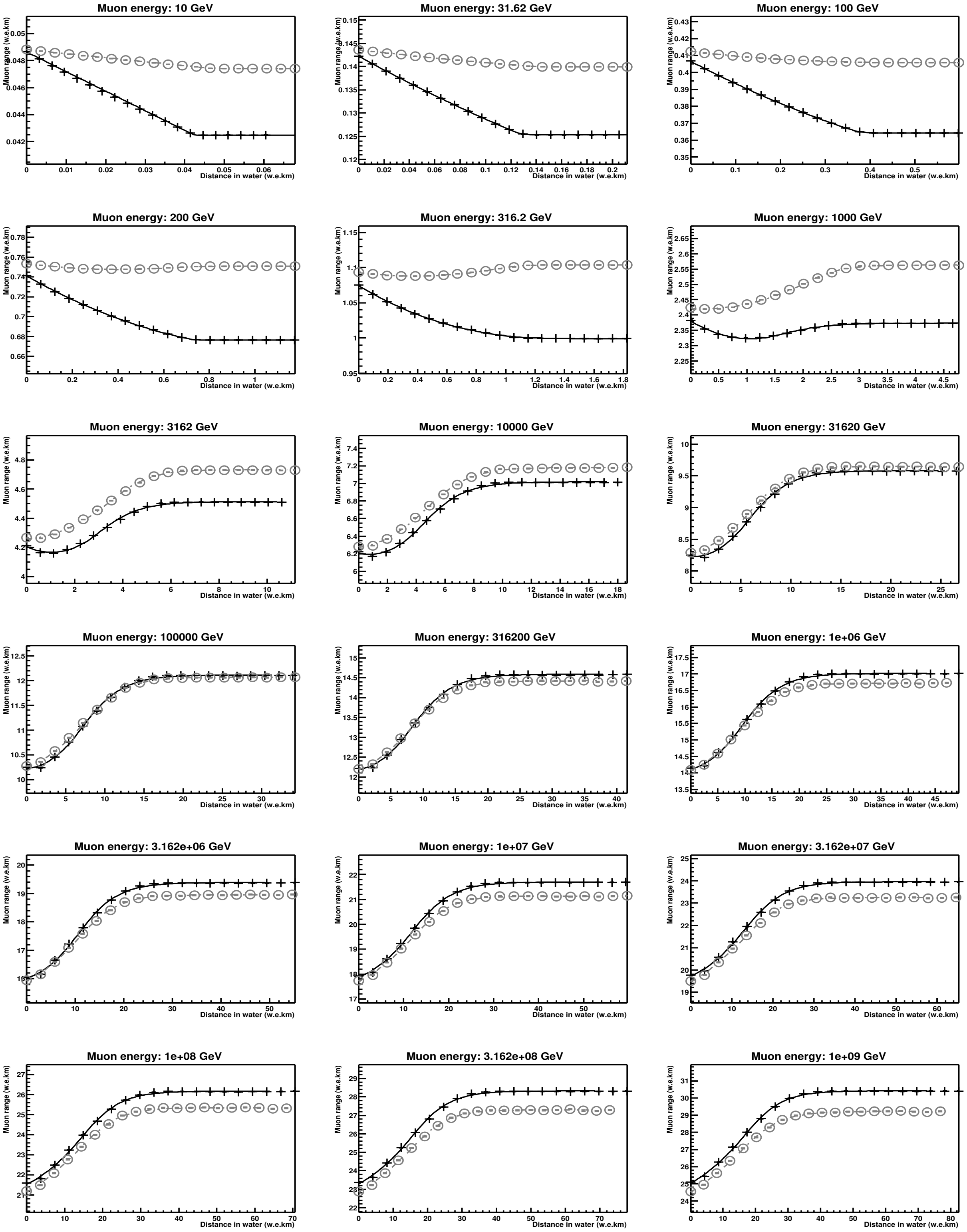

Figure B.1: Fitted effective muon ranges for a range of energies (see Section 3.3.3) as a function of the distance in water at the end of the muon track. The fits are shown for PropMu (grey O) and MUM (black +).

Scattering angle θ (degrees)	$\frac{dN}{d\Omega}(\theta)$	Scattering angle θ (degrees)	$\frac{dN}{d\Omega}(\theta)$
0.100	1.767×10^{3}	50.0	2.275×10^{-2}
0.126	1.296×10^{3}	55.0	1.699×10^{-2}
0.158	9.502×10^{2}	60.0	1.313×10^{-2}
0.200	6.991×10^{2}	65.0	1.046×10^{-2}
0.251	5.140×10^{2}	70.0	8.488×10^{-3}
0.316	3.764×10^{2}	75.0	6.976×10^{-3}
0.398	2.763×10^{2}	80.0	5.842×10^{-3}
0.501	2.188×10^{2}	85.0	4.953×10^{-3}
0.631	1.444×10^{2}	90.0	4.292×10^{-3}
0.794	1.022×10^{2}	95.0	3.782×10^{-3}
1.000	7.161×10^{1}	100.0	3.404×10^{-3}
1.259	4.958×10^{1}	105.0	3.116×10^{-3}
1.585	3.395×10^{1}	110.0	2.912×10^{-3}
1.995	2.281×10^{1}	115.0	2.797×10^{-3}
2.512	1.516×10^{1}	120.0	2.686×10^{-3}
3.162	1.002×10^{1}	125.0	2.571×10^{-3}
3.981	6.580×10^{0}	130.0	2.476×10^{-3}
5.012	4.295×10^{0}	135.0	2.377×10^{-3}
6.310	2.807×10^{0}	140.0	2.329×10^{-3}
7.943	1.819×10^{0}	145.0	2.313×10^{-3}
10.0	1.153×10^{0}	150.0	2.365×10^{-3}
15.0	4.893×10^{-1}	155.0	2.506×10^{-3}
20.0	2.444×10^{-1}	160.0	2.662×10^{-3}
25.0	1.472×10^{-1}	165.0	2.835×10^{-3}
30.0	8.609×10^{-2}	170.0	3.031×10^{-3}
35.0	5.931×10^{-2}	175.0	3.092×10^{-3}
40.0	4.210×10^{-2}	180.0	3.154×10^{-3}
45.0	3.067×10^{-2}		

Table B.9: Petzold's data for the angular distribution of particle scattering (from [137]).

B.2 Detector Monte Carlo tables

The detector Monte Carlo uses a couple of tables of data external to the GEANT Monte Carlo framework and the MUSIC muon propagation code. The first of these is the scattering angular distribution taken from Petzold's data [137]. This is shown as a differential distribution as a function of angle in Table B.9. It is used both within KM3 and in the independent simulation used to parameterise the effect of the wavelength dependence of the refractive index as described in Section 4.3.

In addition, we have the measurements of the effective areas of the ANTARES Optical Modules shown for normal incidence in Table B.10. The data used in the simulations in Chapter 4 includes the full measured angular dependence.

Wavelength (nm)	Energy (eV)	PMT area (m^2)
307.00	4.04886	0.0000192
330.00	3.76667	0.0029198
350.00	3.55143	0.0072341
370.00	3.35946	0.0082788
390.00	3.18718	0.0086441
410.00	3.03171	0.0087832
430.00	2.89070	0.0086005
450.00	2.76222	0.0080876
470.00	2.64468	0.0072576
490.00	2.53673	0.0065589
510.00	2.43725	0.0058779
530.00	2.34528	0.0038987
550.00	2.26000	0.0026499
570.00	2.18070	0.0019886
590.00	2.10678	0.0013460

Table B.10: PMT effective areas in ANTARES simulation codes.

B.3 Setting limits on Poisson distributed data

In Section 5.4.3 and Chapter 6 we used the results of [153] to give upper limits on the rate of observed events from Dark Matter annihilation averaging over a set of experiments which all observe the expected background. This approach uses the data in Table XII of [153] which gives upper limits for background rates up to 15. As we can see from Table 6.1, our rates for 1 year extend slightly beyond this for the largest cone size and will significantly exceed this when considering three years of data.

Within the range of values given Table XII of [153], we linearly interpolate in the values for the 90% confidence limit. For larger values of the expected background, we could perform the full construction as described in [153]. However, this is time consuming and the method is not completely specified from the paper[1]. Instead, we can use the knowledge that, for large backgrounds, the statistical fluctuations are of order $\sqrt{b}$ and fit the data from backgrounds of 10 to 15 with the function $f(b) = P_0 \times \sqrt{b} + P_1$ and extrapolate for higher background rates using that.

As seen in Section 6.4.2, our optimum cone sizes are always less than five degrees and correspond to backgrounds in the range 0 to 15 degrees so we are within the range given directly in [153]. In addition, we also saw in Section 6.4.2 that our dependence on the cone size is weak. Therefore, any error introduced by this extrapolation will be small and will not affect the predicted limits. This remains true provided we are in the regime where the background is small and Poisson distributed.

[1]The scanning of the rate of background has to be modified in some way when the upper limit obtained is not an increasing function of the background. The details of this modification are not given.

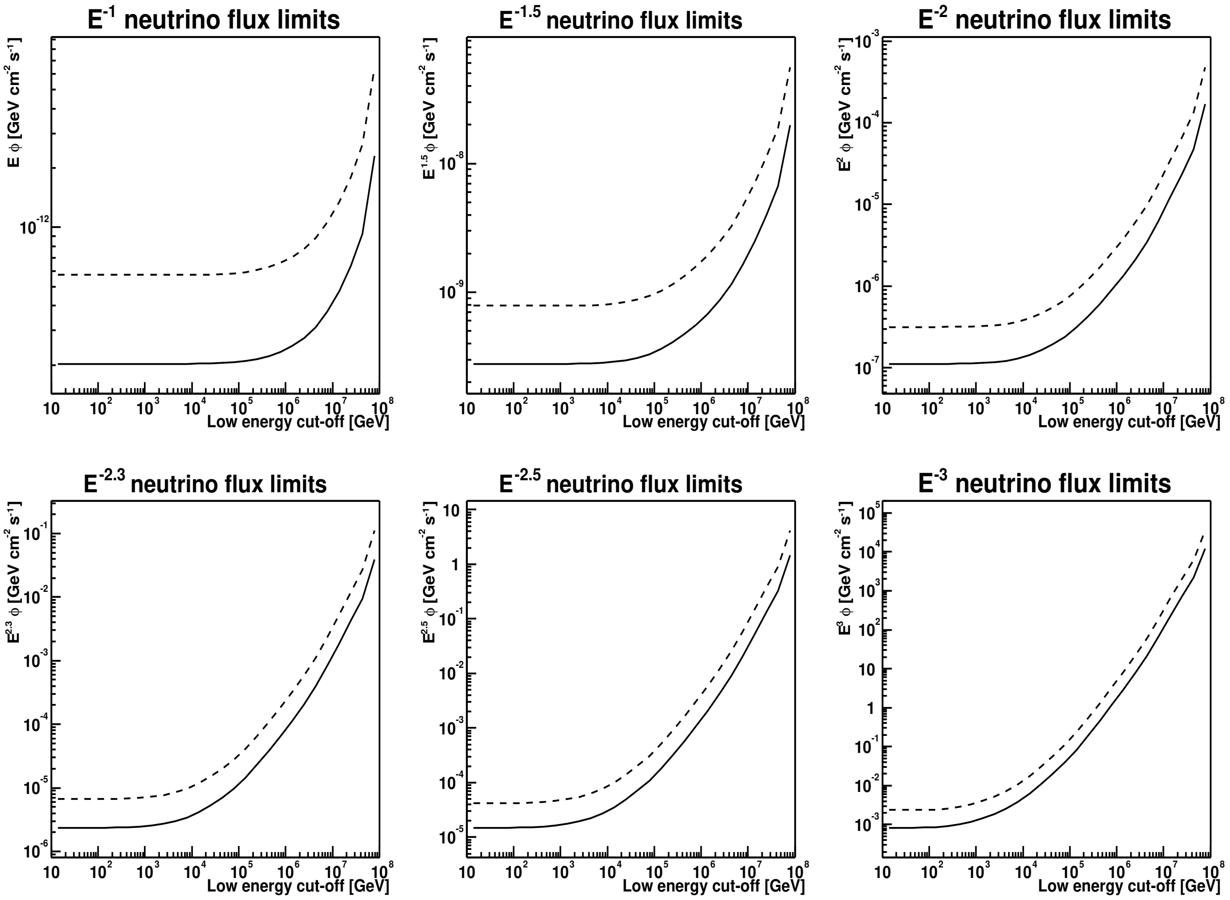

Figure B.2: The ANTARES sensitivity to power-law neutrino fluxes with spectral indices ranging from 1 to 3 as a function of a low energy cut-off in the neutrino spectrum. Note the different vertical scales in each plot.

B.4 Point source neutrino flux limits

In Section 5.4.3, we presented the ANTARES sensitivity to neutrino fluxes with an E_ν^{-2} spectrum as a function of a low energy cut-off in this spectrum. In Figure B.2, we show similar sensitivities (where the sensitivity should be interpreted as the normalisation of the unbroken power-law spectrum at 1 GeV - i.e. A from Eq. (5.16)) for a range of different power law indices ranging from 1 to 3.

From Figure B.2, we can see that the steeper the spectrum (i.e. the more negative the spectral index), the lower the neutrino energy at which the cut-off in the neutrino energy becomes important (as an increasing number of the neutrinos are observed at lower energies). However, even for power-law neutrino fluxes with a spectral index of -3 (which is close to the atmospheric neutrino flux), the sensitivity is not affected unless the form of the neutrino spectrum is modified above 1 TeV. Therefore, in all these models, provided the power-law neutrino energy spectrum remains unbroken down to this energy, the sensitivity is not affected by the details of the spectrum at lower energies.

The reason for this effect is clear: the ANTARES sensitivity increases at higher energies due to the increasing neutrino interaction cross-section and the longer ranges and increased light production of muons. Therefore, for any high energy astrophysical source, the event rate will be dominated by the higher energy neutrinos (up to around 1 PeV at which point the attenuation of neutrinos in the Earth restricts the sensitivity) and hence relatively unaffected by the low energy end of the spectrum.

Appendix C

Production parameters

This appendix contains the input parameters used in the simulations whose results are presented in Chapter 5 and Chapter 6. The parameters described here are the reference choice for all the simulations and, when one is varied to study various systematic effects, the others remain constant.

Event Generation

The input parameters for the event generation are shown in Table C.1. A full description of all of these parameters is given in the context of the event generation method described in Chapter 3. In Table C.1:

- Can Size is the distance the can extends beyond the instrumented volume of the detector (not the total dimensions of the can).
- Spectral Index is the index of the power law spectrum from which the interacting neutrino energies are drawn.
- The muon code, survival probabilities and the neutrino direction cut are the optimal values determined from the simulations in this thesis.

Detector Monte Carlo

The detector Monte Carlo simulations as described in Chapter 4 have the same input parameters for both the high and low energy productions. Except where explicitly noted (i.e. in the studies of systematic effects) they are as shown in Table C.2. The simulation of the potassium-40 is performed as a random rate on each PMT within a window extending before and after the first and last particle induced hit on the detector. The rate and window are as given in Table C.2. To simulate high amplitude events from a single source, the detector Monte Carlo merges hits on a single PMT within 1.0 ns. The ARS simulation integrates all hits within 25 ns and the ARS is then dead for 250 ns (corresponding to the readout time). Two ARS operate together for each PMT to minimise dead time.

Property	Low Energy (LE) Simulation	High Energy (HE) Simulation
Can Size	200 m	200 m
E_{min}	5 GeV	5 GeV
E_{max}	10^5 GeV	10^8 GeV
$\cos\theta_{min}$	-1	-1
$\cos\theta_{max}$	1	1
Spectral Index	-2	-1.35
Events per file	2.5×10^{10}	5×10^9
Number of files	20 ν + 20 $\overline{\nu}$	20 ν + 20 $\overline{\nu}$
Number of energy bins	10	10
Muon code	MUM	MUM
Survival Probability	10^{-1}	10^{-1}
Neutrino direction cut	500 m	500 m
Target Medium	Isoscalar	Isoscalar

Table C.1: Input parameters for the event generation. The "Spectral Index" refers to the power law spectrum for the interacting neutrinos. For an explanation of the other parameters, see Chapter 3.

Property	Value
Potassium-40 rate	60000 Hz
Potassium-40 window	500 ns
PMT hit merging	1.0 ns
Water Model	P2
Number of ARS	2
ARS Integration time	25 ns
ARS dead time	250 ns

Table C.2: Input parameters for the detector Monte Carlo. For a full explanation of the parameters, see Chapter 4.

Appendix D

Simulation packages

A number of different simulation packages are used in this thesis essentially as "black boxes" in order to perform detailed simulations of different aspects of the physics relevant to ANTARES. In this Appendix we give a brief overview of each of the different codes and describe the essential theoretical and experimental inputs to each, commenting on their accuracy and suitability.

D.1 Dark Matter

The calculation of the neutrino fluxes produced by neutralino annihilation at the centre of the Sun involves many different stages to determine the mass and coupling of the neutralino, the relic densities at different times and the resulting capture and annihilation rates in the Sun and finally the spectra of neutrinos produced by these annihilations. Given suitable supersymmetric model inputs, DarkSUSY [63] performs these calculations in detail to give the resultant neutrino fluxes at the Earth. The Suspect code [73] can be used to provide the theoretical inputs to DarkSUSY in terms of the input parameters of a specific supersymmetric model (mSUGRA).

D.1.1 DarkSUSY

A full description of the different elements of the DarkSUSY code is given in [61, 63] and references therein[1]. A determination of the neutrino and muon fluxes from Dark Matter annihilation relies on several stages of calculation:

Particle masses and coupling from supersymmetry The MSSM is used to determine the masses and couplings of all the supersymmetric partners of the Standard Model particles. As there is no direct experimental evidence to support the existence of

[1] According to the DarkSUSY web site, full documentation is in the process of being written although this has been the case for over a year at the time of writing. Additional information is contained in the DarkSUSY source code distribution.

supersymmetry, typically, a range of the MSSM parameter space is scanned to give a range of possible masses and couplings. Limits from accelerator searches (mainly from LEP2) and the branching ratios of $b \to s\gamma$ decays (from the CLEO experiment) are applied to this scan to exclude inconsistent models.

Relic density calculations The relic densities of the lightest neutralino are calculated by numerically solving the Boltzmann equation corresponding to the freeze-out time of supersymmetric particles in the early universe, including the effect of co-annihilations between the lightest neutralino and other supersymmetric particles which are close in mass to M_χ.

Neutrino capture and annihilation rates Given the neutralino-nucleon scattering cross-section (which is predicted for a given supersymmetric model), the capture rate in the Sun can be calculated assuming the local halo mass density and velocity dispersion. The annihilation rate depends on the number density squared and the thermally averaged annihilation cross-section and is taken into account in the evolution of the neutralino density at the centre of the Sun. This then yields a prediction of the annihilation rate at the present time.

Neutrino production The branching ratios of the neutralino annihilation to specific Standard Model particles are predicted for a particular supersymmetric model. The neutrino spectra are calculated by Monte Carlo simulations using PYTHIA/JETSET (see below) to parameterise the neutrino production from the hadronisation of heavy quarks. The results for each channel are tabulated to give the overall neutrino spectrum for a particular model. The softening of the neutrino spectrum from charged and neutral current interactions in the Sun is also simulated and included in the final results. The muon fluxes at the Earth (used in the conversion in Chapter 6) are then calculated in a similar way to that described in Section 5.4.

The dominant uncertainty in all the above calculations is of course supersymmetry. Without any direct evidence for its existence, all parameters consistent with current experimental limits are equally valid and this is reflected in the wide range of model predictions (as seen in Figure 6.9, page 175). For a specific supersymmetric model, there are still significant uncertainties in, for example, the halo mass density which can vary by a factor of two between different models. Therefore, rather than making accurate predictions of neutrino fluxes, these calculation should be seen as giving ballpark estimates of possible fluxes. This situation would of course be vastly improved by the discovery of supersymmetric particles at future accelerator experiments.

D.1.2 Suspect

The Suspect code [73] takes a mSUGRA model (specified in terms of the parameters described in Section 1.4.3) and calculates the particle masses and couplings at the electroweak scale which then form the inputs to DarkSUSY. The same comments which apply to the uncertainty in the appropriate supersymmetric parameters as for DarkSUSY above still apply with the additional assumption that "supergravity" is the correct mechanism for the breaking of supersymmetry.

D.2 Event generators

Event generators take an input set of particles (e.g. two collider beams or a neutrino and a fixed target) and calculate the outgoing particle state at the interaction vertex. The interaction physics can be very complicated and hence codes exist which perform these simulations based on current theoretical and experimental knowledge. Three codes are used in this thesis to simulate different aspects of neutrino interactions on nucleon targets, LEPTO [105], PYTHIA/JETSET [74] and RSQ [107]. In addition, we use parameterisations of modern Parton Distribution Functions supplied by PDFlib [106].

D.2.1 LEPTO

The LEPTO ([105] and references therein) code numerically simulates complete events in deep inelastic lepton-nucleon scattering. The electroweak interaction between the incoming lepton (a neutrino in this case) and the parton in the nucleon is simulated based on the Standard Model electroweak cross-sections and includes QCD corrections to first order and to higher orders in the "leading $\log Q^2$" approximation. The Parton Distribution Functions are drawn from PDFlib (see below) and the hadronisation of the struck nucleon is simulated using PYTHIA/JETSET.

LEPTO is part of the standard particle physics simulation toolkit in use at CERN and elsewhere [104] and has been compared and validated against a range of experimental data. In this thesis, we have used it at energies higher than its stated maximum energy of 10 TeV. The comparison with the results of Gandhi et al. [103] in Chapter 3 have shown that, numerically, it can be used without significant problems up to much higher energies.

D.2.2 PDFlib

PDFlib [106] is part of the CERN program library [104] and is an archive of Parton Distribution Functions published by many different groups. In this sense, it is just a convenient collection of different sets of experimental data and inferences and the accuracy of the code is therefore not an issue. As discussed in Chapter 3, the choice of PDF can affect the neutrino cross-section and therefore PDFlib is a valuable tool for investigating the effects of this choice.

D.2.3 PYTHIA/JETSET

PYTHIA/JETSET [74] is the combination of two codes which perform simulations of the final state particles produced in hard scattering interactions. Here, it is used by LEPTO to calculate the hadronic final state of deep inelastic neutrino-nucleon scattering. These states are complicated due to the non-perturbative interactions of quarks and gluons in the struck nucleus. However, due to their point-like nature and relative non-directionality, ANTARES is not sensitive to the detailed structure of the hadronic shower so the detailed accuracy of the code is not of paramount importance. Having said that, PYTHIA/JETSET has been compared to experimental data, most notably in e^+e^- annihilations and good agreement has been found. We therefore have confidence that it is both suitable and sufficient for our needs.

D.2.4 RSQ

The RSQ package [107] was originally developed to study the atmospheric neutrino background to the Soudan II nucleon decay experiment. Its simulation is based on parameterisations of experimentally measured cross-sections and hadronic multiplicities. Although the code itself is reasonably old (the first version dating from 1987), the contribution of resonant and quasi-elastic neutrino interactions to the overall ANTARES event rate is small (but not negligible) and therefore any uncertainty from these simulations can be neglected.

D.3 Muon propagation

The numerical simulation of the propagation of high energy muons is of interest in both cosmic ray and high energy neutrino physics. Many different codes have been developed to perform these simulations with varying degrees of speed and accuracy. The three codes used in this thesis, MUM [114], PropMu [109] and MUSIC [118], are suitable under different conditions as described below.

As discussed in Section 3.3, all numerical muon propagation codes divide energy losses into continuous and stochastic processes based on the relative energy transfer of a particular interaction (i.e. stochastic interactions resulting in the loss of only a small amount of the total muon energy are treated as part of the continuous energy loss). A lower threshold for the relative energy transfer implies a more detailed, but significantly longer, simulation and this is one of the principle differences between different muon propagation codes. A general discussion of the basic technique of numerical muon propagation is given in [114] and will not be discussed further here.

D.3.1 MUM

The MUM code [114] is the most modern of the codes described here. It was developed to be fast, transparent (in terms of the way it used muon interaction cross-sections) and to be of "adequate and known accuracy". This last point, discussed in detail in [114], ensures that the numerical errors introduced by the propagation algorithm are known and do not exceed the uncertainty from the muon interaction cross-sections. This understood and documented accuracy was one of the principle reasons for its adoption in the event generator described in Chapter 3.

The value of the relative energy transfer chosen to divide stochastic and continuous energy losses in the event generation of 0.01 is sufficient to obtain the correct muon fluxes from neutrino interactions (as discussed in [114]). However, the muon energy losses over small distances (i.e. much less than the interaction length for stochastic interactions) may not be accurately reproduced. Hence, a different code is needed for the detector Monte Carlo.

D.3.2 MUSIC

The MUSIC code [118] performs a simulation of high energy muon propagation in a similar manner to MUM. The principle difference is that the relative energy transfer cut is chosen to be 10^{-3} giving an improved accuracy over small distances. Numerically, the code has been shown [114] to be accurate to better than the uncertainty on its inputs. Additionally, it includes the effect of muon multiple scattering. Whilst being significantly slower than MUM (a factor of 600 is quoted in [114]), it is a suitable choice for the detector Monte Carlo simulation described in Chapter 4 where detailed accuracy is most important.

D.3.3 PropMu

The PropMu code [109] has historically been used for muon propagation in underground and underwater experiments. In [114], it was noted that there were significant numerical errors in the propagation of muons in water (and this effect can also be seen in Appendix A). It is, however, fast and includes the effect of muon multiple scattering. We therefore use it in this thesis to examine this effect as shown in Section 3.4.4 and Section 5.2.3. However, PropMu is not accurate enough to make detailed numerical predictions of event rates for ANTARES.

D.4 Detector Simulation

The detector simulation takes a set of particles, propagates them through the instrumented volume of the detector, calculating their energy loss and any secondary particles they produce and then determining the response of each of the detector elements to the passage of these particles. The underlying code to all ANTARES detector simulations is GEANT [131] (part of the CERN program library [104]). The simulation code used in this thesis, KM3, is describe in detail in Chapter 4. In this section, we give a brief overview of GEANT and the alternative ANTARES detector Monte Carlo, Geasim, which is used in the simulation of Cherenkov light produced by the hadronic shower at the neutrino interaction vertex.

D.4.1 GEANT 3

The GEANT [131] package is in widespread use in high energy physics. It performs detailed simulations of particle transport through a range of different media. It has been used, and therefore verified, by a large number of different physics experiments and its accuracy is therefore well understood and it is a suitable tool for use in these simulations.

There are a large number of tunable parameters which represent trade-offs between accuracy and speed in the simulation. Although care has been taken to ensure the chosen values of these parameters are suitable for ANTARES, this is still something of an open issue and could potentially merit further investigation. However, the real test of the ANTARES detector simulations will depend on the experimental data taken with the ANTARES detector.

D.4.2 Geasim

The main ANTARES simulation code used in this thesis, KM3, is described in some detail in Chapter 4. We also make use of Geasim [129] to simulate the Cherenkov light produced by the hadronic shower as given by the event generator. The simulation of the particle transport is performed by GEANT as discussed above. However, fully tracking all the Cherenkov photons produced is too computationally intensive to be an option for ANTARES. Therefore, the amount of light seen by an optical module is parameterised as a function of the distance and direction with respect to the particle track.

To reduce the dimensionality of the parameterisation, only the case of a photon propagation medium without scattering is considered. This is a limitation of Geasim (as a full analytical parameterisation in a medium such as the ANTARES site including photon scattering would be extremely complicated and no such parameterisation has been found). Therefore, for long muon tracks where the accurate reconstruction of the direction is important, the alternative approach of building photon tables, as described in Chapter 4, is adopted. The detailed particle tracking performed in Geasim (by GEANT) is, however, still useful for the case of the hadronic showers. As discussed above, the accuracy of this approach can only really be tested based on the experimental data taken by the ANTARES detector.

D.5 Summary

All the simulation codes described here are the result of a great deal of work by a large number of people. Where possible, the results of these simulations have been checked against experimental data and, if necessary, corrected to take account of discrepancies with new measurements. We are therefore justified at this stage in taking these packages as "black boxes" and using them in further simulations (with an awareness of their applicability and limitations as discussed in this Appendix). However, where differences between simulation and experimental data do emerge, it is no longer sufficient to treat these simulations as black boxes and their results and assumptions should be re-examined on the basis of this new data.

Bibliography

[1] The ANTARES Collaboration. “A Deep Sea Telescope for High Energy Neutrinos” (1999). astro-ph/9907432. `http://antares.in2p3.fr`

[2] Christine Sutton. “Spaceship Neutrino”. Cambridge University Press (1992).

[3] C. L. Cowan, F. Reines, F. B. Harrison, H. W. Kruse & A. D. McGuire. *Science*, **124** (1956) 103–104.

[4] The KamLAND Collaboration. *Nucl. Phys. Proc. Suppl.*, **91** (2001) 99–104.

[5] The K2K Collaboration. *Nucl. Phys.*, **A663** (2000) 795–798.

[6] F. Reines et al. *Phys. Rev. Lett.*, **15**, 9 (1965) 429–433.

[7] B. Cleveland et al. *Astrophys. J.*, **496** (1998) 505–526. This paper gives the results of 30 years of observations of solar neutrino with the Homestake chlorine detector.

[8] K. Hirata et al. *Phys. Rev. Lett.*, **58** (1987) 1490–1493.

[9] J. C. Van Der Velde et al. *Nucl. Instrum. Meth.*, **A264** (1988) 28–31.

[10] M. Goldhaber, L. Grodzins & A. Sunyar. *Phys. Rev.*, **109** (1958) 1015–1017.

[11] G. Danby et al. *Phys. Rev. Lett.*, **9**, 1 (1962) 36–44.

[12] K. Hagiwara et al. *Phys. Rev.*, **D66** (2002) 010001. `http://pdg.lbl.gov`

[13] The Super-Kamiokande Collaboration. *Nucl. Phys. Proc. Suppl.*, **91** (2001) 127–133.

[14] Y. Fukuda et al. *Phys. Lett.*, **B467** (1999) 185–193. hep-ex/9908049.

[15] The SNO Collaboration. *Phys. Rev. Lett.*, **87** (2001) 071301. nucl-ex/0106015.

[16] The SNO Collaboration. *Phys. Rev. Lett.*, **89** (2002) 011301. nucl-ex/0204008.

[17] V. Barger, J. Learned, P. Lipari, M. Lusignoli, S. Pakvasa & T. Weiler. *Phys. Lett.*, **B462** (1999) 109–114. hep-ph/9907421.

[18] Y. Totsuka. Talk given at the Les Houches EuroConference on “Neutrino masses and mixings” (2001). `http://neutrinhouches.in2p3.fr`

[1]Entries containing references of the form astro-ph/0000000 etc are contained within the electronic preprint archive at http://arxiv.org.

[19] S. Biller et al. *Phys. Rev. Lett.*, **80**, 14 (1998) 2992–2995.

[20] Cristina Carloganu. "Caractérisation des performances à basse énergie du futur télescope sous-marin à neutrinos ANTARES et leur application à l'étude des oscillations des neutrinos atmosphériques". Ph.D. thesis, Université de la Méditerranée, Marseille (1999).

[21] A. Cervera et al. *Nucl. Phys.*, **B579** (2000) 17–55. hep-ph/0002108.

[22] C. Albright et al. "Physics at a neutrino factory" (2000). hep-ex/0008064.

[23] The BOREXINO Collaboration. *Nucl. Phys. Proc. Suppl.*, **91** (2001) 58–65.

[24] The MONOLITH Collaboration. *Nucl. Phys. Proc. Suppl*, **100** (2001) 142–144. hep-ex/0101040.

[25] The ICECUBE Collaboration. "ICECUBE: A kilometer scale neutrino observatory." (2001). The original NSF Proposal. `http://www.ssec.wisc.edu/a3ri/icecube/overview/original_nsf_proposal`

[26] Alvarez-Muniz J., Halzen F., Han T. & Hooper D. "Phenomenology of high energy neutrinos in low-scale quantum gravity models" (2001). To appear in Physical Review Letters. hep-ph/0107057.

[27] R. Barbieri & P. Creminelli an A. Strumia. *Nucl. Phys.*, **B585** (2000) 28–44. hep-ph/0002199.

[28] P. Meszaros. "Theories of Gamma-Ray bursts". To appear in Annu. Rev. Astron. Astrophys. **40** (2002). astro-ph/0111170.

[29] Y. Lithwick & R. Sari. *Astrophys. J.*, **555** (2001) 540. astro-ph/0011508.

[30] Alan Bridle. "Images of Radio Galaxies and Quasars". `http://www.cv.nrao.edu/~abridle/images.htm`

[31] R. Cahn & G. Goldhaber. "The Experimental Foundations of Particle Physics". Cambridge University Press (1989).

[32] The KASCADE Collaboration. "Primary energy spectra of cosmic rays selected by mass groups in the knee region". In "Proceedings of the 27th International Cosmic Ray Conference", volume HE, pages 97–100 (2001). Oral session HE1.2. `http://www.copernicus.org/icrc`

[33] J. Cronin, T. Gaisser & S. Swordy. *Sci. Amer.*, **276** (1997) 44. `http://astroparticle.uchicago.edu/cosmic_ray_spectrum_picture.htm`

[34] Anne Oppelt. "Etude de la résolution angulaire du télescope à neutrino ANTARES". Ph.D. thesis, Université de la Méditerranée, Marseille (2001).

[35] G. Gelmini, P. Gondolo & G. Varieschi. *Phys. Rev.*, **D63** (2001) 036006. hep-ph/0003307.

[36] T. Gaisser. *Nucl. Phys. Proc. Suppl.*, **87** (2000) 145–151. hep-ph/0001027.

[37] J. Jelley. *Phys. Rev. Lett.*, **16**, 11 (1966) 479–481.

[38] K. Greisen. *Phys. Rev. Lett.*, **16**, 17 (1966) 748–750.

[39] G. Zatsepin & V. Kuz'min. *JETP Lett.*, **4** (1966) 78.

[40] Antoine Kouchner. "Possibilité d'observation, par le télescope ANTARES, de neutrinos de haute énergie associés aux sursauts gamma et validation des techniques de détection à l'aide d'un prototype." Ph.D. thesis, Université de Paris (2001).

[41] M. S. Longair. "High energy astrophysics". Cambridge University Press (1981).

[42] E. Waxman & J. Bahcall. *Phys. Rev.*, **D59** (1999) 023002. hep-ph/9807282.

[43] T. Gaisser. "High Energy Neutrino Astronomy - The cosmic ray connection". In "Proceedings of the International Workshop on Observing Ultra-high energy Cosmic Rays from Space and Earth", (2000). astro-ph/0011525.

[44] Thomas K. Gaisser, Francis Halzen & Todor Stanev. *Phys. Rept.*, **258** (1995) 173–236. hep-ph/9410384.

[45] A. Mücke & R. Protheroe. *Astropart. Phys.*, **15** (2001) 121–136.

[46] K. Mannheim. *Astron. Astrophys.*, **269** (1993) 67. TeX source only at astro-ph/9302006.

[47] J. Gaidos et al. *Nature*, **383** (1996) 319.

[48] F. Stecker, C. Done, M. Salamon & P. Sommers. *Phys. Rev. Lett.*, **66**, 21 (1991) 2697–2700. There is an erratum in *Phys. Rev. Lett.* **69** 18 (1992) 2738 which lowers the flux prediction by a factor of ~ 45 but doesn't change the qualitative conclusion of a diffuse neutrino flux being detectable above the atmospheric background at high energies.

[49] E. Waxman & J. Bahcall. *Phys. Rev. Lett.*, **78** (1997) 2292–2295. astro-ph/9701231.

[50] A. Dar & A. De Rujula. "The Cannonball model of Gamma-Ray bursts : High energy neutrinos and γ-rays" (2001). astro-ph/0105094.

[51] A. Levinson & E. Waxman. *Phys. Rev. Lett.*, **87** (2001) 171101. hep-ph/0106102.

[52] C. Distefano, D. Guetta, E. Waxman & A. Levinson. "Neutrino flux predictions for known Galactic Microquasars" (2002). astro-ph/0202200. Submitted to *Astrophys. J.*

[53] K. Mannheim, R. J. Protheroe & J. P. Rachen. *Phys. Rev.*, **D63** (2001) 023003. astro-ph/9812398.

[54] J. Bahcall & E. Waxman. *Phys. Rev.*, **D64** (2001) 023002. astro-ph/9902383.

[55] G. Jungman, M. Kamionkowski & K. Griest. *Phys. Rept.*, **267** (1996) 195–373. hep-ph/9506380.

[56] S. Burles, K. Nollett & M. Turner. *Astrophys. J.*, **552**. astro-ph/0010171.

[57] M. Pettini & D. Bowen. *Astrophys. J.*, **560** (2001) 41–48. astro-ph/0104474.

[58] C. B. Netterfield et al. *Astrophys. J.*, **571** (2002) 604–614. astro-ph/0104460.

[59] P. de Bernardis et al. *Astrophys. J.*, **564** (2002) 559–566. astro-ph/0105296.

[60] S. Martin. "A Supersymmetry Primer". This is an extended version of an article in "Perspectives in Supersymmetry", editor G. Kane, World Scientific. hep-ph/9709356.

[61] Joakim Edsjö. "Neutrino induced muon fluxes from neutralino annihilations in the sun and in the earth". Ph.D. thesis, Uppsala University (1997). `http://www.physto.se/~edsjo/articles/index.html`

[62] P. Gondolo & J. Silk. *Phys. Rev. Lett.*, **83** (1999) 1719–1722. astro-ph/9906391.

[63] Paolo Gondolo, Joakim Edsjo, Lars Bergstrom, Piero Ullio & Edward A. Baltz. "DarkSUSY: A numerical package for dark matter calculations in the MSSM". In "Proceedings of the Third International Workshop on the Identification of Dark Matter", pages 318–323. World Scientific (2000). astro-ph/0012234. `http://www.physto.se/~edsjo/darksusy/index.html`

[64] T. Damour & L. Krauss. *Phys. Rev.*, **D59** (1999) 063509. astro-ph/9807099.

[65] S. Ghigna, B. Moore, F. Governato, G. Lake, T. Quinn & Joachim Stadel. *Astrophys. J. Lett.*, **524**. astro-ph/9910166.

[66] P. Gondolo. *Phys. Lett*, **B494** (2000) 181–186. hep-ph/0002226.

[67] G. Bertone, G. Sigl & J. Silk. "Annihilations from the Galactic Centre". In "Proceedings of the Third International Workshop on the Identification of Dark Matter", pages 311–317. World Scientific (2000). astro-ph/0011553.

[68] P. Ullio, H. Zhao & M. Kamionkowski. *Phys. Rev.*, **D64** (2001) 043504. astro-ph/0101481.

[69] V. Bertin, E. Nezri & J Orloff. "Neutrino Indirect Detection of Neutralino Dark Matter in the CMSSM". hep-ph/0204135. Submitted to *Euro. Phys. J. C.*

[70] The Neutralino Working Group. "First results on ANTARES sensitivity to neutrinos from neutralino annihilation in the Sun and Galactic Centre". ANTARES-Physics/2001-016. ANTARES Internal Note.

[71] Vernon Barger, Francis Halzen, Dan Hooper & Chung Kao. "Indirect search for neutralino dark matter with high energy neutrinos" (2001). hep-ph/0105182.

[72] The ATLAS Collaboration. "ATLAS Detector and physiscs performance Technical Design Report" (1999). See Chapter 20. on the searches for Supersymmetry. `http://press.web.cern.ch/Atlas/GROUPS/PHYSICS/TDR/access.html`

[73] J-L. Kneur. "Suspect". See the README and preliminary Users Manual. `http://www.lpm.univ-montp2.fr:7082/~kneur/suspect.html`

[74] T. Sjöstrand. *Comput. Phys. Commun.*, **82** (1994) 74–90. `http://www.thep.lu.se/~torbjorn/Pythia.html`

[75] Franck Bernard. "Caractérisation des performances d'un télescope sous-marin à neutrinos pour la détection de cascades contenues dans le cadre du projet ANTARES". Ph.D. thesis, Université de la Méditerranée, Marseille (2000).

[76] J. D. Jackson. "Classical Electrodynamics". Cambridge University Press, Second edition (1975).

[77] O. Suvorova. "Status and perspectives of Indirect Search for Dark Matter" (1999). Presented at the 2nd International Conference on Physics beyond the Standard Model. hep-ph/9911415.

[78] G. Giacomelli & A. Margiotta. *Nuovo Cim.*, **24C** (2001) 761–771. hep-ex/0010055.

[79] K. Greisen. *Ann. Rev. Nucl. Science*, **10**, 63 (1960).

[80] The Dumand Collaboration. "Proposal to construct a 148000 $m^2 sr$ Deep Ocean Lab for the study of High Energy Neutrino Astrophysics and Particle Physics" (1988). HCD-2-88, Univ. Hawaii.

[81] The Baikal Collaboration. *Nucl. Phys. Proc. Suppl.*, **91** (2000) 438–444. astro-ph/0011313.

[82] The NESTOR Collaboration. *Nucl. Phys. Proc. Suppl.*, **85** (2000) 153–156.

[83] The AMANDA Collaboration. *Nucl. Phys. Proc. Suppl.*, **91** (2000) 423–430. astro-ph/0009242.

[84] S. Barwick. "Potential of AMANDA-II in HE neutrino astrophysics". In "Proceedings of the 27th International Cosmic Ray Conference", volume HE, pages 1101–1104 (2001). Oral session HE2.5. `http://www.copernicus.org/icrc`

[85] E. Zas, F. Halzen & T. Stanev. *Phys. Rev.*, **D45**, 1 (1992) 362.

[86] I. Kravchenko et al. "Limits on the Ultra-high energy electron neutrino flux from the RICE experiment". astro-ph/0206371. Submitted to *Astropart. Phys.*

[87] C. Bratton et al. "Proposal to construct the GRANDE facility for the study of astrophysical sources and high energy particle interactions" (1988). UCI-Neut-88-39. GRANDE Proposal submitted to the DOE.

[88] K. Capelle, J. Cronin, G. Parente & E. Zas. *Astropart. Phys.*, **8** (1998) 321–328. astro-ph/9801313.

[89] X. Bertou et al. *Astropart. Phys.*, **17** (2002) 183–193. astro-ph/0104452.

[90] The ANTARES Collaboration. "ANTARES Technical Design Report (TDR) v1.0" (2001). ANTARES Internal. `http://antares.in2p3.fr`

[91] Fabrice Hubaut. "Optimisation et caractérisation des performances d'un téléscope sous-marin à neutrinos pour le projet ANTARES". Ph.D. thesis, Université de la Méditerranée, Marseille (1999).

[92] The ANTARES Collaboration. "The ANTARES Optical Module" (2001). To appear in Nuclear Instruments and Methods A. `http://antares.in2p3.fr/Publications`

[93] D. Lachartre. "ARS1 Analogue Ring Sampler and ARS CONV Users Manual version 1.9". ANTARES-Electronics/2000-006. ANTARES Internal Note.

[94] J-S. Ricol. "ARS Simulation". Talk given in the software session at the ANTARES Collaboration meeting at CERN (October 2001). ANTARES Internal presentation.

[95] F. Cassol-Brunner. "Alignment algorithms and software". ANTARES-Slow/1999-001. ANTARES Internal Note.

[96] V. Bertin et al. "Conclusions of the time calibration committee". ANTARES-Calibration/2000-007. ANTARES Internal Note.

[97] Nathalie Palanque-Delabrouille. "Blue and UV transmission in the ANTARES Site (Test 3′)". ANTARES-Site/2001-002. ANTARES Internal Note.

[98] Wolfgang Schuster. "Measurement of the optical properties of the deep Mediterranean - the ANTARES detector medium". Ph.D. thesis, St. Catherine's College, Oxford University. In Preparation.

[99] H. Lafoux. "K40 Simulation". ANTARES-Optical-Modules/1999-002. ANTARES Internal Note.

[100] P. Amram et al. *Astropart. Phys.*, **13** (2000) 127–136. astro-ph/9910170.

[101] P. Amram et al. "Sedimentation and fouling of optical surfaces in the ANTARES Site". To be submitted to Astroparticle Physics. ANTARES-Site/2001-006. ANTARES Internal Note.

[102] Jürgen Brunner. "Event generators for the ANTARES ν oscillation search". ANTARES-Software/1998-005. ANTARES Internal Note.

[103] Raj Gandhi, Chris Quigg, Mary Hall Reno & Ina Sarcevic. *Astropart. Phys.*, **5** (1996) 81–110. hep-ph/9512364.

[104] "The CERN Program library" (2000). `http://wwwinfo.cern.ch/asd/cernlib`

[105] G. Ingelman, A. Edin & J. Rathsman. *Comput. Phys. Commun.*, **101** (1997) 108–134. `http://www3.tsl.uu.se/thep/lepto`

[106] H. Plothow-Besch. *Comput. Phys. Commun.*, **75** (1993) 396–416.

[107] Giles Barr. "The separation of signals and background in a nucleon decay experiment". Ph.D. thesis, Keble College, University of Oxford (1987).

[108] The CTEQ Collaboration. *Phys. Rev.*, **D51** (1995) 4763–4782. hep-ph/9410404.

[109] P. Lipari & T. Stanev. *Phys. Rev.*, **D44** (1991) 3543.

[110] A. M. Cooper-Sarkar, R. C. E. Devenish & A. De Roeck. *Int. J. Mod. Phys.*, **A13** (1998) 3385–3586. hep-ph/9712301.

[111] The CTEQ Collaboration. *Eur. Phys. J.*, **C12** (2000) 375–392. hep-ph/9903282.

[112] M. Gluck, E. Reya & A. Vogt. *Eur. Phys. J.*, **C5** (1998) 461–470. hep-ph/9806404.

[113] Alan D. Martin, W. James Stirling & R. G. Roberts. *Phys. Rev.*, **D50** (1994) 6734–6752. hep-ph/9406315.

[114] Igor A. Sokalski, Edgar V. Bugaev & Sergey I. Klimushin. *Phys. Rev.*, **D64** (2001) 074015. hep-ph/0010322.

[115] L. B. Bezrukov & E. V. Bugaev. *Sov. J. Nucl. Phys.*, **32** (1980) 847.

[116] Igor Sokalski. Private Communication.

[117] Igor Sokalski. "Accuracy of the muon transportation: PropMu, MUSIC, MUM". ANTARES-Software/2001-005. ANTARES Internal Note.

[118] P. Antonioli, C. Ghetti, E. V. Korolkova, V. A. Kudryavtsev & G. Sartorelli. *Astropart. Phys.*, **7** (1997) 357–368. hep-ph/9705408.

[119] David J.L. Bailey. "Genhen v5r1 : Software Documentation". ANTARES-Software/2002-004. ANTARES Internal Note.

[120] Jürgen Brunner. "Updated tag list for the ANTARES event format". ANTARES-Software/1999-003. ANTARES Internal Note.

[121] T. Montaruli & A. Romeyer. "Conventional and prompt atmospheric neutrino fluxes". ANTARES-Physics/2001-005. ANTARES Internal Note.

[122] M. Honda et al. *Phys. Rev.*, **D52** (1995) 4985–5005. hep-ph/9503439.

[123] Vivek Agrawal, T. K. Gaisser, Paolo Lipari & Todor Stanev. *Phys. Rev.*, **D53** (1996) 1314–1323. hep-ph/9509423.

[124] G. Battistoni et al. *Astropart. Phys.*, **12** (2000) 315–333. hep-ph/9907408.

[125] G. Battistoni, A. Ferrari, T. Montaruli & P. Sala. "The FLUKA atmospheric neutrino flux calculation" (2002). hep-ph/0207035.

[126] C. G. S. Costa. *Astropart. Phys.*, **16** (2001) 193–204. hep-ph/0010306.

[127] P. Gondolo, G. Ingelman & M. Thunman. *Astropart. Phys*, **5** (1996) 309–332. hep-ph/9505417.

[128] Sergio Navas & Lee Thompson. "KM3: User guide and reference manual". ANTARES-Software/1999-011. ANTARES Internal Note.

[129] Jürgen Brunner. "Geasim: User manual". ANTARES Internal documentation. `http://antares.in2p3.fr/internal/software/geasim.html`

[130] D. M. Lowder, M. Moorhead, G. Shapiro, G. Smoot & S. Lowe. "Stage I R&D for a km-scale neutrino observatory: Physics and detector simulation" (1997). LBNL Report.

[131] Application Software Group. "GEANT 3.21: Detector description and simulation tool". CERN Program Library long writeup W5013 (1995). `http://wwwinfo.cern.ch/asdoc/geant_html3/geantall.html`

[132] A. Cade et al. H. Lafoux. "Latest Gamelle results". ANTARES-Optical-Modules/1998-001. ANTARES Internal Note.

[133] Nathalie Palanque-Delabrouille. "Optical background measurements - Test 1.10". ANTARES-Site/2000-003. ANTARES Internal Note.

[134] Nathalie Palanque-Delabrouille. "Light transmission in the ANTARES site - Blue or UV (Analysis of Test $3'$ data)". ANTARES-Site/2000-002. ANTARES Internal Note.

[135] Wolfgang Schuster. "Alternative analysis methods of ANTARES light propagation data in the UV (Test $3'$)". ANTARES-Site/2001-004. ANTARES Internal Note.

[136] Curtis D. Mobley. "Light and water: Radiative transfer in natural waters". Academic Press (1994).

[137] Curtis D. Mobley. *Appl. Optics*, **32** (1993) 7484–7505.

[138] Nathalie Palanque-Delabrouille. "Light transmission at the ANTARES site (blue light)". ANTARES-Site/1999-003. ANTARES Internal Note.

[139] V. A. Balkanov et al. "In-situ measurements of optical parameters in Lake Baikal with the help of a Neutrino Telescope" (1999). astro-ph/9903342.

[140] W.H.W. Schuster & David J.L. Bailey. "Optical properties at the ANTARES Site: What we know and what we don't know from Test$3'$". ANTARES-Site/2002-001. ANTARES Internal Note.

[141] L. A. Kuzmichev. "On the velocity of light signals in the deep underwater neutrino experiments" (2000). hep-ex/0005036.

[142] P. B. Price & K. Woschnagg. *Astropart. Phys.*, **15** (2001) 97–100. hep-ex/0008001.

[143] Nathalie Palanque-Delabrouille. “Light velocity at the ANTARES site”. ANTARES-Site/2000-004. ANTARES Internal Note.

[144] Xiaohong Quan & Edward S. Fry. *Applied Optics*, **34**, 18 (1995) 3477–3480.

[145] Jürgen Brunner. “The refraction index at the Antares site”. ANTARES-Site/2001-001. ANTARES Internal Note.

[146] E. Carmona (on behalf of the ANTARES Collaboration). “Reconstruction methods in the ANTARES neutrino telescope”. In “Proceedings of the 27th International Cosmic Ray Conference”, volume HE, pages 1283–1286 (2001). Poster session HE2.6: 268. `http://www.copernicus.org/icrc`

[147] A. Romeyer & Th. Stolarczyk. “Reconstruction algorithms: A handbook for developers”. ANTARES-Software/2000-001. ANTARES Internal Note.

[148] Jürgen Brunner. Private Communication.

[149] E. Carmona & J.J. Hernández. “A new reconstruction technique for ANTARES”. ANTARES-Software/2000-011. ANTARES Internal Note.

[150] E. Carmona. “Update of the new pre-fit for reconstruction”. ANTARES-Software/2001-006. ANTARES Internal Note.

[151] B. Effron & R. Tibshirani. “Introduction to the bootstrap”. Monographs on statistics and applied probability. Chapman and Hall (1993).

[152] David J.L. Bailey. “Calculation of effective muon ranges and application to overall effective areas”. ANTARES-Physics/2001-006. ANTARES Internal Note.

[153] Gary J. Feldman & Robert D. Cousins. *Phys. Rev.*, **D57** (1998) 3873–3889. physics/9711021.

[154] Doriane Stubert. Ph.D. thesis, Université de Haute-Alsace (2002). In Preparation.

[155] Susan Cartwright. “Comparison of Direct and Indirect Detection”. ANTARES-Physics/2002-001. ANTARES Internal Note.

[156] Emmanuel Nezri. Private Communication.

[157] P. T. Wallace. “SLALIB - Positional Astronomy Library”. Starlink user note 67 (1999). `http://star-www.rl.ac.uk/star/docs/sun67.htx/sun67.html`

[158] Lee Thompson. Private Communication.

[159] E. Carmona. “Status of the study of point like neutrino sources”. Talk given in the astrophysics session at the ANTARES Collaboration meeting at CERN (October 2001). ANTARES Internal presentation.

[160] A. Habig (on behalf of the Super-Kamiokande Collaboration). "An Indirect Search for WIMPs with Super-Kamiokande". In "Proceedings of the 27th International Cosmic Ray Conference", volume HE, pages 1558–1561 (2001). Poster session HE3.5: 325. hep-ex/0106024. `http://www.copernicus.org/icrc`

[161] Teresa Montaruli. Private Communication.

[162] A. Benoit et al. "Improved exclusion limits from the EDELWEISS WIMP search". astro-ph/0206271. Submitted to *Phys. Lett. B.*

[163] CDMS Collaboration. "Exclusion limits on the WIMP-nucleon cross-section from the Cryogenic Dark Matter Search". astro-ph/0203500. Submitted to *Phys. Rev. D.*

[164] R. Bernabei et al. *Phys. Lett.*, **B480** (2000) 23.

[165] G. Chardin. Talk given at the Les Houches Euro-Conference on "Neutrino masses and mixings" (2001). `http://marwww.in2p3.fr/Houches/Proceedings/DarkMatter/Chardin.pdf`